Optimizing the structure of scanning probes for atomic manipulation

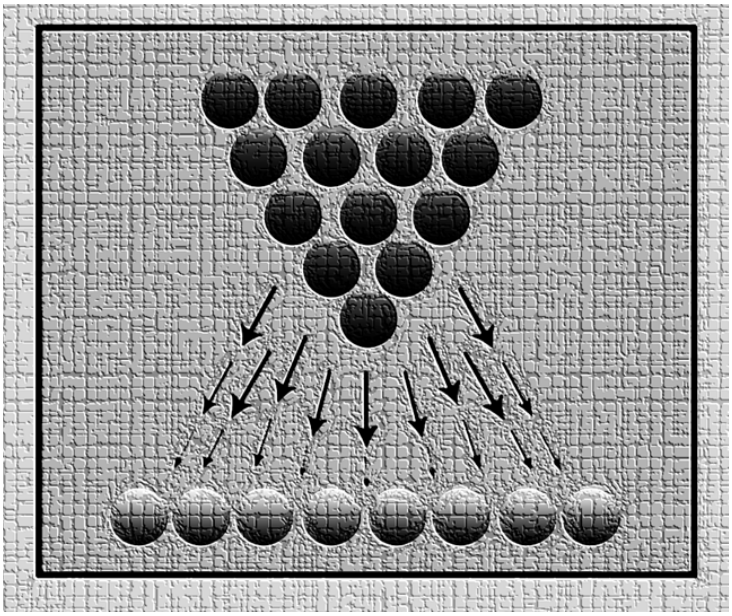

Morten Møller, MSc

School of Physics and Astronomy
University of Nottingham

Thesis submitted to the University of Nottingham
for the degree of *Doctor of Philosophy*

March 2017

Abstract

Scanning probe microscopy (SPM) allows us to directly measure the interactions between a probe and a sample at the atomic scale. Techniques such as non-contact atomic force microscopy (NC-AFM), allows us to to characterize the forces present on a surface, resolve the atomic structure of molecules or examine their chemical properties, while scanning tunneling microscopy (STM) allows their electronic properties to be characterized.

As the interactions take place at the atomic scale, the atomistic state of the probe apex plays a crucial role. In AFM, it is the atomic scale forces between the outermost atoms of the probe and surface that are dominant, while for STM the density of states (DOS) that contribute to tunneling are crucial. Therefore, understanding and controlling the tip termination is crucial to derive meaningful interpretations from experimental data. In this thesis, the role of the tip termination is examined for various surfaces and situations. We find that determining the "right" tip state depends critically on the experiment and several general strategies for shaping the tip apex into a preferred state are therefore outlined.

H:Si(100) surfaces were used as a substrate for lithographic patterning using STM. We have successfully implemented an automated extraction routine for performing large scale patterning with high fidelity and single atom specificity. Our ultimate goal is to combine the extraction routine with SPM image recognition software to allow analysis and manipulation of atomic scale features without human intervention. To perform manipulations reliably, the tip influence on "what we see" (tip imaging states), or specifically on what the recognition software can identify, needs to be considered. We find, counter-intuitively, that atomic scale manipulation with the highest fidelity occurs when silicon dimers are observed as rows as opposed to when atomic resolution imaging occurs.

The tip state influence on measuring surface diffusion of PTCDA on Ag(110) surfaces, was also investigated. We find that the adsorption kinetics of diffusing molecules can only be detected for specific tip imaging states. To allow examination with no-human intervention, the tip state needs to be carefully considered, and a combination of analytical and spectroscopic tools needs to be implemented in conjunction with the experiment.

Additionally, characterization of the tip apex was investigated at the tunnel junction between a STM tip and a metal surface using field emission measurements. Our results suggest that field emission measurements performed at the tunnel junction are sensitive to changes in the nanoscopic/mesoscopic tip apex structure, thus opening up the possibility of automating the process of characterization the tip apex.

List of Publications

M. Møller, S. Jarvis, L. Guérinet, P. Sharp, R. Woolley, P. Rahe, P. Moriarty

Automated extraction of single H atoms with STM: Tip state dependency

Nanotechnology, **28**, 075302 (2017).

M. Møller, P. Rahe, P. Moriarty

Diffusion paper - in preparation.

Acknowledgements

The long road it has taken to complete this thesis and the work it entails would not have been possible without the help and support of a great number of people.

First and foremost I would like to thank my supervisor Professor Philip Moriarty for his continuous and unwavering support through these trying, and rewarding, times. His constant support has been a source of great encouragement throughout my PhD.

Secondly, I would like to thank Richard Woolley which for a large period acted as my "day-to-day" advisor and supervisor for an extended period and whose expertise and guidance were instrumental to complete the work within this thesis.

From the Nottingham science group, I have had the pleasure of working with over the years include Samuel Jarvis, Philip Rahe, Laurent Guiërnet and Peter Sharp, which I would in particular like to thank for their many discussions and scientific collaborations.

On an more personal note, I would like to add thanks to other people such as, Alex Hayworth, Adam Sweetman, Ioannis Lekkas and to my family for their continuous support throughout my career.

Contents

Chapter 1

Introduction

Over the last century it has become increasingly possible to study the nature of matter at the atomic, molecular and supramolecular scale. This area of science is called nanoscience where typical interactions are on the scale of nanometers. In other words, nanoscience is the study of the fundamental building blocks of matter and the interactions between them.

Since its invention, the scanning probe microscope (SPM) has arguably been the most powerful and diverse tool for studying matter at the atomic scale. The basic principle of SPM is to place a sharp object to in close proximity to a surface. By moving the probe across the surface while controlling the interaction between probe and sample, the contours of the surface can be mapped. In principle, if the probe is atomically sharp, the atomic scale variation of the surface can mapped. For scanning tunneling microscopy (STM) the tunneling current between probe (tip) and sample is used as a feedback parameter to control the tip-surface interaction. This is related to not only the tip-sample distance but also the local density of states. For non-contact atomic force microscopy (NC-AFM) it is the gradient of the tip-sample force [1] that measured, which is dependent on both the tip-sample distance and the chemical nature of the surface under study.

The ability of SPM to measure such interactions on the atomic scale has lead to significant advances in a range of scientific fields. In Fig. 1.1 we highlight a history of groundbreaking scientific achievements using SPM is

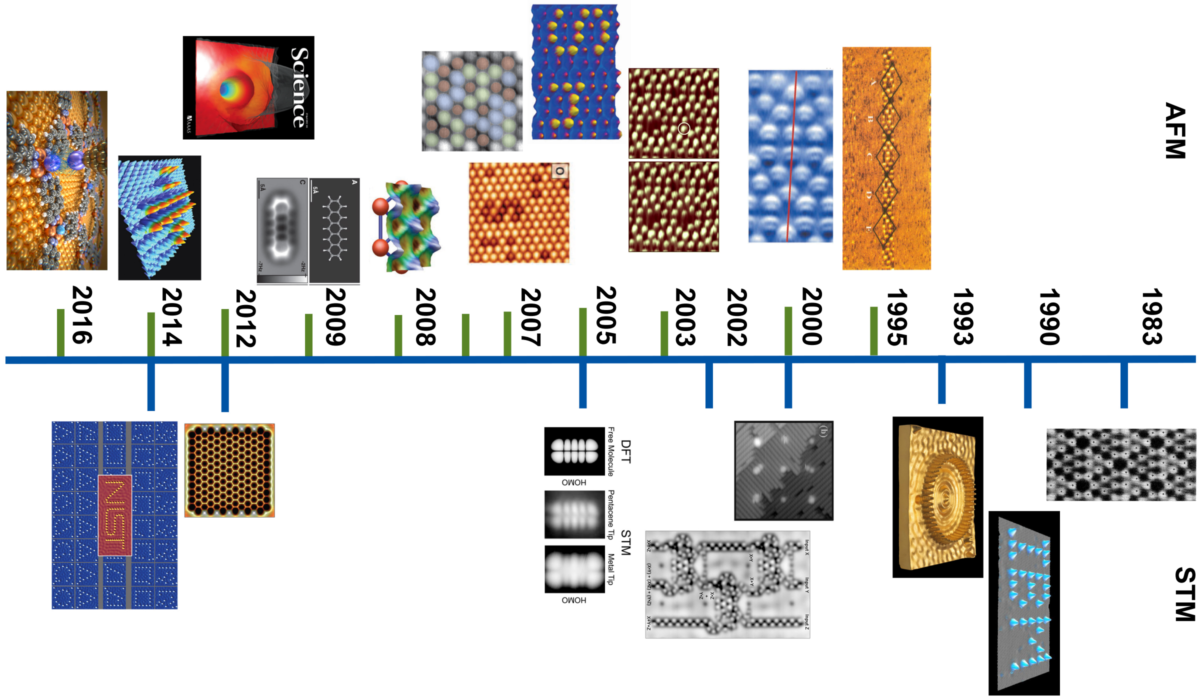

Figure 1.1: A selection of important historical advances in atomic manipulation using SPM: (from top to bottom, and left to right) first atomic resolution image using STM [2], first demonstration of single atom manipulation by STM [3], "quantum corral" structure created demonstrating reproducible atomic manipulation [4], first true atomic resolution cite [5], and "subatomic" resolution [6] using NC-AFM, "selective" single atom manipulation [7] and, assembly of an operational logic gate consisting of CO molecules [8] using STM. Sub-molecular resolution of molecular orbitals using STM [9]. Vertical [10], lateral [11] and, atomically precise vertical manipulation of individual atom(s) [12] using NC-AFM. First chemical identification [13] and, direct measurement of force needed to move single atom using NC-AFM. Sub-molecular resolution of molecules[14] and "sub-atomic" resolution imaging of the tip structure [15] using NC-AFM. Construction of graphene-like sheet using CO molecules by STM [16] and fabrication of Swiss-cross-like structure using bromine ions on insulating surface using NC-AFM [17]. Fully autonomous lateral manipulation of individual atoms on metal surfaces without human intervention using STM [18]. Measuring the van der Waals interaction between two individual atoms [19].

selected. As evidenced, the SPM and in particular the STM can be used for a wide variety of purposes, including atomic scale imaging and manipulation which is most relevant to this work. One of the main limitations of SPM is that the interactions between tip and sample are dependent on *both* systems. For STM, imaging of the surface is a convolution of the tip and surface states [20], whilst AFM imaging is dependent on the forces between the tip apex atoms and surface atoms. Thus, the apex structure needs to be considered when interpreting experiments.

This thesis focuses on examining the influence of the tip using SPM and providing strategies on how to derive meaningful interpretations from experiments. Our results are mainly based on STM experiments. The next three chapters therefore provide a detailed overview of the experimental methods and materials used throughout this thesis. In Chapter 2, the basic operation of STM and AFM is explained, along with descriptions on the tip-sample interactions governing these systems. In Chapter 3, techniques for controlling and characterizing the tip apex is presented. In Chapter 4, materials and methods used throughout our study is presented.

There are four results chapters in this thesis, all focusing on examining the tip apex influence on investigating surface phenomena. Chapter 5 is devoted to obtaining and investigating hydrogen passivated silicon surfaces (H:Si(100)-(2×1)), an interesting material for performing atomic manipulations using STM. We report that the observation of surface features on the atomic scale (tip imaging state) is crucially dependent on the tip apex structure.

Chapter 6, the influence of the tip imaging states observed in the previous chapter is examined when performing atomic manipulations with STM. Towards the end, for controlling the tip state for atomic manipulations, we have utilized automated STM lithography techniques for use on H:Si(100)-(2×1) surface. We show that by applying our lithography techniques on the small scale, single atom manipulations can be achieved with high fidelity using an automated hydrogen extraction routine. Our ultimate goal is to combine our extraction routine with SPM processing and decision-making software to allow autonomous atomic scale manipulations without human intervention.

Since our findings show that the atomic scale manipulations are dependent on what the surface "looks like" (tip imaging sate), atomic scale manipulation should only be performed when certain surface features are recognized.

In Chapter 7, the tip state influence on the diffusion behavior of PTCDA on Ag(110) surfaces is examined. We show that the tip (imaging) state plays a significant role for measuring the adsorption kinetics of surface adsorbates.

In Chapter 8, characterization techniques are used to determine the probe apex geometry while in close proximity to a conducting surface. The ultimate goal is to use these characterization techniques as diagnostic tools for ascertaining the quality of the tip apex and subsequently combine them with SPM decision making software for autonomous (re)-use.

Finally, in Chapter 9, the conclusions of this thesis are summarized and implications for future study are discussed.

Chapter 2

Scanning probe microscopy

A large part of this report involves imaging surfaces as well as performing atomic manipulation on these surfaces using scanning probe microscopes (SPMs) instruments. These instruments include scanning tunneling microscopy and atomic force microscopy. An overview of these techniques and their usage is therefore presented in this chapter.

2.1 Scanning tunneling microscopy

A scanning tunneling microscope (STM) uses the phenomenon of quantum tunneling to control the separation between an atomically sharp tip and a conducting surface. Because the tunneling current is exponentially dependent on the tip-sample separation, variations in the tunnel current can be used to generate exceptionally high resolution imaging. A schematic showing the basic setup of an STM is shown in Fig. 2.1.

By placing a sharp metallic tip close to a conductive surface, and applying a potential difference between them, a tunnel current can be measured. Using constant current mode, a feedback loop is used to adjust the tip position vertically (z) in order to maintain constant current while scanning the surface. The displacement of the tip can then be used to measure the topography of the surface.

The vacuum between the tip and surface acts as a potential barrier U

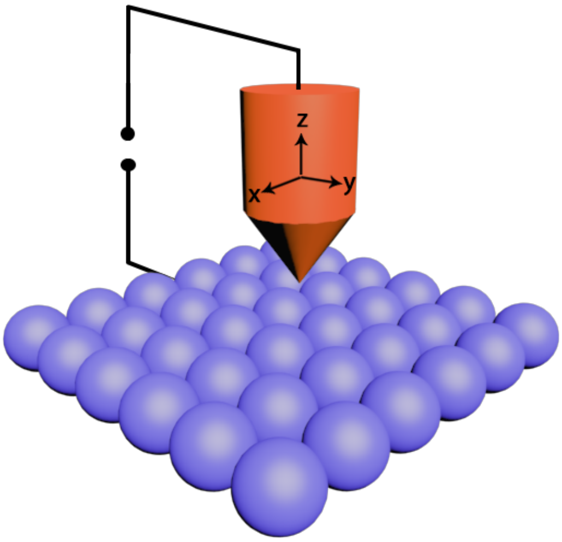

Figure 2.1: Basis of STM operation. By applying a potential difference between a sharp tip and a surface, a tunneling current is measured. When the tip scans the surface, the change in current can be used to record the topography of the surface at the atomic scale.

through which electrons can quantum mechanically tunnel. Electrons possessing an energy E, $(E < U)$, will have a finite probability of tunneling through the barrier. Fig. 2.2 illustrates the principle of tunneling through a square potential barrier of width d:

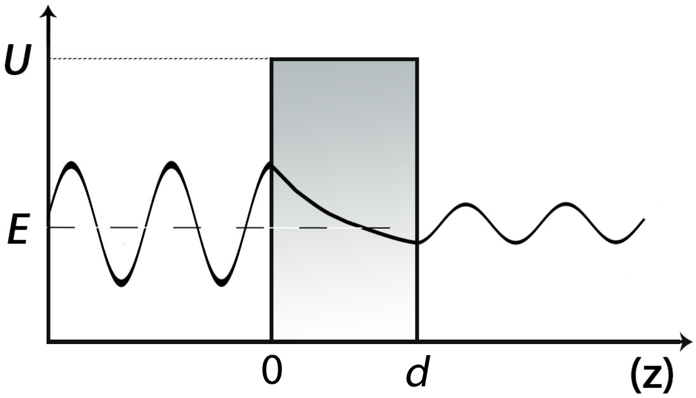

Figure 2.2: Schematic illustration of quantum tunneling through a rectangular potential barrier. The electrons move from left to right.

By solving the Schrödinger equation, the electron wave function, $\psi(z)$, can be described in the different regions as:

$$\psi(z) = \begin{cases} Ae^{ikz} + Be^{-ikz} & z < 0 \\ Ce^{-\kappa z} + De^{\kappa z} & 0 < z < d \\ Fe^{ikz} & d < z \end{cases}$$

where $k = \sqrt{\frac{2m_e E}{\hbar^2}}$, and $\kappa = \sqrt{\frac{2m_e}{\hbar^2}(U - E)}$ is the decay constant. A and B represent the amplitude of the incident and scattered components of the wave function, respectively. When $U > E$, κ is real, and the wave function will decay inside the barrier. The factors C and D describe the wave function decaying in both directions. Continuity relations at the boundaries require that the electron wave functions (and their derivatives) are matched. Combining these equations, the transmission coefficient, T, which is the ratio of the transmitted tunneling current, j_t, with respect to the incident current, j_i, can be approximated as

$$T = \frac{j_t}{j_i} \approx \frac{16k^2\kappa^2}{\left(k^2 + \kappa^2\right)^2} e^{-2\kappa d} \tag{2.1}$$

The tunneling current, which is related to the transmission coefficient, is then

$$I_t \propto e^{-2\kappa d} \tag{2.2}$$

For an ideal tunneling junction, the sample and tip are described as ideal metals in which the electron states are filled up to the Fermi energy E_f. Therefore the barrier height for tunneling $\phi = U - E$, is equal to the work function of the tip-sample material. Typical values of the work function are $\approx$ 4-5 eV [21], leading to $\kappa \sim \text{Å}^{-1}$. Moving the tip 1 Å away from the surface thus leads to approximately an order of magnitude drop in tunneling current. This sensitivity to tip-sample distance is the reason for the extremely high vertical resolution in STM, allowing atomic scale features to be observed.

Fig. 2.3 illustrates the tunnel junction for a tip and sample in electrical contact and separated by a vacuum. By applying a bias voltage V between the tip and the sample, the Fermi levels are shifted by eV with respect to each other, and the barrier now becomes trapezoidal in shape.

A positive tunneling voltage V is here used to represent a lowering of the electrostatic potential of the sample with respect to the tip. When the Fermi levels are aligned ($V = 0$), no net tunneling will occur. When a positive voltage is applied to the sample, a net flow of electrons will tunnel from the filled states of the tip into the empty states of the sample. When V is negative, electrons will tunnel from the filled states of the sample into the empty states of the tip.

The tunneling current, I, is therefore mainly dependent on the tip-sample separation, d, the applied voltage, V, and the number of energy states available for tunneling. These states can be expressed by summing over the density of electron states v for a given energy window. From this, the *local density of states* (LDOS) at position $\mathbf{r}$ close to the energy E can be found:

$$\rho(\mathbf{r}, E) = \sum_v |\psi_v(\mathbf{r})|^2 \delta(E_v - E) \tag{2.3}$$

The tunneling current is therefore highly dependent on the density of states, ρ, of both tip and sample, which are position dependent. For a tunneling current from tip to sample we get [22]:

$$I_{t\to s} = \frac{4\pi e}{\hbar} \int_{E_F}^{E_F+eV} \rho_t(E - eV)\rho_s(E) f_t(E - eV)(1 - f_s(E)) \left|M_{\mu v}\right|^2 dE \tag{2.4}$$

where $f(E)$ is the Fermi distribution function, and $|M_{\mu v}|^2$ represents the wave function overlap between electron states of the tip ψ_μ and sample ψ_v. The Fermi distribution function, ensures that only occupied states in the tip $f_t(E - eV)$ and unoccupied states in the sample $(1 - f_s(E))$ are counted when tunneling from tip to sample. From Equation 2.4 we observe that the tunneling current depends linearly on the LDOS of the tip and the sample.

To take into account the full tunneling current I_T, i.e. tunneling from tip to sample $I_{t\to s}$ and tunneling from sample to tip $I_{s\to t}$, we have to sum the different tunneling contributions together. Assuming the energy resolution is larger than thermal fluctuations, (i.e $E \gg k_B T$) the Fermi distribution function can be approximated as a step function, giving:

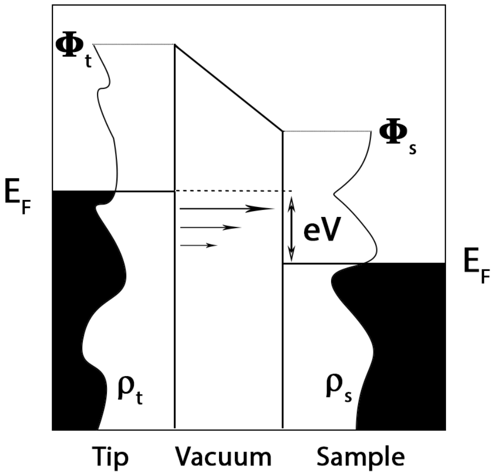

Figure 2.3: Schematic representation of the tunneling process between a tip with LDOS of ρ_t and a sample with a LDOS of ρ_s. When a positive voltage V is applied to the sample with respect to the tip, electrons will tunnel from the filled states of the tip to the empty states of the sample.

$$I_T = \frac{4\pi e}{\hbar}\int_{E_F}^{E_F+eV} \rho_t(E-eV)\rho_s(E)\left|M_{\mu v}\right|^2 dE \tag{2.5}$$

Determining the overlap function $|M_{\mu v}|^2$, is extremely difficult realistically, since it depends on knowing the spatial positions of the atoms in the sample and the tip as well as explicit expressions for their wave functions at given energies. Unfortunately, since both the atomic structure and chemical composition of the tip are generally unknown, $|M_{\mu v}|^2$ has to be approximated using a chosen model function. Using a 1D simplification, the overlap function can be replaced by a tunneling transmission probability $T(z, eV, E) = \sum_{\mu,v} |M_{\mu v}|^2$, giving a tunnel current of:

$$I_T \approx \frac{4\pi e}{\hbar}\int_{E_F}^{E_F+eV} \rho_t(E-eV)\rho_s(E)T(z,eV,E)dE \tag{2.6}$$

where

$$T(z,eV,E) = \exp\left[-2z\sqrt{\frac{m_e}{\hbar^2}(\Phi_t+\Phi_s-eV+2E)}\right] \tag{2.7}$$

for electrons of energy E and an applied bias of V. The tunneling current

(Eq. 2.5) is therefore dependent on the density of states of the tip and sample, and the transmission coefficient. For small biases, ρ_t and T are generally approximated as constant.

From Eq. 2.5, the tunneling current depends exponentially on the tip-sample distance. Thus scanning the tip laterally over the surface results in a modulation of the current, corresponding the surface corrugation. However, this is a very simplified picture. In reality it is not the corrugation of the surface, but the LDOS of the surface integrated over the $E_F < E < E_F + eV$ energy window, that is imaged. The images obtained on metallic surfaces, as they have an approximately constant density of states around E_F, therefore correspond to the geometric surface topography [23]. However, even for metallic surface, the obtained STM image might not represent the surface geometry accurately, because the LDOS might be affected by, for example, surface state modulations [24]. Equally as important as the surface LDOS is the tip LDOS, as the tunneling current is dependent on both. The resulting STM image is therefore a convolution of the tip shape and the sample features. In Fig. 2.4 an example is shown of how the surface features can appear different based exclusively on a change in the tip shape.

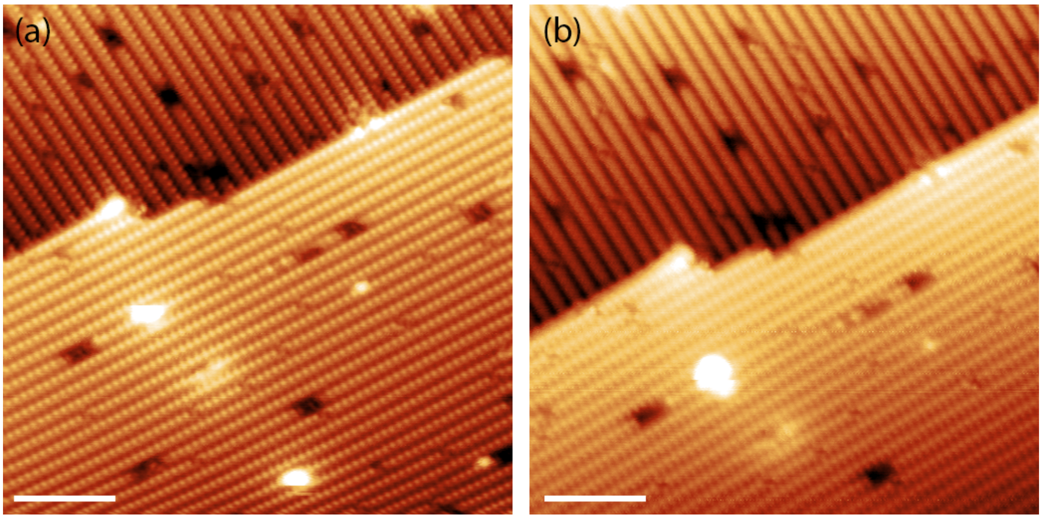

Figure 2.4: Topographic STM images of H:Si(100)-(2×1) surface. The surface features in (b) have changed from (a) due to a change in the tip shape. Images acquired at -2V, 100 pA. Scale bars correspond to 5 nm.

2.2 Atomic force microscopy

Unlike the scanning tunneling microscopy which relies on the tunneling current for imaging, atomic force microscopy (AFM) relies on the force between the tip and sample. As a result, the AFM is not restricted to studying conductive samples. The main problem with AFM is that although it is relatively straightforward to detect long range interactions between the tip and sample, observing variations in force over atomic length scales is considerably more difficult. The key element of an AFM is that the forces between the tip and sample are sensed by the deflection of a flexible beam (cantilever), as illustrated in Fig. 2.5.

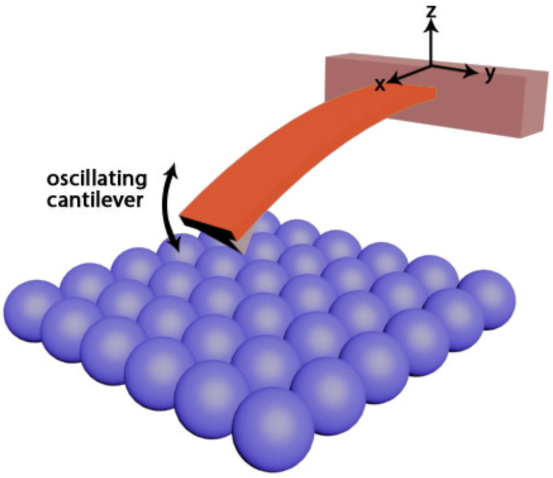

Figure 2.5: Basic setup of AFM operation. A flexible beam can be operated without (static mode), or with (dynamic mode) oscillating the beam. The interaction between tip and sample is used as a feedback signal to control the motion of the cantilever as it scans the surface.

When the cantilever is sufficiently close to a sample, a force will be felt between the tip and sample. This causes the cantilever to bend closer to the surface by a certain amount, depending on the cantilevers stiffness k. Simplistically, the tip-sample interaction force $F_{ts} = k\Delta Z$ is therefore proportional to the stiffness of the deflection and to the amount of displacement Z. From this simple relationship, the surface topography can be recorded using a feedback loop that maintains a constant deflection.

The deflection of the cantilever is usually performed using one of two approaches: (i) measuring the displacement of a laser beam reflected off the backside of the cantilever [25], or (ii) by measuring the deflection using piezoelectric materials [26]. The former method usually employs silicon cantilevers, while the latter is based on quartz tuning forks. For our purposes, Si cantilevers are mainly used, as tuning forks were not compatible with our particular variant of the commercial microscope used (section 4.7.1).

The AFM can basically be operated in two modes: static (contact mode) and dynamic (non-contact mode). In contact mode, the deflection of the cantilever is simply the deformation caused by pressing into the sample. The problem with this type of operation is that when the tip is close to the surface, the tip can experience a very high attractive force due to tip-sample interactions. Because the cantilever is very flexible, this can cause the tip to suddenly crash into the surface. This is known as the jump-to-contact instability. To image the surface in static mode, the stiffness of the cantilever needs to be greater than the maximum force gradient experienced by the probe. As a result, routine imaging with atomic resolution becomes extremely difficult.

To overcome this problem, the cantilever is operated in the non-contact (NC-AFM) mode, where the cantilever is mechanically excited to oscillated at its resonance frequency f_0 using a mechanical actuator. In this case, the oscillation provides a restoring force which the attractive forces needs to overcome in order to pull in the tip into the surface. The maximum attractive force will be felt at the maximum deflection. As a result, the jump-to-contact is avoided if the following criterion is satisfied

$$|kA| > |F_{max}| \tag{2.8}$$

where A is the oscillation amplitude. It is evident that the maximum attractive force in this case needs to be considerably higher than in the static case, as it needs to overcome the *product* of both the cantilever stiffness and the oscillation amplitude. The dynamic mode thus enables the tip to remain close to the surface without causing a 'jump-to-contact'.

NC-AFM can be operated by either responding to changes in amplitude (amplitude modulation, or AM-AFM) or through changes in frequency (frequency modulation, or FM-AFM). In FM-AFM, a cantilever is excited to oscillate at its resonant frequency f_0 while maintaining a constant amplitude. When the tip approaches the surface, the cantilever will experience a small interaction force which will change the oscillation frequency of the free cantilever (i.e. f_0) to $f = f_0 + \Delta f$. Therefore, the frequency shift can be used as a feedback signal for imaging the sample surface. The change in frequency can be measured very rapidly, on a time scale of $\tau_{FM} \approx \frac{1}{f_0}$. Additionally, due to the high resonance frequency, low frequency noise ($1/f$ noise) can be filtered out. By exciting the cantilever at very high frequencies ($10^5 - 10^6$ Hz) and using high Q-factor cantilevers ($10^4 - 10^5$), very small frequency shifts can be measured with very low noise. As a result, FM-AFM is very useful for examining atomic scale features. Since all AFM results in this report are exclusively obtained by the FM-AFM technique, all other AFM techniques will largely be omitted from further discussion.

Fig. 2.6 presents an overview of how the the different feedback signals are used in order to maintain stable FM-AFM operation. For stable operation, three different feedback signals are used: the surface topography, the oscillation frequency, and the oscillation amplitude. Initially, the oscillation frequency is recorded using a deflection sensor and then passed through a bandpass filter in order to remove noise from unwanted frequency bands. The signal is then split into different branches.

To ensure that the cantilever is driven at resonance, one branch is therefore devoted to measuring the amplitude (using a RMS-to-DC converter) and subsequently use it to calculate a driving frequency (using a PI controller) and the dissipation. In order to correctly drive the cantilever at the correct amplitude and resonance frequency, this signal is multiplied with the driving signal. For this purpose, a phased locked loop (PLL) is used. The PLL tracks the frequency of the cantilever and outputs a sinusoidal driving signal that has been phase shifted by $\frac{\pi}{2}$ with respect to the cantilever motion. For a second output, the PLL uses the phase tracker to record the difference between the oscillation frequency $f = f_{ref} + \Delta f$ and a reference frequency, f_{ref}. By

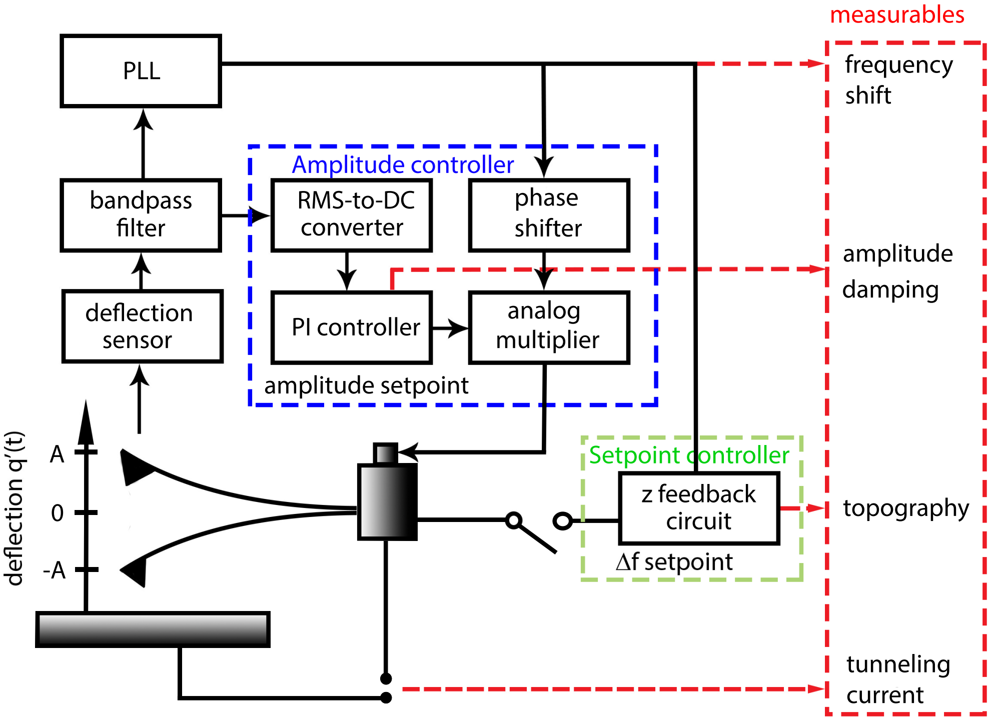

Figure 2.6: Overview of FM-AFM feedback controls used for regulating cantilever oscillation at resonance, constant amplitude, and frequency shifts.

setting f_0 as the reference frequency f_0, the recorded frequency shift Δf can then be used as the imaging signal.

The topography of the surface can be used as an additional feedback loop (z feedback) either to maintain a constant tip sample separation (constant height mode) or constant Δf feedback.

2.2.1 Relating Δf to force

As previously stated, the frequency shift Δf is used as the imaging parameter when operating in FM-AFM mode. We now derive the relationship between the frequency shift of the oscillating cantilever and the tip sample interaction force felt by the tip. The cantilever can be treated as a weakly perturbed harmonic oscillator with a motion of $q'(t) = A\cos(2\pi f_0 t)$, and a resonance frequency of $f_0 = \frac{1}{2\pi}\sqrt{k/m_{eff}}$, where A is the oscillation amplitude and

m_{eff} is the effective mass of the cantilever. When the tip is close to the sample, the force interaction F_{ts} will change the effective spring constant of the cantilever. For small amplitudes, the force gradient is small compared to k, and we can write the change in k as this change as $k' = k - \partial F/\partial z$ [27]. The oscillation frequency will therefore be shifted by an amount Δf relative to its free resonance, f_0, by

$$\frac{\Delta f}{f_0} \approx -\frac{1}{2k}\frac{\partial F}{\partial z} \tag{2.9}$$

For small amplitudes, the frequency shift is thus proportional to the force gradient, rather than the force. However, this approximation breaks down for larger amplitudes as the force gradient can change by orders of magnitude during one oscillation cycle. A more general expression for converting force to frequency shift has previously been derived by Giessibl [28]:

$$\begin{aligned} \Delta f(z_0) &= \frac{f_0}{2k}\left\langle K_{ts}(z)\right\rangle \\ &= \frac{f_0}{2k}\int_{-A}^{A} K_{ts}(z_0 - q')w(q', A)dq' \end{aligned} \tag{2.10}$$

where z_0 is the average oscillation height and the force gradient has been replaced by a weighted average force interaction $\langle F_{ts}\rangle$ for each oscillation multiplied by a weight function

$$w(q', A) = \frac{1}{\frac{\pi}{2}A^2}\frac{q'}{\sqrt{A^2 - q'}} \tag{2.11}$$

The weight function is expressed as a semicircle of a radius A (Fig. 2.7) divided by the area of the semicircle $\Gamma = \pi A^2/2$. Δf is thus a convolution of the force that has been weighted over the oscillation cycle. We observe that the short-range force interaction is weighted considerably higher using smaller amplitudes.

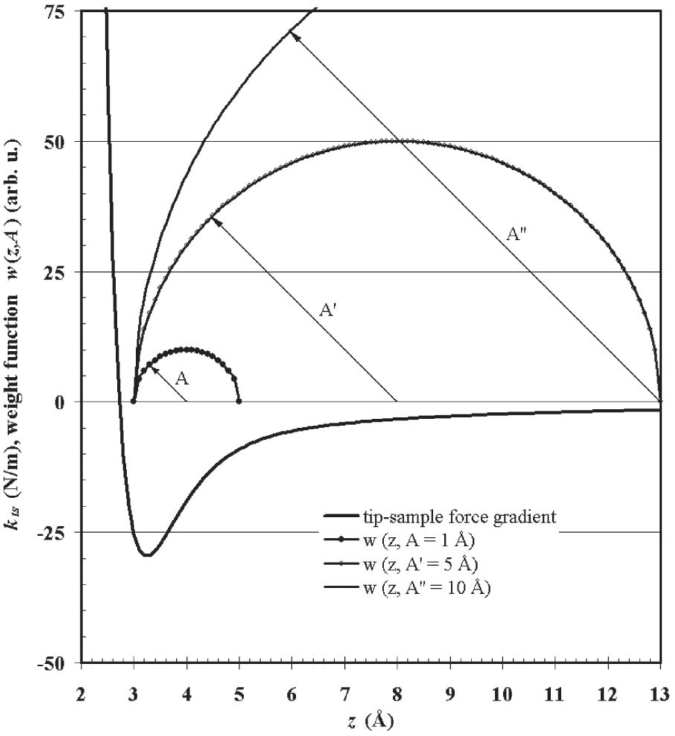

Figure 2.7: Frequency shift calculated as function of short and long range force as a multiplied by a weight function the size of the oscillation amplitude. For decreasing amplitudes, the short range forces are weighted to a higher extent. Taken from [1].

2.2.2 Force interactions

Now we focus on describing the different force contributions to the total force. The problem with AFM is that the measured forces are the sum of *all* interaction forces felt by the tip. These types of interactions can be broadly categorized into (i) long-range forces, such as van der Waals (vdW), electrostatic, magnetic and contact potential forces, and (ii) short range interactions arising from chemical interactions between the tip apex and the atomic features of the surface. For our experiments in UHV, the long-range forces play a role in a range of several tens of nm, while the chemical forces are in the range of several Å.

For AFM measurements, its often desirable to look at the short-range forces without interference from long-range forces. The problem is that even though several long-range forces, such as the magnetic and electrostatic forces, can be minimized under certain conditions such as using non-magnetic tips and minimizing the potential difference between the tip and sample, vdW forces can never be fully eliminated. VdW forces are essentially dipole forces between nearby atoms/molecules. Since a fluctuating dipole can always be induced by the charge distribution of a nearby atom, a minimum dipole interaction will always be present. As a result, separating the short range forces from the long range contributions is extremely difficult. However, it becomes possible to realistically approximate the different force contributions using a long-range vdW component and a short-range Morse type interaction:

$$F_{ts}(z) = -\frac{C}{z+\sigma} - 2\kappa E_{bond}\left(e^{-\kappa(z-\sigma)} - e^{-2\kappa(z-\sigma)}\right) \tag{2.12}$$

where C depends on the tip opening angle and the Hamaker constants of the tip and sample, E_{bond}, σ and κ are the bonding energy, equilibrium distance and decay length of the Morse potential, respectively. Using the derivations obtained by Giessibl [29], the resulting frequency shift can be approximated as:

$$\begin{aligned}\frac{\Delta f(z,A)}{f_0} = &-\frac{C}{kA(z+\sigma)}\left[F_1^{1,1/2}\left(\frac{-2A}{z+\sigma}\right) - F_2^{1,3/2}\left(\frac{-2A}{z+\sigma}\right)\right] \\ &- \frac{2\kappa E_{bond}}{kA}\Bigg\{e^{-\kappa z}\left[M_1^{1/2}(-2\kappa A) - M_2^{3/2}(-2\kappa A)\right] \\ &+ e^{-2\kappa z}\left[M_1^{1/2}(-4\kappa A) - M_2^{3/2}(-4\kappa A)\right]\Bigg\}\end{aligned} \tag{2.13}$$

where $F_c^{a,b}(s)$ is the hypergeometric function and $M_b^a(s)$ is Kummer's function [30]. Fig. 2.8 shows a plot of the different (a) forces using Eq. 2.12 and the resulting relative frequency shift from the total force (b) for different oscillation amplitudes.

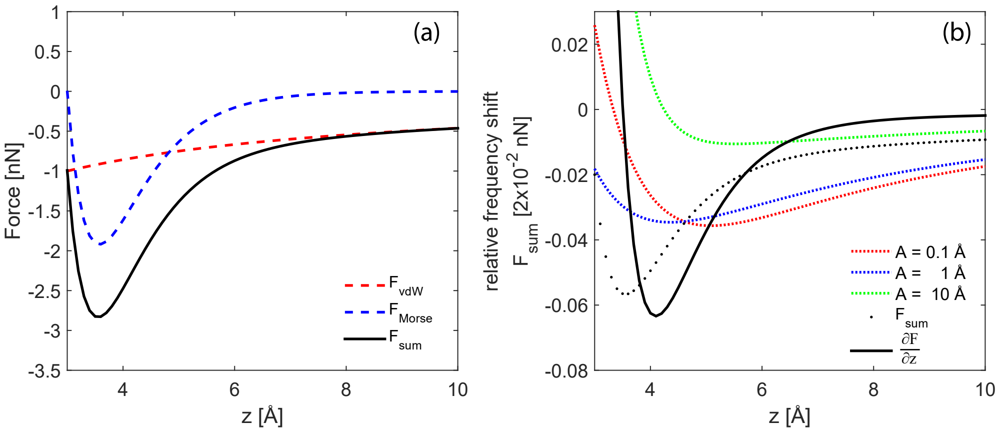

Figure 2.8: Forces and frequency shifts in FM-AFM as a function of distance between a conical or pyramidal shaped tip and a flat surface. (a) vdW (red) and Morse (blue) contributions to the force interaction, and their sum (black) calculated using the following parameters: $\sigma = 3$ Å, $E_{bond} = 2$ eV, $\kappa = 1.2$ Å^{-1}, $C = 6$, $k = 10\ N/m$. (b) Resulting relative frequency shift $\Delta f/f_0$ of the total force (F$_{sum}$, black dotted line) in **a** using different oscillation amplitudes: 0.1 Å (red), 1 Å (blue), and 10 Å (green). The relative frequency shift calculated from the force gradient according to Eq. 2.9 is shown in black.

We observe that for small oscillation amplitudes, the frequency shift has a higher contribution from the short-range forces (as illustrated previously in section 2.2.1) and is proportional to the force gradient, while for larger amplitudes the contributions of the long-range interactions becomes more significant. In other words, by reducing the oscillation amplitude, the sensitivity to the short range forces increases, while simultaneously reducing the sensitivity to long range forces. Thus, in order to properly measure short-range chemical forces, the amplitude of oscillation needs to be reduced as much as possible (≤ 1 nm).

Although Eq. 2.13 works reasonably well as an approximation for some tip shapes and a wide range of amplitudes, it has several limitations. In particular, the vdW contribution is not valid at very small distances. In addition, it does not take into account other force contributions, such as electrostatic or magnetic forces. In order to accurately calculate forces from Δf, the forces needs to be deconvoluted directly from Eq. 2.10. This was accomplished by Sader and Jarvis [31] through a complex mathematical derivation in order to obtain the force:

$$F(z_c) = \frac{2k}{f_0} \int_{z_c}^{\infty} \left[\left(1 + \frac{A^{1/2}}{8\sqrt{\pi(t - z_c)}} \right) \Delta f(t) - \frac{A^{3/2}}{\sqrt{2(t - z_c)}} \frac{d\Delta f(t)}{dt} \right] dt \quad (2.14)$$

where t is used as a dummy variable in order to prevent z_c from being used as both an integration variable, and a lower bound for the integration. Comparison between experimental and simulations, have confirmed the deconvolution formula to be extremely accurate, with a maximum error of 5% [31]. Forces obtained in this report are therefore derived using an algorithm [1] based on this equation.

---

[1] The code used to produce this data was written by Dr. Andrew Stannard at the University of Nottingham (2011).

Chapter 3

Tip modification and characterization

The STM is capable of achieving both atomic spatial resolution and performing atomic-scale lithography by hydrogen resist patterning. A crucial element for enhancing the spatial resolution of both the imaging process as well as the lithographic patterning process is the sharpness of the tip.

Numerous methods have been developed over the years for sharpening of metallic tips. Usually, the tips are first electrochemically etched *ex situ* producing tips with radii of 20-100 nm [32]. The tips are then brought *in situ* to a UHV chamber with a base pressure of 5×10^{-8} mbar (or lower) for further modification using various methods. Different *in-situ* methods include: annealing the tip either directly or indirectly, sputtering using noble gasses, or through the application of high electric fields (field emission). Field emission is primarily used to characterize the tip's radius, and we will therefore describe it in detail in Section (3.3). Only methods that are relevant to our experiments are included here.

To create large scale lithographic structures with atomic precision or perform atomic manipulation under various conditions (or for prolonged periods) requires the ability to perform quality control of the apex of the tip on-the-fly. We have adopted and adapted a technique [33] which allows the tip radius of curvature to be characterized and can be used in conjunction with other processes carried out on the surface (lithography, imaging, spectroscopy etc...). The method will be discussed in detail in Section 3.3.2.

3.1 Tip treatment methods

A vital aspect for performing any STM experiment is the influence of the tip properties on the quality of the obtained data. The two key features relevant for the performance of the tip are its shape and its chemical composition [34]. The chemical composition involves the bulk and surface properties of the tip material and the presence of any materials properties as well as the presence of contaminants on the tip surface. It is essential to remove any contaminants, as they can severely distort the measurements in numerous ways. The presence of an insulating layer on the tip act as an additional tunneling barrier for the electrons, causing a higher instability of the tunneling current. This could lead to all kinds of problems, such as reduced resolution, crashing of the tip into the surface, causing damage to both the tip and sample [35], as well as severely distorting any spectroscopic measurement. Tungsten (W) wires were therefore used to create STM tips, as they possess good conducting properties as well as being very hard and mechanically stable.

3.1.1 Electrochemical etching

In electrochemical etching, the tungsten wire is immersed into a NaOH solution where the tungsten wire functions as one electrode and a ring-shaped stainless steel wire functions as a counter electrode. When a voltage is applied between the two electrodes, the tungsten starts to dissolve, leading to the formation of a neck on the wire, as illustrated in Fig. 3.1.

As the tungsten slowly dissolves, the neck becomes thinner until it finally breaks. The resulting tips can have a radius of curvature of the order of 10 - 100 nm. When the breaking of the neck is detected (rapid decrease in current), the tips are taken out of the solution and rinsed in deionized water

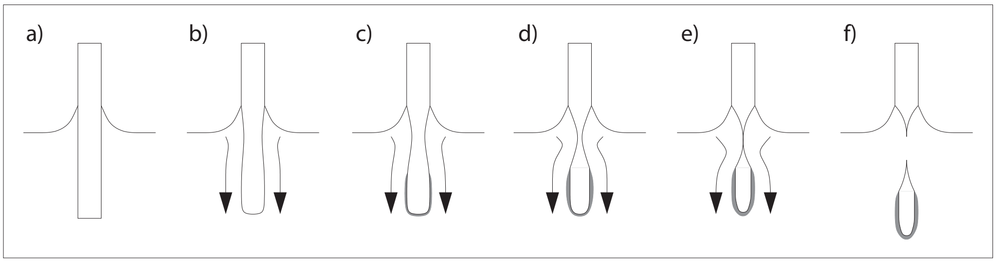

Figure 3.1: Illustration of the electrochemical etching process. (a) shows the formation of the meniscus. (b) to (e) show the flow of oxidized tungsten anions (WO_4^{2-} which are soluble) toward the lower end of the wire, the formation of a dense oxide layer around the bottom of the wire and the necking phenomena in the meniscus. (f) Drop-off: the lower end of the wire breaks off. From [36].

in order to prevent further etching. The tips are now ready to be transferred to the UHV chamber for further treatment.

3.2 *In-situ* tip treatment methods

The major disadvantage of electrochemical etching arises from the exposure of the metal to contaminants and ambient conditions. The resulting tips are covered in a native oxide layer which needs to be removed before using the tip for STM experiments [35, 37, 36]. In addition, the tips end up having variable radii, none of which are remarkably sharp. For our purposes, the tips are therefore further modified *in-situ* under UHV conditions using several techniques. The various techniques include annealing, self-sputtering and field emission characterization which have very similar experimental setups. We therefore illustrate them together in Fig. 3.2.

In the UHV chamber, the tips are initially degassed for 12-16 hours by positioning them on a mechanical arm which is resistively heated to 160 °C. The tips are then transferred to a tip-treatment device where annealing, self-sputtering and field emission procedures can be carried out. Here the tip is put in close proximity to a looped filament (1-2 mm). The loop serves as a counter electrode for all three techniques, and as both filament and "counter

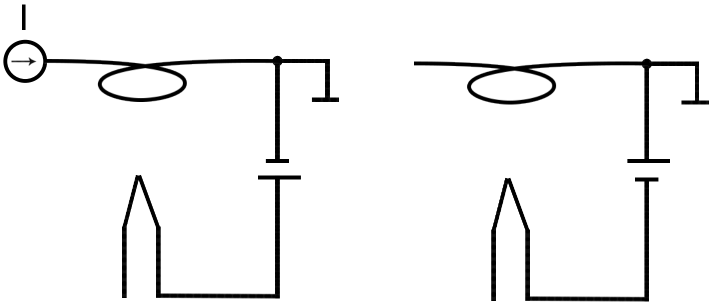

Figure 3.2: Schematic of setup for (left) annealing, (right) self-sputtering and field emission.

electrode" for annealing the tip.

For annealing, a high positive bias V_{HV} is applied to the tip with respect to the filament, (+1 kV). This causes the filament to thermally emit electrons, which are accelerated toward the tip, locally heating the tip up.

For self-sputtering and field emission, the tip is also brought in close proximity to the filament. However, in these cases the polarity is reversed compared to annealing. This causes electrons to be emitted from the tip. Also, for self-sputtering, a gas is additionally leaked into the chamber. The electrical field from the tip causes the gas to be accelerated toward the tip, sharpening it.

3.2.1 Annealing

Annealing tips *in situ* is a very useful way of getting rid of contaminants after tip etching. Most adsorbants are removed at relatively low temperatures. The native oxide layer starts to evaporate at temperatures above, 750 to 800 °C [22, 38]. However, the diffusion of surface atoms increases rapidly at these high temperatures, leading to blunting of the tip [39]. The annealing process is dependent on how much power is applied to the tip, which in turn is dependent on the potential difference between the tip and filament, and on the amount of current that directly hits the apex of the tip. We can thus control the annealing of apex the tip to a certain extent based on how much power we apply to the tip.

The key issue for sharpening and cleaning the tips by annealing is to ensure that the end of the tip reaches high enough temperatures to evaporate the oxide, but at the same time does not get too much power which could melt (and blunt) the tip. In our tip preparation protocol, the voltage was usually kept constant at 1 kV and the emission current was altered. The power is slowly increased until an emission current of 20 mA is detected. As the tip becomes sharper (and cleaner) the emission current starts to rise. By repeatedly lowering the power to ensure that the emission current will remain in the 20-30 mA range, we ensure that the end of the tip is not exposed to too much power, causing excessive blunting. The procedure usually takes 5-10 minutes. The majority of tips prepared this way usually provide atomic resolution images in the first scan (when imaging Si(100) surfaces).

3.2.2 Ion sputtering

STM tips can also be cleaned and sharpened using techniques based on ion sputtering [40, 35]. These techniques are based on using ions to bombard the surface of the tip. The tip material is in effect peeled off, producing a sharper tip. Usually noble gases (in our case, argon) are used as the source of ions to avoid unwanted chemical reactions with the surface. The ions can either be focused in a beam using a gun, or by applying a strong electric field, directed toward the tip. While focused ion beam (FIB) [41] milling stems from the former category, conventional sputter erosion (CSE) [42] and self-sputtering Schiller decapitation [42] fall into the latter category.

The advantage of sputtering, as opposed to annealing, is that the sputtering process is more easily controlled as well as producing sharper tips which are well defined [43]. CSE and Schiller decapitation seem to produce tips of 4-20 nm radii [44, 45], with a lower limit of 4-6 nm [46, 47], while FIB can produce tips with 3-4 nm radii.

The Schiller decapitation process is conceptually quite simple. Similar to the process described in section 3.2, the tip is brought in close proximity to a counter electrode and a noble gas is leaked into the UHV chamber. A high negative bias is then applied to the tip with respect to the counter electrode, causing the gas to ionize and accelerate toward the tip. The subsequent bombardment sharpens the tip. The disadvantage of this method, is that the sharpening process is dependent on the angle of incidence of the impinging ions from the surrounding tip and is dependent on the shape of the tip. This usually leads to the formation of neck on the end of the tip. When the neck becomes wide enough the end of the tip breaks off. The resulting end of the tip is usually much sharper than before [42]. The Schiller decapitation process has several disadvantages, making it unsuitable for reliable tip modification. Firstly, the necking effect does not always form, as it is highly dependent on the the original tip shape. Also, after the necking has fallen off (which can be detected by a rapid drop in current), the sputtering process needs to be stopped quite rapidly, in order to prevent unwanted sharping of the apex. This makes the sharpening quite tedious and unreliable.

Ideally, for performing manipulations on surfaces using SPM, the tip apex should be as atomically sharp as possible. We believe that ion sputtering using the Schiller decapitation process, provides the most opportune tip treatment method using our current setup, as it is capable of providing extremely sharp tip apexes in a reproducible fashion and the technique can, in principle, be automated. However for our purposes, it is the reproducibility of our tip characterization methods that are crucial, and not the sharpness of the tip. As a result, for field emission characterization of the tip apexes (next section), tips were primarily either degassed or annealed to, remove unwanted contaminants, provide variable tip apex geometries which can be compared, and for stabilizing the tip structure.

3.3 Tip characterization methods

Different methods exist for characterizing STM tips. A direct way to determine tip morphology is to visualize them. This can be done at low resolution using an optical microscope, which allows one to see if the tip is macroscopically deformed or irregularly shaped. SEM and TEM allows determination of the tip structure on the nanometer scale but they are time consuming and have to be performed *ex situ*.

Field emission relies on generating electric fields which are dependent on the tip geometry and its physical properties. This is highly advantageous, since it allows the tip geometry to be estimated under opportune conditions, provided specific diagnostic techniques are used. For our purposes, we intend, in the long term, to fully automate estimating the tip radii when the tip is in close proximity to a conducting surface. This characterization method can then be used in parallel with atomic manipulation studies carried out on the surface.

3.3.1 Field emission theory

Field electron emission is a quantum tunneling effect, in which electrons tunnel through the vacuum potential barrier [48]. In metals, electrons reside in a potential well, mainly due to their attraction to the positive ions. For the electrons to escape into vacuum, they must possess enough energy to overcome the potential barrier. For an electrically neutral metal, the height of the potential barrier equal to the work function, $U(x) = \Phi$, as shown in Fig. 3.3(a).

The work function ϕ, is defined as the minimum energy an electron at the Fermi level must possess in order to escape into vacuum. When an external electrostatic field is applied, $U_f(x) = -e\mathbf{E}x$, the shape of the vacuum potential barrier is substantially modified, as shown in Fig. 3.3(b). Here $\mathbf{E} = Ee_x$ is the applied electric field. The effective potential experienced by the electrons can now be described as:

$$U_e(x) = \Phi - e\mathbf{E}x \tag{3.1}$$

As a result, an electron close to the Fermi level therefore experiences a triangular shaped potential barrier, instead of the abrupt step. This allows the electrons to quantum mechanically tunnel through the barrier without requiring enough energy to hop over it, in order to be emitted into vacuum [49]. This is known as field emission. It becomes immediately apparent

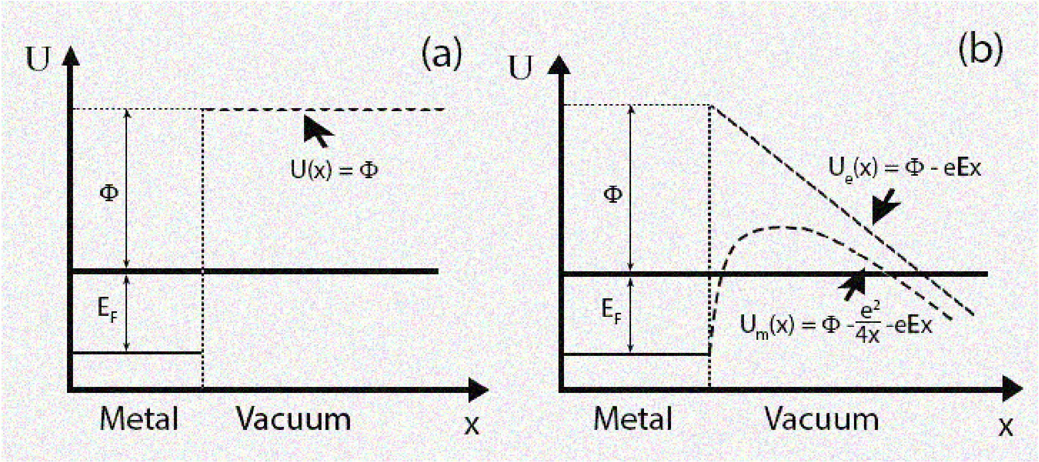

Figure 3.3: Simplified electron field emission model. Potential energy experienced by an electron at a metal surface without (a) and with (b) an external electrostatic field, $U_f = -e\mathbf{E}x$, and when the image charge, $U_i = -\frac{e^2}{4x}$, is considered. The applied electrostatic field modifies the potential barrier so that electrons at the Fermi level can tunnel through it.

that increasing the applied field, E, narrows the tunneling barrier, and thus increases the tunneling probability. The field emission current density J for a conducting surface can be expressed as a general function of the supply of electrons to the barrier from the inside, $n(\delta)$, and the transmission coefficient T of the barrier:

$$J = e\int_0^{\infty} n(\delta)T(\delta, E)d\delta \tag{3.2}$$

The supply function is the fraction of the electrons energy that is associated with the component of momentum normal to the surface of the conductor. The emitted current is therefore dependent on the electron concentration in the conductor, the electron energy distribution ($n(\delta)$) as well as on the height and shape of the barrier, which determines T. Fowler and Nordheim provided a simple approximation for the emission current density J through an infinite plane barrier on metal surfaces, as a function of the applied electric field and work function:

$$J = a\tau_F^{-2}\frac{E^2}{\phi}\exp\left(-\alpha\frac{b\phi^{3/2}}{E}\right) \tag{3.3}$$

where $a = \frac{em_e}{2\pi^2\hbar^3}\left(\frac{e}{g_e}\right)^2$, $b = \frac{2}{3e}g_e$, and $g_e = 2\sqrt{\frac{2m_e}{\hbar^2}}$ are constants, τ_F and α are correction factors for the interaction of an electron outside the metal with its image charge. This equation is known as the Fowler-Nordheim (FN) equation.

3.3.2 Field emission: tip characterization

Field emission can be used to directly ascertain the geometry of the field emitter. Based on the FN equation, the tunneling current is dependent on the applied electrostatic field. The electrostatic field in turn, is dependent on the shape of the emitter. Crudely speaking, surfaces with high curvature will have higher electric fields. Assuming the end of the tip to be spherical of radius R, the relationship between the electric field emanating from the tip can be approximated as

$$E = \frac{V}{kR} \tag{3.4}$$

where V is the applied voltage and k is the geometrical factor of the tip. Sharper (smaller radius) tips produce larger electrostatic fields, and thus higher emission current for a given bias. This can be used to ascertain the tip radius of curvature. The geometrical factor takes into consideration that the end of the tip is positioned on a long shank, which also contributes to modifying the electric field [49]. An approximate value is $k \approx 5$ for most tip geometries, although in some cases it can be as high as 35.

By inserting equation (3.4) into equation 3.3, we get

$$J = a\frac{\tau_F^{-2}}{\phi}\left(\frac{V}{kR}\right)^2 \exp\left(-v_F b\phi^{3/2}\frac{kR}{V}\right) \tag{3.5}$$

which can be transformed into:

$$\ln\left(\frac{I}{V^2}\right) = -v_F\phi^{3/2}kR \cdot \frac{1}{V} + const. \tag{3.6}$$

From Eq. 3.6 it can be seen that a plot of $\ln\left(\frac{I}{V^2}\right)$ vs. $1/V$, also called a FN plot, will give a straight line of slope $-v_F\phi^{3/2}kR$ [49]. The radius of curvature of a tip apex can therefore be extrapolated from the slope of a FN plot obtained using I - V characteristics.

A more accurate calculation of the FN equation requires taking into account the effect of the image charge. Recall from Fig. 3.3 that the addition of an image charge results in a reduction in the effective area of the triangular tunneling barrier which differs by the uncorrected area by

$$\alpha = \sqrt{1 - y} \tag{3.7}$$

where $y = 3.8 \times 10^{-4} E^{\frac{1}{2}} / \phi$. To correct for this deviation an experimental procedure described in [49] was implemented. Field emission measurements have shown that the FN equation is extremely accurate for a planar emitter. However, for very sharp emitters (R $\leq$ 20 nm) the FN equation breaks down[50], and Cutler et. al. [51] have shown that ultra-sharp emitters can deviate from FN emission theory by orders of magnitude for tip radii $<$ 10 nm. To more accurately ascertain the field emission process of atomically sharp emitters, more sophisticated modeling treatments are necessary, which is beyond the scope of this thesis.

In practice, field emission can be performed by applying a negative bias to an emitter with respect to a counter electrode, as illustrated in Fig. 3.4. For

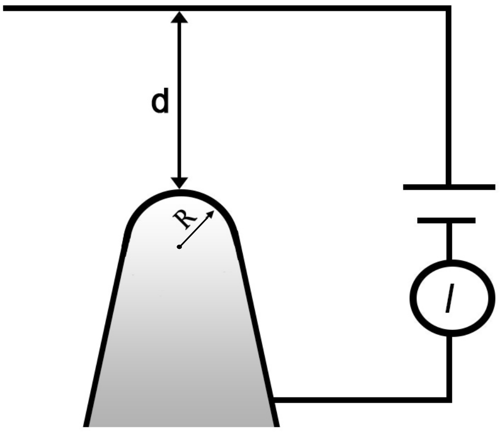

Figure 3.4: Schematic of experimental setup used for field emission. A negative bias is applied between an emitter (tip) and a counter electrode at a separation d.

our purposes, field emission from the tip can therefore be measured using two different methods (i) using the setup described in Section 3.2.1 or (ii) using an STM tunnel junction described in Section 2.1. In the tunnel junction, a potential barrier exists between the tip and the conducting surface.

By applying a bias to the tip with respect to the sample, a current can be measured. As a result, electrons can either tunnel directly into vacuum (field emission) or tunnel between overlapping states of the tip and sample (metal-vacuum-metal (MVM) tunneling). In other words, both tunneling phenomena coexist. Fig. 3.5(c) shows the tunnel current (not drawn to scale) can be divided into 3 different regions based their contributions to the total current. At low bias ($eV \ll \Phi$) and small tip-sample separation, MVM tunneling will be dominant. As the bias of the tip is increased, the barrier for field emission is lowered, causing an exponential increase in emission current. The MVM tunneling current on the other hand, only increases as a result of the availability of more states to tunnel into. As a result, at higher bias, $eV > \Phi_S$ (Fig. 3.5(b)), field emission will be dominant.

Field emission in turn, is determined by the electric field strength at the end of the tip. By operating the STM at constant current mode, the electric field, E_t, at the emitter surface is held constant [52]. However, the electric field between the emitter surface and the metallic surface is dependent on the tip geometry and the tip-sample separation. The current between the tip and sample will be spread outwards in the direction of the electric field lines of the tip (Fig. 3.5(d)). As a result, the current density that impinges on the surface will be dependent on the the electric field distribution on the tip surface and between the tip and sample. The current density is therefore dependent on the geometry of the tip. Sharper tips produce higher electric fields, and therefore higher current density for a given bias and tip-sample separation. The electric field between the tip and sample can therefore be used as a measure to determine the tip geometry based on how the tips behave at different tip-sample separations as a function of bias [33]:

$$z(V) = \frac{V}{E_t}\left(1 - \frac{V}{E_t R}\right)^{-1} \tag{3.8}$$

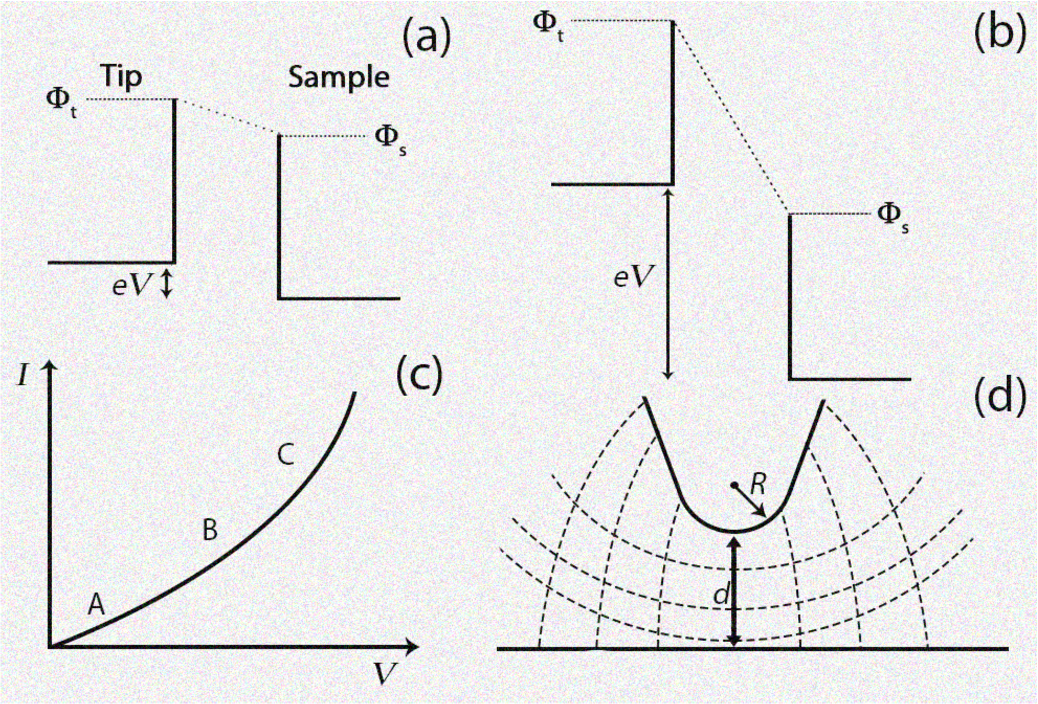

Figure 3.5: Field emission in tunnel junction. When applying a bias between tip and sample, both field emission and MVM tunneling occur. At low bias and small tip-sample separation ((a), region A in (C)), MVM tunneling is dominant. Increasing the bias, causes field emission to increase faster than MVM tunneling. At intermediate bias, (region B in (c)) the tunneling current will be a mixture of the two. At higher bias ((b), region C in (c)), field emission is dominant. (d) Electric field distribution between tip and sample.

where $E_t \approx E_s(z+R)/R$ and $E_s = V/z$. Sharper tips will thus move further away from the surface than a blunt tip at a given bias, when operating in constant current mode.

Field emission can thus be used to estimate the structure of a probe directly at the tunnel junction, which in principle, can be applied to any conducting surfaces. For full autonomous tip characterization without human intervention at the tunnel, the reliability of field emission characterization is examined in Chapter 8, and protocols for tip characterization are implemented.

Chapter 4

Materials and Techniques

A large part of the results sections in this thesis involve the fabrication, investigation and manipulation of semiconductor surfaces using various experimental techniques. Consequently, this chapter is divided into the following sections. First we will elucidate the various surface properties and how to obtain specific reconstructions of interest. Of particular emphasis is the H:Si(100):2×1 surface, which was chosen as a model surface for performing advanced atomic manipulations. We then move on to explaining the various techniques we used for investigating and manipulating these surfaces. These techniques mainly involve using STM and AFM lithography for manipulations as well as using current and force measurement techniques for investigating their physical, chemical and electronic properties which will briefly be reviewed.

4.1 Silicon

Like several other group IV elements such as tin and germanium, the bonding arrangement of silicon crystals is that of the diamond structure, where each atom is tetrahedrally bonded to its four nearest neighbors due to sp^3 hybridization of the orbitals [53]. The diamond bulk lattice structure consists of two overlaying face-centered-cubic (fcc) lattices displaced from each other along the diagonal of the unit cell.

When the silicon crystal is cleaved or grown to expose a surface, some of these bonds will break, creating dangling bonds on the surface. The number and direction of these dangling bonds will depend on the orientation in which the silicon crystal has been cut. The dangling bonds will try to re-bond in order to lower the surface energy, resulting in different reconstructions of the surface structure [53]. The presence of dangling bonds on the surfaces is the reason for the high chemical reactivity of clean silicon surfaces. This is why UHV conditions are necessary in order to prepare and investigate silicon surfaces. Otherwise, exposure to air or other contaminants quickly leads to oxidation of the surface.

4.1.1 Silicon (100)

By macroscopically exposing the silicon wafer along the (100) plane, the surface dangling bonds are very unstable and will consequently react to lower the surface energy. Heating an exposed Si(100) surface to 1200°C in UHV removes the oxide layer and leads to the formation of dimer rows. The dimers are formed by pairing of the two dangling bonds on each dimer along the (110) direction [53]. The pairing takes place, because the surface free energy is lowered as a result of reducing the number of dangling bonds on the surface. The initial model based on LEED measurements [54] suggested that the dimer pairs form up symmetrically, giving a (2×1) reconstruction. The Si atoms on the dimers are bonded through a strong σ bond, as well as a weaker π-like interaction between the dangling bonds. Because the silicon lattice has a tetrahedral bonding arrangement, the direction of the bonds will be rotated 90^o each time one step height is added. Consequently the dimer rows on different terraces separated by a monoatomic step will be perpendicular to each other. As such, two rotated domains, (2×1) and (1×2) will coexist across terraces.

The symmetric dimer model was later modified into a buckled dimer model [56] in order to coincide with experimental data [57]. The buckling arises as a result of Jahn-Teller distortion of the lattice, causing charge transfer from the lower to the upper dimer atom. As a result, one of the Si

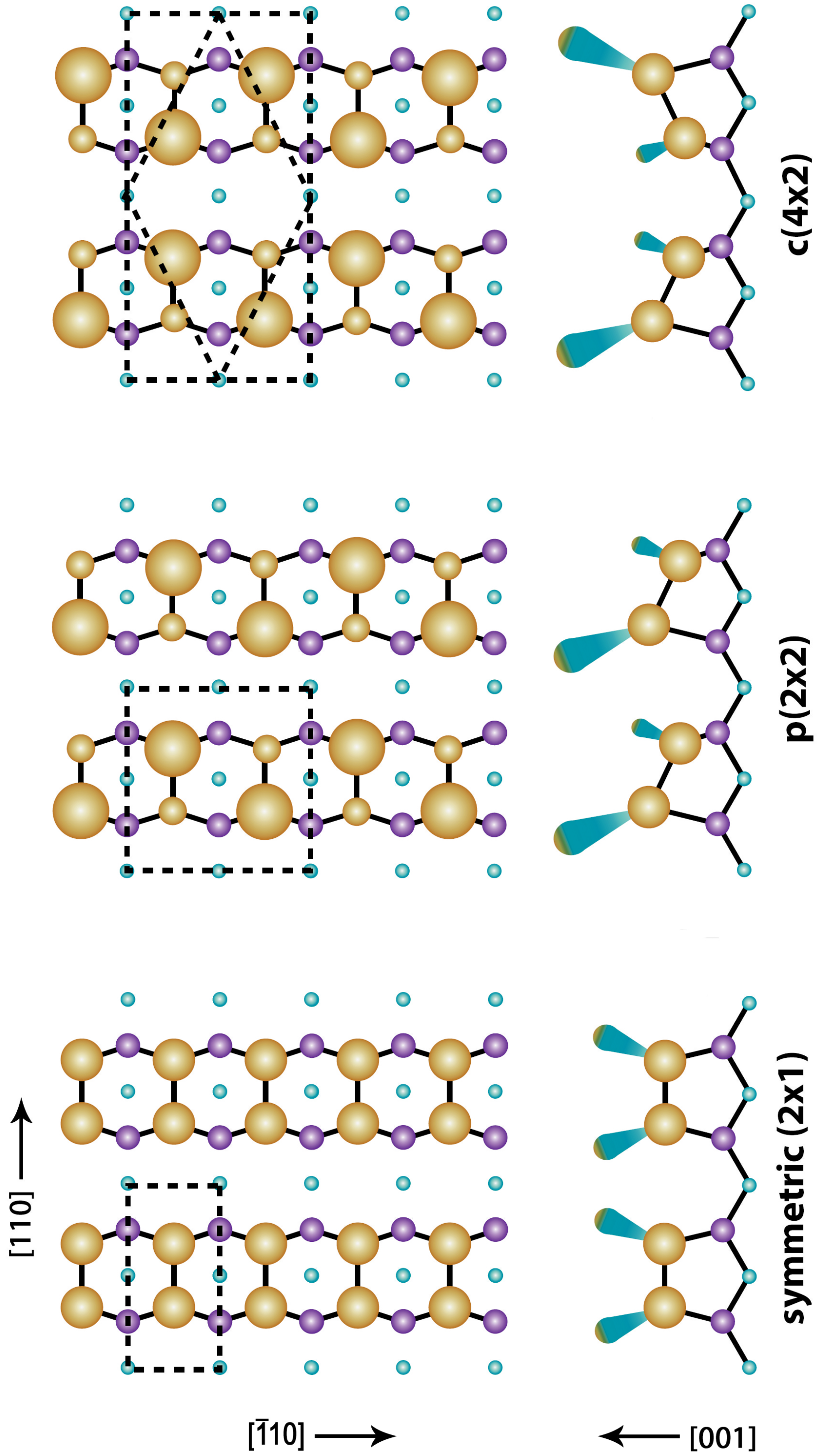

Figure 4.1: Different reconstructions of the Si(100) surface. Adapted from [55].

atoms is raised and the other is lowered in position. Theoretical calculations [58, 59, 60] have shown that buckling lowers the surface energy. Depending on the different orientations of the buckled dimers, different arrangements are possible. However, because the buckling introduces an additional lattice strain to the system, only two further reconstructions become possible: a buckled p(2×2) reconstruction where the neighboring dimer rows buckle in the same direction, and a c(4×2), reconstruction where the neighboring dimer rows buckle in opposite direction, as shown in Fig. 4.1. The c(4×2) phases is the most stable reconstruction, because the surface energy is additionally lowered by switching the buckling direction for each dimer.

STM images at room temperature [61] confirmed the dimer model, but showed both symmetric and buckled dimers, making it hard to interpret which reconstruction was correct. The question was resolved when buckled dimers were observed in much greater numbers at lower temperature [62]. At room temperature the dimer atoms have thermal energy available to switch their relative up-and-down position faster than the feedback response of the STM [63, 64]. The recorded STM images therefore appear as symmetric dimers as a result of the time-averaging of the measurements.

4.2 Hydrogen passivation of Si(100)

Hydrogenation of Si(100) surfaces is obtained by exposing atomically clean surfaces to atomic hydrogen in ultra-high vacuum. This allows the passivation to take place under extremely clean and well-controlled conditions, leading to the creation of well-defined structures, as well as gaining insight into the atomistic mechanisms of the hydrogen adsorption process.

The clean Si(100) surface is quite reactive due to the presence of dangling bonds (DB). Reaction of hydrogen with the reconstructed silicon surface leads to removal of the dangling bonds and the formation of Si-H bonds, lowering the reactivity of the surface considerably [53]. Various surface reconstructions can be created when exposing a clean Si(100) surface to atomic hydrogen in UHV under controlled conditions, depending on levels of exposure and annealing temperature of the sample. The three ideal reconstructions (phases) are shown in Fig. 4.2.

In order to understand how the different phases are formed, we will first look at how the atomic hydrogen reacts with one dimer unit. Initially, incoming atomic hydrogen starts replacing the dangling bonds on the dimer, forming a chemical bond to each of the individual Si atoms. At this stage the dimer unit is preserved, also known as the monohydride (2×1) structure. Additional atomic hydrogen impacts breaks down the Si dimer bond, leading to the dihydride (1×1) structure, where each Si atom is bound to two hydrogen atoms. Further bombardment causes the Si-Si back bonds to break, producing trihydrides, or to complete breaking of the adatoms, forming gaseous SiH_4 i.e etching of the silicon surface occurs.

At room temperature (RT), dihydride as well as the trihydride species starts forming, even before one monolayer (ML) of the monohydride phase has even been completed [65, 66]. The surface etching thus starts already before the monohydride phase is complete, and during the formation of the dihydride phase, the etching of the surface becomes substantial [67, 68, 69]. This is the reason why a truly ordered mono- or dihydride phase cannot be formed at RT. After hydrogen exposures at RT, the surface essentially turn into a mixture of the mono-, di-, and trihydride species [66, 70, 71, 72, 73].

At elevated temperatures the higher hydride species become unstable, presumably as a result of steric repulsion between the hydrogen atoms [75]. As the temperature is increased, it therefore becomes ever more difficult for the higher hydrides to form, as evidenced by a reduced etching of the surface. For instance, at intermediate temperatures of 110 ± 20^{o}C, the well-defined ordered (3×1) mono- and dihydride phase is is formed as shown in Fig. 4.3 (a)-(b) [74, 76, 70, 77, 78], featuring consecutive rows of bright monohydride and dark dihydride units. At even higher temperatures of 350-400^{o}C the well-ordered monohydride phase forms as shown in Fig. 4.3 (c)-(f) [79, 80, 76]. Prolonged exposure of the well ordered monohydride phases to atomic hydrogen at 350-400^{o}C does not induce etching, while even submnolayer exposure at RT does.

High-resolution images of the filled states, Fig. 4.3 (c),(d) show single

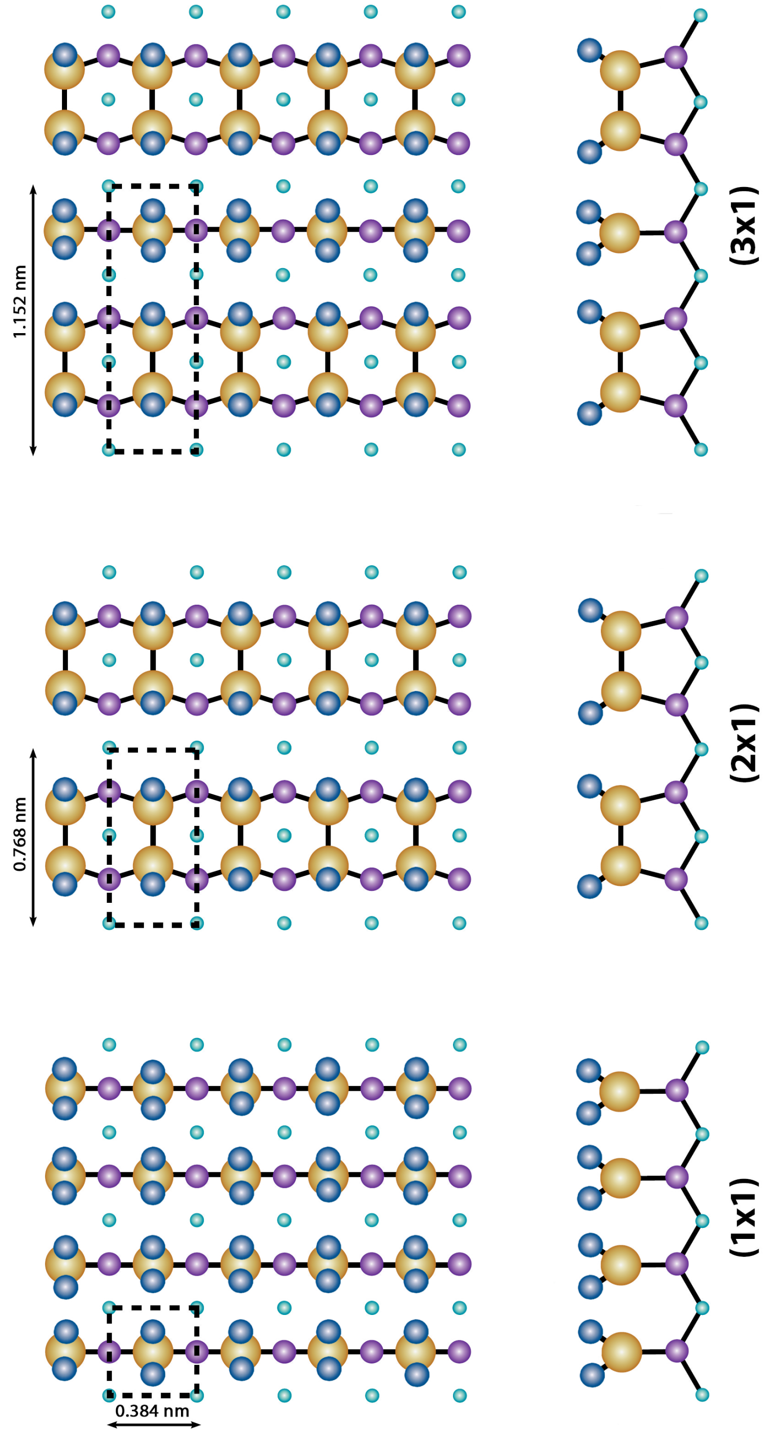

Figure 4.2: Hydrogen passivated Si(100) surfaces: (a) monohydride, (2×1) structure; (b) dihydride, (1×1) structure; (c) (3×1) structure. Adapted from [55].

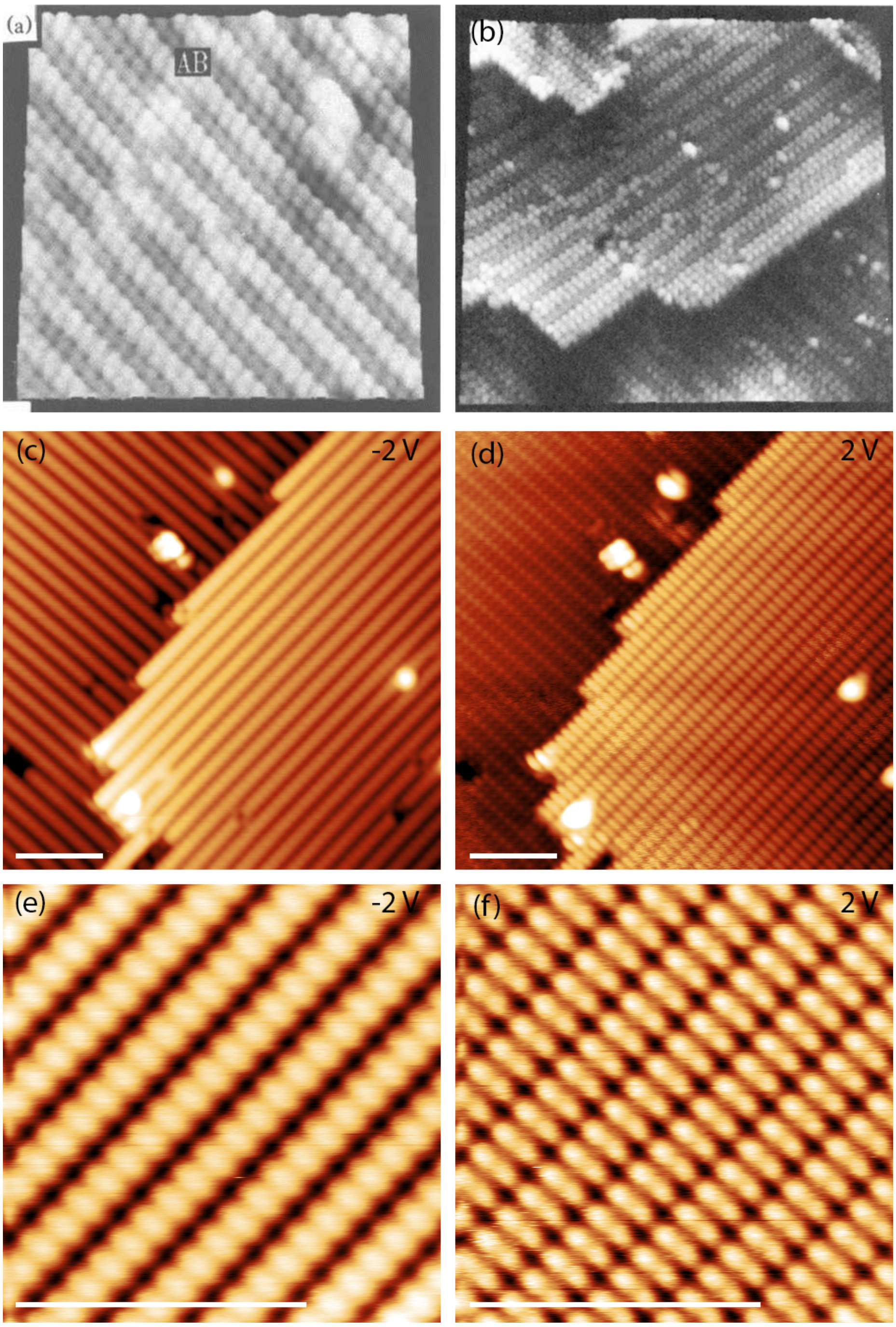

Figure 4.3: STM images of hydrogen passivated Si(100) for the (a)-(b) "(3×1)" phase [74, 75], and the "(2×1)" phase (c)-(f) acquired from experiments. Images (b-d) shows larger scale features where terraces are clearly visible, while images (a),(e-f) shows smaller scale images showing the dihydride (e-f) as well as monohydride plus dihydride (a) rows. Scale bars correspond to 4 nm.

rows of hydrogenated Si dimer units when imaging the filled states of the sample (e), while imaging the empty states of the sample (f), the individual hydrogen atoms of the dimers are clearly resolved. In this thesis, the bias voltages is *always* with respect to the *sample* bias, unless otherwise stated. The hydrogen atoms are visible in empty state images as a result of interaction between the anti-bonding states of the hydrogen atoms [81].

If the monohydride surfaces are well prepared, they are capable of having very low defect densities [75], depending on the sample preparation. Importantly, C-type defects that are commonly found on the clean surface are not present on the passivated surface. However, the passivated surface does contain various types of defects. Common types of defects include vacancy defects, which are essentially missing dimers, and dangling bond (DB) defects, which are essentially Si dimers which have either not been passivated at all or only partially passivated on one Si dimer atom. Other defects include so-called bow-tie (Bt) and split dimers [82, 83], as shown in Fig. 4.4.

Bt defects are essentially dihydride dimers (3×1) which seem to coexist with the monohydride phase to some extent. The split dimer defect has been

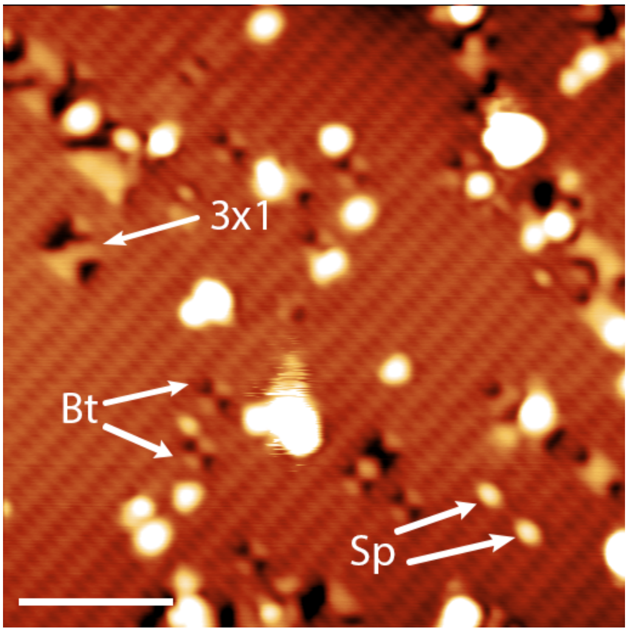

Figure 4.4: H:Si(100)-(2×1) surface showing various types of defects. Bow tie (Bt), split dimer (Sp). Acquired at -1.5 V bias, 10 pA. Scale bar correspond to 5 nm.

been assigned as a dihydride dimer as the most probable structure, based on high resolution AFM imaging [84]. This particular image shows a considerable number of Bt defects after flooding the chamber with Argon ($\leq 5 \times 10^{-6}$ mbar, 1 hour. Additionally, the amount of surface defects seems to have increased considerably. However, we should stress that since the surface was only imaged on one location macroscopically before introducing Argon, it is possible that the observed Bt structures are caused by temperature variations on the sample plate during passivation. The other types of defects however, are caused by surface contamination due to elevated pressure, which were routinely observed. The presence of Bt could easily be tested by scanning the exact same location both before and after introducing Argon.

4.3 Hydrogen desorption

4.3.1 Dangling bond (DB) defects

The DBs are the most interesting surface defects because they are much more reactive than the surface around them, and they can be created in a controlled way using STM. This allows a range of controlled surface modifications. Examples include precise control of dopant positioning [85, 86, 87], templated patterning of molecules [88, 89, 90], self-assembled wires of certain atoms [91, 92], and even a single-atom transistor [93] has been demonstrated. The reverse process, of controllably passivating individual DBs using STM is also possible, which has recently been carried out [94].

Experiments have shown [95] STM tip-induced desorption of paired hydrogen via vibrational excitation using tunneling electrons almost exclusively leads to the extraction of one DB dimer unit, although multiple desorptions do occur. Figure 4.5 gives a good (but not complete) overview of how the different DB types on the surface appear in their unoccupied (a) an occupied (b) states, respectively.

The different sites correspond to: single completely dehydrogenated dimer β [81, 97], dehydrogenated dimer at α with two neighboring dehydrogenated

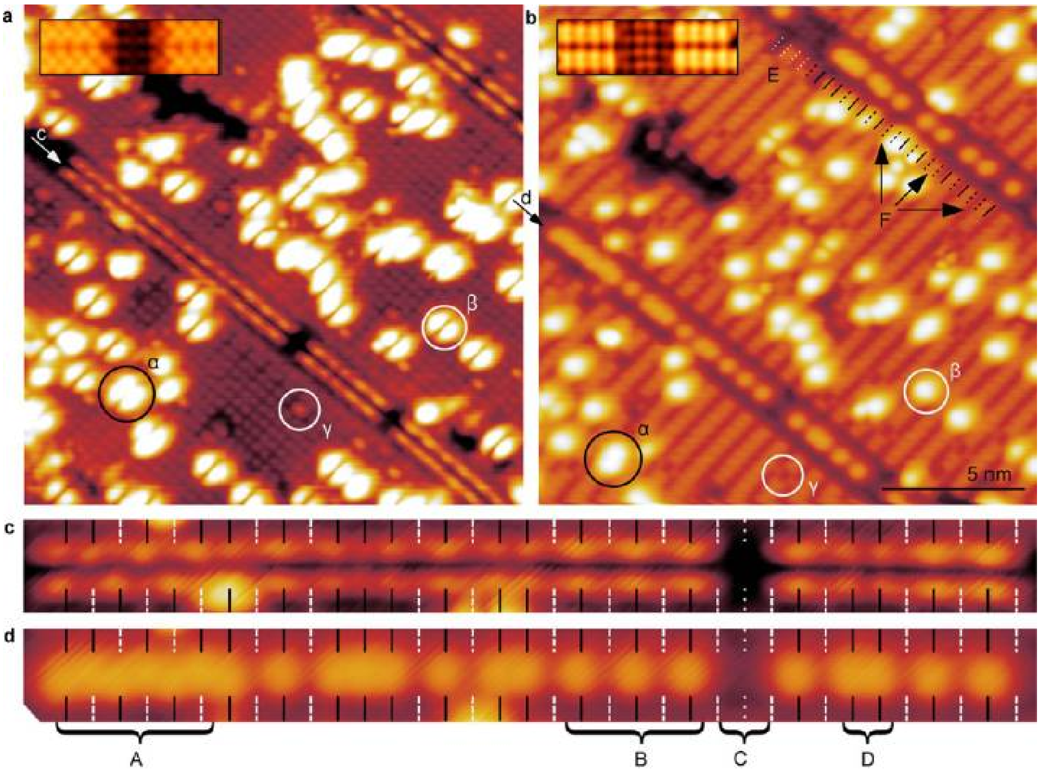

Figure 4.5: Different DB structures on passivated surfaces acquired at (a) 1.8 V, (b) -1.8 V. Labels show: α has two neighboring partially dehydrogenated Si dimers, β single fully dehydrogenated Si dimer, γ split dimer. Zoom in on Haiku line: (c,d). Regions of Haiku line showing (A) buckled dimers, (B,D,F) symmetric dimers, and (C) fully hydrogenated area. Adapted from [96].

Si dimers [98], and γ is the previously mentioned split dimer defect [82, 84, 83]. A single hydrogen extraction on a dimer unit appear as a bright ball-like features which is exclusively located on top of one of the Si dimer atoms.

The DB rows in this illustration, are called Haiku stripes [99, 96], and are not the typical DB rows one usually gets when creating DB rows using STM. The Haiku lines are unusual because the DB dimers are aligned perpendicularly to the Si dimer rows of the passivated surface, through the use of a special preparation technique [99]. Fully dehydrogenated Haiku lines are four atoms wide, (C),(E), while the two innermost atoms are usually dehydrogenated Si dimers forming lines (c),(d). Along the Haiku line, we observe buckled (A) dimers, symmetric (B,D,F) dimers, and fully passivated sections (C,E).

STS spectroscopy measured over the symmetric dimers (Fig. 4.6), show how hydrogenation of the dimer atoms changes the electronic properties of the surface. For the clean surface (i), STS measurements show a gap in the density of states around E_f [100, 81, 101]. In the band gap, two peaks are observed, a large one at -0.9 eV below E_f, and a small one at +0.5 eV above E_f. These peaks are attributed to the bonding π and antibonding π^* states of the π-like interaction between the individual dangling bonds [102]. Additional bands centered at -1.4 eV below E_f, and over the 1.2-2 eV range above E_f are mainly attributed to the Si-Si back bonds on the dimer [103, 104].

The binding of a single H atom to the dimer (ii), breaks the π-like interaction between the dangling bonds, but leaves the σ bond intact. As a result, the remaining unpaired dangling bond shifts up in energy toward E_f giving rise to two small peaks at ($\pm$ 0.5 eV) around E_f. These peaks correspond to the filled and empty states of the remaining dangling bond [101]. These are the states giving rise to the high tunneling current responsible for the bright appearance in the STM images. By contrast, the unreacted (i) and fully reacted (iii) dimers have no states close to E_f, causing them to appear darker in STM images. When two hydrogen atoms are bound to the dimer unit (iii), no dangling bond states exist, and only a single large peak is observed at 1.2 eV as a result of an interaction between the antibonding states of the hydrogen atoms [105].

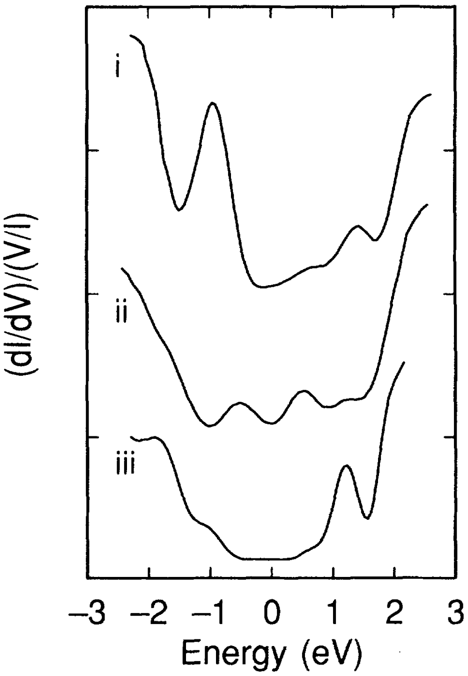

Figure 4.6: STS spectra of Si(100)2×1 surface recorded at one specific site for (i) unreacted dimer sites, dimer sites containing (ii) 1 H atom (iii), 2 H atoms per dimer unit. Taken from [81].

4.3.2 Desorption mechanisms

Desorption of hydrogen using STM can be split into two different regimes, depending on the bias voltage as shown in Fig. 4.7. At high biases ($>$ 6.5 V), the tip is so far away from the surface that electron field emission from the tip is the predominant interaction with the surface. At these high bias voltages, the emitted electrons possess enough energy to directly excite the Si-H bonding orbital σ into its antibonding σ^* state, thereby breaking the bond [107]. The energy needed to break the bond has been calculated to be 2.5 eV [108]. As a result, the desorption yield is independent of sample bias or current and remains constant at 2.4×10^{-6} bond-breaks per electron, as it depends only on the beam diameter [109].

At lower biases ($<$ 6.5 V), the desorption yield is highly dependent on both the sample bias, Fig. 4.7(b), and the tunneling current, 4.7(d) [110, 109, 111], decreasing by several order of magnitude at lower biases. In this regime, the

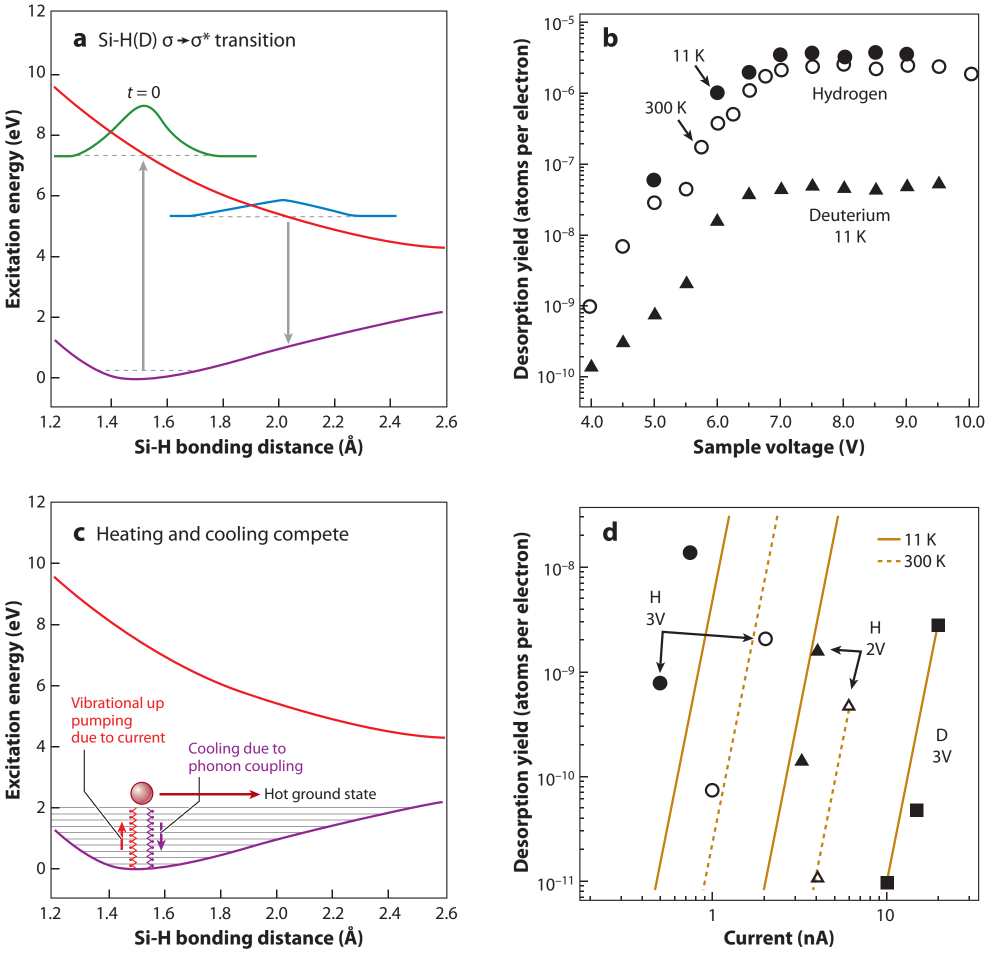

Figure 4.7: The two mechanisms of hydrogen desorption. (a) At high bias ($>$ 6.5 V), bond breaking occurs through direct electronic transition of the silicon-hydrogen bond from the σ bonding to the σ^* antibonding state. (b) A plot of the hydrogen and deuterium yields versus sample bias at room and cryogenic temperatures. (c) At low biases ($<$ 6.5 V), a competition of vibrational excitation and cooling of the silicon-hydrogen bond occurs. In this regime, the desorption yield (d) shows a strong dependence on both the tunneling current and sample bias. Used from [106].

desorption is described by a multi-electron vibrational heating mechanism, Fig. 4.7 (c), where inelastic electron tunneling between the tip and sample causes the bond orbital to be vibrationally excited to a higher energy state [106]. This process is repeated until the vibrational excitation has been excited high enough to break the Si-H bond. Experiments have shown that at least two electrons are needed for breaking the bond [112], and that multiple vibrational layers are usually climbed during each excitation event [112].

The desorption process is only possible because the vibrational lifetime is sufficiently long ($\sim$ 100 ns) allowing for multi-excitations to take place, before the excitation is cooled by phonon interaction with the rest of the substrate. Because multiple excitation events are necessary in order break the bond, the desorption process is critically dependent on the tunneling current, as shown in Fig. 4.7 (d), where the desorption yield follows a power law dependence as a function of the tunneling current.

4.3.3 Desorption lithography

Hydrogen desorption based on these two mechanisms allow patterned lithography to be carried on various length scales and precision, Fig. 4.8, with high flexibility. At lower biases, also called the atomically precise (AP) lithography mode, the tip-sample separation is sufficiently small for creating patterns with a high precision, as illustrated in Fig. 4.8 (i). We observe that the pattern accuracy improves as we lower the bias. Also in this regime the desorption is dependent on the electron dosage, which can be controlled through the writing speed. Thus, the patterning accuracy and speed can thus be controlled simply by changing the bias, tunneling current and writing speed.

In the high bias regime, also known as the field emission (FE) mode lithography, the tip-sample separation is quite large, causing electrons emitted from the tip to be spread out over a wide area. The patterning resolution is therefore limited to $\sim$5 nm in this mode [110]. Performing lithography on different scales in this mode can therefore only be carried out by: having a more well-defined tip geometry, or by exposing the electron impinged area to different electron dosages, as sown in Fig. 4.8 (ii), where different writing speeds are used.

Using these two lithography modes, it therefore becomes possible to create various structures, as shown in Fig. 4.8, ranging from creating a simple rectangle (iii), individual atomic rows (iv) to extracting single hydrogen atoms (v)-(vi). It is even possible to create complicated structures (vii), in this example a prototype device geometry. More advanced techniques have been developed, such as feedback-controlled lithography (FCL), which allows extraction of single hydrogen atoms in a controlled way (viii)-(x). FCL works by monitoring the STM feedback signal during patterning. When a desorption event is detected (triggered as a sharp rise in current), the patterning conditions (e.g. bias and current) are switched off and the tip is moved to a new position [7]. This allows patterning of complex structures to be carried out in a continuous and controlled way, with atomic accuracy. In the AP regime in particular, where atomic precision of the patterning process is sometimes required, the tip geometry becomes a significant parameter in addition to the bias and current [115, 112]. The FCL technique has been refined [117] into using a second feedback loop which monitors the tip-sample spacing in order to take into account uncertainties introduced by the tip geometry.

The lithography patterning process has been continuously refined over the last few decades, ever since the initial desorption attempts by Lyding *et al* [107] in 1994. In a recent approach, by J. Randall *et al* [113], (xi)-(xiv), the entire patterning process of large-scale structures with atomic precision is fully automated. The patterning is considered a digital process (x), where each hydrogen atom is identified and removed automatically, using a given writing pattern. The AP (xi), and FE (xii) modes are subsequently combined (xiv), in order to perform the patterning with optimum speed and efficiency.

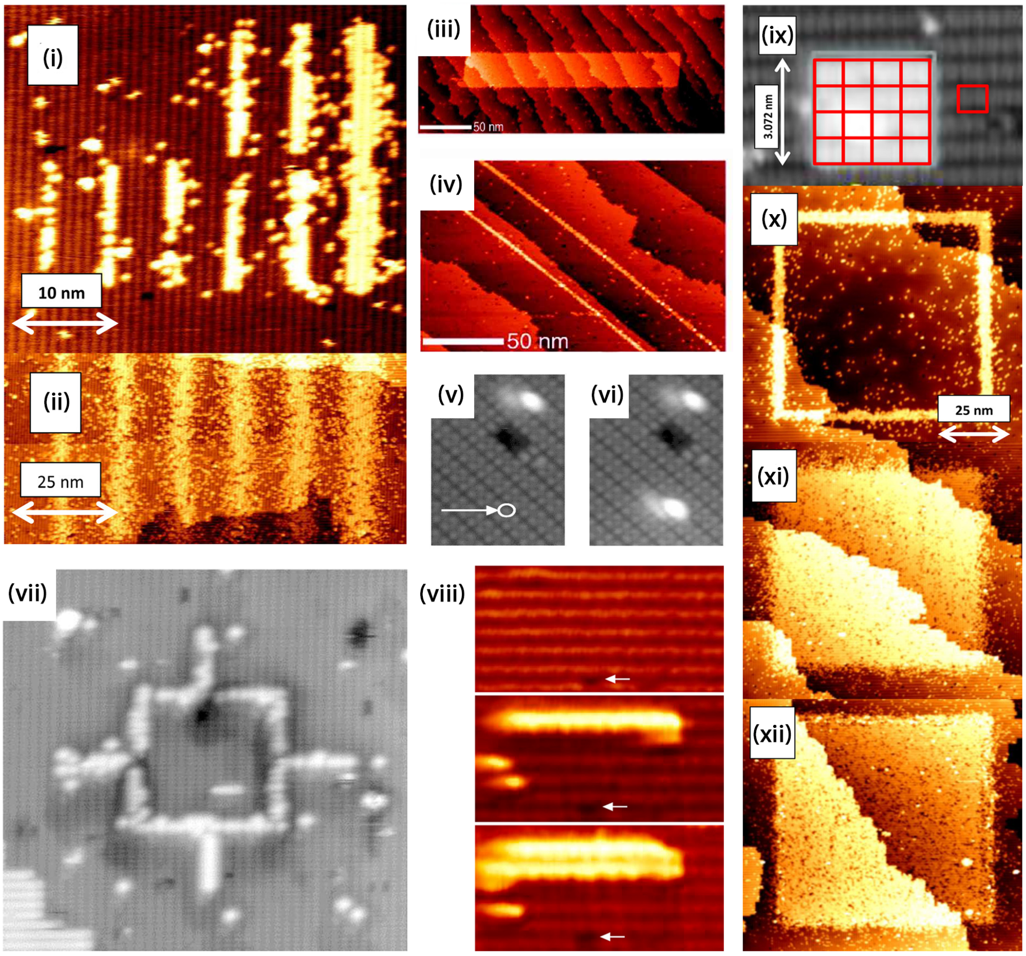

Figure 4.8: Capabilities of hydrogen desorption lithography on Si(100)(2×1):H. (i) At low bias (< 6.5 V), different AP modes (vibrational excitation of the Si-H bond) are possible, depending on the sample bias [113]. Desorption lines from left to right were written at 2.5-5 V in 0.5 V increments. (ii) In FE mode (direct excitation of the σ bond to its σ^* antibonding state) at high bias (> 6.5 V), different desorption line-widths become possible by altering the writing speed. Lines from left to right were written at 0.05 to 0.3 mC/cm in 0.05 mC/cm increments [113]. Based on these two modes, structures ranging from (iii) a rectangle, (iv) single atomic rows [114], (v-vi) single hydrogen atoms [95], to (vii) complicated structures, have been created [115]. Desorptions can be performed by (v), (vi) voltage pulses, or in more controlled way (viii) using FCL [116]. (ix) Automated identification and desorption routines of dimers, combining the: (x) AP and (xi) FE modes for (xii) efficient and precise atomic manufacturing [113].

4.4 Experimental techniques

4.4.1 Molecular deposition

Deposition of molecules onto surfaces was performed by exposing the surface inside the UHV system to a heated glass crucible containing the molecules of interest. A photograph of one cell, including the support, is shown in Fig. 4.9. The basic design for heating the molecules involves wrapping a heating coil (tantalum wire) around a glass crucible. The molecular material (e.g. PTCDA) is inserted into the crucible and protected from dropping out by glass wool. By attaching a thermocouple to one end of the crucible the applied heating (and thus temperature) can be controlled. To avoid contamination, a distinct cell is manufactured for each molecule. Our molecules of interest follow a sublimation rate that is exponential with temperature. By using small sublimation rates, the surface coverage could be adequately controlled by changing exposure time. As a result, small sublimation rates were used. Prior to deposition, each cell was degassed extensively at 200 °C, followed by a brief degassing at 10° above deposition temperature in order to remove contaminants.

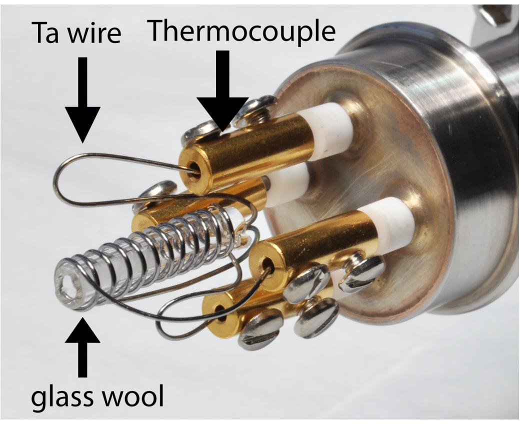

Figure 4.9: Experimental design for molecular deposition.

4.4.2 Bakeout

In order to obtain extremely low pressures relatively quickly (less that one week), UHV systems are baked at elevated temperatures (145°C) for several days. The standard procedure during cool-down is to degass equipment that needs to be extremely clean, such as the manipulator arm and the thermal gas cracker, while they are still hot. This allows further outgassing than normal degassing procedures, and thus much cleaner equipment. To further reduce reduce outgassing during passivation (see section 4.4.4) the system was baked *twice*.

4.4.3 Si(100) sample preparation

As-doped (i.e. n-type, 0.006 Ω cm) Si(100) wafers measuring 3 × 10 mm^2 were used for hydrogen passivation. Atomically clean (2 × 1) reconstructed surfaces were *in situ* prepared by the following procedure: A sacrificial sample was first used to thoroughly degas the sample holder and surrounding region of the manipulator arm. The sample is then loaded onto the arm and degassed at 600 °C for 12 hours. The sample is then subsequently heated at 750-800°C for an additional hour while maintaining a pressure below 5×10^{-10} mbar. The degassing helps to minimize any unwanted outgassing during both flashing and the subsequent slow cool-down step. Additionally, they also help to minimize the number of flash cycles needed in order to to achieve a low pressure during flashing. The samples were then flashed at 1150 °C while maintaining a low pressure ($<10^{-10}$ mbar). The flashing was repeated until the base pressure would remain below 10^{-10} mbar for 20 seconds. The sample was then subsequently flashed for 10 seconds before rapidly lowering the temperature to 900 °C, followed by a slow cooling ($\sim$ 1 K sec^{-1}) down to room temperature. This ensures that the last reconstruction is kept at a base pressure of 5×10^{-10} mbar or lower. This procedure resulted in Si(100) 2 × 1 surfaces with very low defect densities of $\sim$ 1% with a high reproducibility.

4.4.4 Si(100) hydrogen passivation

The passivated surfaces resulted from exposing Si(100) 2 × 1 samples with very low defect densities to atomic hydrogen. The experimental setup for hydrogen passivation is shown in Fig. 4.10.

Molecular hydrogen (from a cylinder) was fed into a gas line, which is directly connected to a SPECS [118] thermal gas cracker via a leak valve. The gas line is filled to 2 bar of hydrogen and the line is subsequently closed to the outside environment using two valves. A cold-trap is installed on the line in order to maintain a high cleanliness of the hydrogen gas during exposure of the sample to atomic hydrogen.

The cracker use electron bombardment to produce an intense localized heating of a metal (tungsten) capillary. During standard passivation conditions, the capillary is heated to 1500-2000 °C. The intense localized heat causes the molecular hydrogen to dissociate into atomic hydrogen with an efficiency that is dependent on the capillary temperature and pressure.

The cracker is slowly heated up in order to prevent the pressure spiking above 10^{-10} mbar. The valve connected to the turbo pump is then opened and the ion pump is switched off. The shutter is opened, and the gas is leaked into the thermal gas cracker such that the pressure of the UHV chamber is 3-6 $\times 10^{-7}$ mbar. The atomic hydrogen then bombards the sample, which is aligned in direct line of sight with the outflow of the gas and positioned at roughly 8 cm from the cracker. A shutter is placed at the end of the cracker in order to rapidly switch on-and-off the exposure of the sample to atomic hydrogen. The sample is exposed to 10-80 Langmuir by keeping the shutter open for 1-2 minutes. The cracker is then switched off, followed by closing the shutter, rotating the sample to face away from the cracker and stopping the flow of hydrogen into the chamber. The annealing temperature of the sample is subsequently reduced to roughly 300°C. When the system has recovered to a low pressure, the sample is gradually cooled down to room temperature. The sample is then transferred to the STM scan head for imaging.

The cracker is connected to a heat sink, which is regulated to a constant temperature of (400±10)°C during conditioning, by maintaining a constant

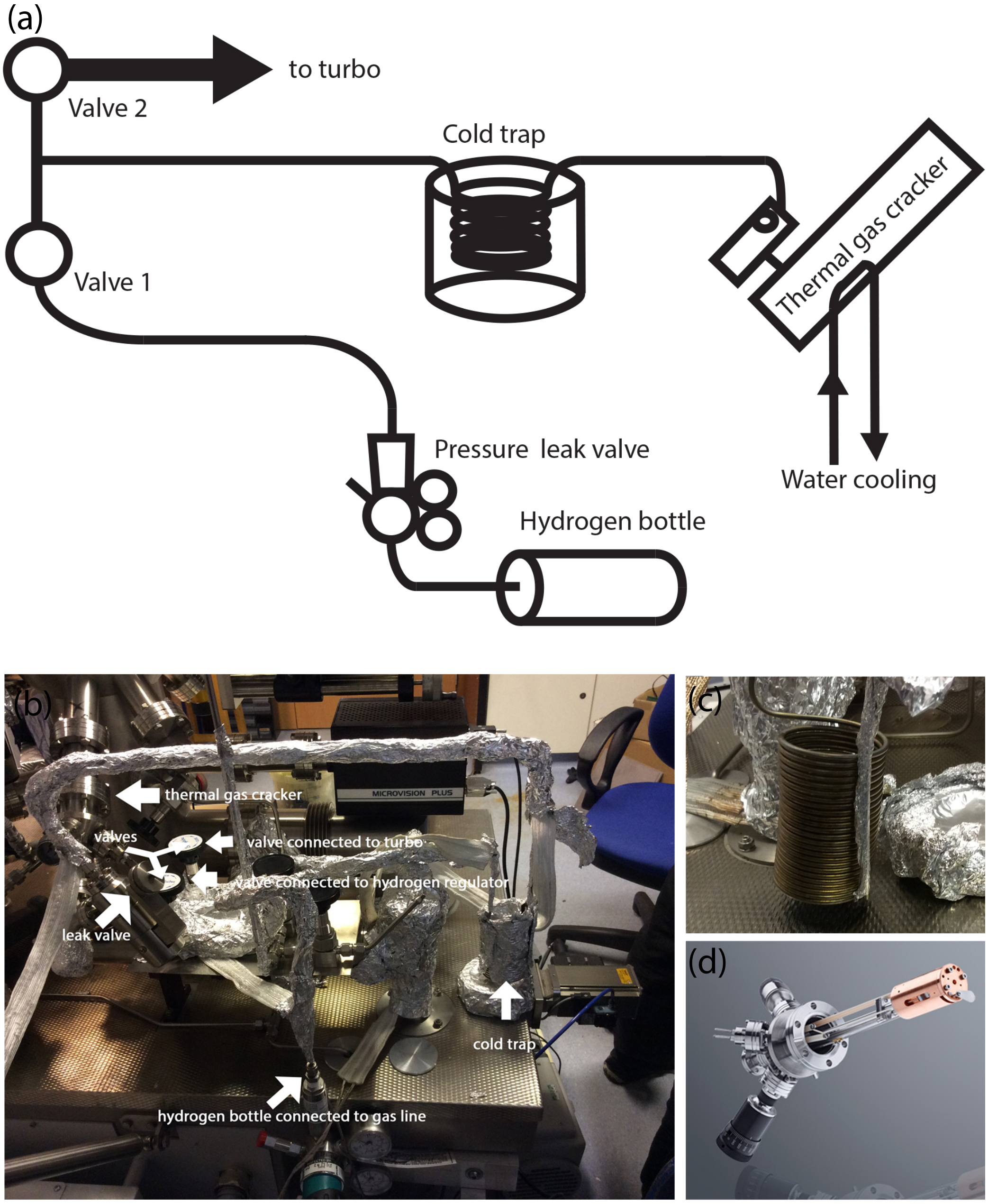

Figure 4.10: (a) Diagram and (b) photograph of experimental setup for hydrogen passivation. (c) Close up view of cold trap. (d) SPECS thermal gas cracker.

flow of water, in order to prevent it from overheating and excessive outgassing during passivation. During passivation, the water flow is increased to maximum to ensure that the cracker is heated as little as possible to minimize outgassing. Since the temperature of the filament cannot be measured directly, we are forced to rely on the temperature of the heat sink as an indication of the filaments temperature. This still gives a reasonable prediction of the filament temperature as the temperature of the heat sink and the filament are related to each other.

During passivation the sample was annealed to 380°C by direct heating. Heating is applied for at least 5 minutes before passivation in order to maintain a stable temperature during exposure. The temperature was measured directly using an infrared temperature sensor which is specifically calibrated to measure the optical reflection of silicon surfaces. Annealing is performed out shortly after flashing in order to minimize exposure to unwanted contaminants.

4.5 Spectroscopy

4.5.1 STM spectroscopy

Using scanning tunneling spectroscopy (STS), it becomes possible to obtain spectroscopic data with atomic resolution. Specifically, the electronic structure of the sample can be examined by directly measuring the LDOS. Additionally, it becomes possible *in principle* to elucidate other surface properties, such as chemical composition and electronic properties.

From Eq. 2.5, the tunneling between the tip and sample is dependent on three parameters: the tunneling current I_t, the bias voltage V, and the tip-sample separation z. Using STS, one one of these parameters is kept fixed, while a dependence is drawn between the other two. Hence, spectroscopic measurements are generally performed in three different modes: I-z, V-z, and I-V. For examining surface properties, I-V measurements are generally performed. In practice, I-V characteristics are obtained by placing the tip over a point of interest on the sample. The tunnel current is then measured as a function of voltage while maintaining a constant z (feedback off). The changes in the slope of the obtained I-V curve reflect the conductance variations between the tip and the sample. Unfortunately this simple approach often gives too much noise in the tunneling current to provide any meaningful data, as it requires numerical differentiation of the curves. A lock-in amplifier can therefore be used to measure the dI/dV signal directly, which is significantly less noisy. Here, a small sinusoidal signal V_{ac} is added to the constant dc voltage V_0. This modulation results in a sinusoidal modulation of the tunneling current as illustrated in Fig. 4.11(a).

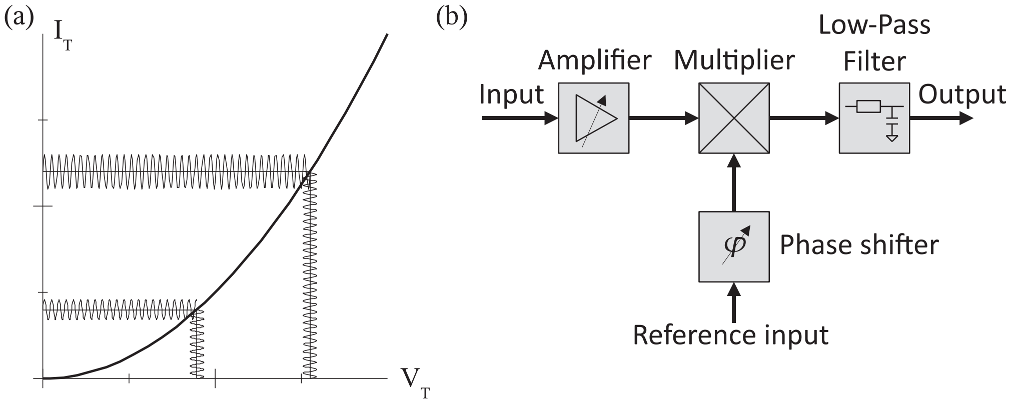

Figure 4.11: Overview of lock-in amplifier operation. (a) Model illustrating the modulation of the tunneling current as a result of the modulation of the tunneling voltage. (b) Schematic representation of a phase and frequency sensitive lock-in amplifier. Adapted from [119].

To ensure that the modulation does not influence tunneling current imaging, the modulation frequency is set at much higher values than the feedback regulation of the tunneling current. For a small applied sinusoidal signal $V_{ac} = V_m \sin(\omega t)$, the modulated current can be expanded in a Taylor series:

$$I(V_0 + V_m \sin(\omega t)) = I(V_0) + \left.\frac{dI}{dV}\right|_{V_0} \cdot V_m \sin(\omega t) + \dots \tag{4.1}$$

From Eq. 4.1, the current modulation signal at frequency $f_m = \omega_m/2\pi$ is proportional to dI/dV at V_t and therefore proportional to the LDOS of the sample. The lock-in amplifier is used to measure the modulation of I_t at this frequency. Fig. 4.11(b) shows a schematic representation of how the lock-in amplifier works. Initially, the modulated current is amplified while the reference signal passes through an adjustable phase shifter φ. The two signals are subsequently multiplied at a certain frequency. The key issue is that only the contribution of the input signal that has the exact same frequency and phase as the reference signal is converted to a dc signal. All other signals are filtered out by a narrow band-pass filter. The advantage of this technique is that it allows the detection of extremely low AC signals (down to nanovolts) even when other noise signals can be thousands of times larger.

4.5.2 Force spectroscopy

The strength of NC-AFM, is that forces are directly related to the frequency shifts of the cantilever, which can be measured. This allows, in addition to imaging on almost any surface with atomic resolution, the ability to directly ascertain forces at the atomic scale. From Eq. 2.9, in the limit of small oscillation amplitudes, the frequency shift is proportional to the *gradient* of the force. As a result, any method used to deconvolute F_{ts} from Δf only produces the relative difference in force rather than absolute force.

To overcome this, force spectroscopy measurements are used. In this mode of operation, the tip is initially held at a fixed position z (feedback regulation disabled) and Δf is recorded. The tip is then swept over a large range of z while simultaneously recording Δf. At far away tip-sample distances, the force interaction can be considered negligible and can be set to zero. The forces at closer distances can therefore be calculated relative to this point. As a result, the absolute force for each z is obtained [120].

Unfortunately, the measured forces consist of both short and long-range contributions. Long-range interactions such as vdW interactions between the surface with a macroscopic tip often dominate the frequency shift. In order to calculate the interaction of interest, these contributions to the total force needs to be separated.

Separating short and long range forces

From Eq. 2.12, the forces that are measured is the sum of all force contributions: vdW and short range forces. In order to accurately estimate the short range forces, the contribution of the long range forces to the frequency shift needs to be estimated and subtracted from the original measurements. The principle corresponds to a background subtraction. The conceptually most straightforward way of achieving this is to take force spectra over a range, that spans over the short (0-2 nm) and long (0-10 nm) range forces. As the tip retracts further away than the short range forces ($\sim$ 2 nm), the long range forces become dominant. In this range (2-10 nm), the long range forces can be approximated using an empirical power law, and interpolated over the entire range of measured spectra. The short range forces can then be extrapolated by subtracting the long range forces from the data. Unfortunately, this method leads to inaccurate results, as the fitting can only be performed at distances where short range forces are known to be zero. The forces that are measured in this regime are smaller, and the fitting can therefore lead to significant deviations as a result of choosing an arbitrary cut-off or changes in noise levels [121].

A more accurate method is to perform a so-called null measurement. In this scenario, two equivalent force spectra are taken, but where one of the measurements does not have the interaction of interest. For example, for a particular surface, a null site can be a vacancy or a hole in the lattice. By performing a force spectroscopic measurement on top of an atom, both the short and long range forces are measured. However, when performing the same profile on top of the vacancy, the short range contributions are missing. By subtracting the spectra over the null site from that performed on top of the atom, the long range forces can be subtracted.

Amplitude and force calibration

In order to obtain meaningful forces from experimental frequency shifts, the amplitude of the oscillating cantilever needs to be known in correct units (nanometers). Here we have to remember that the cantilever is merely oscillating in response to a driving signal. The frequency shift (Eq. 2.9) can be normalized with respect to a parameter $\gamma(z_c)$ [27, 29]:

$$\gamma(z_c) = kA^{3/2}\frac{\Delta f(z, A)}{f_0} \tag{4.2}$$

which is a function of the point of closest approach $z_c = z - A$ of the probe apex with respect to the amplitude and frequency shift from the center of oscillation z. In practice, A is calibrated by the following method: first $\gamma(z_c)$ is determined for a given A and Δf, while in Δf feedback close to the sample. By keeping $\gamma(z_c)$ constant while increasing A, both the frequency shift setpoint and the z-piezo extension will correspondingly be adjusted in order to maintain a constant tip-sample separation. The amplitude can then be extrapolated from slope of the frequency shift $A^{3/2} \propto \gamma(z_c)\Delta f(z, A)$, in physical units of nm/V.

4.5.3 3D spectroscopy

As previously shown, using force spectroscopy, atomic scale forces interacting between tip and sample can be characterized by sampling the interaction in certain directions. Similarly, STM spectroscopy allows examination of the electronic properties at the atomic scale. By moving the tip in all 3 dimensions, a detailed mapping of these characteristics becomes possible. Data acquisition is often performed in form of constant height images at different tip-sample (Z) distances. This mode is illustrated in Fig. 4.12(a).

Comparable with this protocol is the sampling of ZX slices as depicted in Fig. 4.12(b). A third very common strategy is to acquire single line data along the Z-axis, such as Δf(z) curves shown in Fig. 4.12(c). The curves are sampled systematically on a raster and combined to a 3-dimensional data set. The main problem with all these protocols, is that they rely on virtually zero drift. As a result, the duration of data acquisition (especially under room-temperature conditions), is limited to a few minutes. This limitation can be overcome by applying more advanced data acquisition protocols, which are based on the atom tracking principle, and can handle large and especially

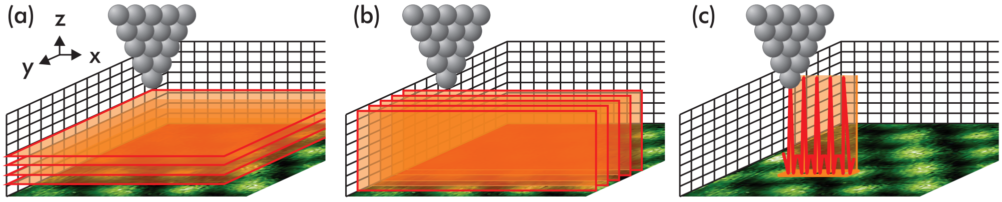

Figure 4.12: Acquiring 3D data. (a) Slices of constant height images acquired at different tip-sample distances. (b) Similar strategy, but along other axis. (c) Acquisition of single line data such as $\Delta(f)(z)$ or $\mathrm{d}I/\mathrm{d}V$ along Z-axes. Used from [122].

non-linear drift.

4.6 Atom tracking

Initially the atom-tracking technique was developed for the study of diffusion kinetics of atoms and and molecules by tracking the movements of single adsorbates using an STM [123]. Prominent examples involve the diffusion and rotation kinetics of Si-Si and Si-Ge dimers on Si(001) [124, 125, 126, 127]. The technique has since been adopted by the NC-AFM community [128, 129, 130], where it has since been used for drift compensation. In contrast to the STM experiments, a stable surface feature is chosen as the tracking reference. Consequently, the relative movement between tip and sample is measured as a virtual feature movement. By adding a feed-forward to the relative displacement and regularly correcting the displacement, drift can be virtually eliminated [123].

In this section the atom tracking technique is introduced. The technique is important, not only for eliminating drift, but also for tracking specific features in general. As a result, throughout this work, atom tracking is used when attaining grid spectroscopic measurements (Chap. 5, 6) desorbing single atoms (Chap. 6), determining the diffusion tensor of mobile molecules on the surface (Chap. 8), and tracking molecules in real time.

Although the atom-tracking technique technique can be used to monitor different types of input signals, for convenience we will describe the principle using frequency shifts Δf as the input signal. In Fig. 4.13 the basic principle of atom tracking is presented.

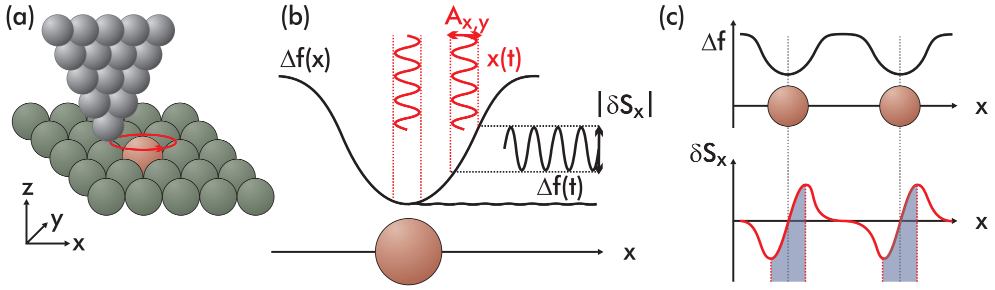

Figure 4.13: Principle of atom tracking. A single surface feature is tracked by dithering the tip around the feature (a). For the x-direction, the dithering causes a nearly sinusoidal oscillation with amplitude $|\delta S_x|$ in the Δf channel, if the tip is offset from the feature centre (b). More specifically, the signal δS_x depends on the dithering centre position relative to the surface feature (c). Adapted from [122].

For dithering, a small AC voltage is applied to the tip, causing it to oscillate (dither) with frequencies f_x, f_y and amplitudes A_x, A_y in an elliptic trajectory around a surface feature. For simplicity, we here set $f_x = f_y = f_{x,y}$, $A_x = A_y = A_{x,y}$ and introduce a phase shift of 90° between the two components. The tip dithering motion around the object then becomes circular. Depending on the experiment, the feature can be selected to be: a single surface atom, a surface depression, or adsorbed atoms/molecules. When applying drift correction, the main common element is the assumption that the feature can be reliably identified throughout the experiment. Suitable values for the dithering amplitude $A_{x,y}$ and frequency $f_{x,y}$ are mainly determined by: the size of the feature, the bandwidth of the detection system, and the rate of movement of the feature. For simplicity, we assume that the feature is an atom.

If the atom is perfectly circular and centered in the origin of the dithering circle, the tip will follow a trajectory of equal interaction. As a result, the $\Delta f(t)$ signal is virtually constant in time, as illustrated in Fig. 4.13(b) along the x-direction. However, if the atom is displaced so that it is no longer perfectly centered in the dithering circle, the frequency shift will be experience a small modulation δS_x over time, which in turn depends on the lateral offset from the dithering center and the tip-sample interaction strength. Fig. 4.13(c) illustrates the relationship between the frequency shift and the modulation for displacement in one direction. For small dithering amplitudes, the frequency shift and the modulation will be in-phase with each other (blue shaded regime). In this regime, the modulation δS_x corresponds to the derivative of the frequency shift change along the x-direction. From this relationship, the displacement of the tip from the center of the atom can be corrected for by adding additional feedback loops. However, if the displacement or amplitude becomes too large, the in-phase behavior breaks down (outside blue area), and it is no longer possible to track the atom.

Once the tip is "locked" on to the surface atom, it can be used to track its movement simply by recording the tip positioning data and correct for the change by re-adjusting the tip position. If the feature is stable on the surface, the tip movement will be identical to the drift movement. On the other hand, if the feature is highly mobile, the tip will follow its movement on the surface.

4.7 Instrumentation

4.7.1 SPM Instrumentation

Most experimental results obtained by the author were carried out using a commercial Omicrom GmbH variable-temperature STM-AFM ultra high vacuum (UHV) system shown in Fig. 4.14.

The chamber is mainly pumped using a single ion pump, as well as a titanium sublimation pump (TSP). For most of our purposes, the system is kept at a very low base pressure of 2-5$\times 10^{-11}$ mbar. Additionally, the system can be pumped using a combined rotary and turbo molecular pump, when introducing gases, for either sputtering tips or samples, or depositing molecules on surfaces. The system is optimized for quick use as well as flexibility, allowing samples and tips to be replaced and modified relatively quickly. The scan

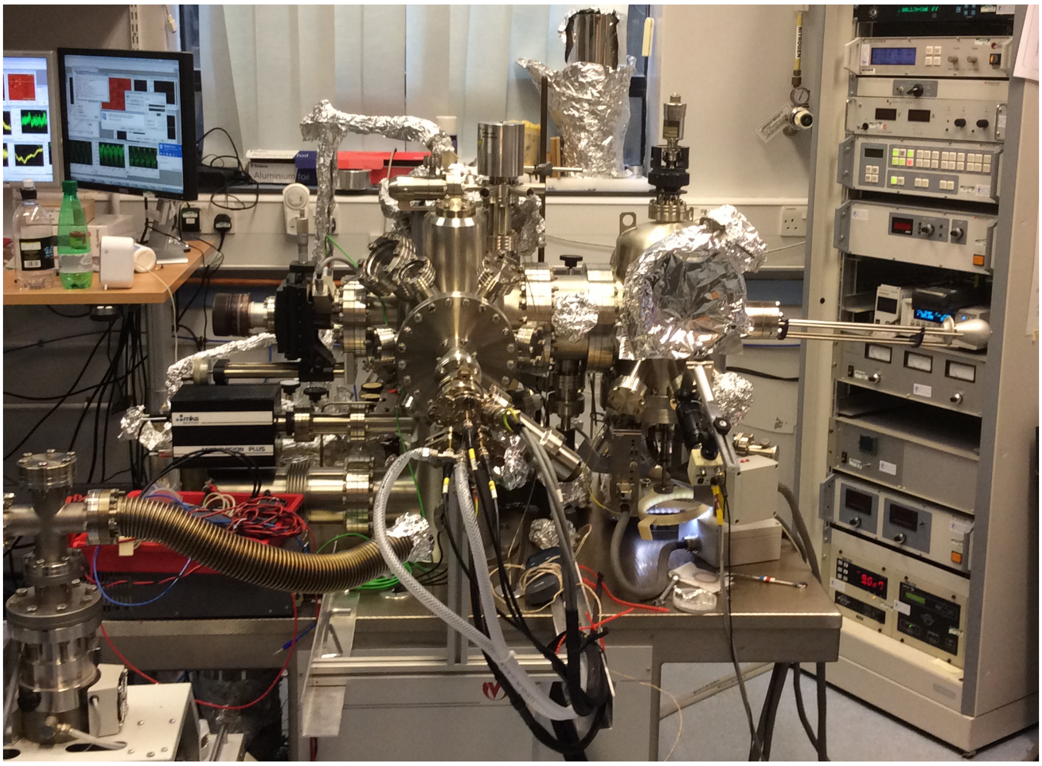

Figure 4.14: Photograph of Omicron VT STM/AFM system.

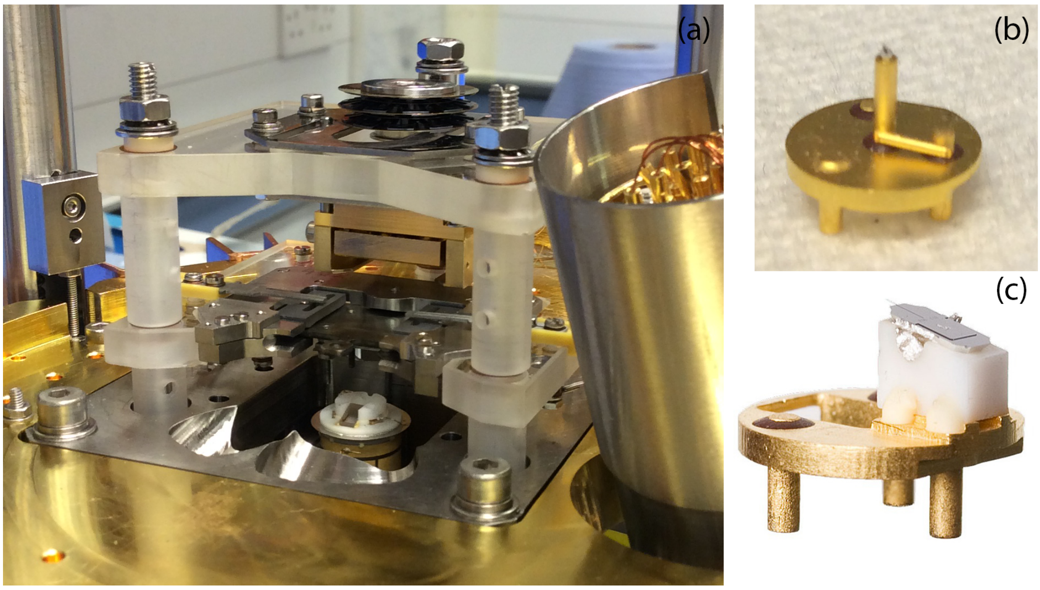

Figure 4.15: (a) Omicron VT-STM/AFM scan head, (b) STM tip made of W and (c) Si cantilever. (c) Used from [131].

head can be used perform conventional STM with etched tungsten probes or AFM using cantilevers supplied by Omicron (Fig. 4.15).

For hydrogen passivation, the thermal gas cracker was installed directly on the system (see Fig. 4.10). The system has several useful tools for carrying out both sample and tip preparation: an argon sputtering gun for both sharpening tips and preparing samples, a tip annealer for cleaning/sharpening tips, and a manipulator arm for heating samples. The manipulator arm has the capability for both directly heating a sample plate to 1200 K, as well as indirect heating to 600 K (see Section 4.4.3). Samples are mainly prepared in the manipulator arm, and then subsequently transferred to the scan head for AFM/STM imaging. The scan head can be suspended by springs in order to reduce vibrations, which can have a huge influence when imaging at the atomic scale.

For H:Si(100) samples, measurements were performed at RT. As a result, it was necessary to reduce thermal drift substantially in order to perform spectroscopic measurements (Chap. 6,7) as well as automated STM lithography (Chap. 7). Thermal drift was minimized primarily by (I) minimizing external influences on the system by covering the windows in silver foil while maintaining stable temperature regulation in the room (II) temperature regulating the sample, by heating the sample plate either directly (VT samples) or indirectly (LT sample plates) and (III) compensating for thermal drift using atom tracking.

The scan head is in thermal contact (via a copper block) to a cryostat which can be temperature regulated either by cooling using liquid nitrogen or heated using direct heating. The temperature can be automatically regulated with high precision, through a temperature monitoring and corresponding current adjustment system. Using specially designed sample plates for the VT system, it is possible regulate the temperature of the samples in the scan head while imaging by attaching them to the copper block. For H:Si(100) samples, modified sample plates dedicated for the LT system were primarily used, and were thus unsuitable for temperature regulation under normal operating conditions. Due to their design, they can not be attached to the copper block, and therefore not cooled using liquid nitrogen. However, due to their proximity to the copper block, LT sample plates were temperature regulated by regulating the heating of the copper block to 301 K. By combining method (I) and (II), the thermal drift can be reduced to within a range of 50 pm/min (LT plates). Adding (III) regularly, the drift was lowered to a range of 1-10 pm/min (depending on how often atom tracking was used).

Chapter 5

Passivation and imaging of H:Si(100)

As stated previously, a key objective is to create patterns of dangling bonds with atomic precision and high reliability. In order to achieve this aim it is necessary to have a fully hydrogen passivated Si(100) surface with extremely low defect density and to be able to image these surfaces reliably, neither of which is trivial. As the central contribution of this thesis is to elucidate the role of the tip when interacting (imaging, manipulating etc.) with the sample, we therefore wish to examine the chemical and electronic properties of the sample for different tip structures.

This chapter is therefore divided into two sections. First we start by explaining step-by-step how we were able to obtain these surfaces. We will then describe the physical and electronic properties of the surface and their adsorbents based on STM and AFM imaging and spectroscopic measurements carried out at RT. Most STM measurements were performed using tungsten (W) tips while AFM measurements were predominantly performed using Si cantilevers (Section 4.7.1). For all STM imaging in this thesis, the bias voltage is performed with respect with the *sample* bias, unless otherwise stated. We show that the topography observed using STM imaging is highly dependent on the state of the tip, while the topography observed using AFM is considerably less tip state dependent. The tip state dependency on the imaging conditions is investigated further in the next chapter when performing manipulations on the surface using different tip terminations. By combining our experimental results with theoretical calculations using different different tip terminations, we hope to gain a better understanding on the tip state influence with the sample which could be used to further improve our automated atomic manipulation routine.

5.1 Passivation of surfaces

Obtaining hydrogen passivated Si(100) surfaces of very high quality is far from trivial. Basically three requirements are needed:

1. The molecular hydrogen gas, fed in to the thermal gas cracker in order to passivate the surface needs to be as free of contaminants as much as possible.
2. The thermal gas cracker used for dissociating H_2 at elevated temperatures (1500-1700 C) needs to be as clean as possible (conditioned) in order to prevent outgassing of contaminants during passivation.
3. The Si(100) surface for passivation needs to have a very high surface quality.

I will elucidate how we addressed these issues, ending up with a highly optimized passivation procedure for obtaining a H:Si(100)-2×1 surfaces of high quality.

5.1.1 Si(100) surface quality

In order to achieve H:Si(100) surfaces of high quality, it is important to initially have a bare Si(100) of high quality (i.e. low defect density). Clean n-type Si(100) surfaces were achieved by flashing as described in Section 4.4.3. Initially, the surfaces showed only medium surface quality when imaging using STM. The reason for the low surface quality was suspected to be due to water contamination, as a result of the increase in vacuum pressure during mechanical movement (both rotational and translational). We will now illustrate this problem by providing an example experiment using the wobblestick. The wobblestick is used to transfer the samples from the manipulator arm (where they are prepared) to the scan head (where they are imaged). Moving the wobblestick causes an increase the vacuum pressure of the system which we has been suspected to cause water contamination on the samples. Fig. 5.1 compares the surface quality of a Si(100) sample (a) after it has been moved extremely carefully to the scan head ($P_{added} < 1\times10^{-10}$ and (b) after moving the wobblestick back and forward a few times.

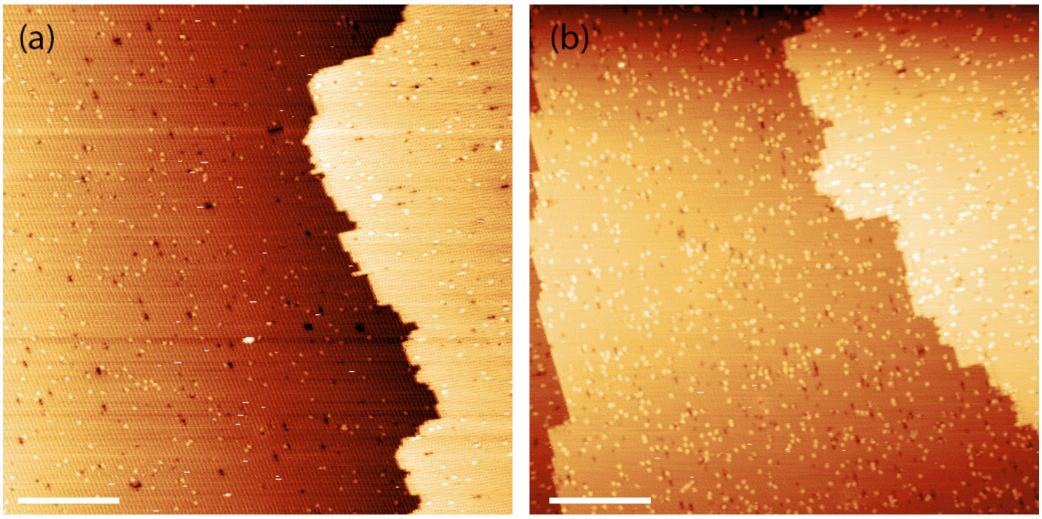

Figure 5.1: DSi(100) surface after (a) moving the wobblestick very slowly and (b) moving wobblestick back and forth for ∼ 1 minute. Scale bars correspond to 20 nm.

It is evident by comparing the two images that moving the wobblestick (even moderately) causes a significant increase in the the amount of C-type defects on the surface, indicating the presence of water contamination. This indicates that despite long bakeout and degassing periods, water contamination in the system cannot be fully eliminated, and can therefore have a significant impact on the silicon surface quality when (most likely) any type of mechanical movement is involved. Most importantly, the amount of contamination seem to correlate with the increase in the vacuum pressure.

Minimizing the increase in vacuum pressure during mechanical movement and avoiding unnecessary movement is therefore a prerequisite for producing high quality silicon surfaces. In order to improve the passivation conditions, subsequent surfaces were therefore passivated directly after flashing, without first confirming their surface quality in the scan head, which would require a lot of mechanical movement.

In order to achieve high quality Si(100) surfaces, the samples were flash heated to 1150°C for a small period of time. The intense heat from the sample (and its surroundings) unfortunately causes the vacuum pressure to rise quite considerably. Experiments have shown that the density of A, B and C type defects increases with the increase of vacuum pressure during flashing. In other words, by maintaining an extremely low vacuum (base) pressure, the number of surface defects can be kept extremely low.

After performing double-bakeout of the system (Section 4.4.2) followed by extensive degassing of both the sample and its surroundings, surfaces of comparable quality to the images shown in Fig. 5.2 were routinely achievable when flashing at base pressures of 5 $\times 10^{-11}$ mbar (or lower).

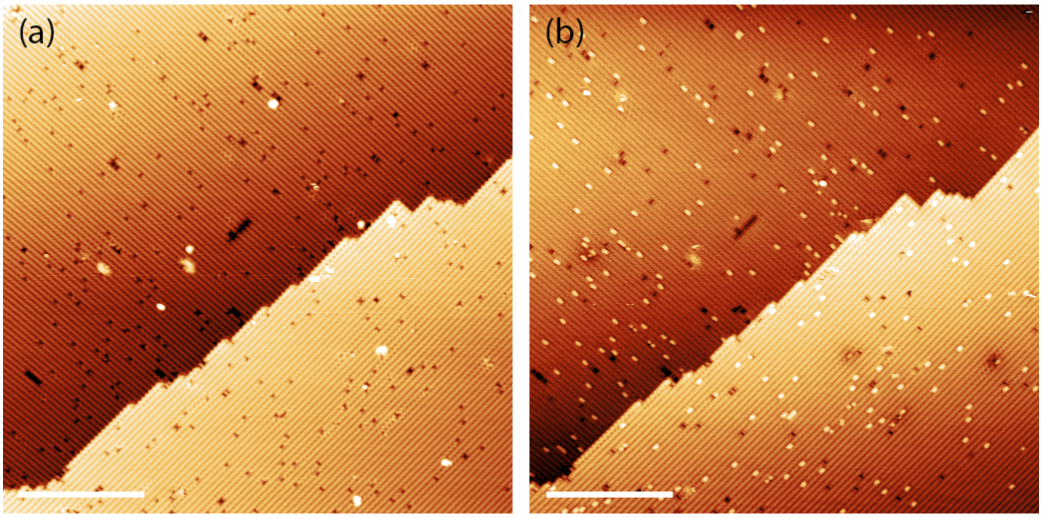

Figure 5.2: STM image of Si(100) surface taken at (a) 2 V, 10 pA and (b) -2 V, 10 pA. Scale bars correspond to 20 nm.

It should be noted that the surface quality right after flashing is probably even better than the images suggest, because they have to be moved to the scan head in order to be imaged and most of the defects we observe on the surface are C-type. Additionally, we remark that the double-bakeout is not necessary in order to achieve the low base pressure nor to clean the manipulator arm. Its main purpose is to degass the cracker as explained in Section 5.1.5.

5.1.2 Contamination during passivation

During passivation, the hydrogen is fed from the hydrogen tank into a gas line which is directly connected to the thermal gas cracker. The hydrogen gas is then leaked in to the chamber through the cracker which dissociates the hydrogen. The key element in achieving passivated surfaces is to ensure that the Si(100) surface only gets exposed to atomic hydrogen without any unwanted contaminants. A mass spectrometer was therefore used to measure the abundance of the different species in the chamber during passivation. Fig. 5.3 shows the most abundant species during one successful passivation, marking each stage by an arrow.

It can be seen that the ratio of the hydrogen pressure is at least two orders of magnitude higher than the other species during the preparation. Initially the gas cracker is slowly heated (A), causing an increase in the amount of contaminants, most notably CO. Once the temperature of the cracker has stabilized, the hydrogen gas is then leaked in (B). Note that this in particular gives rise in water pressure, indicating that the hydrogen gas line is the main water contamination source. Once a steady flow of hydrogen pressure has been achieved, the shutter is opened (C), and the sample is exposed to atomic hydrogen. Note that opening the shutter also increases the CO fraction indicating that the shutter prevents some of it from entering. At the end of step (C), the cracker is switched off, the shutter is closed, and the gas is closed leading to a rapid drop in CO pressure and a slower drop in water and hydrogen pressure. The take-home message is that contaminants emanate from both the gas cracker and the hydrogen gas.

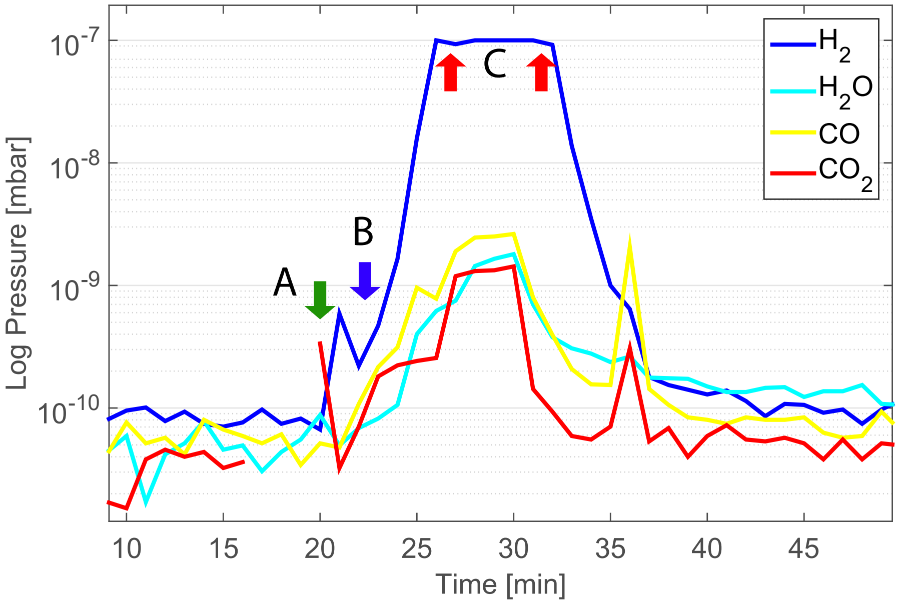

Figure 5.3: Partial pressures of several gases in the chamber during hydrogen passivation by mass spectra. A: Heating of cracker, B: hydrogen gas leaked in, C: shutter open.

5.1.3 Cold trap

As explained in the previous section, in order to achieve passivated surfaces of high quality the hydrogen gas needs to be very clean (i.e. devoid of other gasses such as O_2, CO_2 etc.). Passivated surfaces (that could be imaged using STM) were only obtained when the gas line was baked for a minimum of several hours. Initially, in order to reduce the amount contaminants (such as H_2O), the gas line was baked at elevated temperatures (> 100 C) for extensive periods (4-6 hours) prior to passivation, while the cracker was degassed at (~ 1700 C) for several hours as well. Even with both of these measures, the sample quality of the passivated remained extremely low as evidenced in Fig. 5.4(a).

A 'cold trap' was therefore installed on the hydrogen gas line as shown in Fig. 4.10. The cold trap is essentially a coiled section of the gas line which can be immersed into a liquid nitrogen tank. The coil functions as a cold-trap, where most gasses will adhere to the inner wall of the coil. The outcome

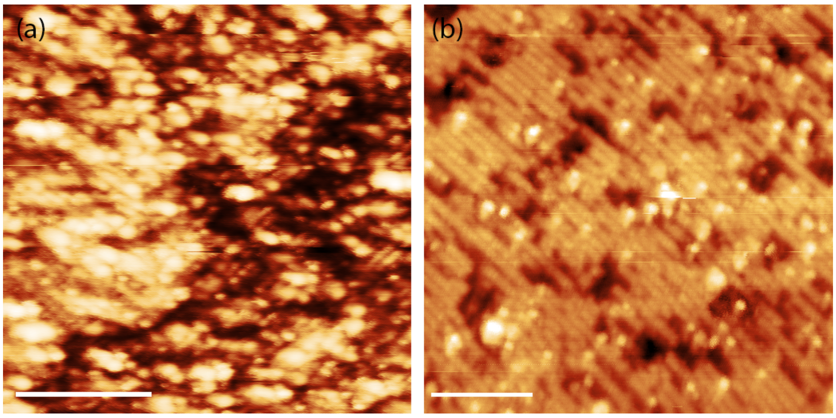

Figure 5.4: Si(100)-2×1:H surface before (a) and after (b) installing a cold trap. Scale bars correspond to 10 nm.

is that the ratio of the hydrogen versus other gases in the line will increase dramatically (higher purity). A key finding, was that the cold trap needed to have a high surface area in order to lower the defect density of the passivated surfaces appreciably. By first baking the gas line, flushing it with hydrogen, and then subsequently immersing the cold trap in liquid nitrogen for more than 30 minutes prior to (and during) exposure to a surface dramatically increased the surface quality of the passivated surfaces. Surfaces were now of comparable quality to the image shown in Fig. 5.4(b).

5.1.4 Thermal gas cracker

The second limitation in obtaining clean passivated surfaces stems from the thermal gas cracker (Section 5.1.2). During passivation, the metal capillary is heated to somewhere between 1500-2000°C in order to dissociate the molecular hydrogen into atomic hydrogen (Section 4.4.4). Due to the intense localized heating, other gasses such as CO will inevitably outgass from the capillary. Since the sample is in direct line of sight with the cracker, it will inevitably be impacted by outgoing contaminants. To test how severe the contamination is, a sample was exposed to the heated cracker for 10 minutes without leaking in gas. The result is shown in Fig. 5.5.

It can be clearly seen that this causes a significant amount of contami-

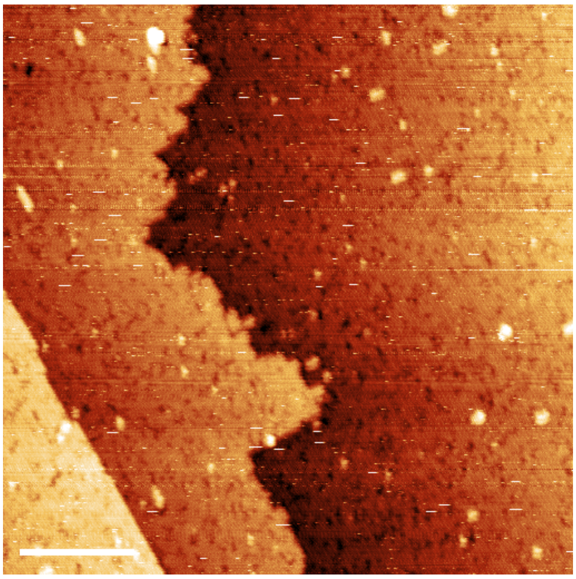

Figure 5.5: STM image of Si surface taken at -1.62 V, 140 pA after exposure to heated thermal gas cracker for ≈ 10 minutes. Scale bar correspond to 20 nm.

nation to the sample. It is therefore necessary to minimize the amount of exposure of the sample to the cracker while still be able to fully saturate the surface with hydrogen. Our results indicate that exposing the sample to the cracker for a very short time (60 seconds) while leaking in hydrogen to the chamber at a pressure of 1-2$\times10^{-6}$ mbar produced the best results.

The cracker can be conditioned (heated to 1500-2000°C for several hours without leaking in hydrogen) such that the outgassing of the various gasses decreases by a certain amount. However, even prolonged conditioning only seems to marginally reduce the outgassing. Ideally, during passivation, the cracker should be heated within the low temperature range of 1400-1580°C while degassing the cracker should be carried out at 200° above the passivation conditions. Unfortunately, since we can not directly measure the temperature at the capillary, the emission current/filament current was used as a proxy for the temperature. It was found that applying a low filament current of 4.0 A (30-35 mA emission current) during conditioning (while regulating the copper block at 400°C using low water cooling) and 3.8 A (15-20 mA emission current) during passivation (with maximum possible water cooling) produced the best results.

5.1.5 Double bakeout

As mentioned previously (Section 5.1.4) despite extensive degassing of the cracker, the pressure during conditioning remained too high, causing severe contamination on the samples. To overcome this problem, a double-bakeout of the system was carried out. During each cool-down, elements such as the manipulator arm and the cracker (filament as well as capillary) were extensively degassed. After cool down the cracker was further conditioned (using the same parameters). This allowed the cracker to become extremely clean, reaching pressures of 5-7 × 10^{-9} mbar during conditioning (Section 5.1.4). Passivated surfaces of comparable quality to the one shown in Fig. 5.6 thus became routinely possible.

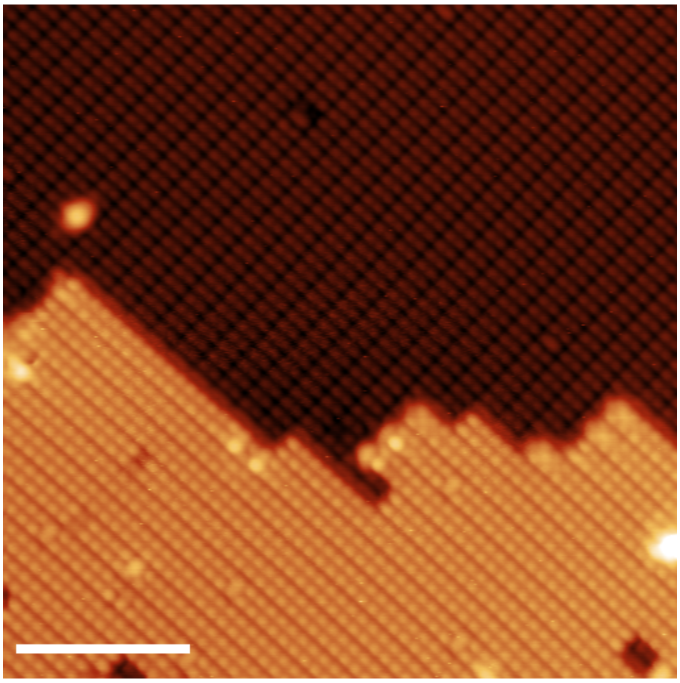

Figure 5.6: STM image of H:Si(100) surface of high quality taken at 1.5 V, 10 pA. Scale bar correspond to 5 nm.

Additionally, the double bakeout also increased the cleanliness of the manipulator arm, thus providing higher quality Si(100) surfaces by lowering the vacuum pressure during flashing. However, this effect is more moderate and the main advantage of the double bakeout is to clean the cracker.

As previously shown (Section 5.1.2), both the hydrogen gas purity and the cracker represented bottlenecks for achieving high purity H:Si(100) samples. Initially, the hydrogen gas was shown as the main bottleneck (Fig. 5.4(a)). However, after substantially modifying the gas line and extensive cleaning of the cracker (using double bakeout) it is at this point unclear where the new bottleneck lies. Further experiments are necessary in order to determine the limitation of the passivated surfaces.

5.2 STM imaging of surfaces

Fig. 5.7 shows conventional STM images of a H:Si(100) surface acquired at different bias using a W tip. The surface appears to consist exclusively of the (2×1) reconstruction, with very few defects present. Similar to the Si(100) surface (Fig. 5.2), the most common defect types appear to be vacancies and bright features, which can be attributed either to exposed dangling bonds or adsorbates such as water. The high surface quality is most likely a result of a very low exposure to contaminants during passivation (see previous section). For high quality surfaces, silicon islands (due to etching) and Bt structures (local regions 3×1 reconstruction) were virtually never present. However, large quantities of Bt defects did appear on one high quality surface after introducing Argon to the chamber (Fig. 4.4). This suggests that the annealing conditions of the sample during passivation is appropriate. However, split-dimers (which are most likely dihydride dimers), also appear among the most frequent type of defects. This suggests that the surface quality might be further improved by improving the annealing conditions (and thus further reducing the number of split dimers) during passivation [83].

We found imaging low-and medium quality H:Si(100) surfaces to be notoriously hard when using standard STM tips. However, imaging high quality surfaces with high resolution proved relatively easy. The stability of the tip seemed to rarely change, even when imaging over large areas ($\geq$ 40 nm^2). This suggests that most (but certainly not all) tip instabilities were caused by surface adsorbate contaminants interacting with the tip.

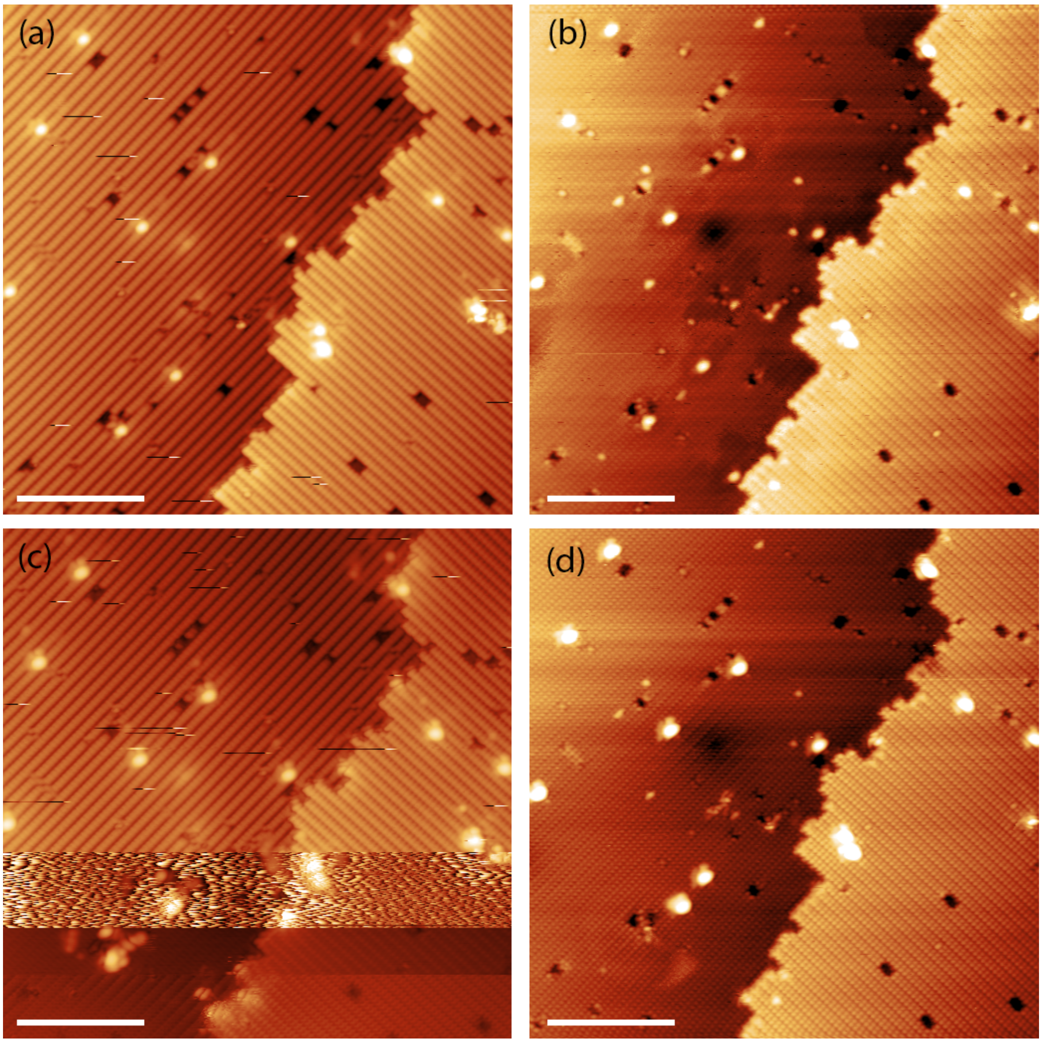

Figure 5.7: STM image of Si(100):H surface of high quality taken at (a) -2 V, (b) 2 V, (c) -1.5 V, and (d) 1.5 V bias. All images were performed at 10 pA. Scale bars correspond to 10 nm.

For some reason, imaging at negative bias proved more difficult than positive bias, as exemplified in Fig. 5.7. Previous experiments from our group [84], support this finding. In those cases, an unexcited qPlus sensor was used to map the overlapping current and amplitude traces during acquisition. It was found, that the amplitude traces correlated strongly with the topography of the surface, indicating a high degree of interaction with the surface. This suggests that instabilities, are caused by either tip-sample interactions or cross-talk between the amplitude and current channels. Since we observe similar behavior for a tungsten tip, we can rule out cross-talk as the cause. This behavior seemed to occur in general, but at this time, it remains uncertain if it occurs for all types of tip states. It would be interesting to compare this instability behavior as a function of bias for all tip states to determine if this is related to certain tip geometries, adsorbates on the surface, or phenomena.

To date, most imaging has been performed at positive bias. Fig. 5.8 shows a selection of the most commonly observed high resolution contrasts of the dimers using the same imaging conditions, with a more extensive selection presented in Appendix A. The different image contrasts should therefore represent variations in the tip structure. In general, the STM imaging contrasts can be divided into four main categories: *row*, *dimer*, *single atom*, and *asymmetrical* representation of the dimers/atoms. However, we should note that other more infrequent surface representations were also observed. In the next chapter, the tip imaging state dependence on hydrogen desorptions are examined.

Ideally we wished to combine simultaneous STM/AFM imaging with force spectroscopic investigations and theoretical calculations to allow better understanding of the specific tip geometries and chemical interactions that give rise to the various tip imaging states. The hope was that this could provide us with a better understanding of which tip geometries and/or tip terminations that are most suitable for hydrogen desorptions, which we will talk about in the next chapter. Unfortunately due to time-constraints this has not been implemented. Only as small subset of AFM images and spectroscopies were investigated, which we will discuss in the next Section.

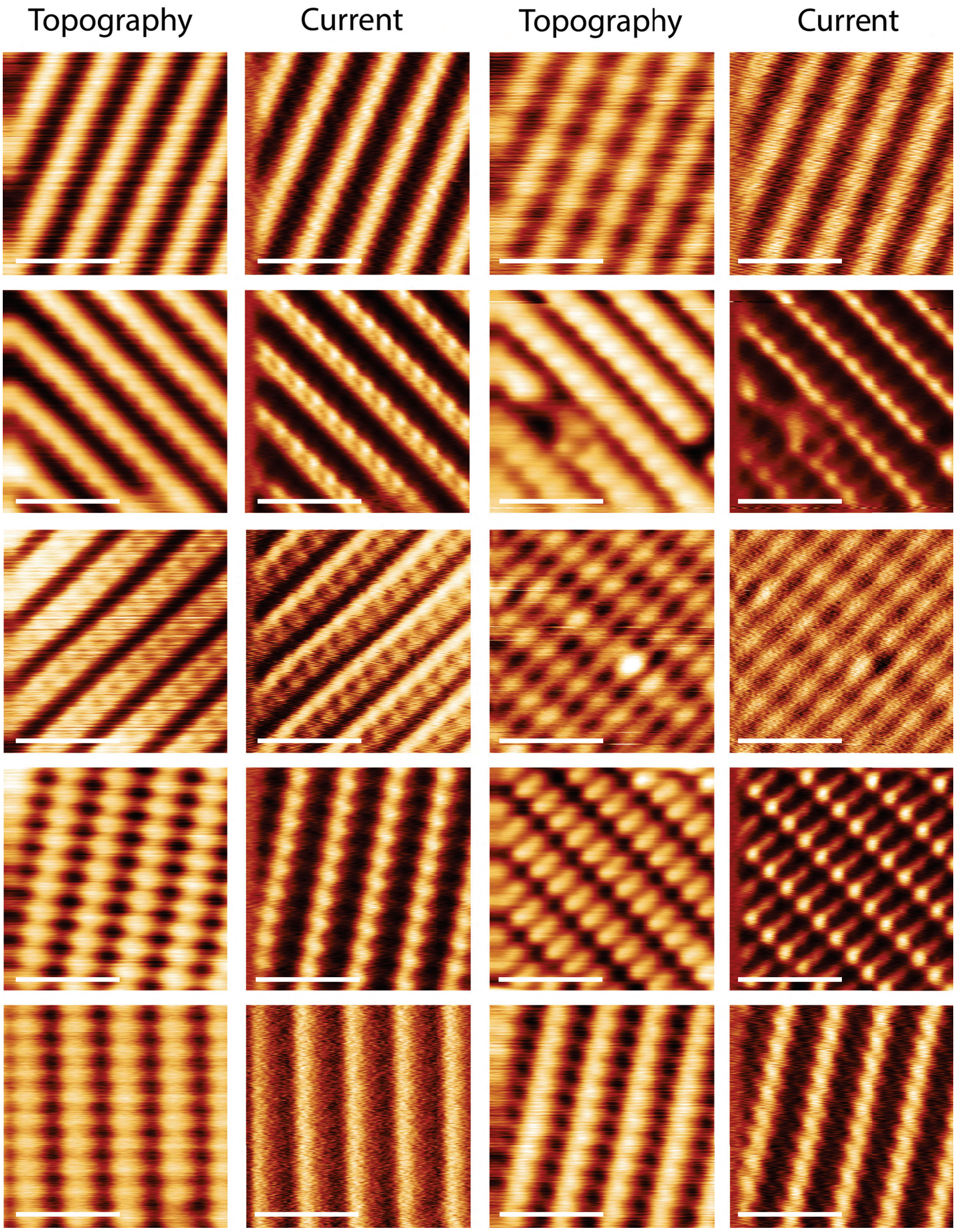

Figure 5.8: Selection of STM images using same imaging conditions (1.6 V, 10 pA). By applying the same imaging conditions, the different surface contrasts should therefore represent different tip states. Scale bars correspond to 2 nm.

5.3 Outlook: AFM imaging and Spectroscopy

AFM studies of H:Si(100) surfaces were conducted using Si cantilevers at RT (Section 4.7.1). Surprisingly, imaging of high quality surfaces produced very stable atomic resolution imaging with exceedingly rare tip crashing. The most likely cause for this stability, seems to be the very clean and atomically flat surfaces. The lack of adsorbates, and reactive species prevent unwanted tip-sample interactions. This was tested, by initially imaging smaller areas and then subsequently constantly zooming out while imaging ever larger areas. At large scale images ($\sim$ 25 nm) the tip encountered non-flat features on the surface, immediately followed by tip crashing. This indicates that the surface itself (provided high surface quality) is reasonably easy to image using AFM.

Previous experiments [132] suggests that the dimers appear similar during AFM imaging, for a multitude of tip states. In Fig. 5.9(a) these typical AFM images of the H:Si(100) surface are shown, where the hydrogen atoms appear as dark (repulsive) features. Contrary to previous studies, we observe additional imaging states as shown in Fig. 5.9(b-d). However since only a small subset of images were acquired, it becomes difficult to generalize on possible multitudes of tip imaging states that can be observed using AFM and AFM/D-STM imaging. For this particular tip imaging state, when imaging with a bias (5.9(b)), the dimer structure appears symmetric. By removing the bias, an interesting asymmetry of the dimers appears (Fig. 5.9(c)). At smaller tip-sample separation (larger Δf), the asymmetry becomes more prominent (Fig. 5.9(d)). The exact cause for this asymmetry remains unknown, although the geometry of the tip is suspected to play a large role. Force spectroscopy measurements were performed on top of hydrogen atoms, and compared force measurement curves performed at null sites to subtract long range interactions as shown in Fig. 5.10(a). In Fig. 5.10 (b) the calculated force-interactions are shown when averaging over five atomic sites.

Contrary to previous experiments [132] we find an attractive force between tip and sample. Previous theoretical calculations [132] show that Si terminated tips produce an attractive interaction of $\sim$15nN (similar to our

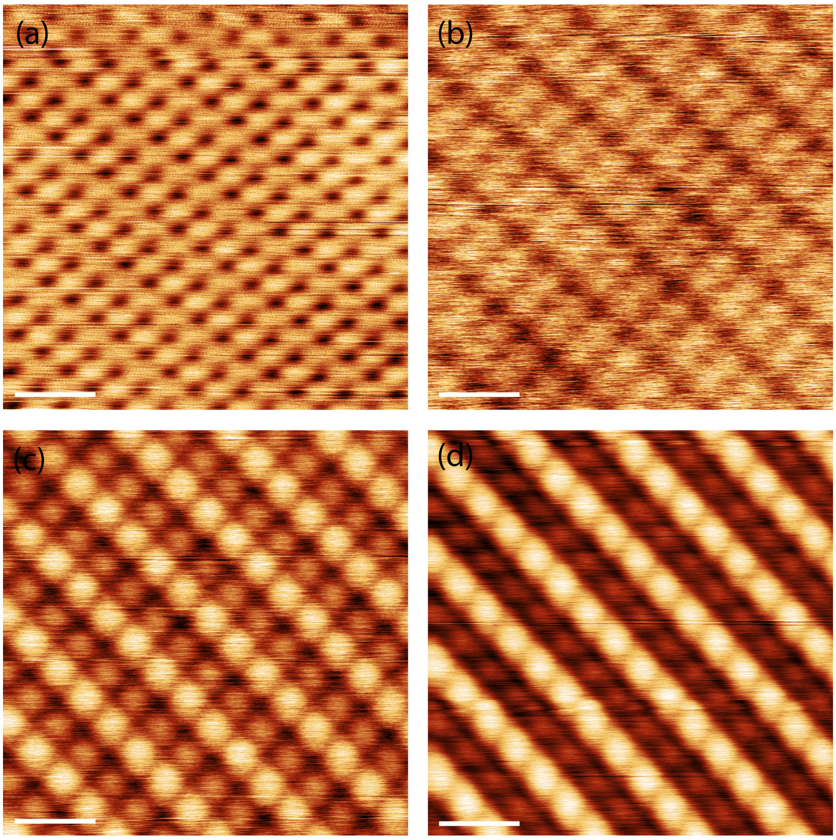

Figure 5.9: NC-AFM images of H:Si(100) surface over same area at small tip-sample separations. Images (b)-(d) acquired over same location. Image parameters: (a) $\Delta f = 152.6$ Hz, $A = 5.36$ nm, 0 V, (b) $f = 503.4$ Hz, $A = 5.36$ nm, 1.8 V, (c) $\Delta f = 400$ Hz, $A = 5.36$ nm, 0 V (d) $\Delta f = 460$ Hz, $A = 5.36$ nm, 0 V. Scale bars correspond to 1 nm.

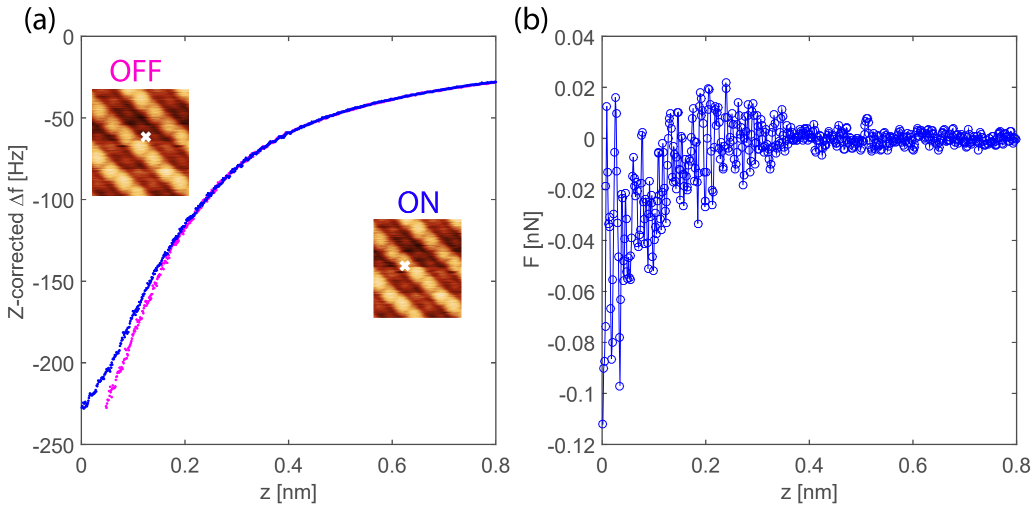

Figure 5.10: Experimental $F(z)$ interaction using the on/off method. (a) Δf measurements taken over surface hydrogen atom (blue) and between rows (magenta). (b) Calculated $F(z)$ when averaging over five atomic sites. Note: $z = 0$ correspond to tip-sample separation during image acquisition at $\Delta f = 460$Hz.

experimental findings) while hydrogen terminated tips show almost no attractive interaction. It it therefore possible to speculate that the AFM topographs observed in Fig. 5.10(a) (5.10(b-d) have Si (H)-tip terminations. Unfortunately, the results of these measurements are inconclusive, as only a limited number of spectroscopic and image acquisitions have been obtained. Additionally, a positional uncertainty also exists due to the discrepancy in the imaged tip position of the forward and backward image traces.

Combined AFM/D-STM imaging using Si cantilevers has been performed by applying a bias between cantilever and sample. D-STM (tunnel current) imaging in this case proved exceedingly difficult. In this case, certain artificial features re-appeared throughout long periods of imaging. These features are caused by cross-talk between the frequency and current channels, when a bias is applied [133], also known as the 'phantom force' [134]. This was observed for nearly all images where a bias was applied.

Conventional STM imaging was also attempted using unexcited Si cantilevers, which produced poor results. Although it was relatively straightforward obtaining atomic resolution, the images were very noisy and showed unstable imaging. Conventional STM imaging using a metallic tip usually resulted in a wide array of contrasts of the dangling bonds. However, for Si cantilevers, the dimer structure nearly always looked similar to the ones shown in Fig. 5.11. It is suspected that this particular image contrast, is a result of Si termination on the tip. Due to the poor quality obtained using Si cantilevers, we are planning on using Pt/Ir coated cantilevers for improved combined AFM/STM imaging and force spectroscopy for all future AFM studies on hydrogen passivated surfaces.

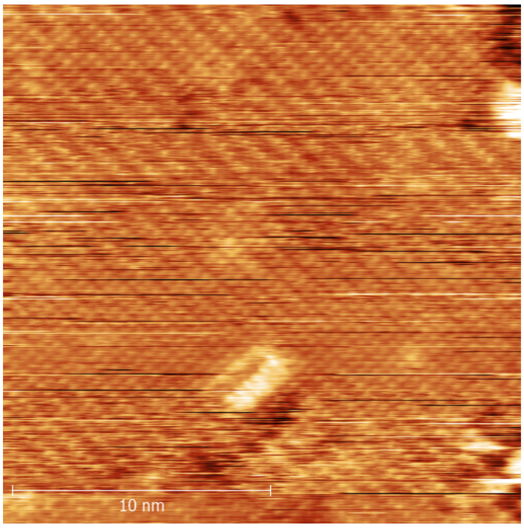

Figure 5.11: STM imaging using an unexcited AFM Si cantilever. Acquired at 2 V, 50 pA.

To conclude, a hydrogen passivation procedure has been implemented to obtain high quality H:Si(100)-(2×1) surfaces. For STM imaging the dimers appear very dissimilar depending on the tip state but can but the most commonly observed imaging states can be categorized into *row*, *dimer*, *atom* and *asymmetrical* representations of the dimers/atoms. To provide a better understanding of the STM contrast mechanisms, AFM imaging and force spectroscopic measurements have been performed on the surface. Contrary to previous studies [132], we observe that the dimers can appear dissimilar based on the tip, suggesting that AFM imaging is possible using several tip terminations. We are therefore planning on acquiring performing 3D force spectroscopy while acquiring simultaneous STM/AFM imaging using a multitude of tips and tip (imaging) states and combining it with theoretical calculations will allow a better understanding of the STM contrast mechanisms.

Chapter 6

Towards autonomous SPM manipulation

In scanning probe microscopy (SPM), the ability to image and perform manipulations has been shown to be crucially dependent on the state of the tip. Since their creation, these instruments have been invaluable for investigating and manipulating surfaces and adsorbates at the atomic scale. An especially important class of atomic manipulation is the scanning tunneling microscope (STM), which has been shown to perform hydrogen resist lithography on hydrogen passivated Si(100) surfaces with single atom specificity [135]. This technique has been used in the process of creating functional electronic devices, including single electron transistors [93], at the atomic scale. One of the main advantages of this technique is that it allows atomic scale imaging during the patterning process, thus offering flexibility and operational control during patterning.

Our ultimate objective is to create atomic scale structures, in an entirely automated and autonomous fashion, without any human intervention. The author has been involved in two lines of work trying to achieve this objective; (i) one performed at Zyvex Labs, where the focus of research is devoted to large-scale autonomous patterning and (ii) the other conducted at the University of Nottingham where single atom manipulation and specificity is emphasized. This chapter is therefore divided into two sections: The first section covers the work at Zyvex Labs performed by the author, but presented in the light of "the grand scheme of things" at Zyvex. A publication on this Zyvex-based work is in the pipeline. In the second section, work performed at the University of Nottingham is covered, from which a publication has recently been submitted [136].

6.1 Autonomous SPM manipulation: Large scale patterning and control

This first section deals with large scale patterning of DB assemblies, and how to overcome some of the difficulties associated with creating them. At room temperature (RT), this process is severely inhibited by effects such as creep, drift and hysteresis behavior of the tip. In order to create large scale patterning it is therefore crucial to minimize (at least some of) these effects. Particularly, in order to minimize creep and hysteresis it becomes necessary to both minimize and optimize the path of writing.

As explained in section 4.3.3 in order to perform hydrogen desorptions, an STM tip is used as a lithography instrument. The STM instrument is extremely convenient, as it allows atomic scale imaging of the surface both before and after desorptions. As a result, the the exact writing features can be identified and placed with atomic deterministic precision.

The focus at Zyvex Labs is to fully automate the patterning process, with single atom accuracy. Although, like both Simmons et al [93] and Schofield et al [85], we have achieved H-depassivation lithography with atomic precision (see Chapter 5), the focus of our work is not on performing lithography with the highest spatial accuracy. Instead, our objective is to implement least-path algorithms to minimize influences of effects such as creep and hysteresis (explained below) on the writing accuracy.

The patterning is performed by combining two different writing modes: atomically precise (AP) and field emission (FE) mode (Section 4.3.3). For deterministic writing, the AP mode is selected to write single atom lines while the FE mode is selected for multiple lines. Since the FE mode can extract many atoms relatively quickly, it can be used for fast writing on large scale sections the patterning where the accuracy is less crucial. By combining the two, as shown in Fig. 4.8(xiv-xvi), large scale patterns can be written with atomic accuracy relatively quickly.

Using this multi-mode writing procedure, the author was able to create DB assemblies as exemplified in Fig. 6.1. Initially, the optimal parameters (V,I, and dosage) for writing AP and FE profiles are determined by writing

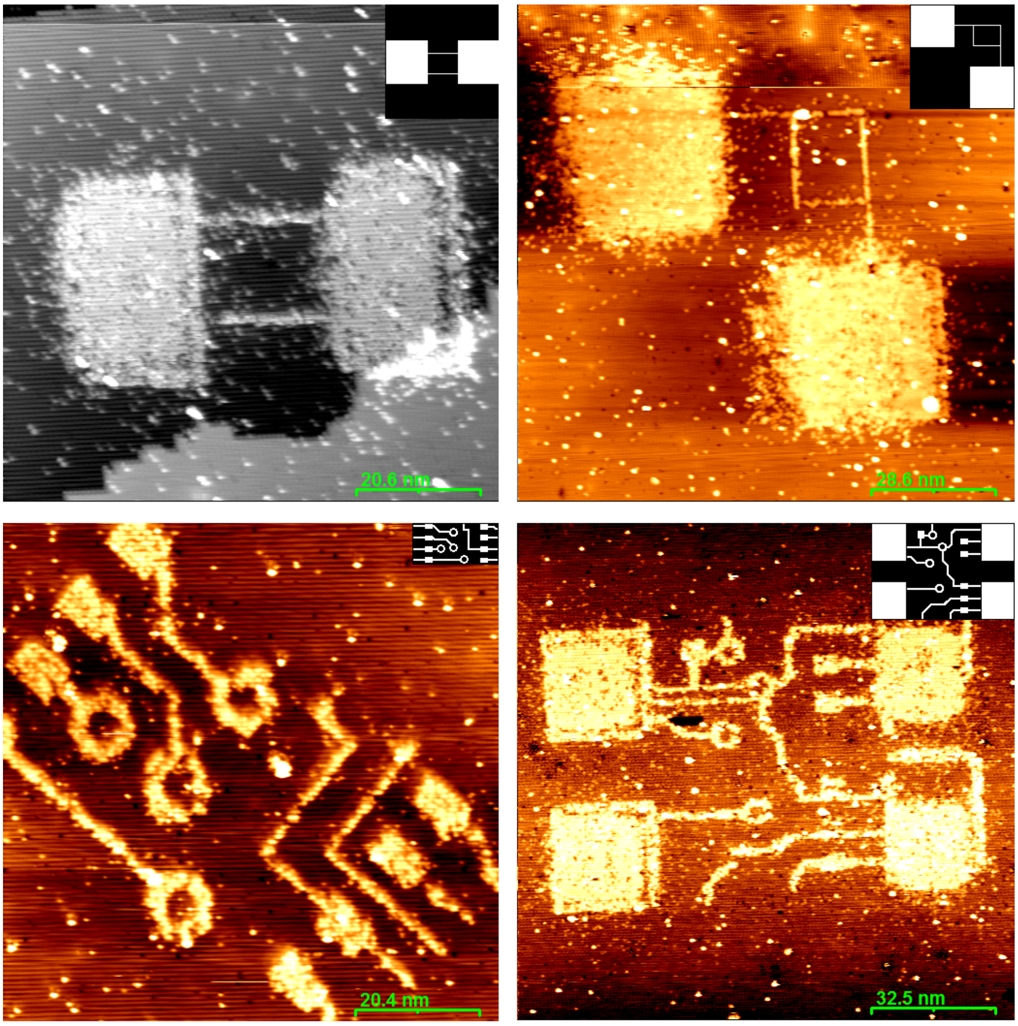

Figure 6.1: Selection of large scale patterning based on bitmap images (inserts) used as input for writing vectors. For the bottom left image, the writing vectors have been rotated after the image has been converted to writing vectors.

AP desorption lines similar to the ones shown in Fig. 4.8(i) using different mixtures of desorption parameters. The desorption parameters producing the most atomically precise linewidths are chosen, and are subsequently used as input to a multi-mode lithography compiler to determine optimized tip paths for AP mode and FE mode in order to minimize write time while maintaining atomic precision edges. A given pattern (in the form of a bitmap) is then fed into a compiler which will convert the bitmap into writing vectors for the FE and AP mode. From the identified writing area, FE vectors are selected first. The area where the FE vectors "do their work" is then subtracted from the total writing area. The remaining area is then used for writing AP vectors.

However, one may notice that when writing large scale patterns (Fig. 6.1(d)), the writing becomes less precise. In this case, there is a large misalignment between some of the AP and FE vectors. The problem is caused by several factors. Drift between the tip and sample causes the surface to be shifted out of alignment. This causes the writing pattern to be shifted as well. So in general, the longer the patterning takes, the larger the discrepancy becomes. Although drift can be minimized, at room temperature it can never be completely eliminated. Although a drift compensation routine has been implemented from Zyvex [137], we will not discuss it here as it plays a minor issue (assuming the patterning process is reasonably fast) in terms of accuracy, and does not affect the bahavior of the tip. The two main problems associated with writing large scale patterning (assuming a perfect tip that does not change during writing) is creep and hysteresis of the tip which are both tip dependent. Fig. 6.2 shows how creep is caused (top) and its effects on imaging the surface (bottom).

Creep occurs as a direct result of moving the tip. Moving the tip on the nanometer scale is carried out by extending/contracting the piezo by applying a voltage to it. Although most of the motion occurs instantaneously, the piezo will keep extending over a period as a result of the new voltage. As a result, the images that one observes, becomes smeared. The creep is proportional to the tip movement. In other words, the creep becomes larger for larger tip movement. As a result, creep therefore represents a serious is-

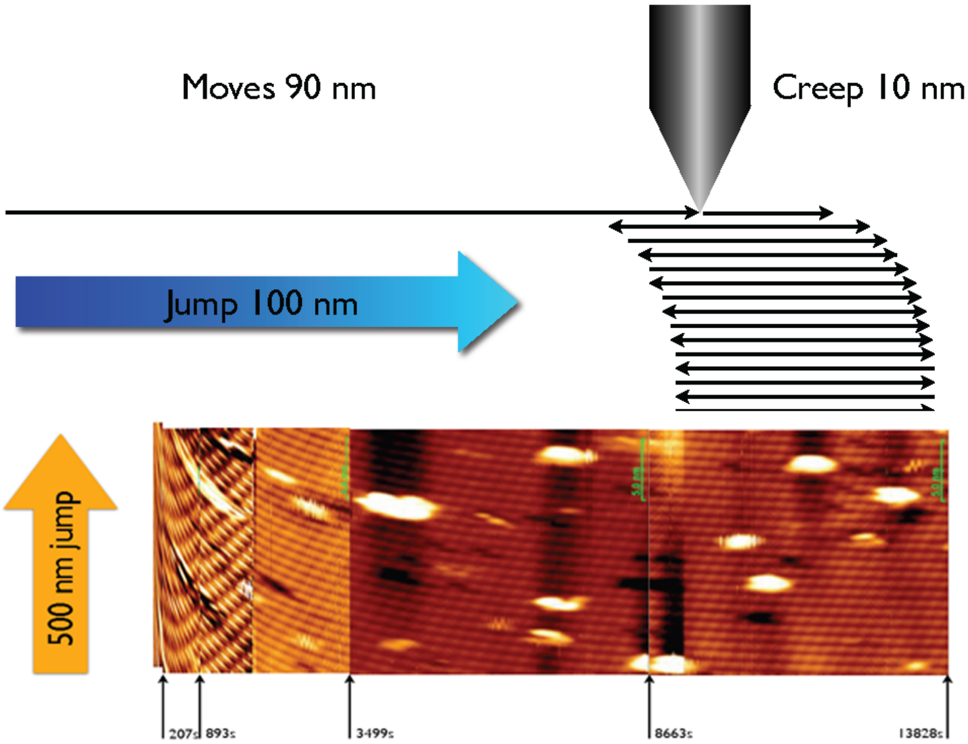

Figure 6.2: Creep associated with tip movement. (top) moving tip on large scale causes the tip to traverse most of distance instantaneously, but still extending slowly due to extension/contraction of peizo material. (bottom) Images appear distorted as a result of further movement during scan. From [138].

sue in terms of accuracy when performing large-scale patterning. Creep can be minimized in several ways: either by moving the tip very slowly, preventing the tip from jumping large distances, pausing the writing conditions at specific convenient times, or smoothing out large scale motions by writing in localized areas over an certain time period. Note, that these choices are by no meant the only possibilities for minimizing creep. At Zyvex, an electronic feedthrough has been developed to correct for creep in real-time. The creep correcter works by adjusting the image coordinates using predetermined coefficients for the creep correction at different time scales. As the tip moves, the creep correction coefficients are then multiplied proportional to the tip movement and the image coordinates are thus corrected in real time. Although this technique does help in minimizing the creep, it has several drawbacks.

Firstly, the correction factors are dependent on the materials properties, and therefore needs to be determined for different equipment. Secondly, the the correction factors only apply a averaging of the tip movement, while the real position of the tip can be more erratic. It thus still becomes important to minimize tip movement (either by moving slowly, avoiding large movements, or constraining movement at specific times), during patterning in order to reduce creep.

The second major issue with writing is caused by hysteresis of the probe. Fig. 6.3 an attempt is being made on writing five large scale desorption lines of equal length. One observes that the hysteresis causes the lines to be of unequal length. Experiments have shown [1], that the hysteresis is proportional to L^2 of the writing length, and is dependent on the history of the tip. As a result of these effects writing large scale patterning with high (atomic)

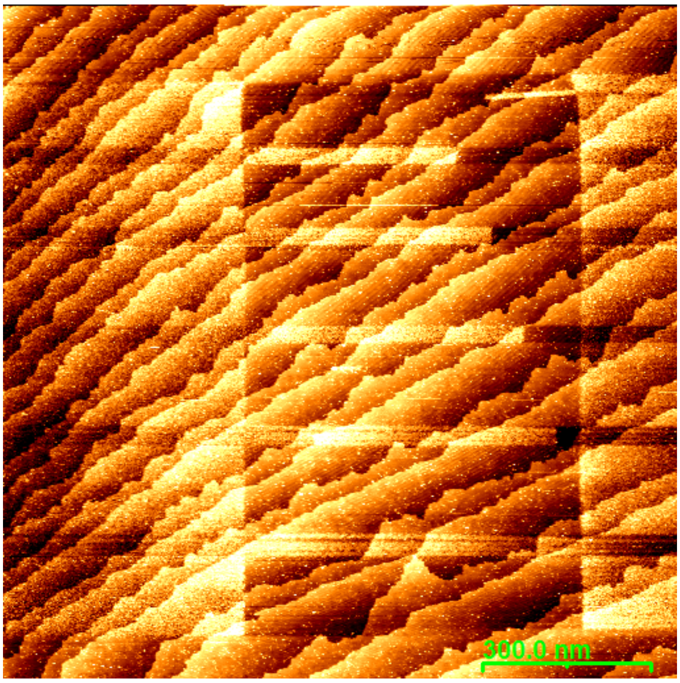

Figure 6.3: Problems caused by tip hysteresis. After attempting to create five BD lines of equal length, hysteresis of the tip causes the lines to be stretched out proportional to L^2 of the writing length. From [138]

---

[1] Comments by J. Ballard, Zyvex Labs

accuracy becomes extremely difficult. The author was therefore assigned to implement an algorithm for both optimizing and minimizing tip movement to be used for writing large scale arbitrary patterns.

6.1.1 Minimum path algorithm

As explained in a publication from Zyvex ([113]), patterns are written by (i) loading in a bitmap image of the selected pattern. Each pixel represents a dimer to be written. From this image (ii) horizontal and vertical vectors are generated (FE vectors are generated first, and the area they cover are excluded from the area where AP vectors are generated). (iii) Overlapping vectors are excluded with respect to the longest vector. (iV) The process of generating and excluding overlapping vectors is then repeated for the shorter vectors, until there are no more vectors to exclude. Patterns are written by first writing the longest vector. The tip then moves to the endpoint of the nearest vector and writes that line. This is repeated until all vectors are written. Fig. 6.4 shows a simple example of this principle.

In Fig. 6.4(a), the path for tip movement between writing vectors when starting from the longest vector is shown. Since in this particular case, all writing vectors are of equal length, the tip will start from an arbitrary position. As a result, the total minimum path for tip movement is clearly not optimal. At some occurrences, the tip makes large jumps back and forward, in order to complete the writing. To avoid this, the author modified the writing path algorithm to include all possible combinations of writing paths and subsequently select the path which provide least tip movement. In Fig. 6.4 the result for this particular example is illustrated. Although it has been shown through testing, that this procedure only moderately improves overall tip movement, it does significantly minimize any unwanted jumps that could cause creep to the tip.

Despite this improvement, the method is still extremely crude for minimizing tip movement both during and between writing. For instance, if the vectors in Fig. 6.4 had varying length, the minimum path would look quite different and even when selection the optimal path, it might not be possible

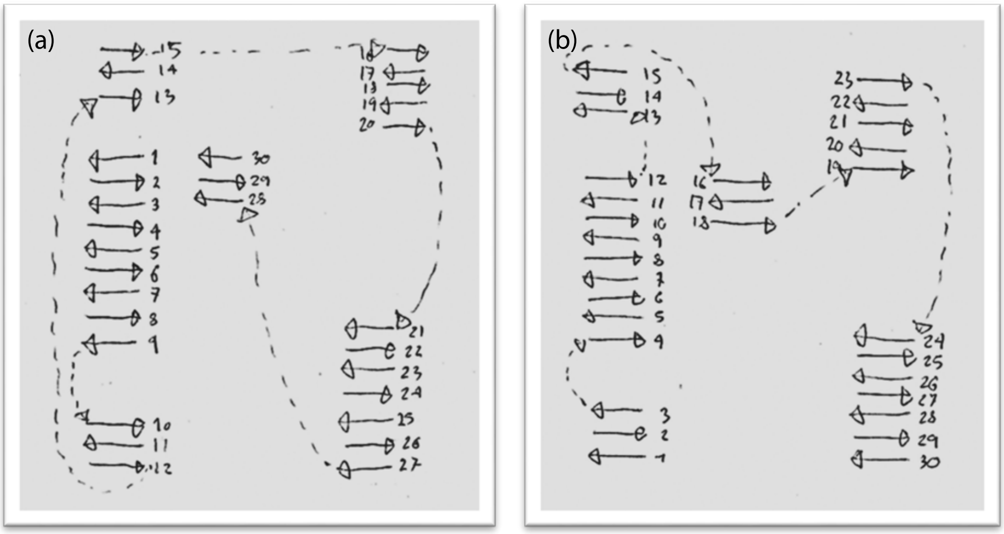

Figure 6.4: Simple diagrams used to illustrate principle of minimum path procedure, where arrows represent writing vectors used to write AP desorption lines and the dashed lines represent the selected path of tip movement (without desorption) between writing clusters. (a) The tip moves from an initially designated position (vector 1) along a minimum path in the direction the arrows are pointing. (b) Modified minimum path to include all possible combinations of tip path movements between vectors. The length of all writing vectors are presumed equal.

to avoid sudden jumps. When selecting arbitrary patterns, this becomes even more complicated. The author therefore modified the least-path algorithm to segment the image into clusters based on the density of writing vectors. If the density of writing vectors within a certain area is higher than a certain amount, the minimum path between these vectors will be determined and written first. The tip will then move the least path between the clusters. In principle, this method will allow the tip large scale movement in a more smooth way, as it slowly writes one cluster after another. The author implemented this algorithm but it was never tested experimentally. It is assumed by the author, that the algorithm is still being modified by the people at Zyvex and that a publication is in the pipeline.

6.2 Autonomous SPM manipulation: Atomic scale control and specificity

With the ultimate goal of autonomously fabricating atomic scale structures, we have implemented the following protocols. (I) In order to automate and control the H:Si(100) patterning process with single-atom specificity, a feedback-controlled lithography (FCL) approach based on the technique developed by Lyding et al. [7] was implemented. By actively monitoring the STM feedback signal and controlling the desorption parameters during patterning, individual atoms can selectively and 'autonomously' be desorbed. This type of automated atomic-precision lithography has been developed and expanded over the last few years by Randall and co-workers at Zyvex Labs;[113] the resulting control system, ZyVector, is now commercially available. We show that for the variant of the FCL technique we have adopted, robust detection of single desorption events is possible. More importantly, the automation protocols we have developed enable the systematic generation and analysis of thousands of hydrogen desorption events, which in turn have provided key insights into the role that the atomistic structure of the tip apex plays in the extraction process. Additionally, although FCL has been used to extract single atoms as proof-of-concept [7], we examine the fidelity of our extraction routine for autonomous lithographic patterning. (i) An SPM software package was developed providing routines for image processing and feature recognition(s). Part (i) was mainly developed by the author and Laurent Guirnet. Part (ii) was mainly developed by Julian Stirling [139], Richard Woolley [140], and later on, others [141, 142] in our group. The SPM software package (SPIW) has been applied to demonstrate tip conditioning in an autonomous manner [143]. However, our autonomous SPM software lacks one crucial component: image comprehension - the ability to make intelligent decision making based on the image features. Our initial goal was to combine (i) and (ii) into a fully autonomous SPM manipulation tool. However, due to time constraints this was not implemented.

The rest of this chapter is therefore divided into 3 sections: in Section 6.2.1, our automated single atom manipulation routine is presented. In Section 6.2.2 the state of progress of our automated image recognition routine is reviewed, along with strategies for successful combination of the two routines. Finally in Section 6.2.3, (iii) the tip state influence on the manipulation(s) and image recognition process is examined. Hopefully, this could lead to improved classification and decision making for future autonomous SPM implementation(s). A publication covering the work in part (i) and (iii) (performed mainly by the author) has been submitted [136]. We conclude the chapter with an examination of additional physical properties of the surface and the generated DB structures, and outlines strategies for future improvements and investigations.

6.2.1 Automated extraction routine

In order to automate and control the H:Si(100) patterning process with single-atom specificity, a feedback-controlled lithography (FCL) approach based on the technique developed by Lyding et al. [117] was implemented. Fig. 6.5 shows a flow diagram of our automated dangling bond (DB) generation routine. Upon activation of the automation routine, the tip was positioned at the desired location for atom extraction, and the initial parameters were subsequently changed to the desired desorption parameters V_D, I_D. The desorption parameters were initially determined from trial and error as the lowest voltage needed to desorb an atom for a given current over a certain amount of time. Upon reaching the desorption parameters, the *Z(t)* feedback signal is then used to monitor in real-time for a jump in *Z*. A desorption event will trigger a jump in the tip position which is used as a spectroscopic signature for the desorption process. A threshold jump height of 0.3 Å was found most suitable for detecting a desorption event, as higher thresholds potentially lead to desorption events not being detected, while smaller thresholds increase the probability of false detections. If a step in Z ($Z_{step} \geq 0.3$ Å) is detected, the desorption parameters subsequently rebound to the initial scan parameters. For step detection, a 10 ms integration time was found to be most appropriate as larger integration times could lead to multiple desorption events. A successful detection of one DB using our

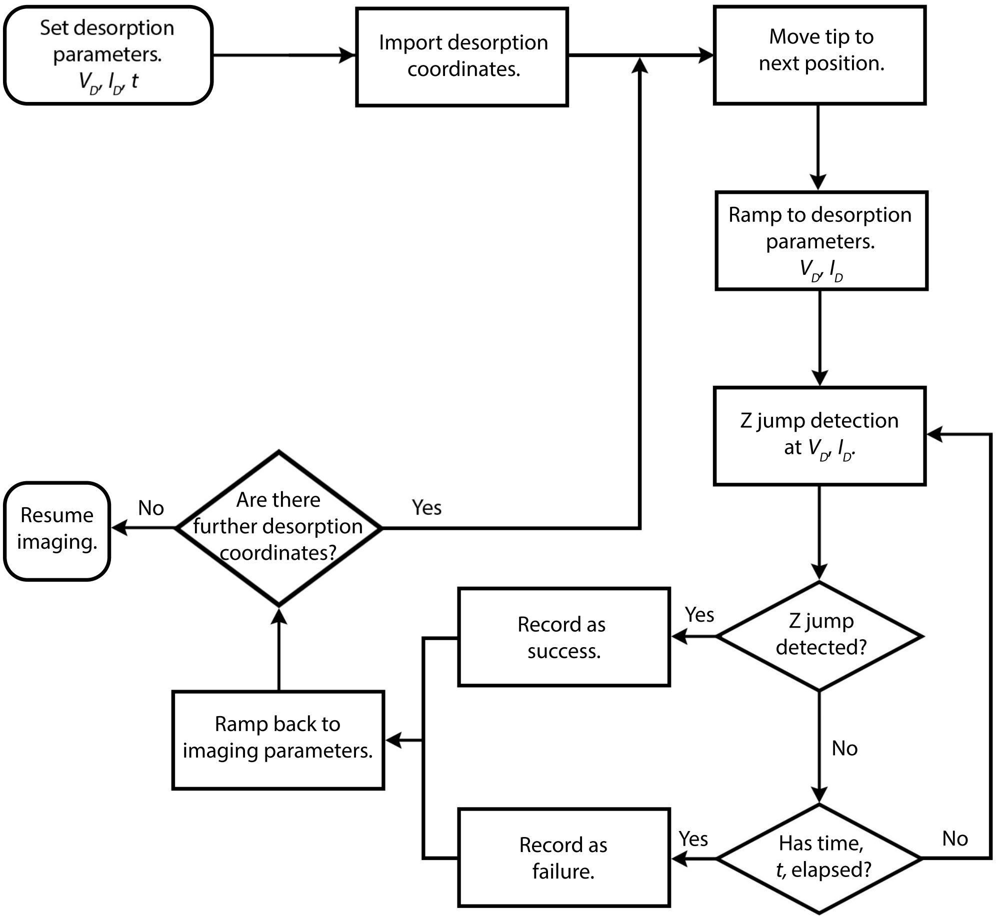

Figure 6.5: Flow diagram showing implementation of automated DB generation. The tip is initially positioned using predetermined desorption parameters and coordinates, followed by a change from scanning conditions to desorption parameters (V_D, I_D, t). The feedback signal, $Z(t)$, was then monitored in real time. Following detection of a jump in Z, or an elapsed time t, the parameters were subsequently restored to the imaging conditions. The desorption procedure was then repeated for all input coordinates.

automated extraction routine is shown In Fig. 6.6

The automated extraction routine can be used for arbitrary patterning

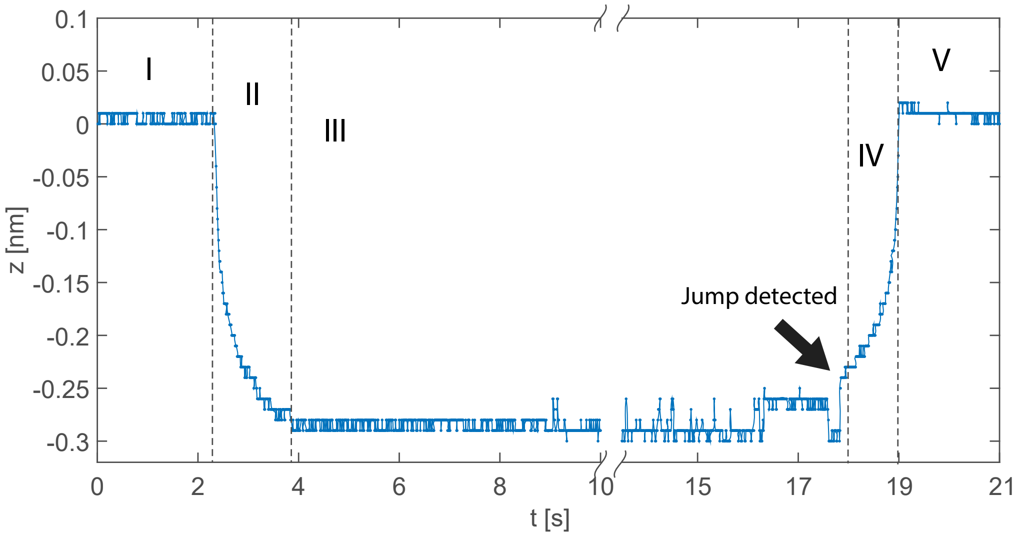

Figure 6.6: The feedback (z) for automated DB generation performed at fixed position. (I) moved to position, (II) ramping I_D, (III) Z jump detection at I_D, V_D, (IV) ramp I_D back to imaging parameters, and (V) reached imaging parameters.

with high fidelity as shown in Fig. 6.7. The reliability of the automated extraction routine was evaluated by comparing step detections from the routine with the true outcome as observed from STM imaging. The results are plotted in Fig. 6.8, for 1126 trials. For each trial, the extraction routine is run for 60 seconds using similar desorption parameters. Desorption events are classified based on whether *any* desorption occurs directly underneath the tip (primary) or if *none* occurs directly underneath the tip. Desorption events with either an uncertain number, or more than four dangling bonds generated, are collectively called clusters. We find that our step detection algorithm reliably detects any type of desorption, whether they occur directly underneath the tip (primary) or not, but elsewhere (secondary). Single atom extraction events are detected with a 90% accuracy. Other unwanted events, such as multiple desorption events, or secondary desorptions, are similarly reliably detected.

It is well known that the structure of the tip can change during a des-

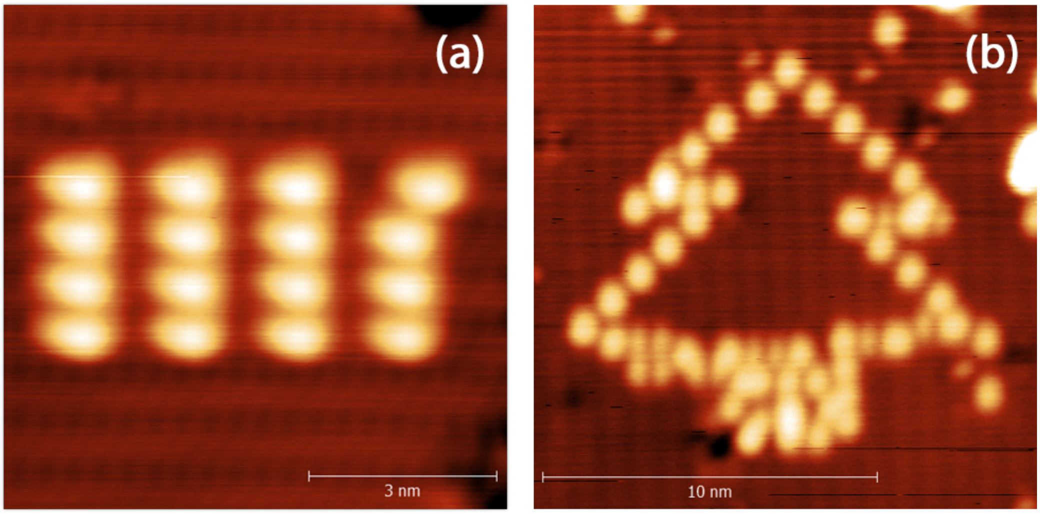

Figure 6.7: Construction of multiple DB arrays using an automated extraction routine. Images acquired at 1.6 V, 10 pA.

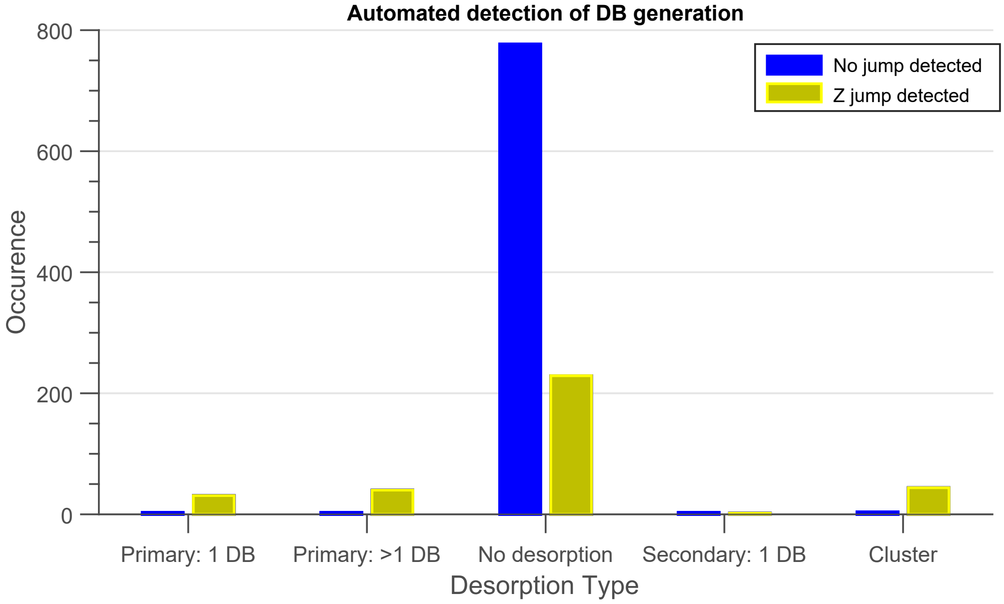

Figure 6.8: Detection efficiency for different desorption types using the automated detection algorithm. Here, *primary* refers to the generation of at least one dangling bond directly underneath the tip (preselected desorption coordinate), while *secondary* is used when *no* desorption occurs underneath the tip (but occurs elsewhere). *Clusters* refers to the generation of more than four dangling bonds (DBs) or an indistinguishable number of DBs.

orption event as a result of tip-surface interactions [115]. To investigate the desorption efficiency under practical conditions, data containing tip changes *during* desorption were not excluded. Influences of tip states changes on desorptions were investigated in more detail in Appendix B.1. We find that only a small subset (8.9%) of the total number of trials involved tip-state changes. All tip imaging states were classified based on the image observed prior to desorption. Only data that could not be classified into the four tip imaging states (row, dimer, atom, asymmetric) *prior to desorption* were excluded (constituting 1.7% of trials).

Unfortunately, the automated desorption algorithm does, unavoidably, register false jumps (22.7%). This is mainly due to noise fluctuations in Z and a low Z-threshold value which triggers false jumps. For reliable autonomous lithographic patterning, an improvement in the detection of a desorption is needed. Possible strategies for detection of a desorption include (I) identification of a desorption event through image visualization, (II) combining the extraction routine with additional spectroscopic signatures for desorption [144], (III) detecting desorption by monitoring current fluctuations [117], or (IV) by increasing the performance of the extraction routine. General ways of improving the performance extraction algorithm include (i) reducing/avoiding noise influences by carefully selecting the-tip sample interactions that lead to the most reliable signals (tip-sample distance, desorption parameters, tip state influence etc..), (ii) filter/smooth the noise fluctuations either electronically or algorithmically or (iii) improving the Z-jump detection algorithm. The Z-jump step detection algorithm focuses exclusively on looking for a jump in Z. It is possible, that desorptions (and unwanted signals) causes more distinguishable real time responses on the feedback signal than simply looking for an abrupt jump. The Z dependence on V, *z(V)*, was therefore examined using an automated extraction routine that looks for a change in Z while changing the voltage in small incremental steps. The data are then used to examine if there is a correlation between the rate of change in height $\mathrm{d}z/\mathrm{d}V$ with actual step detections. The results are shown in Fig. 6.9, and were analyzed by Peter Sharp in our group. Events where tip changes or adsorbate transfer between tip and surface occur are classified

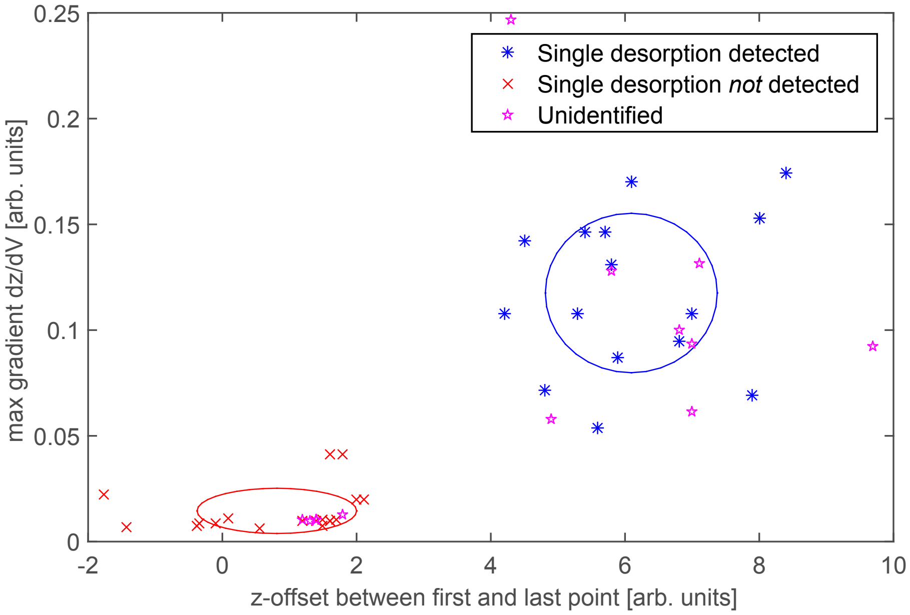

Figure 6.9: Examining the distribution of successful desorption detections by comparing the the absolute magnitude of Z-jump with the rate of change in Z with respect to voltage changes (i.e. $\mathrm{d}z/\mathrm{d}V$).

as "unidentified". We observe, that single desorptions leads to clearly defined jumps in Z, and that the rate of response of the feedback circuit ($\mathrm{d}z/\mathrm{d}V$) has a clear progression. Combining the $\mathrm{d}z/\mathrm{d}V$ dependence with step detection thresholds could lead to improvements in the desorption efficiency. However, due to time-constraints, this avenue has not been examined further.

Combining our automated extraction routine with our automated image recognition software could potentially lead to full autonomous single atom manipulations with high fidelity. We will therefore turn our attention on the current progress in our image recognition and decision-making software and how we plan to combine the two.

6.2.2 Automated SPM processing and decision making

SPM is an extremely effective tool of imaging, manipulating and spectroscopically probing atoms and molecules on surfaces. To perform any one of these attributes, the tip state of the probe apex is extremely important. Often the user starts with an unknown tip state and an inability to recognize surface properties. Based on experience, the scanning probe microscopists uses a selection of tip conditioning and scanning parameters, until the "correct" tip state is obtained. This approach can be both extremely time-consuming and ultimately unreliable.

A highly desirable goal for the SPM community therefore is therefore to be able to automate the *entire* SPM imaging and manipulation process without human interference. Ultimately, it is desirable to be able to identify surface features and and apply analytical tools to investigate the surface properties without assuming any prior knowledge of the surface or the tip. In other words, every aspect of the decision making process would be based exclusively on machine learning.

To address this issue, the Scanning Probe Image Wizard (SPIW) toolbox was developed by Julian Stirling and coworkers[139] in our group. The SPIW package contains analysis tools ideal for scanning probe data processing. Using image analysis tools from the SPIW package and combining them with machine learning techniques, an automated STM tip conditioning software was developed [143]. The automated tip conditioning software was successfully tested on a Si(111) 7 × 7 surface under UHV conditions without any prior knowledge of the surface structure.

To give an idea of how it works, we include some examples of the types of images commonly acquired during STM imaging in Fig. 6.10, and show how the automation software is able to not only distinguish between them, but make rational decisions on how to obtain the "right" tip state. In one example (Fig. 6.10(a)) although flat areas can be observed, the image features change quite frequently. Often SPM users infer that these types of images are attributed to unstable tip terminations. In another example, in Fig. 6.10(b), the underlying surface structure seems to be "smeared out" suggesting that the tip state cannot resolve the surface structure. However, at the same time, 3,4,9,10-perylene-tetracarboxylic-dianhydride (PTCDA) islands (see Chapter 7) are observed quite distinctively and with high resolution, suggesting that the tip is in a state capable of resolving high-resolution features. For such types of images, the SPM user has a difficult time making any interpreta-

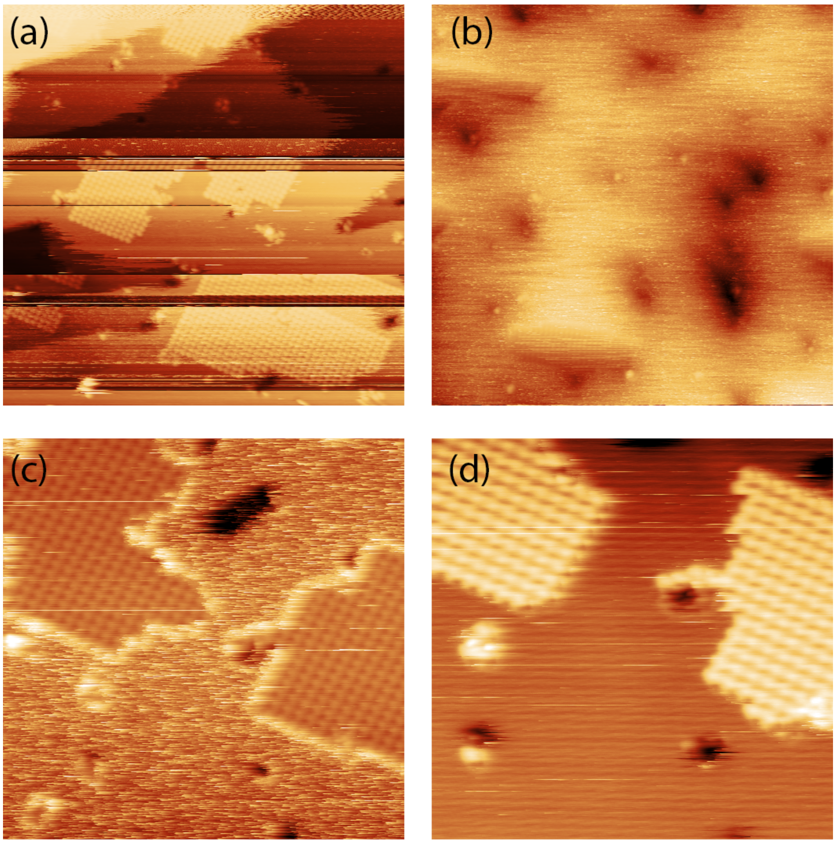

Figure 6.10: A selection of commonly observed STM image types on PTCDA covered Ag(110) surfaces.(a) observation of surface features, but with tip changes and unstable/noisy imaging, (b) unknown problem, (c) surface looks "noisy" due to diffusion of mobile species (PTCDA) on the mobile phase (see Chapter 7), while island features are clearly distinguishable, and (d) observation of underlying surface structure but where the mobile species are not visible.

tions, the "smearing" of the image could be hypothesized to be a result of tip effects or attributed to surface properties, such as contamination on the surface. The SPM user often approaches this problem through a selection of tip conditionings combined with image acquisitions until enough parameter space has been collected to satisfy the SPM user. From the collections of acquired images, the SPM user often infers the underlying surface structure from the images with the fewest number of defects or surface adsorbates, or alternatively from the images with the most distinct features.

Similarly, for automated tip conditioning, a collection of images needs to be analyzed and assessed. In principle, one could condition a tip; collect images and process them; gain an understanding of what the images represent, and use this knowledge to make decisions on tasks such as further modifying the tip, perform spectroscopic measurements, or perform manipulations. In the case of automated tip conditioning, the decision process for obtaining good tip states from an unknown starting point is derived using a specific strategy: (i) initially large-area scans are are obtained. Images are then selected based on the surface roughness; if the images satisfy a certain criteria, the tip will proceed to perform smaller-scale imaging. Alternatively if the criteria is not met, a selection of tip conditionings and scanning conditions are applied. Similar smaller-step increments and image recognition protocols combined with decision makings based on selection criteria are applied until high resolution images have been identified.

The analytical tools for data processing are therefore an important aspect of the automation routine. Rochard Woolley in our group further improved upon many of these tools as exemplified in Fig. 6.11. Here we observe that many common species on the surface can not only be identified (6.11(b)) but even distinguished (6.11(c)) based exclusively on appearance. With the ability to recognize (almost) any atomic structure/feature individually 6.11(d), selective manipulation becomes possible. The intent was to combine our automated hydrogen desorption routine with the automated image recognition routine for full autonomous SPM manipulation. Unfortunately, due to time constraints this has not been implemented. Additionally, a key component is missing in order to allow intelligent decision making is image comprehension - making intelligent decision making based on the image collection.

Another problem with autonomous SPM manipulation is that determining the "right" state is anything but trivial. Usually, the observation of single atoms are thought to represent "good" tip states. However, as we show in 6.2.3, atomic scale resolution represents the least favorable tip state for hydrogen desorptions. To give an example of how "good" and "bad" tip states are selected, we show two images (Fig. 6.10(c-d)) taken over the same area, but with different tip states. In Fig. 6.10(c), the surface appears "noisy", suggesting that the tip is not discerning the surface very well or that the tip is

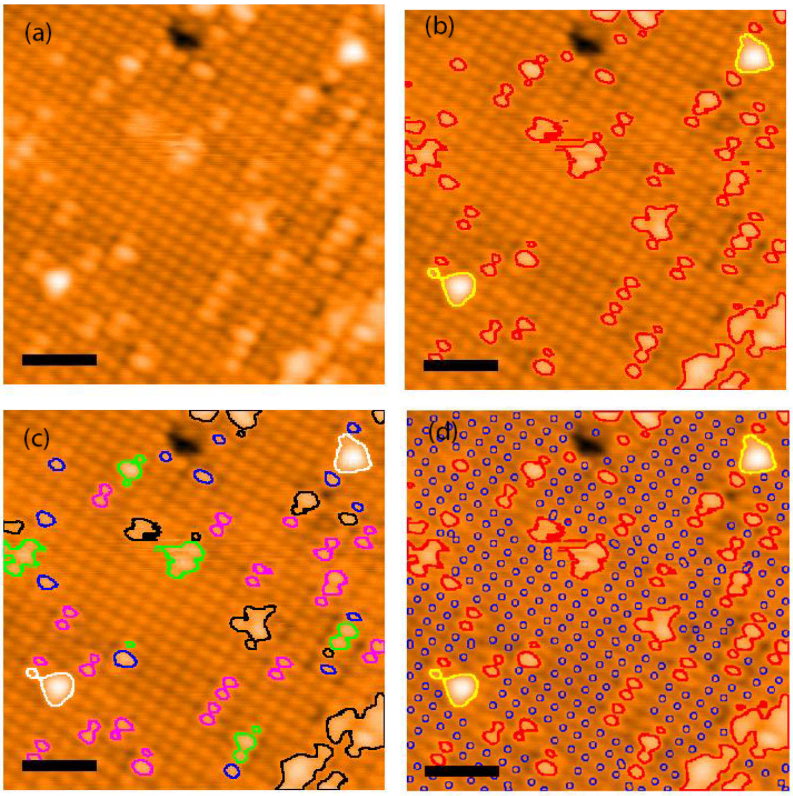

Figure 6.11: Identification of specific surface features on H:Si(100)-(2×1) surface using SPM processing software. Unpublished work by Richard Woolley.

somehow unstable, while in Fig. 6.10(d), the surface is clearly defined. Normally, an SPM user would simply ignore ignore the "noisy" images. However, as we will show in section 7.2, these types of tip states are the "good" states for investigating diffusion PTCDA on that surface. One way to solve this is would be to include analytical tool for analyzing spectroscopic signatures (such as the step detection) or to search for surface contours while imaging as reliable identification criteria. As an example, a simple I(z) spectroscopic reading showing exponential behavior could be used as an indicator for tip stability. Adding further spectroscopic tools could thus improve the decision making process, while simultaneously allow autonomous examination of the physical properties of the surface.

6.2.3 Atomic manipulation: tip state dependency

As previously stated, our ultimate goal is to fully implement an automation routine that will identify the surface structure, provide reliable manipulations on the surface, and subsequently identify changes to the surface, caused by the manipulations. To reliably perform manipulations based exclusively on images, the tip state dependency needs to be examined. The dependence of the desorption efficiency on the atomistic structure of the tip apex was determined by grouping the tip states into a set of broad classes. Fig. 6.12 (a)-(d) shows a selection of observed tip states, and their respective grouping into the following classes: (a) rows, (b) dimers, (c) atomic, and (d) asymmetric.

The desorption efficiency is plotted in Fig. 6.13 as a function of voltage, for each respective type of observed tip states ((a) row, (b) dimer, (c) atomic, and (d) asymmetric). All tip states that could be classified into these groupings (2023 out of 2074 trials) were included in our analysis. Each data value

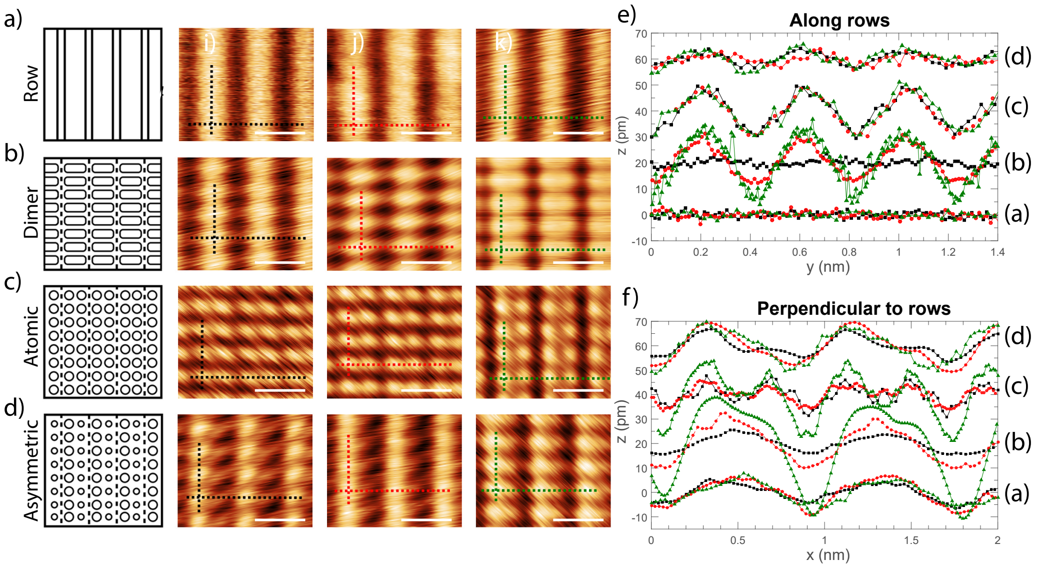

Figure 6.12: Classification of tip imaging state into: (a) rows, (b) dimers, (c) atoms, and (d) asymmetrical. Images (a,k), (b,i), (b,j), (c,i), (c,j), (c,k), (d,i), (d,j), (d,k) have been rotated to align the direction of dimer rows. Line profiles (e) along and (f) perpendicular to rows from positions indicated in (a)-(d).Note that some of the profiles have been shifted by an onset of 20 pm for clarity. Scale bars correspond to 0.77 nm (i.e. the dimer row separation on Si(100)).

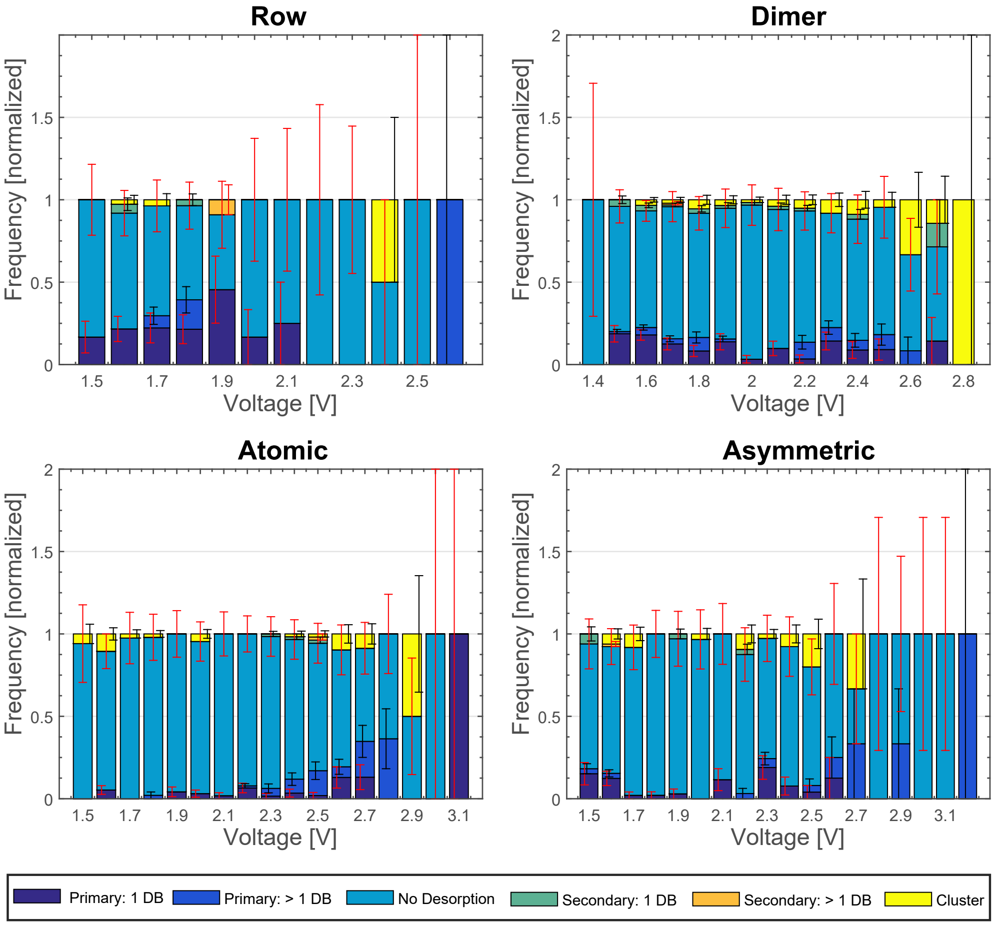

Figure 6.13: Desorption frequency for each desorption type as a function of voltage for different tip imaging states. Each data point corresponds to a run of the automation routine over a fixed voltage value V_{fixed} (normalized to 1 for each V_{fixed} value) for 60 s.

in the figure corresponds to an experimental run of the automated extraction routine. In order to gauge the desorption efficiency as a function of voltage, all data were acquired by keeping the desorption parameters fixed (1.2 nA, V_{fixed}) for a given bias for the same amount of time (60 s). All experimental trials performed at each voltage value (V_{fixed}) were therefore normalized to 1. Data where false detections occurred before 60 seconds were excluded. Standard error bars were obtained by dividing the standard deviation for each desorption type for a given tip state with the square root of the number of events for each voltage.

We observe that the onset of desorption follows the general tip classification rule: $V_{row} \geq V_{dimer}, V_{asymmetric} \geq V_{atomic}$ for a given bias, respectively. This translates into a desorption probability that follow the same rule: $P_{row} \geq P_{dimer}, P_{asymmetric} \geq P_{atomic}$. These results are further corroborated by similar findings using other STM tips and using different FCL automation routines (not included).

Our findings show that row-resolved tip states produce a single desorption event more reliably than other tip states, and that other unwanted reactions (such as producing clusters) are less likely for the row-resolving tip apex than for other states. The reason for this remains as yet unclear but an obvious candidate explanation relates to the density of states of the tip apex. Although the STM image contrast mechanism has been investigated for bare,[103, 104] and passivated Si(100) surface,[145, 146] this has been in the context of the density of states and band structure of the substrate; the influence of the atomistic structure of the tip on the contrast mechanism has not yet been investigated.

For our desorption conditions (electron energies <4 eV), the dominant desorption mechanism is attributed to inelastic scattering of the tunneling electrons of the Si-H bond [110, 147]. Using this model, the tunneling probability is dependent on several factors, including, of course, the local density of states (LDOS) of the tip. It is therefore reasonable to speculate that for the H:Si(100) surface, tip states producing row-like STM topographs might have a greater density of states (in the energy window defined by the tip-sample bias) than other classes of tip apex. This will directly affect the available flux of electrons and, thus, the desorption probability.

Although early theoretical studies suggested that while the electric field under the tip is insufficient to directly induce H atom desorption, it could nonetheless play a significant role via spatial localization of the excitation [148, 149, 150, 151] due to a Stark effect. However, subsequent experiments, where neighboring hydrogen atoms were extracted, show that interdimer extraction is more favorable than intradimer extraction, suggesting that the presence of an electric field does not play a significant role in the desorption process [95]. Our results support these latter findings. Moreover, we find that the distribution of different types of neighbouring desorption events is also tip-state dependent (Appendix B.4), where intradimer desorption occurs more frequently for atomically resolved STM topographs. We are planning a systematic combined density functional theory (DFT)-non-equilibrium Greens function study in order to elucidate the origin of the higher desorption efficiency of the row-resolving class of tip apexes (and to ascertain the extent to which the H desorption process is mediated by the structure and density of states of the tip apex).

In Appendix A, the desorption mechanism is examined in more detail by examining additional parameters, such as examining how many DBs are generated (Appendix B.2), or if specific atomic sites are favored (Appendix B.4). These parameter influences are furthermore examined for the various tip states. We observe, that the generation of $N_{DB} > 1$ increases for higher U_{Bias}. Additionally the generation of multiple DBs seem s to follow the general rule $Pm_{row} \leq Pm_{Dimer} \leq Pm_{Atomic}$, where Pm is the probability of multiple desorptions. Multiple desorptions thus occurs more frequently for tip states displaying atomic resolution than dimer or row-like resolution.

To summarize, our findings have shown that extracting single H atoms is best achieved for row-resolving tip imaging states and low bias voltages. Additionally, at these conditions, undesirable side effects such as multiple or secondary desorptions are also minimized. The low bias voltage probably plays a significant role in limiting the number of unwanted desorptions as the desorption yield is highly dependent on the the bias voltage and electron dosage [110, 152, 115]. Based on our findings we conclude that the best strategies for controlling the automated patterning process can be obtained by (I) carefully selecting the proper tip geometries for desorption, (II) controlling the desorption yield (affected by desorption parameters, tip-sample distance), and (III) through reliable detection of H extraction by either minimizing/excluding noise influences or improving the step detection algorithm. The remainder of this chapter will focus on examination of DB assemblies to understand their physical properties and provide an outlook for future investigations.

6.3 Outlook: Physical Properties of DB assemblies

In this section we will examine the physical properties of the DB assemblies generated by our automated single atom extraction routine and provide an outlook for future experiments. One of the main advantages of of our extraction routine is that, it allows creation of well-defined atomic scale structures. Of particular interest, is the examination of coupled DB assemblies. For example, one dimensional (1-D) DB wires show metallic behavior along the line at RT due to coupling of the DB states within the wire. As a result, 1-D DB wires could be used as atomic sized interconnects [153]. As the DB bound surface state can be engineered to have different charged states, DB assemblies can serve as atomic-scale electronic devices or in the use of quantum computing devices [154]. The study of DBs is therefore crucial for future implementation of such devices.

Using our automated atom extraction protocol, DB assemblies of varying sizes were created. Fig. 6.14(a) shows an empty state STM image of a coupled (left in image) and an uncoupled (right in image) 2 DB wire along the atomic row of the Si(100):H surface. A structural model of the two DB structures is presented (6.14(b)), showing the positions of the atoms on the surface. Additionally, the uncoupled DB pair is separated by one atom. To investigate the electronic properties of the DB pairs, scanning tunneling spectroscopy (STS) $\mathrm{d}I/\mathrm{d}V$ spectra were performed across at specific points

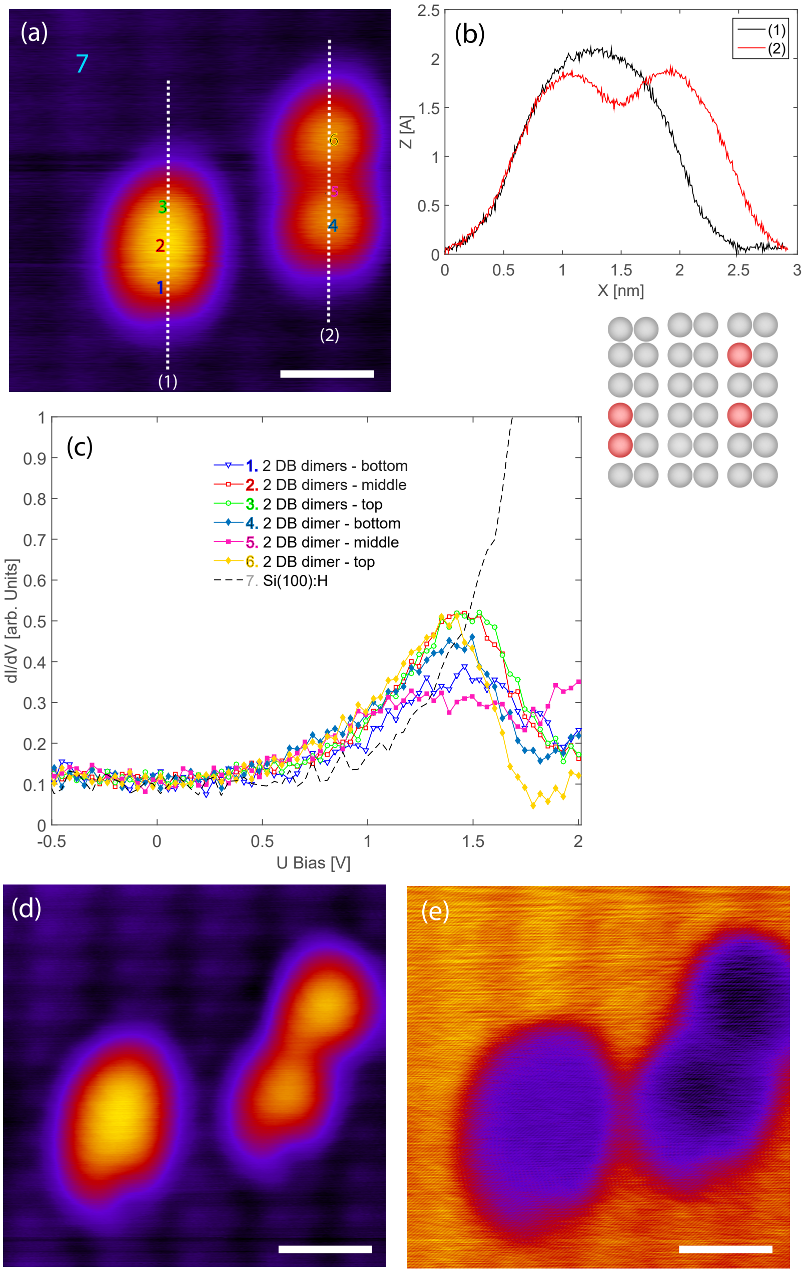

Figure 6.14: (a),(d) Empty state STM images (+1.6 V) of DB lines DB lines containing 2 coupled (left in STM images) and 2 uncoupled (right in STM images) neighboring DBs. (b) height profile taken from the STM image in (a). Structural models of presented structures are also shown, where grey and red circles depict hydrogenated and bare silicon atoms, respectively. (c) STS dI/dV spectra acquired after obtaining image (a). (e) Concurrent dI/dV image (+1.4 V, 100 pA) for image (d). Scale bars corresponds to 1 nm.

along the wires (6.14(c)). For dI/dV spectroscopy, an 30 mV, 3.8 kHz a.c. modulation to the d.c. bias voltage was used. An offset of 1.6 V, 100 pA was used for each spectroscopic measurement.

Collected dI/dV spectra for the DB lines show similar electronic structures, with a peak around +1.4-1.5 V which correspond to ρ^* antibonding states of the Si dimer back bonds [155]. The uncoupled DB line have a lower density of states at the center of the line, demonstrating that the DBs are uncoupled.

In addition to performing dI/dV spectroscopy at specific points, dI/dV imaging was performed over DB structures on the surface. dI/dV spatial imaging can be obtained by performing a slow constant current topographic image, while simultaneously recording the dI/dV signal using a specific bias voltage V. The resulting dI/dV spatial map is directly related to the LDOS of surface at a defined energy eV, in contrast with normal topographic imaging which involves integration of states from the Fermi level. In Fig. 6.14(d)-(e) an STM topographic image is shown (6.14(a)) with its simultaneously obtained dI/dV image 6.14(b). We observe that at +1.4 V, that the surface state of the unpaired BDs appear more localized than the paired DB.

Despite the advantages of using our automated extraction protocol for creating DB structures, creating coupled DB structures, where at least one DB for each dimer is created, proved exceedingly difficult. Most commonly, dangling bonds would be generated for every second dimer along the row as exemplified in Fig. 6.15. In line with our findings, previous experiments have shown that single DBs are predominantly produced [95]. It has been suggested that the lower yield of paired DBs on adjacent dimers is due to a lower desorption rate. In other words, it is more unlikely to desorb two atoms than one. As evidenced [152], the desorption probability is critically dependent on the energy of the tunneling electrons and the electron dosage. It is therefore conceivable that the fabrication of DB assemblies can be more accurately controlled by providing more suitable desorption parameters, but creating paired DB assemblies is considerably more challenging.

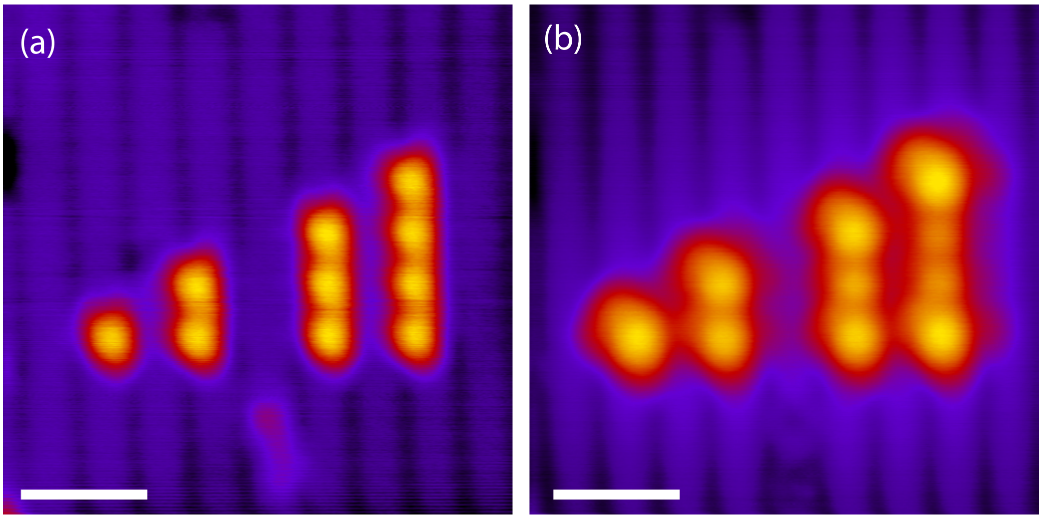

Figure 6.15: DB wires/assembly of length 1,2,3 and 4 DB from left to right. (A) 1.5 V, 10 pA (b) -1.5 V, 10 pA. Scale bars correspond to 2 nm.

Chapter 7

Surface diffusion: adsorbate dynamics and mobility

Of high interest in both chemical and materials science is the study of the mobility of adsorbates, and the resulting surface functionalization from their assembly. In general, adsorbates are deposited randomly from a source on the surface, until they undergo structural rearrangement into some energetically favorable arrangement [156]. The processes have been intensively investigated to understand nucleation and growth phenomena. The lateral mobility of adsorbates in general and molecules in particular play a vital role in forming these structures. Molecular rearrangements generally occur via thermal activation [157, 158] leading to diffusive motion. Therefore, understanding diffusion properties, such as the diffusion coefficients and activation energy, play a new part in controlling and steering the formation of surface assemblies. To date, the motion of surface adsorbates has primarily, though not exclusively, been studied by imaging the surface at regular time intervals, thereby acquiring snapshots of adsorbate movement [156]. It has been shown that the diffusion of adsorbates on surfaces can be derived *directly* using STM [159, 160, 161]. By monitoring how fast a molecule passes underneath the tip, it has been shown that the diffusion coefficient can be derived [161]. The diffusion coefficient was determined by analyzing signal fluctuations in the tunneling current signal. From this, three approaches have been developed to extract the diffusion coefficient [162]. The experimental approaches adopted so far use a spatially fixed tip. We have implemented a new experimental method where the tip is oscillated. With this non-stationary probe we aim to measure the anisotropy of diffusion as has recently been suggested theoretically [163].

This chapter is therefore divided into three parts. First, the particular molecular adsorbate we have studied, and the techniques for examining its diffusive motion are presented. We then challenge the reliability of the fixed probe (FIP) method, where the kinetics of adsorbates passing underneath a locally fixed probe on the surface have been recorded. We find that the tip state, and tip-sample/adsorbate interactions, again play a significant role and need to be very carefully considered when examining adsorbate motion using a locally fixed probe. A key limitation of the locally fixed probe (FIP) method is that any observable molecule passing underneath the tip is registered, regardless of its directionality (i.e. isotropic diffusion is assumed). In the second part, the FIP method is extended by oscillating the tip in the x-y plane. It is expected that adsorbates passing underneath the tip will be measured when entering and leaving the oscillation circle, providing information on the directionality of their movement (i.e. allowing the measurement of anisotropic diffusion). We show that the radially oscillating probe (ROP) can be used to detect rapidly diffusing species and can be used to reliably ascertain adsorbate motion from their signal fluctuations in the *I(t)* signal.

7.1 PTCDA diffusion

We selected 3,4,9,10-perylene-tetracarboxylic-dianhydride (PTCDA) for our diffusion studies as it is a well studied molecule on metal surfaces, and is highly suited to our purposes, i.e., it is a planar molecule which lies rather flat on surface [164], is rectangular in shape, is rather inert, and has previously been studied in depth on Ag(110) surfaces [165, 166, 167, 168, 169] (but not in the context of diffusion), while diffusion of PTCDA has been examined on a similar surface, Ag(100) [161]. Fig. 7.1(a) shows the basic structure of

PTCDA. The geometric footprint of PTCDA has been approximated as an $(L_x \times L_y)$ rectangle based on the vdW contours of the molecule. Although rotational movement is, in principle, possible [171] we will not explore this possibility here.

Previous experimental studies show, that on silver surfaces, PTCDA forms a commensurate monolayer structure. On the Ag(110) surface, PTCDA forms a brick-wall adsorption pattern with one molecule adsorbed per surface unit cell [165]. Within this structure, the long axis of the molecule is parallel to the [001] direction and the center of the molecule is located on the bridge site between the close-packed atomic rows parallel to the $[\bar{1}10]$ direction, as illustrated in Fig. 7.1(b). The center of the PTCDA molecule is located between two close-packed Ag rows.

At sub-molecular coverages, PTCDA molecules on Ag(100) form islands which coexist with a two dimensional gas phase of freely diffusing molecules [161]. We show later that similar behavior is observed on Ag(110). In Fig. 7.1(c) the adsorption geometry of PTCDA on Ag(110) is shown. The PTCDA molecule lies relatively flat on the surface, with an arch-like adsorption geometry. Theoretical calculations revealed an adsorption energy of 3.39 eV per molecule on the Ag(110) surface [170] with the main contribution to the adsorption energy due to vdW interactions (73 %) while chemical interactions contribute (27%) to the total binding energy [170]. The strong chemical interaction is mediated by covalent bonding primarily between the π-electrons of the perylene core and the substrate, leading to the formation of hybrid orbitals involving the LUMO, HOMO and HOMO-1 and the metal 5s- and 4d-states [166].

7.1.1 Ag(110) surface

The close packed Ag(110) surface was selected due to the anisotropy of the lattice structure as shown in Fig. 7.2. As a result, the potential energy barrier for diffusion experienced by the adsorbate along the different symmetry directions is expected to be different, and should lead to anisotropic diffusion [156]. Additionally, Ag(110) surfaces can conveniently be prepared with large

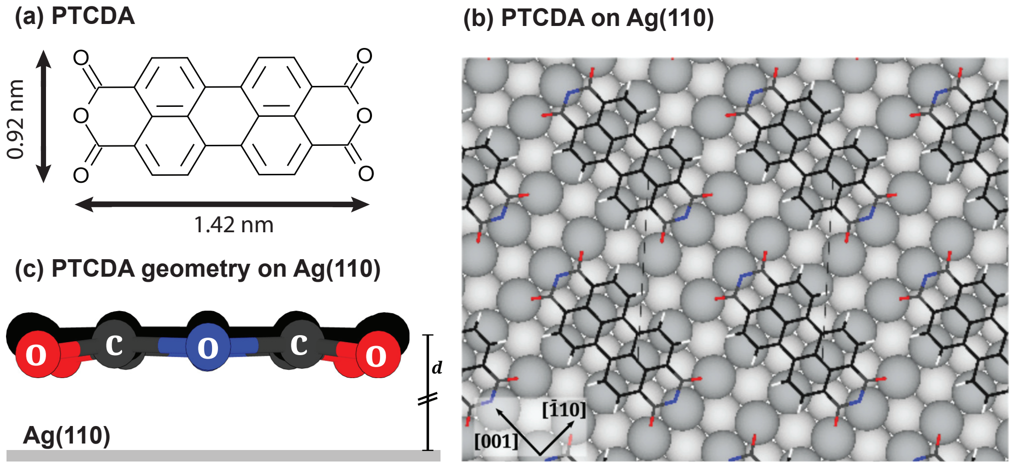

Figure 7.1: PTCDA structure on the Ag(110) surface. (a) Structural drawing of a PTCDA molecule with scale bar based on its vdW contours. (b) Real-space model of the PTCDA brick-wall superstructure on Ag(110). (c) Geometry of PTCDA with equilibrium distance d from surface. Adapted from [170].

flat terraces, making them suitable for examining diffusion of mobile species.

The surface was prepared using repeated cycles of Ar^+ ion sputtering of the surface (with an energy of 800 eV, 10 min), and sequential annealing (0.8 A, 5.4 V, 20 min). The sputtering removes unwanted contaminants from the surface. However, it causes a rippling effect [173]. Therefore, the surface was subsequently annealed to flatten it again. In practice, flat surfaces were obtained through repeated sputtering and annealing cycles. After multiple sputtering and annealing cycles, including parameter optimization for both steps, flat terraces of sizes of hundreds of nm^2 could routinely be found.

7.1.2 PTCDA on Ag(110)

PTCDA was deposited on the Ag(110) surface as described in Section 4.4.1. At sub-monolayer coverages, molecules form islands which coexist with a two dimensional gas phase of freely diffusing molecules [171]. As we will show later, the mobile species is not always visible (e.g. see Fig. 7.9), as will be discussed in Section 7.2.2. Here, a 0.25 ML PTCDA island coverage was obtained using a 20 min, 290 °C deposition as exemplified in Fig. 7.3(a-b).

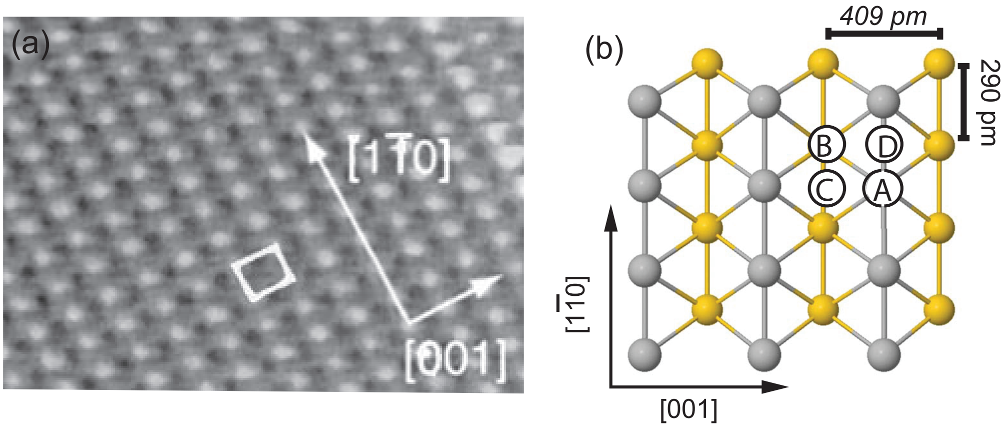

Figure 7.2: Atomic structure of Ag(110) surface. (a) STM image of close-packed Ag(110) surface. The surface unit cell and high symmetry directions are marked. (b) Ball-and-stick model (top view) of surface, for first (gray) and second (yellow) layer. The surface unit is marked (dashed rectangle). Adapted from [156, 172].

The molecules can be imaged at positive and negative bias and appear as protrusions. For freely, non-interacting adsorbates and in the absence of an STM tip, the only barriers for diffusion are those due to the lattice potential. PTCDA molecules at the edges of islands, however, additionally interact strongly with neighbouring molecules of the island [165, 174]. Thus edge contributions will lead to a barrier sufficiently higher than that for freely diffusing species. Structural rearrangement of the island, and escape of molecules from the island, will not correspond to freely diffusing molecules. However, an intuitive understanding of the energetic barriers involved can be obtained from the dynamics of PTCDA islands at various temperatures. As mobile PTCDA molecules move too fast to be imaged directly at room temperature, the dynamics of the island edges were initially used as a measure for the presence of freely diffusing molecules with respect to different substrate temperatures.

In Fig. 7.4 the structural rearrangement of molecules at the edges of PTCDA islands was investigated by imaging an island using STM for prolonged time periods at various temperatures. We observe that at low temperatures ($T \leq 200$ K), the islands never changed on the timescale of hours. In the course of this experiment, only one single rearrangement event was

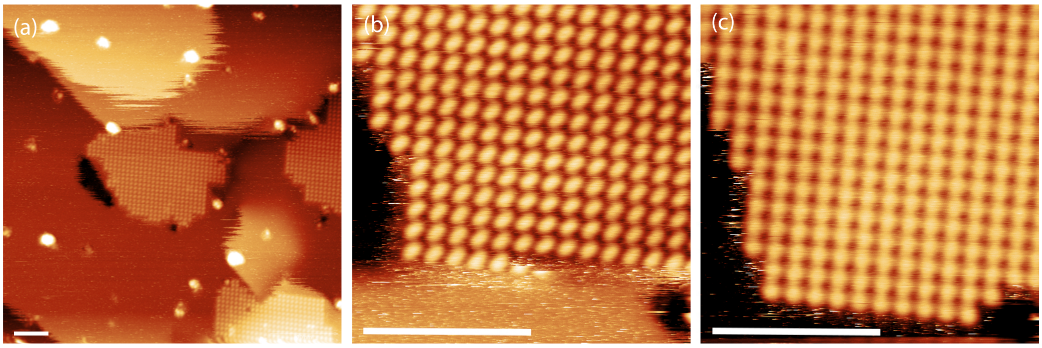

Figure 7.3: (a) STM image of PTCDA islands. (b)-(c) Zoom in on island using scanning parameters: (b) +1 V, 10 pA, (c) -1 V, 10 pA. Scale bars correspond to 10 nm.

observed at 200 K 7.4(f-h). No visible change was observed at temperatures below 200 K. The diffusion event observed in Fig. 7.4(f-h) leads to a rearrangement of molecules at the island edge, but causes no structural change of the island or dissociation of a single molecule from the island.

At temperatures of $\geq$ 250 K (Figs. 7.4(j-p) and 7.5), we observe island edges changing shape on the timescale of a single scan (several minutes). The islands themselves are non-vanishing but change shape over the temperature range 250 K $< T <$ 300 K, (see also Fig. 7.5). We observe, that on a time-period of single scans (several minutes) significant changes of island shape occur at RT, while in the low temperature limit (250 K), the changes in the island edges are significantly smaller, mostly only involving the addition or removal of a few molecules. In the low temperature limit (250 K), the re-arrangement of the island edges due to de- and attachment when imaging over prolonged periods often result in little or no change in the island shape. As exemplified at 250 K, the islands even revert to prior shapes, suggesting that specific island formations are more favorable than others, possibly due to interaction with the substrate. Although the exact cause of this remains unknown, the presence of defects, step locations or screw locations could act as preferential adsorption sites for PTCDA. From the images it seems that step edges are not preferential nucleation sites, but the "defective clusters" on the surface might be.

A closer examination of the consecutive images at 250 K (Fig. 7.4(j-

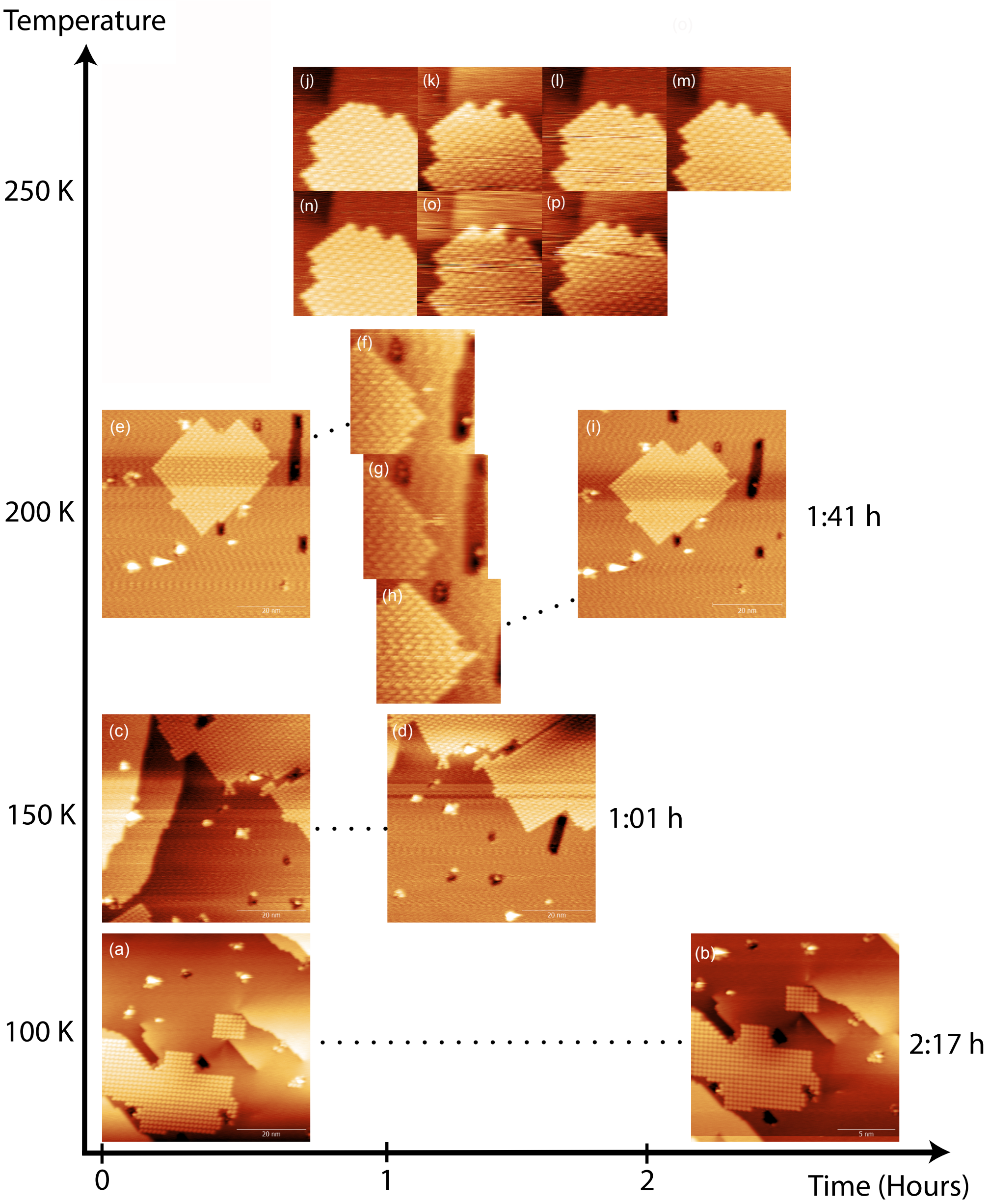

Figure 7.4: Observing PTCDA island mobility by STM imaging over the same location for prolonged periods. Experiments were performed at (a-b) 100 K, (c-d) 150 K, (e-i) 200 K, consecutive images (j-p) at 250 K, and RT (see Fig. 7.5). Only at 200 K and above was any change in the islands observed. At 200 K, only a single diffusion event (f-h) was observed over a prolonged period. However, at 250 K, changes in the island edges were observed for almost every consecutive image, as shown in (j-p).

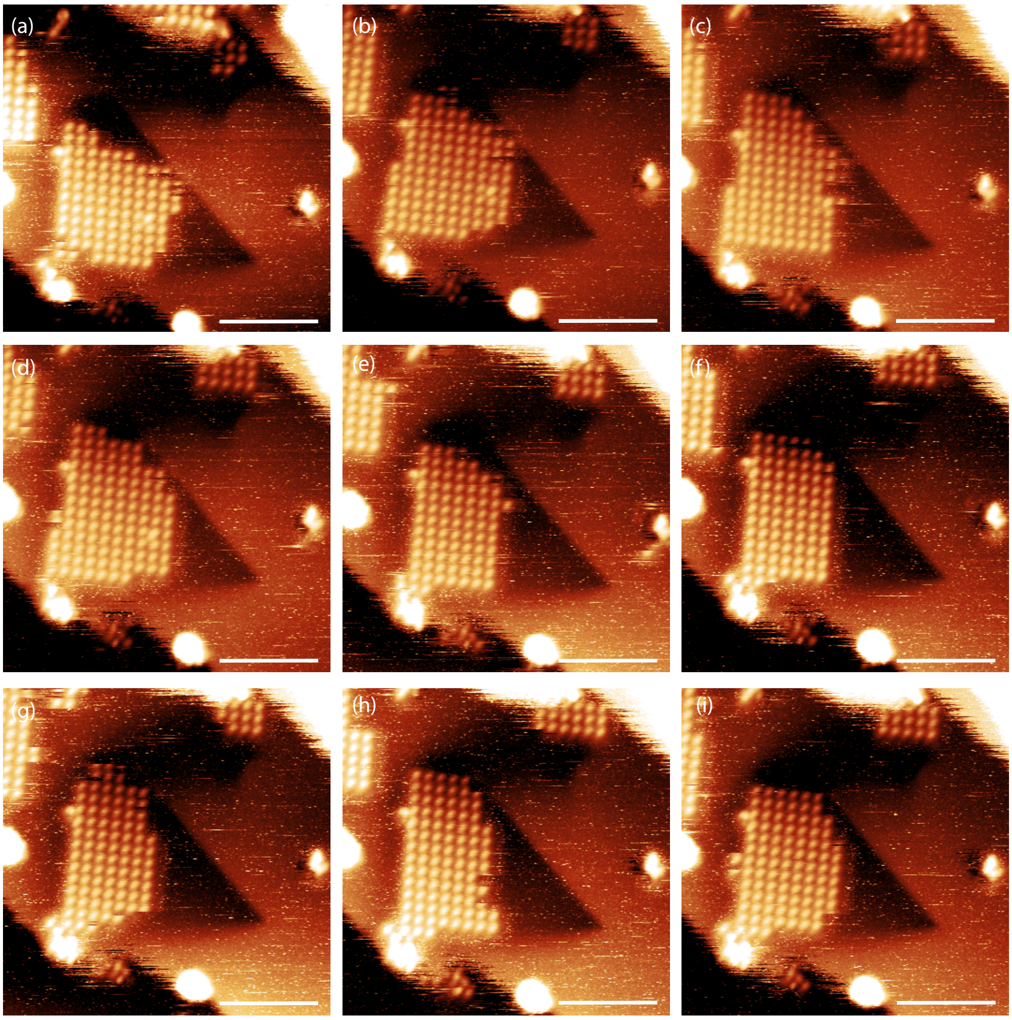

Figure 7.5: Consecutive STM images (≈ 13 min per image) of PTCDA islands at RT. Acquired at 1 V, 10 pA.

p)), show that the number of molecules only changes twice (Fig. 7.4(l) and (o)), while the changes over (j)-(k) and (o)-(p) only lead to a rearrangement of the molecules. The lack of change in number of molecules as the island edge changes shape suggests that the structural rearrangement we observe is caused by detaching and attaching molecules interacting with free diffusing molecules or is the result of edge diffusion.

At RT, as shown in Fig. 7.5, we observe that the shape of PTCDA island edges changes rapidly, undergoing significant changes in each consecutive image. At RT, individual rearrangement events occur too rapidly to be observed on the timescale of the STM imaging process. The island rearrangement is a thermally activated process but the process could be a combination of thermal activation and tip-assisted diffusion, for which a temperature dependency would not be expected. Based on these findings a temperature range of 200-300 K for measuring the diffusion of free PTCDA molecules was selected.

7.2 Isotropic diffusion

This section covers our results using the fixed probe (FIP) technique used to estimate an effective isotropic diffusion coefficient of PTCDA molecules on the Ag(110) surface.

7.2.1 Analysis of FIP data

Fig. 7.6 illustrates the principle of FIP measurements. An adsorbate passing underneath a stationary STM tip (7.6(a)) causes fluctuations in the *I(t)* signal (Fig. 7.6(b)). These manifest in the form of pulses in the current signal having a temporal width τ, also known as the residence time (Fig. 7.6(c)). This time is dependent on how long the adsorbates reside in the detection area under the tip and defines the residence time distribution (RTD) from the distribution of the pulse durations. It has been proposed [161] that the diffusion of surface adsorbates can be extracted from the time dependence

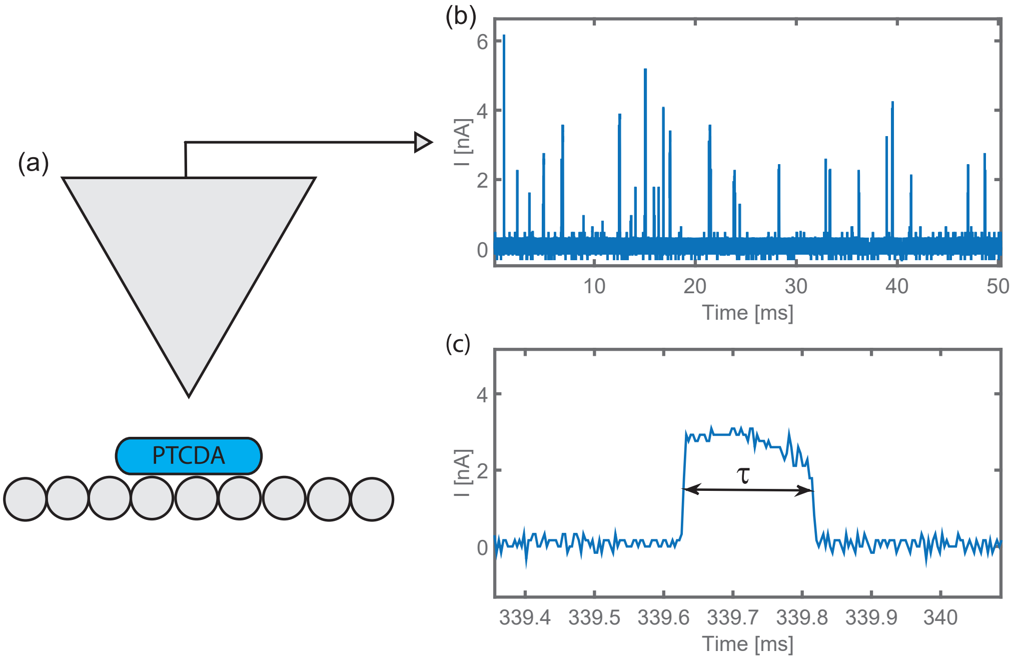

Figure 7.6: (a) Schematic diagram of fixed probe (FIP) diffusion measurement setup. (b) Part of *I(t)* spectrum acquired from FIP measurements. (c) Zoom in on pulse with residence time τ marked.

of the tunneling current *I(t)*. Specifically, the residence times τ are taken to be the time intervals between entrance and exit of a molecule into the detection region M of the probe, as illustrated in Fig. 7.7(a). For FIP acquisitions, a sampling rate of the analog-digital converter was 300 kHz, while the bandwidth of the preamplifier, specified to 80 kHz defines the effective time resolution for detecting the signals.

For the coverages used, the freely diffusing molecules are assumed to be independent, and non-interacting. The detection region is defined as the tip-molecule interaction area that gives rise to a tunneling current I above a noise-defined current threshold I_c, and is approximated as a circle of radius R. Furthermore, the time between the peaks is defined as the inter-peak time τ' (Fig. 7.8(c)), which leads to the interpeak time distribution (ITD). Both distributions, namely the RTD and ITD, enable the calculation of diffusion coefficients although different benefits or drawbacks can be identified for each method [162, 171]. Here we use the RTD method for analyzing the experi-

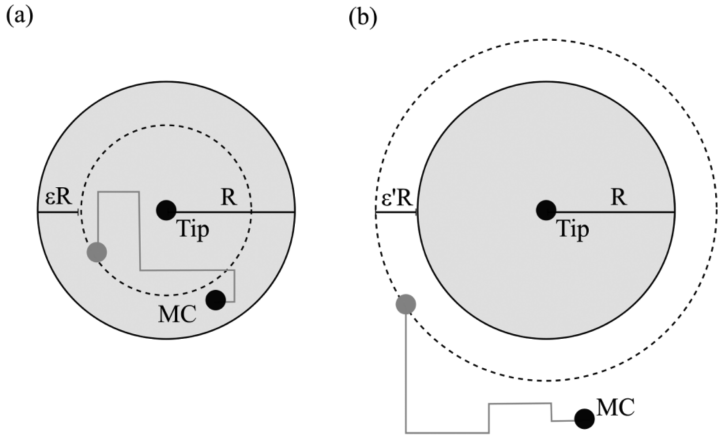

Figure 7.7: Illustration of the detection region M (shaded area) used for describing (a) the residence time distribution (RTD) and (b) the interpeak time distribution (ITD). MC stands for diffusing molecule center. Used from [162].

mental FIP data acquired for PTCDA/Ag(110).

Several rather involved steps are required in order to determine the diffusion coefficient. First, we will discuss pre-processing of the experimental data. As a first step after data acquisition, a histogram of the tunneling current is generated for the entire time series, as shown in Fig. 7.8(b) for a time series of 40 s. In the absence of pulses (i.e. no adsorbate movement), the tunneling current distribution for the fixed probe is represented by a Gaussian distribution with a maximum around the current setpoint. This distribution is a result of noise in the STM detection system. In this figure the current setpoint (maximum of the histogram) has been shifted to zero. Values beneath the current setpoint are purely caused by noise and their distribution can be fitted to a half-sided Gaussian distribution. By extrapolating the Gaussian fit to cover values above the current setpoint (dashed line in Fig. 7.8(b)), the noise contributions on the signal can be identified and removed. Diffusing molecules cause deviations from the Gaussian distribution at larger I values. To separate diffusion-induced fluctuations from inherent noise of the signal, a threshold value, I_c, is used as a upper limit for measuring signals that fall within the Gaussian distribution, and is defined as the current where the Gaussian fit of the histogram values at the positive

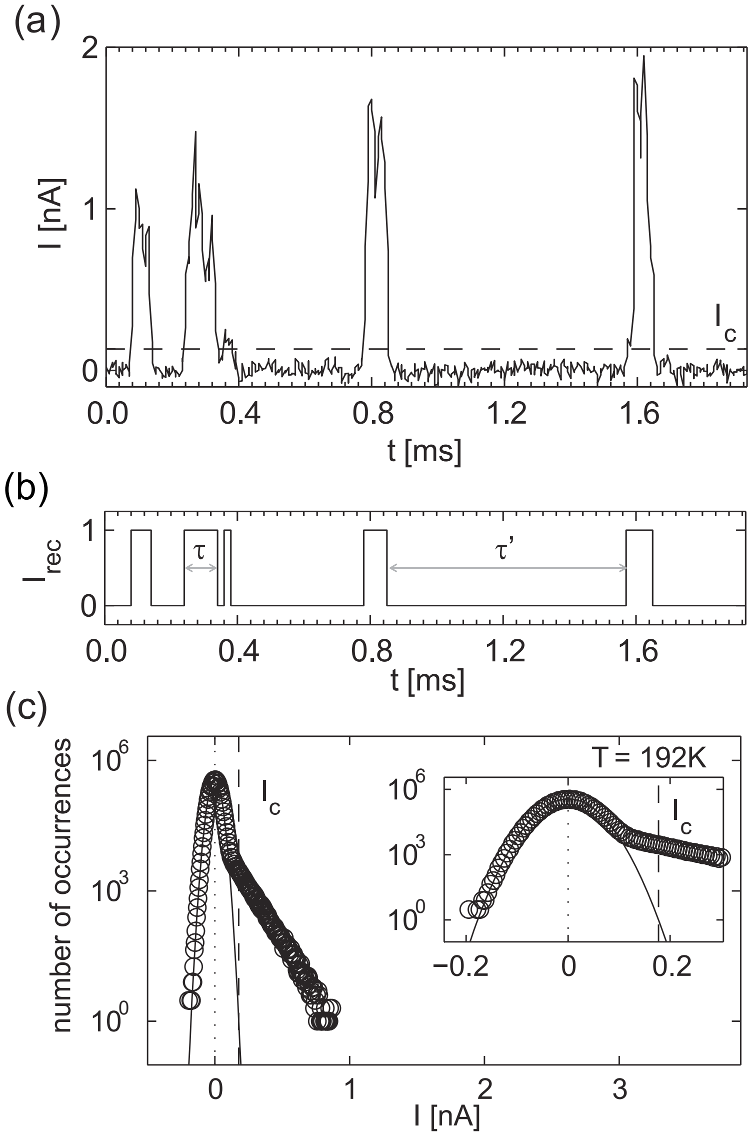

Figure 7.8: (a) Fluctuating STM tunneling current observed during PTCDA diffusion on Ag(100) at 192 K. The dashed line marks the threshold value I_c, above which the distribution of the current no longer has a Gaussian shape. (b) Conversion of signals into binary on/off signals. The width of the rectangles give the residence times τ and the distance between the rectangles give the inter-peak times τ'. (c) Histogram of the tunneling current, determined for the whole time series of 40 s. The solid line marks a Gaussian fit with zero mean and standard deviation determined from the histogram for negative currents. The maximum of the histogram has been shifted to $I = 0$. Adapted from [162].

side drops below 1. Signals above I_c thus show departure from Gaussian behavior and, for subsequent determination of the diffusion coefficients, data below the I_c threshold are therefore excluded. Similarly, for our experiments, only values above this threshold are of interest. As we are not interested in the heights of the pulses, the pulses are subsequently transformed into binary on/off signals (Fig. 7.8(c)).

Through collaboration with the group of Prof. Philipp Maass in Osnabrück the analytical technique described in [163, 171] is used to derive the diffusion coefficients based on fluctuations in the *I(t)* signals. This method involves analyzing the distribution of peak widths in the signal, which corresponds to the residence time of single molecules underneath the tip. We will refer to it as the residence time distribution (RTD). The RTD, $\Psi(\tau)$, can thus be considered as an ensemble of randomly diffusing molecules passing through a detection area for a given time period. In the long time-limit $t \gg \tau_R$ the probability of a molecule passing through the detection area can thus be approximated using a simple Poisson distribution

$$\Psi(\tau) \propto \frac{1}{\tau_R} \exp(-\tau/\tau_R) \tag{7.1}$$

where $\tau_R = R^2/D$ is the mean residence time of a molecule passing under the tip, from which the diffusion coefficient, D, can be determined. To a crude approximation, the diffusion coefficient can be derived by fitting experimental data to Eq. 7.1 in the long time limit $t \gg \tau_R$ [171]. A more accurate model includes the detection area of the probe as a variable, which becomes important for shorter time scales $t \ll \tau_R$. To fit to the exponential distribution, a self-consistent check is performed for the lower boundary set for τ_R.

7.2.2 Influence of the tip state on recovered diffusion parameters

A key issue for investigating diffusion behavior is the tip state influence on our experimental measurements. We found that it is only possible to measure/observe adsorbate kinetics when specific tip states are present. Specifically, FIP acquisitions producing suitable non-Gaussian current distributions over the mobile phase would only occur for specific tip imaging states. In this chapter we refer to a specific tip state (labeled using values $1...N$) as having a specific apex termination. While the atomistic apex configuration is unknown from the experiments, we label the tips with the same value of N if no tip change was observed during the series of experiments. Using this convention, it is not excluded that similar tip states were characterized by different values of N, but we can identify a similar tip configuration throughout a larger series of data acquisition for reliable comparison. Tips undergoing a tip change or tips used for the first time, are identified by a new value of N. In addition, we classify tips by their 'imaging state' using capital letters A, B, C. These states are found across different sessions and different tips, but are classified as the same if the imaging of PTCDA islands and the Ag(110) areas in between show similarly recognizable features. Tip states for a given tip imaging state (i.e. A.1, A.2 ...) correspond to independent tip modifications for the same tip imaging state. As a result, diffusion experiments were investigated systematically for various tip (and tip imaging) states on the PTCDA-covered surface. In this section, all measurements were performed at RT unless otherwise stated.

Figs. 7.9(a)-(c) present the three typical imaging modes revealed during our experiments, labeled from A to C. We explain these modes by the three tip-molecule interactions sketched in Fig. 7.9(d)-(f). For tip imaging state A the tip-adsorbate interaction is small, allowing the adsorbate to pass the tip (relatively), as will be discussed later, unhindered. For tip imaging state B, adsorbates are prevented from passing underneath the tip, either due to repulsive interaction with the tip or due to steric hindrance resulting from a small tip-sample gap. One possible origin for tip imaging state C, could be due to an adsorbate attached to the tip while scanning which could affect the observation of mobile species.

These findings are supported by height profiles (Fig. 7.9(g)) as the height profiles show similar height differences between the Ag(110) surface and the top of the PTCDA island, for tip imaging states A and B, while the PTCDA

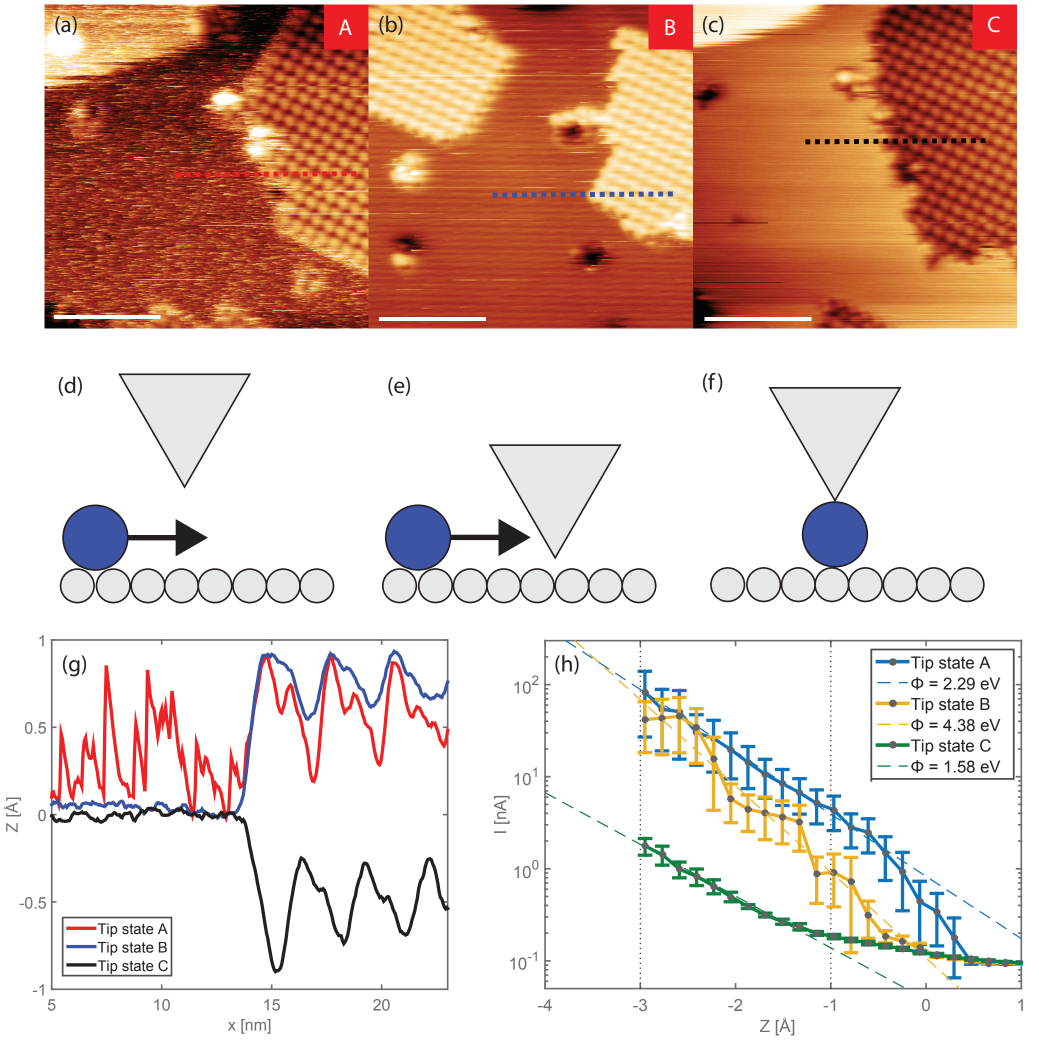

Figure 7.9: Tip imaging states used to investigate diffusion are classified as (a) *A*, (b) *B*, and (c) *C*, based on observing similarly recognizable features on and between PTCDA islands using STM topographs. (d)-(f) Models of tip-molecule interaction corresponding to situation in images above. (d) Molecule passing tip, (e) molecule blocked from passing underneath tip and (e) molecule trapped on tip. (g) Height profile from STM images (a) to (c). Extrapolation of work function Ψ from *I(z)* spectra for the different tip imaging states presented in (a)-(c). Plotted are the mean values when averaging over 15, 11 and 20 measurements for imaging states *A*, *B* and *C*, respectively. Exponential fits to tunneling current (dashed lines) were fitted over a range (horizontally dotted lines) for each imaging state. $z = 0$ corresponds to 0.5 V, 50 pA for all measurements. Scale bars in images (a-c) correspond to 10 nm. Scanning parameters: 0.5 V, 50 pA.

island is shown as a depression in the STM topograph for tip imaging state *C*. The reduction in height when the tip scans over the island, can be attributed to a decrease in tunneling conductance as the adsorbate attached to the tip hinders tunneling.

The models of tip-molecule interaction is further supported by measurements used to estimate the mean barrier height $\bar{\Phi} = (\Phi_{Probe} + \Phi_{Sample})/2$ of the tunneling junction, as it is related to the local work function. The local work function, in turn, is dependent on on the local chemical and structural properties of the materials present in the tunnel junction. $\bar{\Phi}$ can estimated using $I(z)$ or $z(V)$ spectroscopic measurements [175]. Using Eq. 2.2, $\bar{\Phi}$ was estimated for the various tip imaging states by performing a series of $I(z)$ spectroscopic measurements (Fig. 7.9(h)) over the mobile phase of the surface. All measurements were performed using the same STM tip. Attempts to estimate the work function for the various tip imaging states using $z(V)$ spectroscopic measurements [176] produced too noisy spectra to discern field emission resonance. We find relatively similar mean barrier heights for tip imaging states *A* and *C*, showing relatively low magnitudes as compared to the free surface (4.14 eV for Ag(110) [177] and 4.5 for W [178], respectively). This is expected as the barrier height is lowered by a few eV relative to the free surface due to the image charge for the metal surface [179]. Possible causes of a higher mean barrier height for tip imaging state *B* than *A* and *C*, could be due to a decreased reactivity of the surface, a decreased tip-sample interaction, or a variation in the tip apex geometry. For future experiments of the local work function, we suggest using a lock-in amplifier, as it allows simultaneous STM and work function imaging [180]. The work function $\Phi \propto d(\ln I)/dz$ can be measured by modulating the gap distance z by dz adding a small sinusoidal voltage to the z-piezo, the lock in amplifier would then measure the small response variation in the tunneling current $d(\ln I)$.

In Fig. 7.10 the corresponding histogram distributions of the *I(t)* signals acquired for the different tip imaging states presented in Fig. 7.9 using FIP measurements over the mobile phase are shown. We observe that fluctuations in the *I(t)* signal using FIP measurements *are radically different* for the various tip imaging states. The observation of streaks for tip imaging state

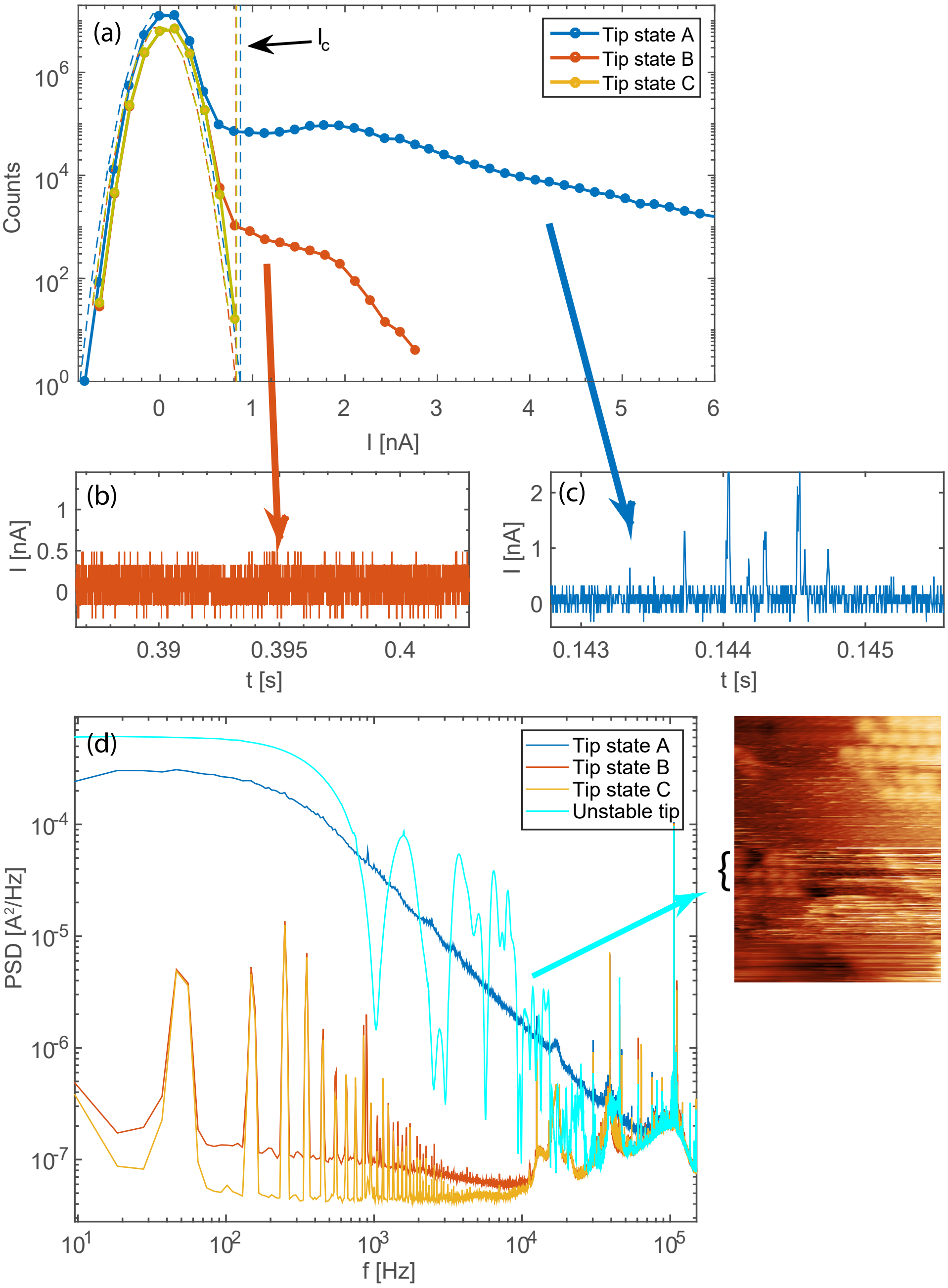

Figure 7.10: (a) Histograms of *I(t)* traces for typical tip imaging states A to C acquired using FIP measurements performed on the mobile phase of the Ag(110) surface. Gaussian fits (dashed lines) and corresponding I_c, obtained using procedure described in section 7.2.1, for the different tip states are also shown. Panels (b)-(c) show short intervals of the time-series data for imaging state (b) A, and (c) B. (d) Corresponding PSD spectra. (e) Unstable tips produce fluctuating frequency spectra. Acquired at 0.5 V, 50 pA.

A coincide with the observation of pulses during FIP acquisitions, while no streaks coincide with a lack of pulses during FIP acquisitions for tip imaging state B and C, respectively. In Appendix C.1 the signal distributions from the FIP measurements are analyzed in more detail for tip imaging states A, B, C and for the clean Ag(110) surface, where no PTCDA has been deposited, having different tip states (A.1, A.2 ... etc.). We find that imaging states B and C produce *significantly fewer signal fluctuations, in a range similar with the clean surface*; current distributions appear Gaussian over the mobile phase (Fig. 7.10), or stated otherwise, no diffusion is detected.

Using the signal distributions, the surface coverage of PTCDA over the mobile phase was estimated for the various tip (and tip imaging) states (Appendix Fig. C.1(b)). The time-averaged (apparent) coverage, Θ, can be calculated from the sum of the full width of all pulses above I_c for an acquisition, divided by the total acquisition time. The apparent coverage describes the coverage of molecules based on information from *signal fluctuations* and is different from the coverage achieved after a molecular deposition, which includes the nucleated islands. For tip state A, the apparent coverage Θ was estimated to be around $2 - 5\%$. At these low apparent coverages we regard the molecules as non-interacting on short time scales as the probability of interaction scales with l^2/D where D is the diffusion coefficient, $l \sim c^{-1/2}$ is the mean intermolecular distance and c is the number density of molecules. Tip imaging states B and C produced apparent coverages of *similar magnitude as the clean surface*, $0 - 0.5\%$, which are considerably lower apparent coverages than for tip imaging state A.

Residence time distributions for the various tip imaging states (Appendix Fig. C.2(a)) show that, although the duration of pulses vary for different tip states, the duration of pulses for tip imaging state B and C are considerably more short-lived ($\tau \leq 100$ μs) than the pulses for tip imaging state A. The rapid pulses observed for tip imaging state B and C *have similar durations as FIP measurements acquired on the clean Ag(110) surface* as well as over the PTCDA islands (for example see Fig. 7.12). The origin of the (rapid) pulses is suspected to be due to tip instabilities, as they are observed on both the bare substrate and over the PTCDA islands and both the duration of pulses increases with increasing setpoint (Appendix section C.2). Another point of observation, is that the mobile species is observed already during imaging as streaks (see Fig. 7.9(a)), while the islands are stably reproduced. The latter is important to rule out any tip instability.

Based on these results, we designate tip imaging state A as the most promising candidate for measuring diffusion. As a result, all experiments presented for the remainder of this chapter have been performed exclusively using tip imaging state A and the tip was re-prepared if imaging state A was not present during the experiments.

For some tip (imaging) states, signal fluctuations are observed both during imaging and from FIP measurement (e.g. insert in 7.10(d)) which gives an appearance of mobile species on the surface. These fluctuations are most likely attributed to tip instabilities as they appear randomly (including over islands) during imaging and the corresponding power spectral densities (PSDs) of the full time-series signal, appear distorted. Consequently, only signals producing non-fluctuating frequency spectra are included for the remainder of the chapter.

Although tip imaging state A can be clearly distinguished by the SPM user, the presence of other factors such as random noise fluctuations or tip artifacts could make it difficult to automate the process of reliably identifying the presence of diffusive species. A more straightforward way of distinguishing between reliable tip states, where diffusion can be observed (such as imaging state A) and where not (i.e. tip imaging state B,C and for the clean Ag(110) surface), was found through calculating the spectral power by integrating the PSD spectra over the range $f_{min} < f < f_{max}$, where $f_{min} = 1/60$ Hz ($f_{min} = 1/120$ Hz) for 1 (2) min of signal acquisitions, respectively, and plotting against f_{max} as shown in Fig. 7.11. All spectral power data was acquired for 2 min, except B.3 and C.1, which were acquired for 1 min, respectively. We found that the spectral power is much lower for all other tip states than tip states where diffusion is observed, especially in the low frequency regime ($\sim 10^3$ Hz). Obtaining high intensities in the spectral power could therefore potentially be used as a criteria for finding suitable tip states for observing/measuring diffusion which is easily accessible during the exper-

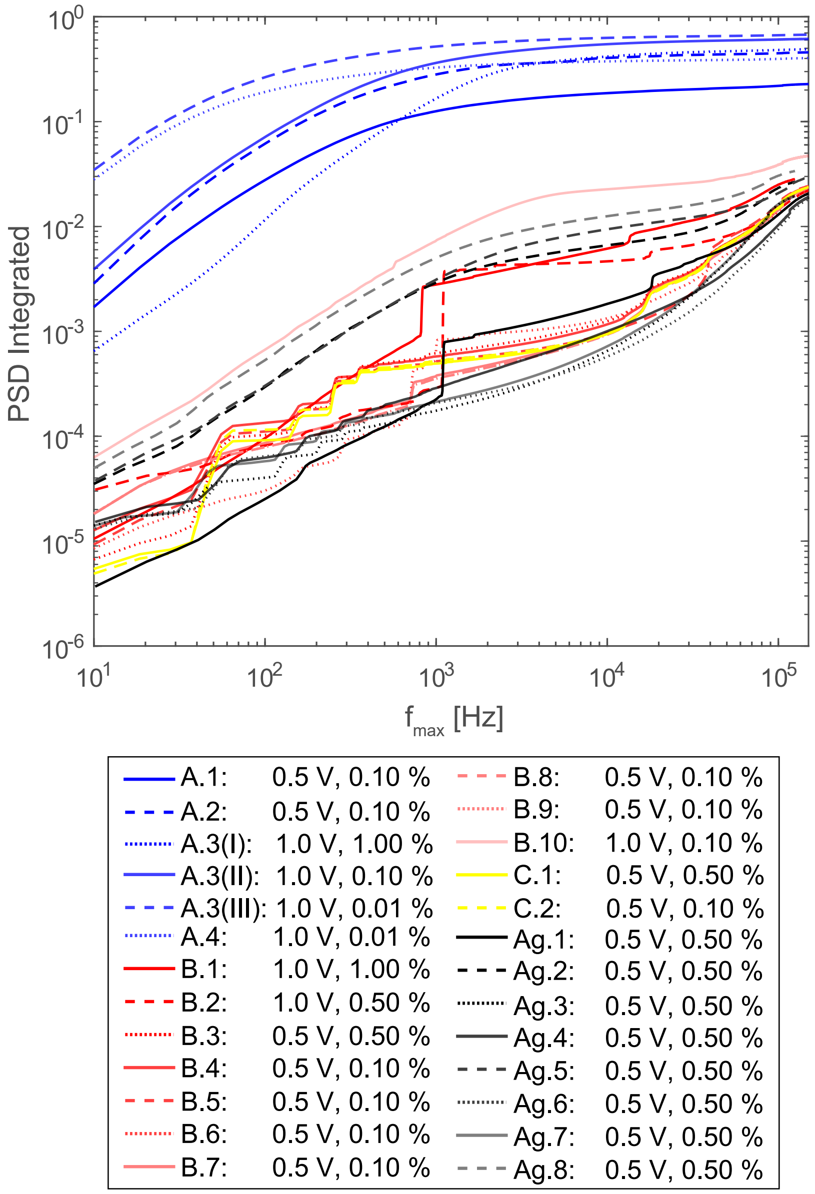

Figure 7.11: Integrated PSD for various tip states (1... N) for tip imaging states A, B, C, and for the clean Ag(110) surface. Roman numerals represent parameter changes.

iment. At higher frequencies ($\geq 10^3$ Hz), a saturation in the spectral power is observed for tip states belonging predominantly tip imaging state A which we speculate are attributed to a lack of high-frequency content in the signals.

7.2.3 FIP measurements: methods

In order to determine if the fluctuating *I(t)* signals above I_c are attributed to diffusing molecules, and are not caused by other factors such as tip instabilities during the experiment, we implemented an experimental procedure for FIP measurements, the on-off-on island protocol. The procedure is shown in Fig. 7.12.

Initially, *I(t)* signals are recorded over ordered PTCDA islands (Fig. 7.12(a)), followed by recording data over the mobile phase (Fig. 7.12(b)), and finally over the islands again (Fig. 7.12(c)). On the mobile phase, FIP measurements were performed in close proximity to, and between, PTCDA islands, as the concentration of diffusing molecules is expected to be highest at those locations [181]. Importantly, *I(t)* signal distributions on top of the PTCDA islands should ideally appear purely Gaussian (7.12(e)), indicating that no (or very little) motion is occurring underneath the tip. As we don't expect second-layer diffusion, finding a virtually pure Gaussian current distribution on a PTCDA island suggests a stable tip during the FIP measurements. If a mostly pure Gaussian distribution is detected on the island before and after the FIP measurement, then a non-Gaussian distribution on the mobile part of the surface would be a clear indicator for measuring diffusion. In other words, the *on-off-on island procedure is used as a control to ensure that observed signal fluctuations are a result exclusively of the physical characteristics of the mobile phase.* Consequently, all diffusion experiments mentioned for the remainder of this chapter were performed using this procedure. As (near) Gaussian behavior is expected over the islands, if any acquisitions either before or after performing FIP over the mobile phase contained too many pulses, the entire acquisition set (on-off-on island) was excluded. As shown in Appendix B Section 3, the upper limit of for any *pulse* over the island is $N_{pulses} \leq 250$ pulses/s (Appendix Fig. C.6), while

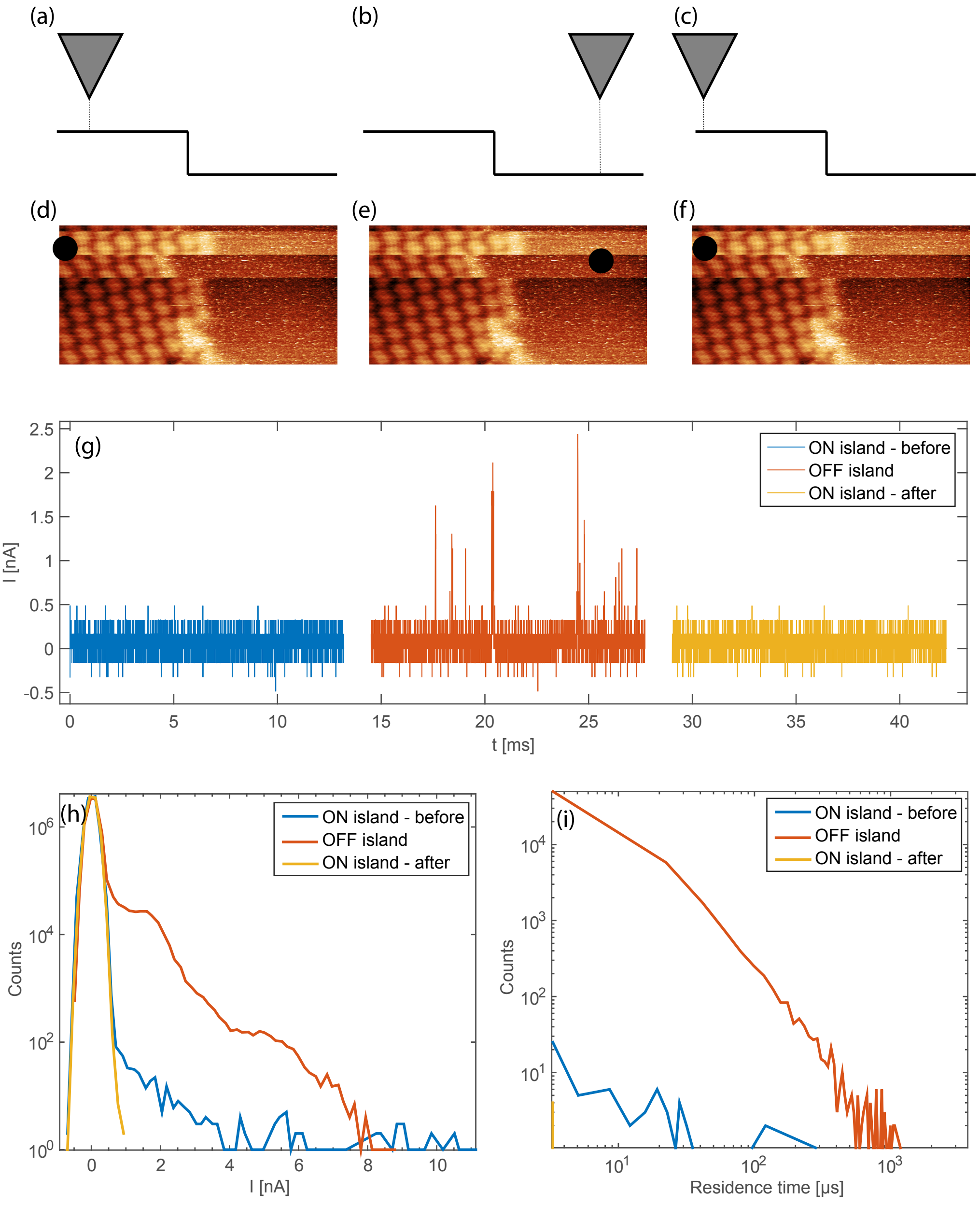

Figure 7.12: Experimental procedure for on-off-on island FIP acquisition. FIP measurements are performed sequentially (a) over PTCDA island, (b) mobile phase, and (c) over PTCDA island again. Corresponding (d-f) *I(t)* signals, (g) time-traces, (h) histograms, and (i) RTDs of *I(t)* signals at each site. Acquired in constant height at the reference parameters 1 V, 50 pA + 0.01 Å. Time-traces show only short excerpts from each FIP acquisition.

nearly all acquisitions contain significantly fewer pulses.

In general, FIP acquisitions were recorded in intervals of 30 sec to 5 min at each location. In some experiments, multiple short-time series acquisitions were obtained and subsequently appended for further analysis. Atom tracking was used in order to minimize lateral drift to drift velocities less than 10 pm min^{-1} during acquisitions.

For each on-off-on island experimental procedure, the time-series data was manually post-processed in order to check for discrepancies or unusual behavior occurring during the acquisitions. Fig. 7.13, shows a number of undesirable acquisitions which were disregarded for analysis. As the first and last acquisitions produce kinks in the *I(t)* signals, this will lead to inaccurate I_c threshold estimations and thus incorrect estimation of the diffusion parameters; these two datasets are therefore discarded. If a tip state change had been observed in either the *I(t)* signal (Fig. 7.13(c)) or observed through imaging, the entire experimental acquisition set (on-off-on island) would be disregarded. Acquisition sets containing no pure Gaussian *I(t)* signals on the island *both* before *and* after the mobile phase were discarded. Additionally, acquisitions showing significant vertical drift were discarded.

7.2.4 FIP measurements: parameter influences

In order to establish if our experiments, and FIP measurements in general, provide a reliable measurement of the diffusing species, the diffusion behavior was investigated extensively for different STM scan parameters and exclusively for tip state *A*. For example, previous experiments performed in the group of Prof. Sokolowski [161] concluded that an increasing attractive tip-molecule interaction occurs for small positive bias voltages and concomitant small tip-to sample distances. As a consequence of their findings, they performed their diffusion experiments at $U_{gap} > 1.6$ V. Our investigations led us to examine the tip-molecule interaction systematically with respect to the following parameters:

I. Feedback response of the tip

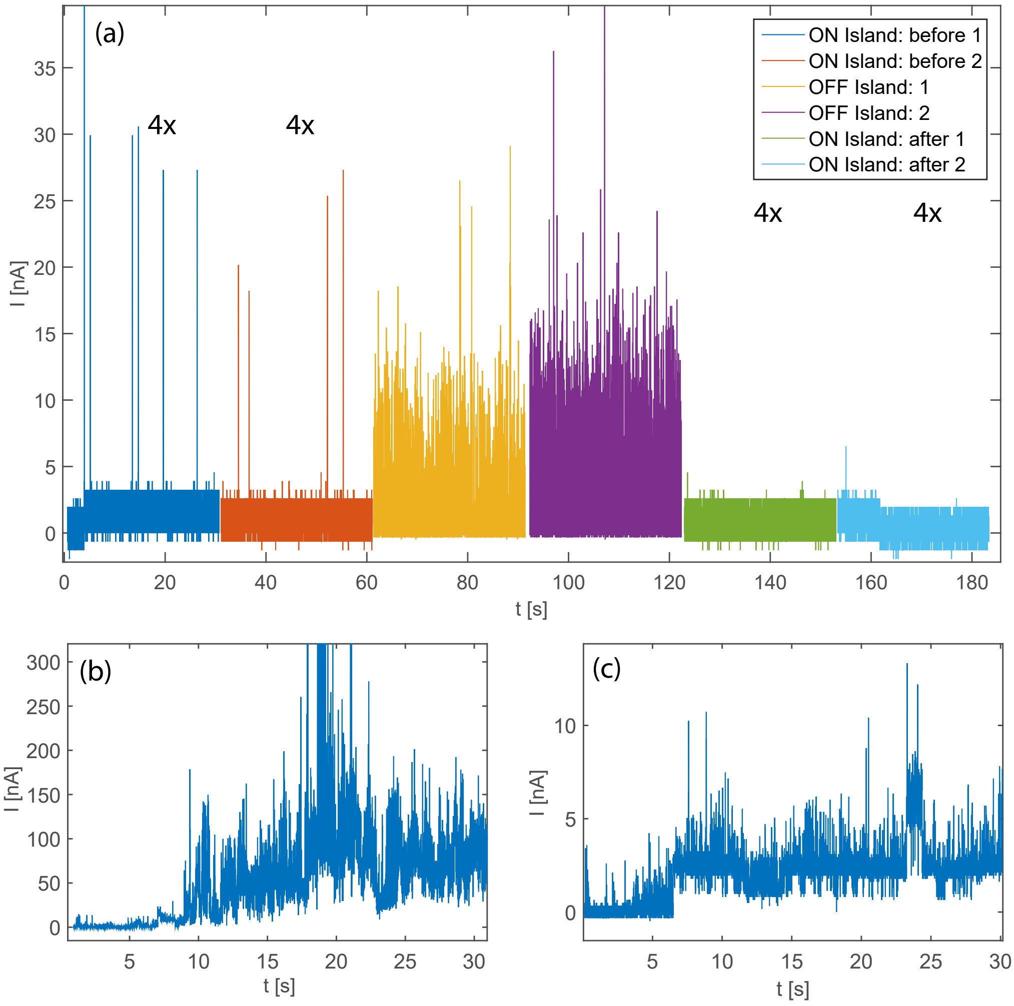

Figure 7.13: A selection of undesirable time-series acquisitions. (a) Full on-off-on island experimental procedure with two acquisitions on each location. Two acquisitions produce an undesirable kink and are subsequently discarded. (b) Drift occurring during constant height acquisition, causing uncontrollable changes in the *I(t)* signal. (c) Tip change during acquisition.

II. Current setpoint influence

III. Bias voltage influence

IV. Tip-sample distance

V. Tip state influence

By changing these parameters, the goal is to determine if and how this affects the experimental signals, and ultimately, the estimated diffusion coefficients. The calculations of the diffusion coefficients require a detailed analysis [171], which will be performed by collaborators from the Universität Osnabrück. In our analysis, we first focus on investigating how the following quantities are affected by changes in the parameters space:

1. Number of pulses
2. Apparent coverage
3. Residence time distribution

The first quantity to analyze is the number of pulses normalized by time. Although the pulses for tip imaging state A are supposedly due to diffusing molecules, we know by observing the other tip (imaging) states, that (uncommon) rapid pulses can occur additionally. The precise causes of these signals remain unclear, but are suspected to be due to tip-sample interactions or tip instabilities. It is therefore important to consider how the tunnelling signal time trace behaves for different parameters, and how it affects diffusion estimations. If the molecules are attracted towards the tip in the tip-sample gap, the number of pulses should increase in that case.

The second quantity to analyze is the apparent coverage Θ of the diffusing species. As explained previously, Θ is estimated from the sum of the full time width of all pulses above I_c for an acquisition, divided by the total acquisition time. The apparent coverage therefore depends on both the duration and number of pulses. If the molecules are attracted toward the tip in the tip-sample gap, both number of pulses and the duration of pulses should increase in that case. Finally the distribution of residence times normalized to time is examined. If the molecules are attracted towards the tip in the tip-sample gap, the residence time distribution should increase in that case. Error bars (95 % confidence interval) are obtained by splitting FIP acquisitions into two sections. The standard error is then obtained from the standard deviation of the evaluated quantities for each of the two sections.

I. Feedback response

The effect of changing the response of the distance feedback controller on diffusion experiments was tested systematically over a range of a highly responsive loop to a relatively unresponsive loop by changing the gain. The results are shown in Fig. 7.14(a)-(c). We observe that slowing down the current feedback response has a clear effect on the signal fluctuations, in particular with their associated RTDs. We attribute this to the following reason. When the tip responds relatively fast to changes in current, the pulses are shorter in time as the tip moves quickly out of tunneling range. As the response of the feedback loop slows down, the pulses become wider, now detecting the molecules during their whole residence under the tip. The likely explanation is that if the tip responds too quickly, the pulses attributed to diffusing molecules will prematurely be aborted as the signal falls below the noise threshold I_c. As a result, the RTDs will be distorted for fast feedback response settings. In other words, the slower the feedback response, the better the RTDs will be represented. As changing the feedback response only affects the duration of pulses, we would expect the number of pulses to remain unaffected, while the apparent coverage increases, which coincide with our findings. The fact that the number of pulses *decreases* at lower feedback responses might be explained by "blind spots" that occur after pulses as the tip moved to a larger tip-sample gap. Therefore, pulses with amplitudes lower than a preceding pulse might not be detected.

As the pulses are more accurately represented using lower feedback responses, we acquire data with either extremely low settings or ideally in constant-height mode where the feedback loop is deactivated. However, per-

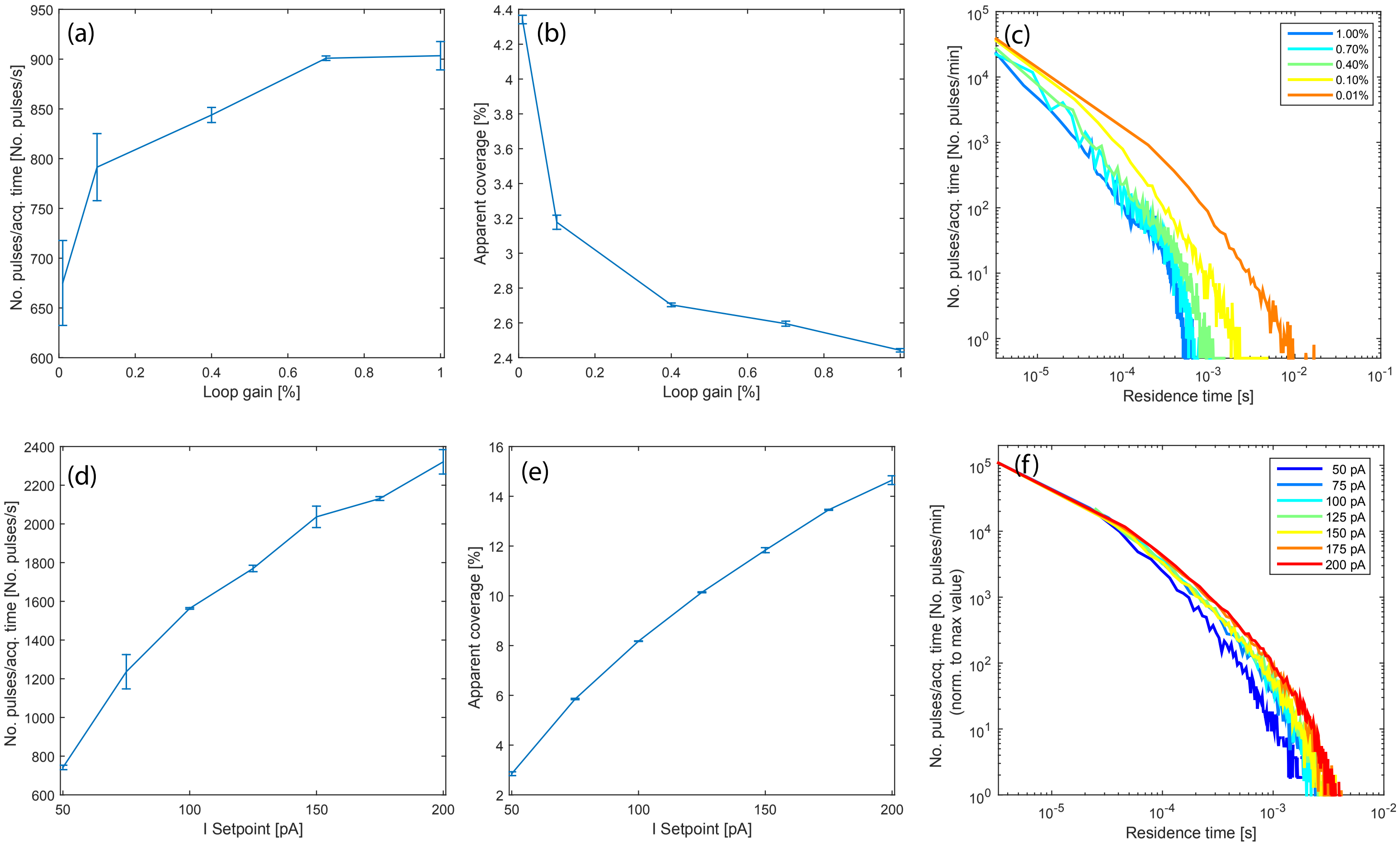

Figure 7.14: Analysis of STM parameter influence on FIP experiments, (a,d) number of pulses, (b,e) apparent coverages, and (c,f) RTDs of pulses over mobile phase for different, (a-c) feedback responses (loop gain), and (d-f) current setpoints. FIPs acquired using (a-c) 1 V, 50 pA, (d-f) 0.5 V, loop gain = 0.1%.

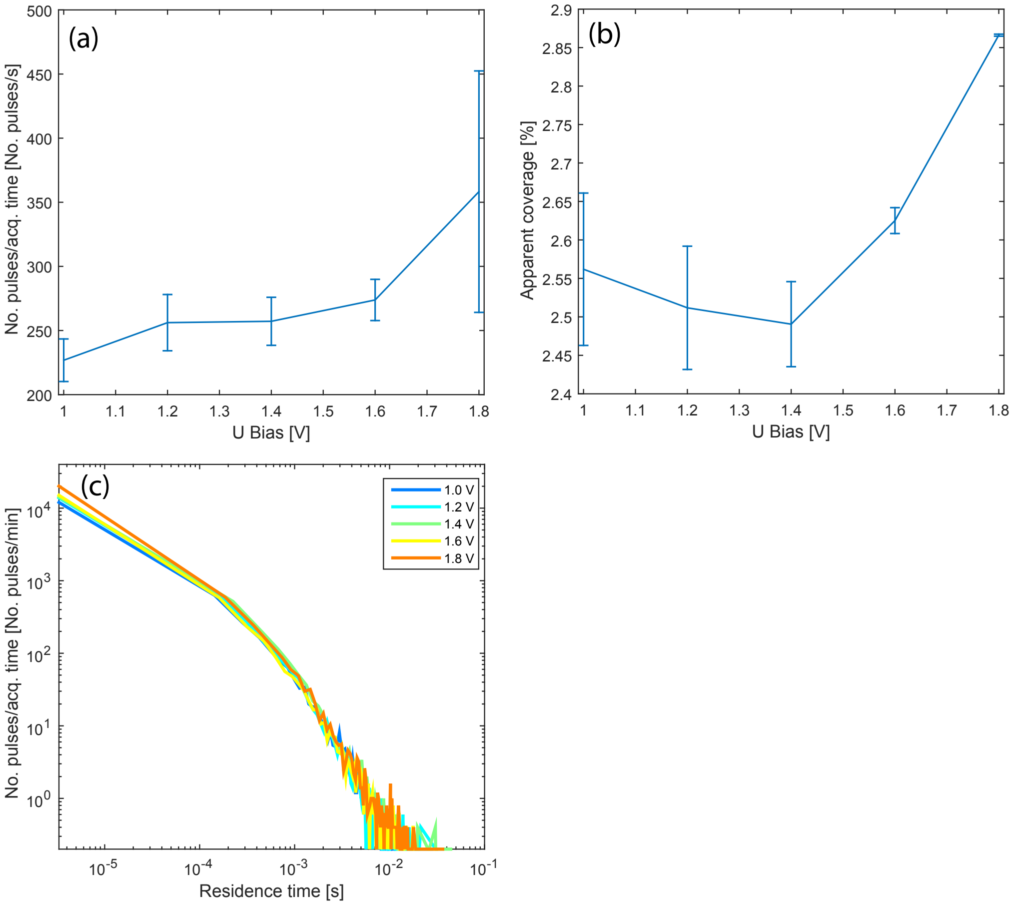

Figure 7.15: Analysis of STM parameter influence on FIP experiments, (a) number of pulses, (b) estimated coverages, and (c) RTDs of pulses over mobile phase for different bias voltages. FIPs acquired using 50 pA, loop gain = 0.01%.

forming constant-height FIP measurements over prolonged periods is exceedingly difficult at RT as the tunnelling current is exponentially dependent on the vertical drift and, therefore, strong affects in the *I(t)* traces will emerge. Constant-height FIP measurements were therefore acquired in succession using short time intervals (30s), and in conjunction with active atom-tracking and feed forward drift compensation [182].

II. Current setpoint

The current setpoint influence on the diffusion experiments was investigated next by systematically changing the current setpoint (Fig. 7.14(d-f)) using a low feedback response. As the current setpoint increases, the number of peaks and the apparent coverage clearly increase, providing a substantial increase in the number of data points (counts) for their respective RTDs. In order to allow a comparison of the residence time distributions all RTDs are normalized with respect to the highest number of data points. Additionally, we observe a small systematic increase in the residence time of the pulses at higher current setpoints. We surmise that as the current setpoint increases, the sensitivity of measuring the pulses increases due to (i) a closer tip-sample proximity and more importantly (ii) an increase in detection region *M*. Consequently, the amount of time the molecule spends passing the detection region also increases. The closer proximity of the tip to the surface also leads to a higher electric field in the tip sample gap which might affect the adsorbate motion. Alternatively, at shorter tip sample distances, the molecules may simply (temporarily) trap the molecules in the in the tip-sample gap, thus gradually increasing residence time of the molecules under the tip. In section 7.2.4 constant-height FIP acquisitions are performed for various tip-sample distances and bias voltages to ascertain if the tip height has an effect on adsorbate motion.

III + IV. Bias voltage and tip-sample distance

In this section, we investigate the dependence of the bias voltage on the diffusion measurements. Experiments were performed at low feedback settings and at a low current setpoint at different bias voltages. The results are shown in Fig. 7.15(a-c). We observe that the number of pulses increases with increasing bias voltage in the regime $1 - 1.8$ V, but the apparent coverage Θ changes only sightly and the distributions of pulse durations (RTDs) remain unchanged. Based on these results, it is unclear if the tip bias has within this tested regime an influence on the adsorbate motion, or not. As will be discussed below, two effects might leave an impact on the diffusion properties of the molecules. First, the presence of the STM tip causes a van-der-Waals attraction toward the molecules and might, depending on the tip termination, exhibit further specific interactions with the molecules on the surface, ultimately attracting or repelling to or from the detection area. Second, the strong electric field will polarize molecules and attract them to the tip-sample gap, or can otherwise interact electrostatically with the surface bound molecules. We therefore need to disentangle distance and electric field dependencies on the diffusion behavior by performing constant-height (feedback response off) FIP measurements for systematic changes of the tip-sample distances ($\mathrm{Z_{offset}}$) and bias voltages V. The results are shown in Fig. 7.16. Experiments performed on the islands within the on-off-on measurement protocol are shown in Appendix Fig. C.6.

Our results show a clear decrease in the number of pulses when increasing $\mathrm{Z_{offset}}$ (see Fig. 7.16(a)). The decrease in the number of pulses with increasing tip-sample distance suggests a decrease in the detection area M due to the tunneling barrier gap widening. A more detailed examination of the peak height distribution of the pulses as a function of the tip-sample distance might shed some light on the subject, but is beyond the scope of this thesis. We additionally observe from residence time distributions (7.16(c)-(f)) that the duration of pulses becomes longer for increasing V, and becomes shorter for increasing $\mathrm{Z_{offset}}$. From this we infer that an attractive long-range interaction is at play between the tip and adsorbate, causing the adsorbate to be (temporarily) trapped within the tip-sample gap. The interaction decreases with distance, and is (at least partially) dependent on the applied bias.

Contrary to measurements performed on the mobile phase, the corre-

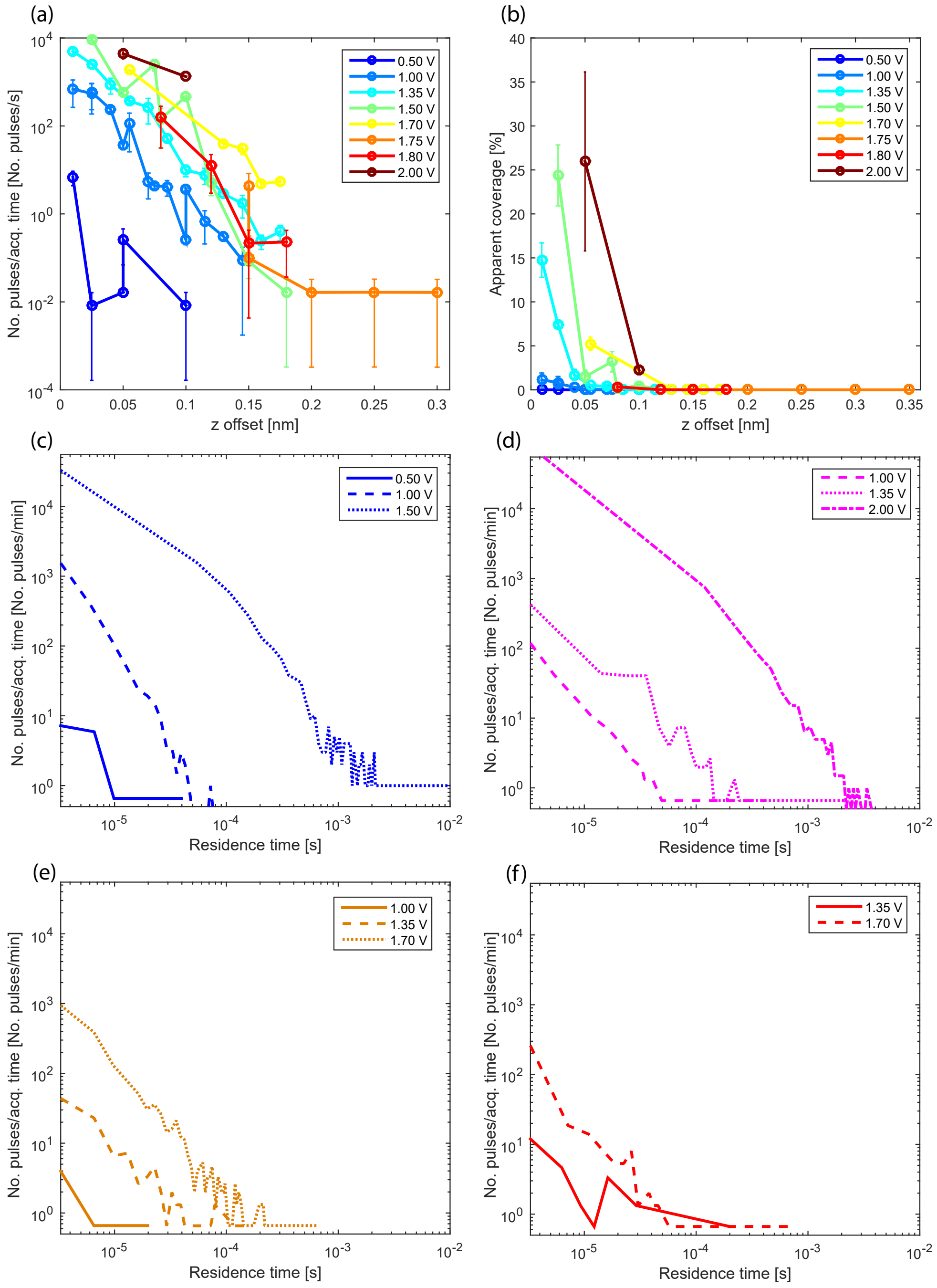

Figure 7.16: (a)-(b). Constant height FIP acquisitions over the mobile phase as a function of Z_{offset} for different bias voltages. $Z_{\mathrm{offsets}} = 0$ corresponds to 1 V, 50 pA for each set. (c)-(f) A selection of RTD's corresponding to constant height measurements in (a) and (b) and are plotted as a function of voltage for a Z_{offset} of (c) 0.05 nm, (d) 0.10 nm, (e) 0.145 nm, and (f) 0.175 nm.

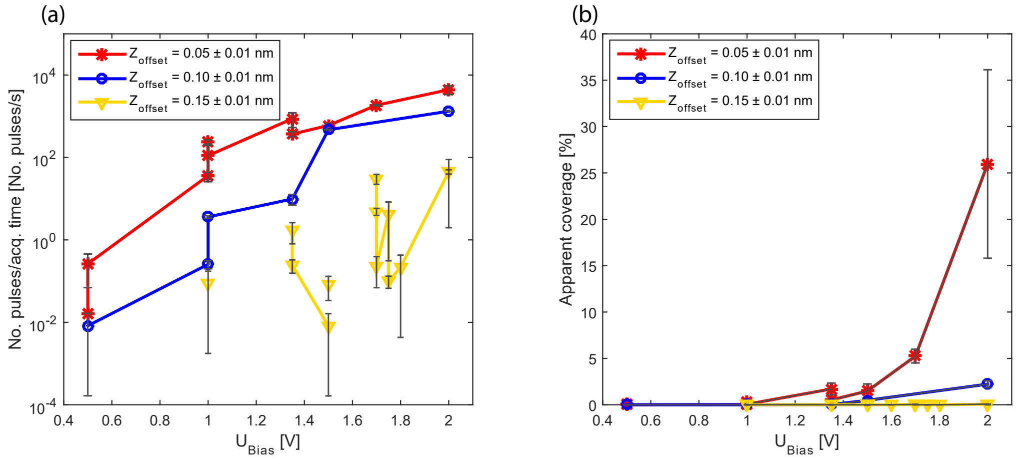

Figure 7.17: A selection of data from constant height measurements shown in Fig. 7.16, are plotted as a function of bias voltage at specific tip-sample distances (Z_{offset}).

sponding on-island measurements (Fig. C.6), show that neither the number of pulses nor the the apparent coverage are affected by changes in the bias voltage or by changes in the tip-sample gap distance. Similarly, the duration of pulses seems also relatively unaffected by changes in the bias voltage and tip-sample distance, all showing extremely rapid pulses ($\tau \leq 10$ µs). Consequently, it seems unlikely that any secondary layer diffusion takes place on top of the PTCDA islands, with diffusion taking place only over the mobile phase of the surface. Additionally, the fact that systematic changes occur for our measured quantities over the mobile phase, but not over the PTCDA islands when changing our adjustable parameters; the bias voltage and tip-sample distance; suggests that the changes that occur over the mobile phase are the result of an interaction between the tip and the mobile species.

In Fig. 7.17 constant-height measurements from Fig. 7.16 are examined in more detail by plotting the measurements as a function of bias voltage for different tip sample distances. We observe that the number of pulses and the apparent coverage increases proportionally with respect to the applied bias voltage. At higher gap distances the measured quantities continues to increase with respect to the bias voltage, suggesting that (at least at larger gap distances) that the electric field of the tip plays a dominant role on the tip-adsorbate interaction. To investigate the influence of the presence of an STM tip on adsorbate motion, we will briefly discuss in section 7.2.4 which types of influences are at play an on how to distinguish them in practice. Before, we will investigate possible influences due to the state of the tip.

V. Tip state influence

In order to determine how reproducibly a given tip state will yield reliable diffusion signals, the diffusion measurement quantities were investigated systematically for tip imaging state *A* using different tip states (numerated using values 1...*N*). The results are shown in Figs. 7.18, while changing the bias voltage and $\mathrm{Z_{offset}}$ position.

We observe that the resulting quantities for different tip states follow similar trends. The number of pulses increases with decreasing tip-sample distance although when comparing data across different tip states, a difference in the absolute number of peaks per second by an order of magnitude is found. Similarly, the duration of pulses also varies on the scale of at least an order of magnitude. However, these conclusions are drawn under the assumption that the absolute Z-position is identical across the different tip states. While the vertical position of the tip is vey precisely controlled using the atom-tracking and feed-forward techniques [182], the absolute tip "height" might be different for different tips even when using the same STM parameters of 1 V, 50 pA.

VI. Discussion

In the absence of an STM tip, an adsorbate bound to a surface experiences a periodic lateral potential (Fig. 7.19) due to interaction with the surface. When the STM tip apex is brought close to the substrate (above or near the adsorbate), the potential energy of the adsorbate is modified relative to its value in the absence of the tip. This has been specifically exploited already early for STM-based manipulations, e.g. for the movement of Xe atoms on a Ni(110) surface [3, 184], or using Cs atoms on GaAs and InSb(110) surfaces

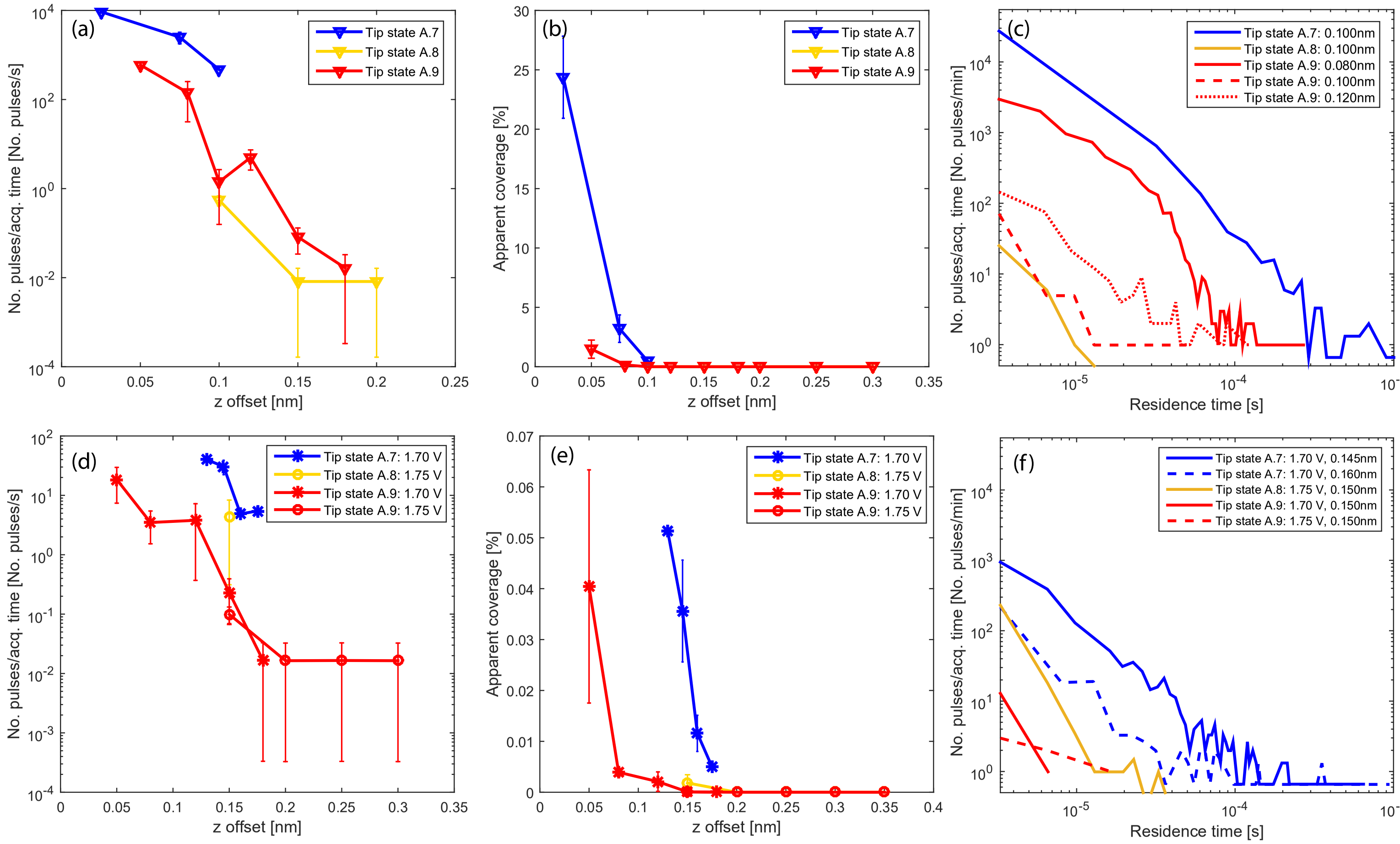

Figure 7.18: Tip state influence on diffusion experiments of tip imaging state A for a range of bias voltages and $\mathrm{Z}_{\mathrm{offsets}}$. (a)-(c) 1.5 V, (d)-(f) 1.7-1.75 V. $z = 0$ corresponds to 1 V, 50 pA.

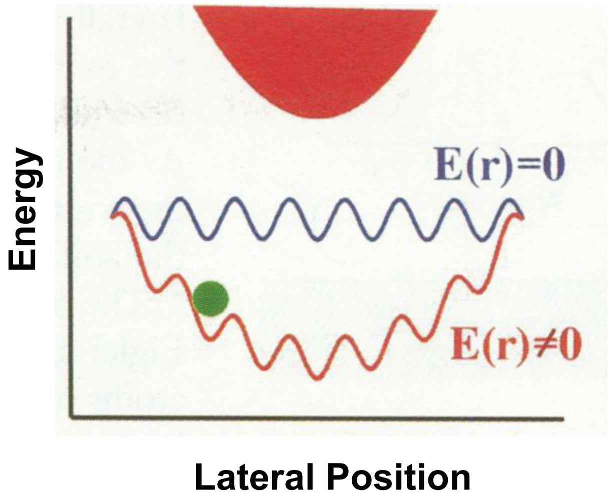

Figure 7.19: Modification of adsorbate (green) potential energy due to interaction with the STM tip. The electric field of the tip causes polarization of the surface adsorbate, thus altering its surface periodic potential into a broad potential well under the tip apex, where the adsorbate experiences a force to pull it toward the bottom of the well. Adapted from [183].

[185]. We can assume two interactions between the tip and the molecules: van-der-Waals (vdW) forces and electrostatic forces due to the applied bias. The presence of an electric field causes a polarization of the adsorbate, leading to a modification of its adsorption energy [186]. The resulting surface potential barrier for diffusion can be modified, and could have a substantial influence on the kinetics of motion of the adsorbate. As these electrostatic and vdW forces have different dependencies with the $\mathrm{Z}_{\mathrm{offset}}$ and the applied bias, it might be possible to disentangle, their contributions to influencing the diffusion by systematically changing the tip-sample separation and tip-sample bias.

Based on our observations, the residence time of molecules at RT using low feedback responses and permissible current setpoint settings ($I_{min} > 50$ pA) can be quite long, with a few pulses reaching an order of magnitude longer durations (in milliseconds) than for diffusion experiments of PTCDA conducted on the Ag(100) surface at 192 K [161].

Using constant height measurements, the residence time of pulses increases with increasing bias (Fig. 7.16(c)-(f)), which is contradictory to our findings using low feedback responses (Fig. 7.15(c)). The increase in the duration of pulses with increasing bias suggests an electric field dependence on the adsorbate motion. Experiments performed at biases above 2.0 V proved challenging as they usually led to unstable tips, and were thus omitted from further analysis. From the residence time distributions in Fig. 7.16(c)-(f), we observe that pulses at low bias (assuming short gap distances) are extremely rapid, $\tau \leq 10^{-2}$ms. This suggests, that at low applied biases, the tip-adsorbate interaction is small, thus indicating that any potential vdW interaction affecting the adsorbate motion would be significantly weaker than the electric field dependence of the tip.

The vdW and and electrostatic interactions between tip and adsorbate were estimated using simple theoretical models using experimentally and theoretically obtained parameters. Specifically, we aim for estimating the energies of interaction with the tip and compare this energy contribution with the diffusion barrier. The adsorbate is assumed directly underneath the tip apex, and the interactions are calculated strictly as a function of the tip-molecule distance, ignoring any surface contributions to the interaction. The results are plotted in Fig. 7.20 for both the vdW and electric-field induced interactions.

The vdW interaction force between tip and the PTCDA molecule was approximated using a two sphere model [187], where the tip is modeled as a sphere with different radii and the PTCDA molecule is modeled as a sphere of fixed radius. As the size of PTCDA has been estimated to be 0.92×1.42 nm [165], an effective radius of $R_{PTCDA} = 0.6$ nm seems reasonable for a crude approximation. The results are plotted in Fig. 7.20(a) as a function of tip-molecule separation for different tip radii, and a fixed sphere approximation of $R_{PTCDA} = 0.6$ nm for PTCDA.

The electric field dependence on the surface adsorbate is modeled as an induced dipole interaction. In the presence of a static electric field $\mathbf{E}$, an adsorbate becomes polarized by

$$\mathbf{p} = \boldsymbol{\mu} + \boldsymbol{\alpha}\mathbf{E} + \boldsymbol{\beta}\mathbf{E}^2/2 + \ldots \tag{7.2}$$

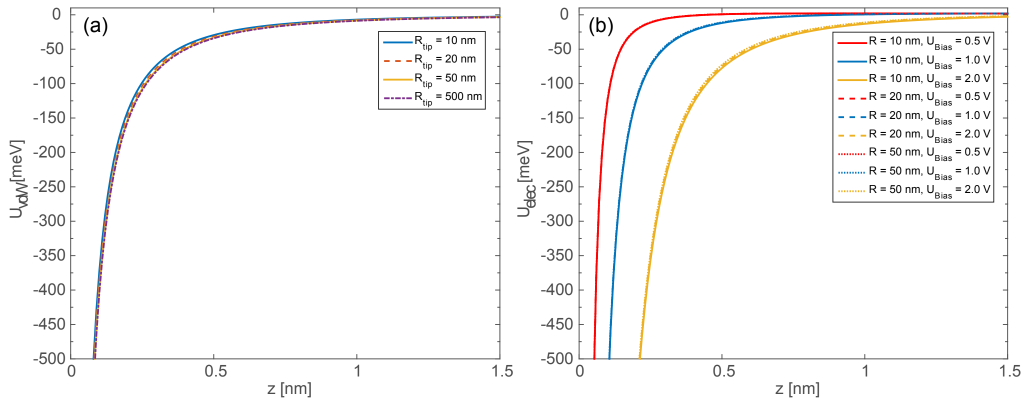

Figure 7.20: Modeling tip-adsorbate interaction plotted as a function of tip-molecule separation of an adsorbate placed directly beneath the tip apex. (a) vdW interaction energy between a PTCDA molecule and an STM tip for different tip radii. $R_{PTCDA} = 0.6$ nm, $A_{Hamaker} = 10^{-19}$ J. (b) Change in adsorbate potential energy due to dipole interaction between electric field of tip and adsorbate for various applied biases U_{Bias}.

whose magnitude is dependent on the static dipole moment $\boldsymbol{\mu}$, the induced dipole moment, $\boldsymbol{\alpha}\mathbf{E}$, the polarizability, $\boldsymbol{\alpha}$, and hyperpolarizabilitities, $\boldsymbol{\beta}\ldots$ of the adsorbate. The spatially dependent potential energy change $\Delta U(\mathbf{r})$ of the adsorbate then becomes [188]

$$\Delta U(\mathbf{r}) = -\boldsymbol{\mu} \cdot \mathbf{E}(\mathbf{r}) - \frac{1}{2}\boldsymbol{\alpha}\mathbf{E}(\mathbf{r}) \cdot \mathbf{E}(\mathbf{r}) + \boldsymbol{\beta}\mathbf{E}(\mathbf{r})^2/2 \cdot \mathbf{E}(\mathbf{r}) + \ldots \tag{7.3}$$

Although PTCDA has no static dipole moment, a work function change on the metal surface can occur after adsorption, due to the formation of an interface dipole [189]. Previous experiments established a very small *net* work function change of 0.1 eV for the adsorption of 1 ML PTCDA on the Ag(111) surface [166], indicating a very small interface dipole $\Delta\mu = \frac{\varepsilon_0 A}{e}\Delta\Phi \approx -0.35$ D, directed along the surface normal, where $\Delta\Phi$ is the work function change, and A is the area of the molecule. Systematic calculations of work function changes of PTCDA on several metal surfaces, suggests that most high-workfunction metal surfaces have little or no *net* work function change upon adsorption of PTCDA [189]. We therefore apply a static dipole moment of -0.35D to our calculations. Although hyper-polarization effects can play a role for some molecules, in particular π-conjugated molecules, their calculations are challenging for complex molecular systems [190], and have thus been omitted from our calculations. Also, as the electric field from the STM tip is normal to the plane of the molecule it follows that $a_{k\perp} \cdot E = 0$, where a_k are all the in-plane polarizabilities of the molecule. As a result, only the polarizability for PTCDA normal with respect to the plane of the surface, $\alpha_N = 18.06$ Å^3 [191], is used.

The electric field of an STM tip placed on top of a metallic surface, assuming a spherical apex geometry, can be approximated as [192]

$$E = \frac{V}{z} \frac{(u + u^2)^{1/2}}{\ln[u^{1/2} + (1 + u)^{1/2}]} \tag{7.4}$$

where V is the bias voltage, and $u = z/R$ with z the tip-sample distance and R is the radius of curvature of the tip apex. Combining Eq. 7.3 and 7.4, the potential change of the PTCDA molecule at the point directly underneath the tip was calculated as a function of the tip-molecule distance for different applied bias voltages. The results are shown in Fig. 7.20(b).

Under normal STM imaging conditions on metal surface, typical tip-sample distances are in the range of approximately 0.5 - 1 nm. Note that this gap distance can vary considerably for different applied biases (assuming constant current mode). As the PTCDA molecule is positioned at a distance d = 2.56Å above the surface [193], we assume the tip-molecule distance to be in the range of $d = 5 - 10$Å $- 2.56$Å $\approx 2.5 - 7.5$Å, for tip imaging state A. Thus for normal STM imaging conditions, the vdW interaction seems reasonably small ($\approx$ 20-100 meV) and is not strongly dependent on the tip radius in our model. At larger tip-molecule separations the vdW interaction is further reduced. The change in potential energy of the adsorbate, on the other hand, has a strong dependence on the applied bias, but similarly not on the tip radii modeled. For low biases $V_b \leq 0.5V$, the interaction quickly drops significantly as the tip moves further away from the adsorbate, even entering the repulsive regime at larger distances ($z \geq 0.45$ nm) due to the presence of the interface dipole. However, at larger applied biases (2 V), the interaction potential becomes very significant ($\sim 50 - 450$ meV) under normal

STM imaging conditions. A potential change of 450 meV on a molecule with an adsorption energy of 3.39 eV (see section 7.1) could have a substantial influence on its surface kinetics.

Our theoretical calculations support the model of tip-molecule attractive interaction that is dominated by a dipole interaction with the electric field of the STM tip. These calculations coincide with our experimental finding, and in particular, our constant-height measurements (Fig. 7.16), where we observe short-duration pulses at low biases (0.5 - 1 V) and short tip-molecule separations (Fig. 7.16)(c). These pulses do not seem to diminish for higher tip-sample separations (1 V in Fig. 7.16(d), suggesting that the tip sample interaction has not diminished appreciably. Around these experimental parameters, it is conceivable that we are approaching the borderline between the repulsive and attractive regime due to the presence of a static dipole moment of the molecule. The number of pulses and the apparent coverage also increases with the applied bias, suggesting a higher latency or accumulation of molecules in the tip-sample gap for higher biases.

The conflicting findings between measurements performed in constant-current mode (see Fig. 7.15 where no change in the duration of pulses is observed) and measurements performed in constant-height (see Fig. 7.16 where changes in RTDs are observed for different applied biases and tip-molecule separations), can be explained by the differences in electric field effects on the surface adsorbates for the different measurement schemes. When applying constant current mode, the tip-sample electric field remains constant for different applied biases, as the tip-sample separation is adjusted to maintain constant current. As a result, the duration of pulses remain unaffected. Conversely, for constant-height measurements the electric field does change for different applied biases, as the tip sample separation remains unaltered. This suggests, that any potential vdW interaction between tip and adorbate for our used experimental parameters is very low, as the residence time distribution of the pulses remain unaffected under a constant electric field (Fig. 7.15(c)).

7.3 Anisotropic diffusion

One major drawback of using a locally fixed probe for measuring adsorption kinetics is that any adsorbate passing through the detection area is recorded, regardless of the their directionality. In other words, FIP acquisitions assume isotropic diffusion. However, and especially on anisotropic surfaces, diffusion can be anisotropic. For motion of adsorbates on surfaces reasons can include for example an asymmetric molecule structure [194] or an anisotropic surface structure [195]. To investigate anisotropic diffusion, Ag(110) surfaces were chosen due to the anisotropy of the surface atoms along the high symmetry directions (see Fig. 7.2) which should lead to different anisotropic barriers along the different surface directions. Consequently, the experiments before will yield 'averaged' diffusion parameters, but we preferred to perform all experiments on the same surface for comparison. For anisotropic diffusion, the diffusive motion is characterized by a diffusion tensor [196]. It has been suggested theoretically [163] that determining the diffusion tensor becomes possible by modifying the fixed probe method instead of sampling the data at one fixed surface position, the tip periodically moved across the surface duing data acquisition. For our experimental treatment, we introduce two versions: one, where the probe oscillates in a straight line, and a second, where it rotates in a circle around a fixed point, as illustrated in Fig. 7.21.

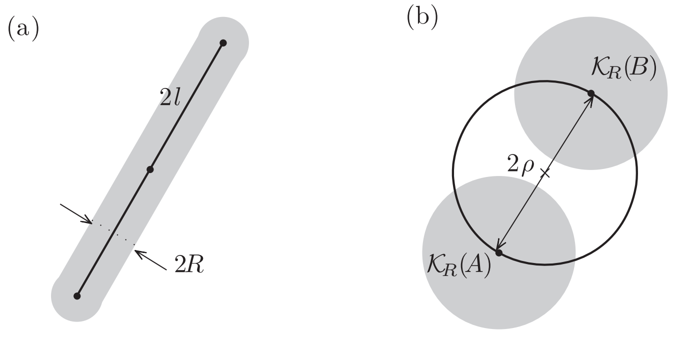

Figure 7.21: Basic tip trajectories of (a) LOP and (b) ROP setups. Detection regions are marked in gray while the solid lines mark the traces of the tip probe. The detection areas in (b) are only used for the designated probing sites $K_R(A)$ and $K_R(B)$. Adapted from [163].

The first method has been used to introduce the principle, while the second method is used experimentally within this work. Using a linearly oscillating probe (LOP) to detect a passing molecule, any diffusing molecule would give rise to a signal whenever its center enters a stripe of width $2R$ around the line. The shaded area (gray) marks the detection full region of the oscillating probe.

Assuming the probe oscillates in one specific direction, and if the probe oscillates considerably faster than a molecule moving perpendicular to the line, the probe will be able to record the passing molecule multiple times. If the probe were able to oscillate infinitely fast, the exact motion of the passing molecule could be recorded. By recording the signal for different orientations of the oscillating probe, the directionality (diffusion tensor) of passing molecules can be derived by analyzing the RTDs of the different time series [171, 163].

So far we have considered an infinitely fast oscillation, in which any molecule passing the detection area will give rise to a signal (assuming infinitely fast recording of signal) regardless of how fast the molecule moves. In practice, however, this is not possible. In order to reliably resolve the molecular residence, the probe oscillating with a frequency f needs to oscillate considerably faster than the amount of time τ_R it takes for the molecule to pass the detection region. In other words $\tau_R^{-1} \ll f$. On the other hand, the oscillation frequency needs to be sufficiently smaller than the sampling rate r in order to have sufficient resolution of the detection events. All requirements are satisfied when $\tau_R^{-1} \ll f \ll r$.

A typical sequence of peaks (after transforming them into on/off signals as explained for the FIP experiments in section 7.2.1) is exemplified in Fig. 7.22(a). Each cluster of peaks represents how many times the probe bounces into a passing molecule. The residence times can be sampled by considering the cluster widths as indicated by the dashed lines in Fig. 7.22(a). A disadvantage of using this method – besides the challenge of determining the optimal oscillation amplitude – is that for a reliable measurement of the diffusion coefficient one need not only align the direction γ of the probe with the high-symmetry directions of diffusion, but also to the values in-between. As

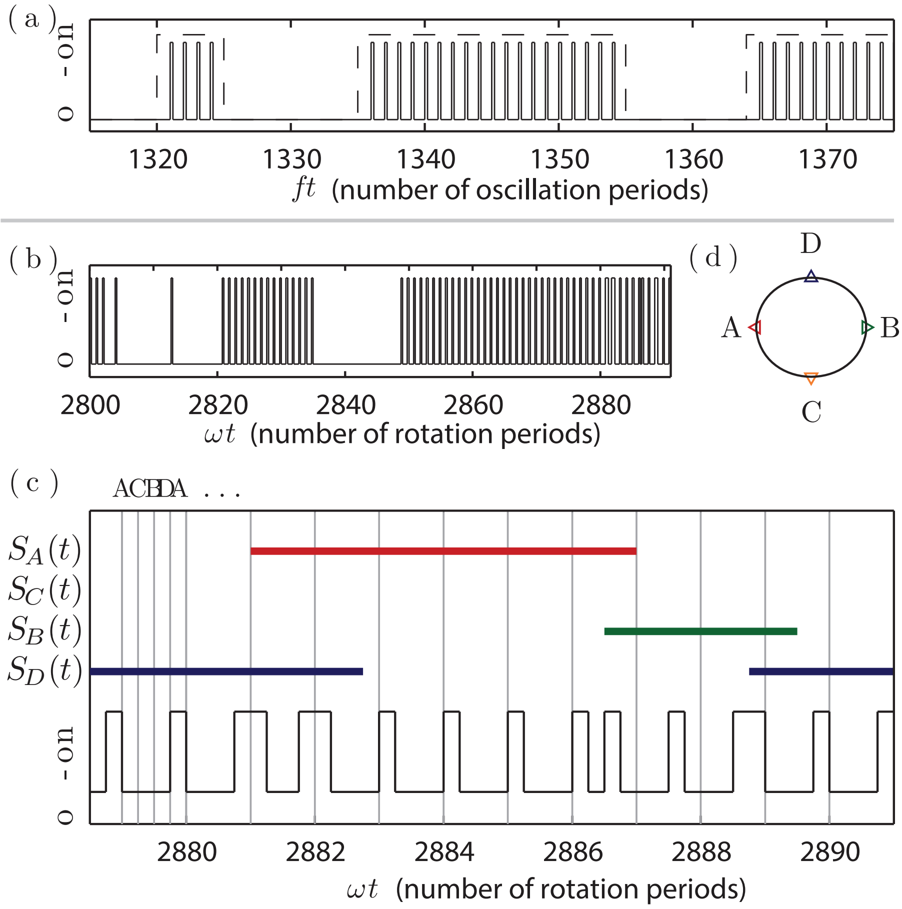

Figure 7.22: Examples of peak sequences obtained using the (a) LOP and (b) ROP methods. If the period of the moving probe is considerably smaller than the time an adsorbate needs to cross the detection area, the adsorbates will appear as short peaks (solid lines). Each cluster of peaks correspond to a detection period between the adsorbate moving within the detection area of the probe, and are transformed into on/off signals (dashed boxes). (c) Assignment of the peaks in the last cluster in (b) to 4 different detection points $A \dots D$ on the circle shown in (d) used to split signal into reconstructed signals $S_A \dots S_D$. The colored bars mark the "on" periods of the reconstructed signals with these pints. From [163].

a result, acquisitions needs to be performed for many different orientations of the probe in order to derive the diffusion coefficients.

The radially oscillating probe (ROP) method (Fig. 7.22(b)-(d)), on the other hand, allows simultaneous evaluation of the diffusion coefficient in arbitrary directions. Similarly to the FIP probe method, the probe is centered at a fixed position. In this case however, the STM probe is dithered on a circular trajectory (see section 4.6 for technical implementation) with an oscillation frequency f and a dithering radius ρ. Similar to LOP, clusters of peaks appear whenever the molecule is within the detection region along the circular trajectory of the tip. The diffusion tensor can be determined from an analysis of cross correlations of the fluctuations recorded at different points along the circle. Theoretical calculations suggest an optimal correlation is reached when $\rho = 1.1R$ [163], where R is the radius of a circular molecule.

For determining the diffusion tensor based on the cross-correlation of time series at different points, the clustered peaks are transformed into an on-off time series signals. These signals are then compared with virtually fixed points of the circle, e.g. $A \dots D$ marked in 7.22(d). Whenever a continuous signals is "on" when the probe passes a respective point, a reconstructed signal $S_A(t) \dots S_D(t)$ is obtained, as shown in Fig. 7.22(c). The diffusion tensor can thus be determined by cross correlating $C(t) = \langle S_B(t+t) S_A(t) \rangle$ between antipodal points (e.g. A and B), for the reconstructed signals [171, 163].

7.3.1 Implementation

In practice, limiting factors for determining diffusion coefficients from experiments depend on (i) the detection system bandwidth (sampling rate r), (ii) the probe oscillation rate and amplitude, and (iii) the stability and reliability of the oscillating probe. To give an example, the time resolution of n points per rotation is given by [171]:

$$\Delta t_{rec} = \frac{(2\rho)^2}{nD} \tag{7.5}$$

where ρ is the oscillation radius and D is the diffusion coefficient. With this minimal time resolution, accurate identification of diffusion from one measurement point to another is ensured.

In order to ascertain the stability of the dithering trajectory, first, the experimental implementation of the ROP method is critically evaluated. Due to resonances and bandwidth limitations within the electronics for the scanning probe, the behavior at various dithering frequencies needs to be investigated. The stability and reliability of the dither circle was analyzed by performing atom tracking of surface adsorbates on the Ag(110) surface for various dithering frequencies and amplitudes. The results are shown in in Fig. 7.23.

We observe that stable tracking of surface adsorbates is possible for certain frequencies, even at high frequencies ($f_{dither} \sim 10^4$ Hz). However, in several cases (i.e. at specific frequencies) there is no stable atom tracking error signal from dithering across a feature, therefore the atom tracking is not stable. The unstable error tracking signal most commonly occurs when the tip produces non-circular, or non-planar dither circles. The limiting factor to perform stable dithering seems to be resonances of the piezo scanners as well as stray signals within the tunnelling current signal, i.e. at the line frequency of 50 Hz and its overtones. Unstable atom tracking conditions,

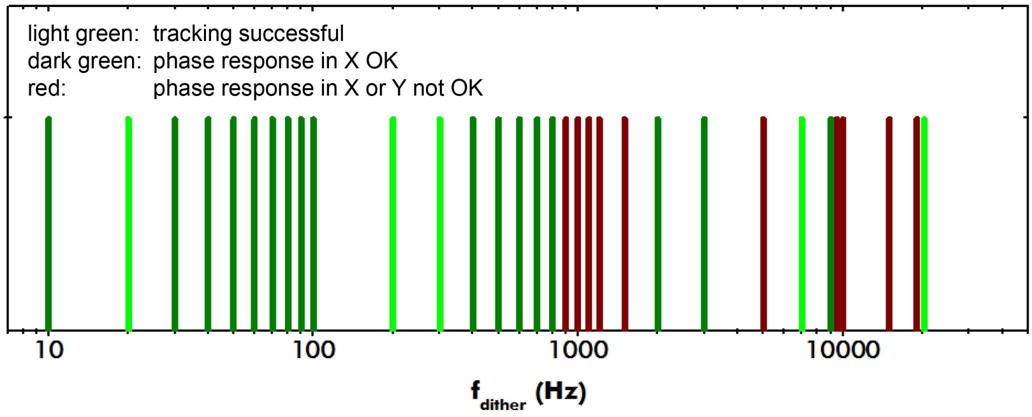

Figure 7.23: Successful (green) and unsuccessful (red) atom tracking of surface adsorbate at various frequencies. $\rho_{dither} = 0.31$ nm. Measurements performed by Philipp Rahe in our group.

and therefore unstable dither circles, were most commonly observed in multiples of 50 Hz and at high frequencies, such as 2, 10 ,15, 17, and 20 kHz. A dithering frequency of 7.31 kHz was therefore carefully chosen for most ROP measurements where a good and stable atom-tracking response was found.

ROP acquisitions were performed using the same acquisition procedure as FIP measurements. The same sampling rate (300 kHz) and bandwidth of the preamplifier (80 kHz) was used as for the FIP measurements. All measurements were performed at RT.

To examine adsorbate motion for tip imaging state A, ROP experiments were first performed for different dithering amplitudes (ρ) at a dithering frequency of $f_{dither} = 7.31$ kHz. When the dithering amplitudes approaching zero ($\rho \to 0$) we would expect to see a FIP experiment, while for large dithering amplitudes we would expect single pulses at the same frequency as f_{dither} when a feature enters the detection region. In Fig. 7.24 the influence of dithering the probe is analyzed by comparing FIP with ROP acquisitions for different dithering amplitudes. We observe that the number of peaks increases, while their coverage decrease for larger dithering amplitudes. For small dithering amplitudes, the residence time distribution of pulses only changes marginally, compared to a FIP measurement, while the distribution shifts to smaller times for larger amplitudes.

To explain these changes, we also investigate the time traces itself. In Fig. 7.25, a selection of time series acquired for different dithering amplitudes is presented, along with its corresponding reference signal. Signals comparable to the theoretical predictions (Fig. 7.22) are found. For each pulse, we observe depressions in the pulse (Fig. 7.25(d-e)), which grow more prominent for higher dithering amplitudes. Additionally, the frequency of these depressions coincide with the oscillation frequency of the probe. *This is a clear indication that the depressions are caused by a species present within the detection area of the oscillating tip* (see Fig. 7.21 for illustration). As the tip moves away from the detection area, the the molecule is no longer detected, causing a depression in the pulse. This leads us to conclude that the pulses we observe for tip imaging state A *are indeed attributed to the detection of diffusing species rather than caused by other artifacts such as random noise*

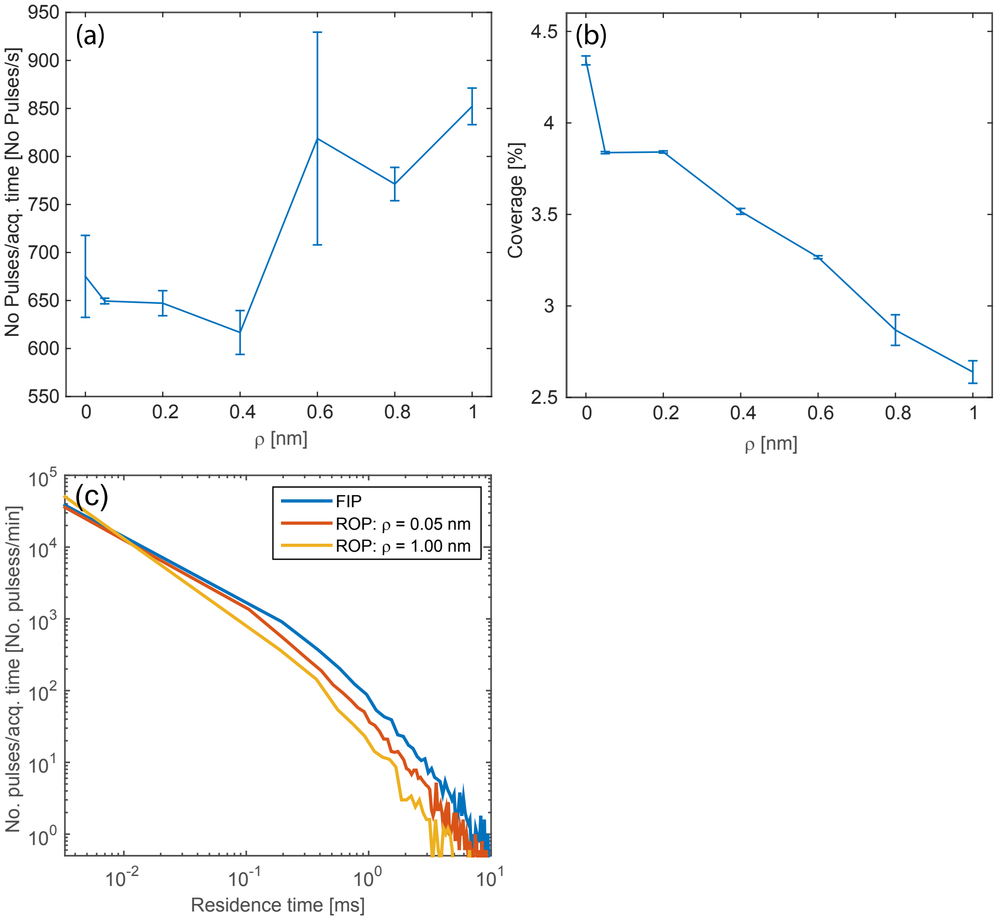

Figure 7.24: Comparison of FIP and ROP acquisitions on mobile phase for different dithering amplitudes ρ_{dither}. $f_{dither} = 7.31$ kHz for ROP acquisitions. (a) Number of pulses, (b) estimated coverages, and (c) RTDs of pulses. 1 V, 50 pA, 0.01 % used for all acquisitions.

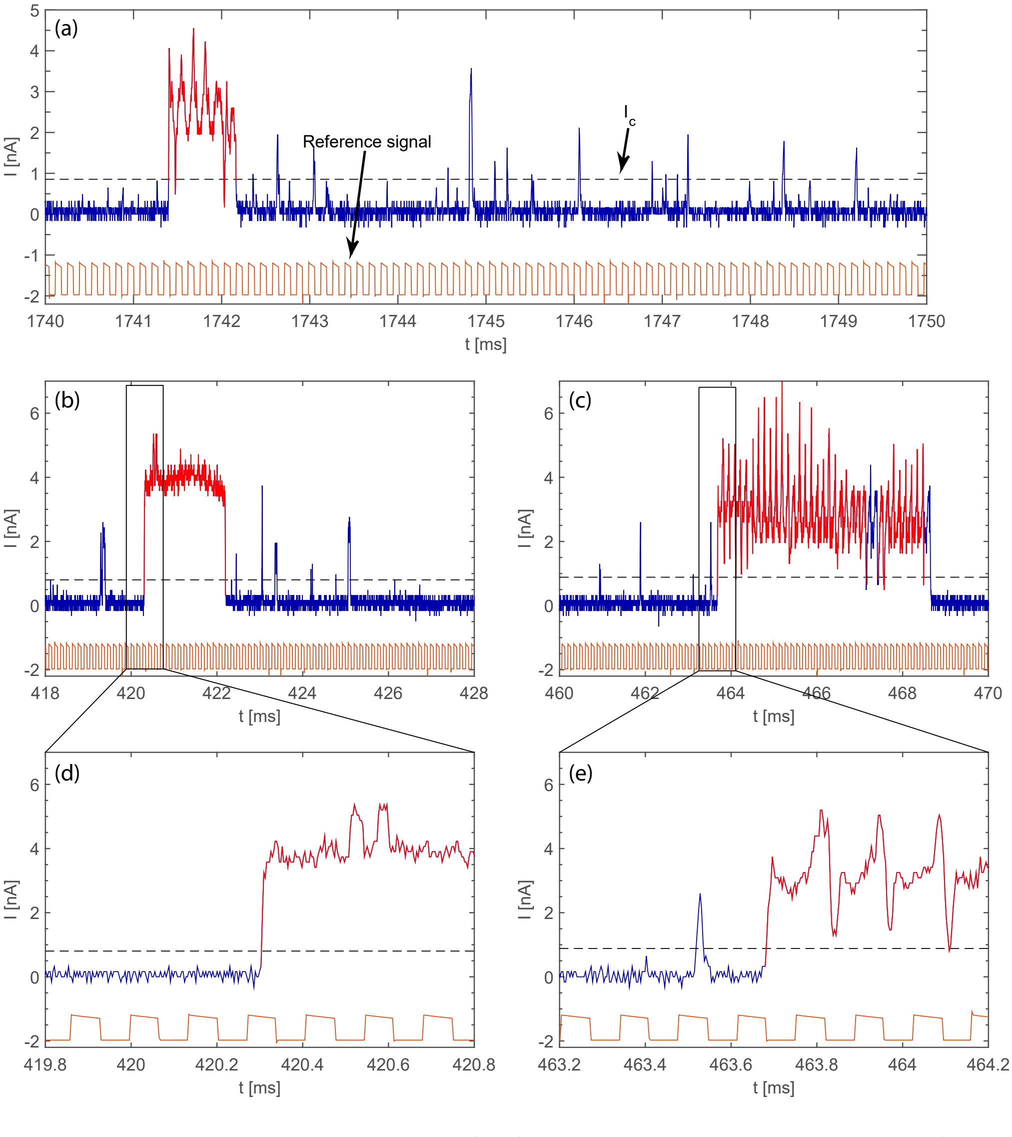

Figure 7.25: Exemplary time traces of ROP signals with corresponding reference signal used for dithering. (a) $\rho = 0.6$ nm, (b) $\rho = 0.05$ nm, $\rho = 1.0$ nm. (d)-(e) Zoom ins. 1 V, 50 pA, 0.01 %, $f_{dither} = 7.31$ kHz was used for all acquisitions.

fluctuations or other resonant signal generation.

Our collaboration partners performed preliminary experiments where the distribution of peaks within the single cluster is mapped along a circular trajectory with a frequency of $f_{dither} = 7.31$ kHz, for the entire acquired *I(t)* signal. Ideally if no diffusion tensor is expected, the distribution of peaks should be distributed randomly along the circular trajectory. Alternatively, if a diffusion tensor is expected, one would assume two peaks along the trajectory with a 180° phase difference between them. However, our collaborators findings suggests that the peaks within one cluster are located mostly at one position of the circle, as exemplified in Fig. 7.26 for one dithering amplitude and frequency. This behavior is unexpected as we would expect

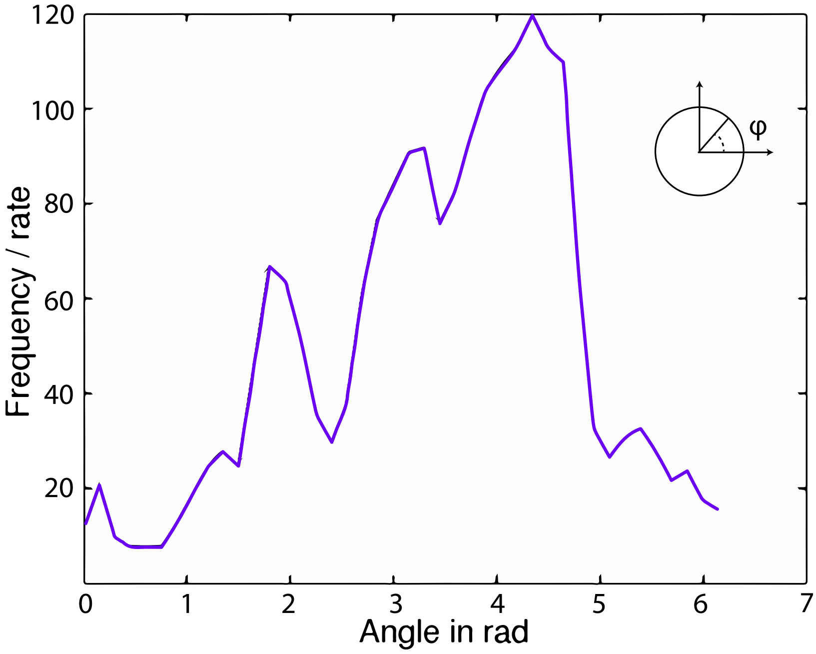

Figure 7.26: Distribution of signals along circular trajectory of $f_{dither} = 7.31$ kHz, $\rho_{dither} = 0.6$ nm . Analysis performed by our collaborators at Osnabrück.

PTCDA to diffuse anisotropically on the Ag(110) surface. Based on these findings the transition of a single molecule could not systematically be revealed. We tentatively explain this effect by an inclination of the dithering circle relative to the sample surface due to sample tilt or non-linear piezo scanner behavior, combined with a stronger trapping of molecules at closer tip-sample distances. Consequently, it should be tested if tilting the plane of the dither trajectory has an influence on this observation. Implementing a tilt of the dither plane within the atom-tracking system is planned for future work.

7.4 Conclusion and Outlook

In order to reliably measure the diffusion properties of surface adsorbates using an STM tip, we have successfully implemented a procedure for acquiring *I(t)* signals using a fixed probe. Especially, we introduce a protocol of successive measurements on, off and on PTCDA islands to establish stable tip and system conditions. We find that diffusion of molecules can only be observed and acquired using FIP protocols when specific tip imaging states are available. Our results indicate, when the tip is in the reliable *imaging* state, the influence of the state of the tip (specific apex termination which is experimentally unknown) on the diffusion experiments is uncertain, as the number of peaks critically depends on Z_{offset}. Consequently, across differnt tip states, this should be chosen similarly.

The reliability of using *I(t)* signal acquisitions (using suitable tip state) for measuring adsorbate diffusion properties was examined by systematically changing several STM system parameters. Our results show that the fast feedback response of the distance loop inadvertently prevents detection of long duration pulses, as the tip retracts too quickly. The distance feedback response therefore needs to be carefully selected to ensure accurate detection of the diffusing molecules. The most reliable data are achieved in constant-height mode as they do not (in principle) involve changes in the tip-sample distance for different parameters. Increasing the current setpoint lead to a systematic increase in the residence time of the pulses, leading us to surmise that higher current setpoints lead to larger detection areas for measuring diffusing molecules.

From constant-height measurements, the increase in the duration of pulses at higher applied bias (for similar tip-sample distances), indicate that an attractive electric field dependent tip-molecule interaction can be present, causing the mobile PTCDA molecules to be (temporarily) trapped in the detection area of the tip. Conversely, residence time distributions of pulses remain unaffected when performing FIP measurements using constant current mode (constant electric field), suggesting that the the dominant influence on affecting dadsorbate motion is dependent on the applied bias. These findings coincide with theoretical calculations, indicating that the electric field dependence of the STM tip plays the dominant role.

In order to extend the measurement to anisotropic diffusion, where the diffusion tensor of surface adsorbates is determined from $I(t)$ signal acquisitions using an STM tip, the measurement method was modified by using an atom tracking system to oscillate the tip on circular trajectories at high dithering frequencies. We found resonances in the setup for certain dithering frequencies. Dithering frequencies should therefore be selected with care. Using the same on-off-on island experimental protocol as FIP acquisitions, ROP acquisitions were performed for different dithering radii. We observe clusters of peaks for larger dithering amplitudes, coinciding with theoretical predictions, thus proving the presence of mobile species for tip imaging state A. Preliminary analysis, however, suggests the presence of molecules mostly at one circle position, therefore trajectory needs to be tilted (outlook, not available for this thesis).

Currently our collaborators at Osnabrück University are in the process of estimating diffusion coefficients from both our FIP and ROP acquisitions. From our FIP acquisitions, diffusion coefficients are expected to be derived for our presented findings (loop gains, bias voltage, current setpoint, and tip state influence) throughout their parameter space. Hopefully, this should provide insight into the reliability of using these signal acquisitions for deriving adsorption kinetics. Assuming or FIP acquisitions provide reliable diffusion estimates, diffusion tensors will be derived based on our ROP acquisitions.

Chapter 8

Toward automated characterization of tip apex geometry

In order to perform atomic manipulations using scanning probes, one often desires to mold the tip apex into a specific condition. The precision of creating hydrogen resist using nanolithography, for instance, has shown to be crucially dependent on the sharpness of the tip apex [197]. To date, modification of scanning probe apexes involve a combination of initial macroscopic modifications of the tip, such as annealing, sputtering, or macroscopic field emission (explained in section 3.2), followed by controlled manipulations of the tip apex on sample surfaces (e.g. voltage pulses or controlled crashing into surfaces). Both types of manipulations (macroscopic and in-situ on surfaces) are often time-consuming and based on intuitive experience by the users. Ideally, we desire to automate the manipulation process of molding the tip apex into the desire state for a given purpose. Controlling the tip apex into desired state(s) for manipulations, could potentially lead to full automation of the manipulation process. One key aspect of this involves controlling the tip geometry. In order to control the tip geometry on-the-fly in-situ characterization of the tip apex geometry becomes necessary.

In this chapter we will present our result on experimentally determining the tip geometry in-situ on metal surfaces using characterization techniques based on field emission (see section 3.3.2) from the scanning probes. As explained in section 3.3.2, in the tunnel junction, metal surfaces having different geometries are expected to have different V-z characteristics (assuming constant current mode). We have implemented experimental protocols for using V-z characteristics to estimate tip apex geometries and implemented them to determine the tip geometry for various STM tips and tip conditions. The characterization technique is compared with other tip apex characterization techniques to establish the reliability of the technique. Our results can then be used to automate the tip characterization process at the tunnel junction, which we are considering implementing.

8.1 In-situ tip apex characterization

This section covers our results on characterizing the tip apex geometry in-situ at the tunnel junction on metal surfaces.

8.1.1 Tip apex characterization: methods

As a first step toward automated analysis of the tip apex geometry using STM at the tunnel junction, a procedure for acquiring and processing experimental data was implemented. Fig. 8.1 shows a flow diagram of our experimental data acquisition and post-processing procedure used for many of our experiments.

Characterization of the tip apex geometry is derived by studying V-z characteristics using *z(V)* spectroscopic measurements on the surface as described in section 3.3.2. For each experimental acquisition, the tip is placed at a desired location and *I(z)* spectroscopic measurements are subsequently performed (feedback off). To investigating the tip apex geometry, the initial scanning parameters were often altered to desired values (V_p,I_p), followed by *z(V)* spectroscopic measurements in constant current mode. The spectroscopy parameters were subsequently changed back to initial scanning

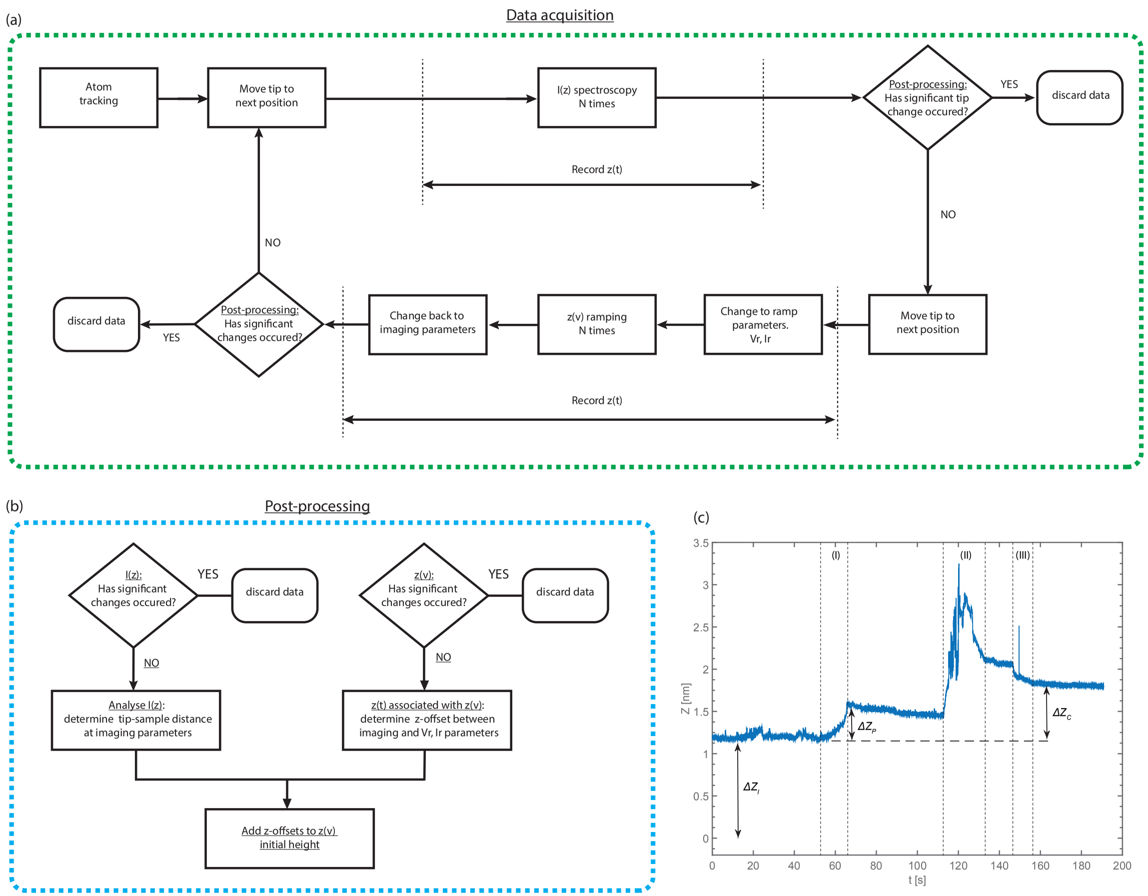

Figure 8.1: Protocol for obtaining and analyzing experimental data. (a) Flow diagram showing implementation of experimental protocol. The tip is initially positioned using specific scanning parameters (V_s, I_s), and I(z) spectroscopic measurements are subsequently performed (feedback off). The tip scanning parameters are subsequently altered to specified *z(V)* spectroscopic conditions. *z(V)* spectroscopic measurements are subsequently performed in constant current mode, followed by a change from spectroscopic conditions to scanning conditions. The absolute tip height is monitored continuously by recording the feedback signal, *Z(t)*, while performing spectroscopic measurements. (b) Post-processing protocol of experimental data. Provided no significant tip changes are observed, the the tip-sample gap distance for *z(V)* spectroscopic conditions are is ascertained by (i) first extrapolating the tip-sample gap distance (ΔZ_i in (c)) from *I(z)* measurements and (ii) by adding the height difference between imaging and spectroscopic conditions (ΔZ_p in (c)) to the imaging conditions. (c) The recorded height position, Z(t), is used to add the height differences between imaging and spectroscopic conditions.

parameters. Atom tracking and feed-forward techniques were routinely performed in order to eliminated drift, in particular vertical drift. For each *z(V)* spectroscopic acquisition, the relative tip height, *Z(t)*, was recorded simultaneously with each *I(z)* and *z(V)* spectroscopic acquisitions. Post-processing of the data (see flow diagram in Fig. 8.1(b)) involved, (i) ascertaining and excluding significant tip change(s) for each spectroscopic acquisition (both *I(z)* and *z(V))* and, (ii) ascertaining and correcting the absolute tip-sample gap distance or each *z(V)* spectroscopic measurement.

For each spectroscopic measurement, two criteria were used as a discernment of possible tip changes during acquisitions. The first criteria involves using the relative tip height profile, *Z(t)*, to ascertain if a change ΔZ_c (Fig. 8.1(c)) in the tip-sample gap occurred during an acquisition. A large change in the relative tip-sample gap distance could signify that the tip has undergone a structural change due to interaction with the surface. As a result, *I(z)* and *z(V)* spectroscopic measurements having significant changes in the relative height were omitted from further analysis. The second criteria involves examining the *z(V)* profiles for unwanted behavior. *z(V)* profiles in constant current mode are expected to follow a trajectory correlating with the geometry of the tip. Spectroscopic measurement showing significant abrupt changes in the tip sample distances, were therefore suspected to deviate from this behavior and were thus omitted from further analysis.

For each *z(V)* spectroscopic measurement, the absolute tip sample gap distance $d = \Delta Z_i + \Delta Z_p$, (see Fig. 8.1(c)) was obtained during post-processing by first extrapolating the tip-sample gap distance, ΔZ_i, from *I(z)* measurements using specific scanning parameters. This gap distance is then added to the height difference between imaging spectroscopic parameters, ΔZ_p, to obtain the absolute tip-sample gap distance for each *z(V)* spectroscopic measurement.

8.1.2 Tip apex characterization: implementation

The tip apex geometry was investigated at for various polycrystalline STM (W) tips and for various macroscopic tip alterations (i.e. annealing and macroscopic blunting). All measurements were performed at the tunnel junction on Au-on-mica(111) metal surfaces. The measurements were performed by monitoring the tip-sample distance during a voltage ramp at constant current by measuring the feedback signal applied to the z-piezo drive. A similar feedback response for the z-piezo drive was used for all tips and tip conditions (loop gain = 1 %). The results are plotted in Fig. 8.2 for three different tips undergoing macroscopic structural changes. From Eq. 3.4, the electric field emanating from the tip is highly dependent on the radius of the tip. As a result, sharper tips produce a higher field for a given bias and tip-sample separation. Sharper tips thus require a larger gap to achieve the same emission current because of the higher field associated with high curvature [198]. As observed Fig. 8.2, this effect becomes more pronounced at high bias voltages, leading to a more non-linear V-z characteristics for sharp tips. Field emission measurements using different emission currents shows little variation in the V-z characteristics for a given tip (not shown).

We observe quite different V-z characteristics for various tips and tip conditions. The blunt tip (tip 1) show little change in its V-z characteristics even after performing two consecutive 50 nm crashes into the surface. The V-z characteristic for tip 7 does not change appreciably after its second macroscopic annealing, but does change considerably after its third anneal, suggesting a blunting of the tip. These measurements coincide with measured emission currents, showing high emission current for the first two consecutive annealing steps, followed by a substantial decrease in emission current during the third anneal, suggesting a blunting of the tip during the third anneal. Tip 8 shows a similar behavior. Initially, the newly degassed tip (tip 8) shows unpredictable behavior in its V-z characteristics. V-z characteristics for the first and second anneals suggests a sharpening of the tip apex. Following a macroscopic crash into the metal surface, the tip shows very small tip-sample separations, even for high bias, suggesting a blunt tip. These findings suggest that field emission measurements performed at the metal-vacuum-metal junction are sensitive to the macroscopic geometry of the tip, but not necessarily on exact nature of the tip apex terminations. This demonstrates that the V-z measurements can be used as a diagnostic

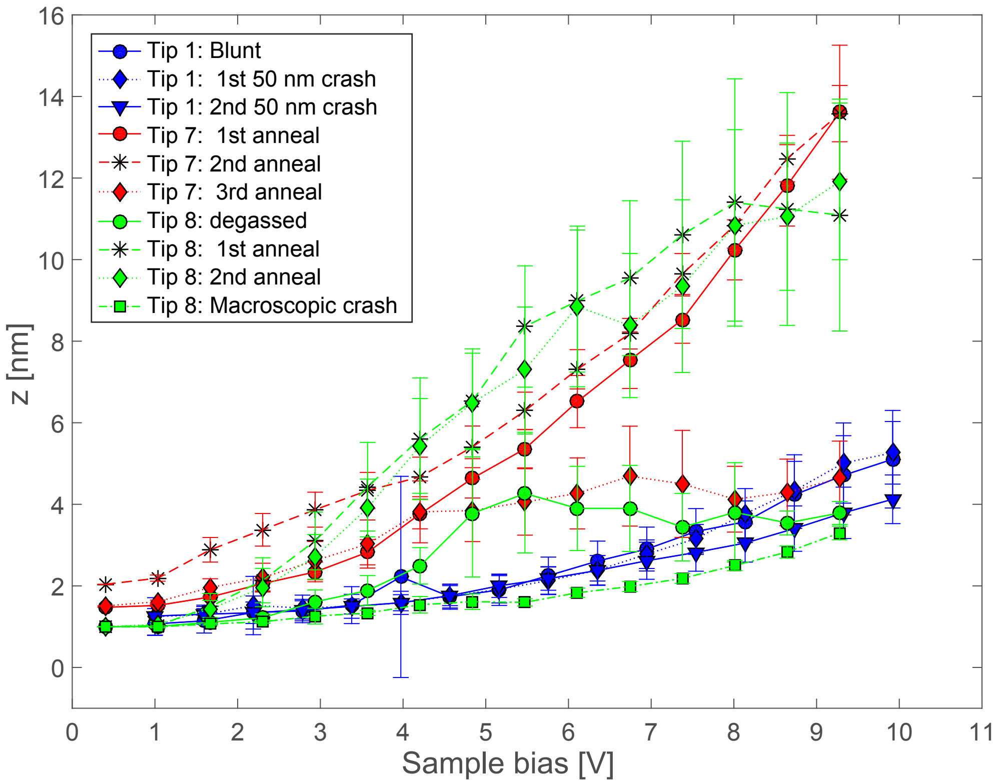

Figure 8.2: In-situ tip geometry characterization at tunnel junction. Plotted are V-z characteristics for several STM tips following sequential annealing and macroscopic blunting on Au-on-mica(111) surfaces. Initial parameters used for *z(V)* ramping: 1 V, 2-50 pA for STM tip 1, 0.4 V, 100 pA for STM tips 7 and 8, respectively, corresponding to z = 0 in Fig. **??**.

tool to estimate the apex of the tip when for various tip geometries. We should note, that our field emission measurements varied considerably from measurement to measurement, and most of our data were averaged over a large population size.

Field emission studies were similarly performed at the tunnel junction for both positive and negative sample tip biases, respectively. For negative *sample* biases, field emission from the metal surface to the tip is expected. The results are shown in Fig. 8.3 for six different tips. We observe an asymmetry in the *z(V)* between the positive and negative *z(V)* profiles for each tip, respectively.

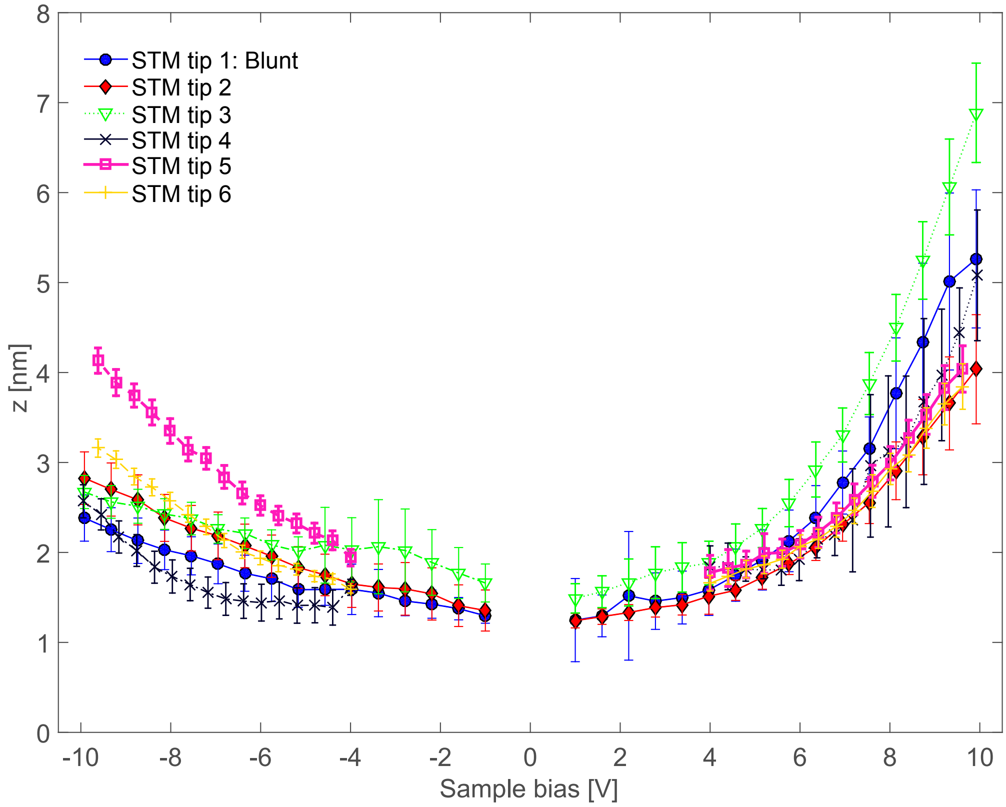

Figure 8.3: Field emission measurements at tunnel junction on Au-on-mica(111) surfaces at positive and negative sample bias for various STM tips. Initial z(V) ramping parameters for positive (negative) sample biases: 1 V, 2-50 pA (-1 V, 2-50 pA) for STM tip 1, 1 V, 1 nA (-1 V, 1 nA), for STM tip 2, 1 V, 2 pA (-1 V,2 pA) for tip 3, 4 V, 100 pA (-4 V, 100 pA) for STM tip 4, 5 and 6, respectively.

8.2 Validation of characterization technique

The reliability of using field emission at the tunnel junction was investigated by examining the tip geometry using two field emission methods (at the tunnel junction and mesoscopically) for various tips and tip conditions. Field emission at the mesoscopic scale was measured using the experimental setup illustrated in Fig. 3.2(b). Ideally one could perform field emission measurements using well-known tip geometries and use them as references. However, we believe that for the technique to ultimately to be utilized as an automation tool for characterizing the tip geometry, our field emission acquisitions should be applied to randomized tip structures. What is important, is that the different techniques should give similar results when applied to the same tips and tip states. Mesoscopic tip apex characterization was performed for various tips and following macroscopic tip alterations, such as annealing. The tips were subsequently transported to the tunnel junction to compare the different characterization techniques. The results are shown in Fig. 8.4 for 3 different tips.

The field emission current at the mesocopic scale was measured by applying a voltage source to the tip and performing a voltage sweep. Voltage sweeps were performed at the range of 0 - 500 V. For each tip, voltage sweeps were performed multiple until the emission current became stable. For mesoscopic field emission performed prior to TJ, the last voltage sweep is shown, and similarly, for mesoscopic field emissison performed after the TJ, the first voltage sweep after field emission on the surface is shown for all tips. For mesoscopic field emission, the radii of the tip was estimated from the Fowler-Nordheim (FN) plots shown in Fig. 8.4(b). For minimum radius estimation, the radius was experimentally determined from the slope of the graph where we have assumed the following values: $\phi = 4.5$, $\alpha = 1$ and $k = 5$. For the image-corrected FN derivation, the same initial values were used to estimate the lower bound of the radius, which was then used to obtain the image correction factor (and thus corrected radius) using the iteration method described in [49]. The estimated radii shown in table 8.1 was obtained by averaging over all relevant *z(V)* profiles followed by a fitting to Eq. 3.8. *z(V)* profiles showing severe tip instabilities or tip alterations were omitted. For each of the 3 tips presented, an arbitrary height of 1.2 nm was added to the tip position. Their standard error was obtained fits to Eq. 3.8 from individual *z(V)* profiles that did not fail (i.e. where the range of estimated radii were $\leq$ 1000 nm).

We observe relatively small changes in the estimated radii for for tips 9 and 10 following macroscopic annealing but a significant blunting of tip 11. By comparing mesoscopic field emissions performed before and after performing tip characterization at the TJ show no change in estimated radii, indicating that performing field emission at the TJ does not significantly affect the tip attributes. As tip instabilities and tip apex changes are expected

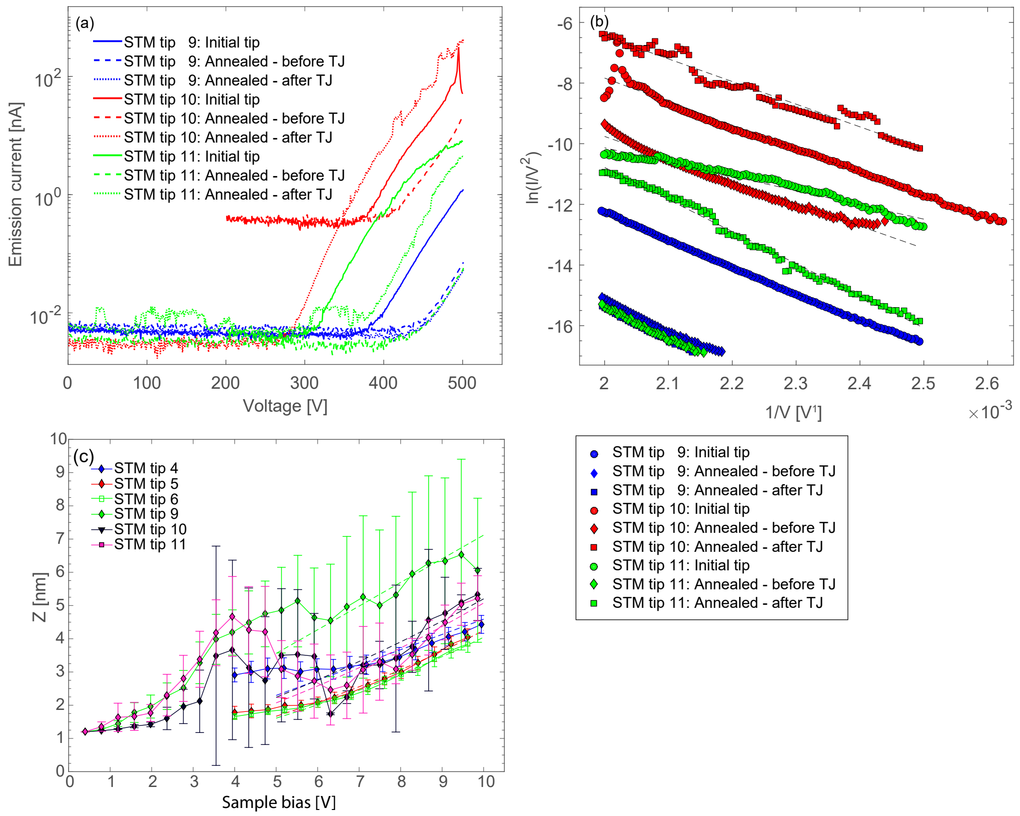

Table 8.1:

		Fowler-Nordheim (FN)			Tunnel junction (TJ)		
Tip	Tip condition	R (nm)	Iterated R (nm)	α value	R (nm)	[R_{min} - R_{max}] (nm)	E (V/nm)
9	Initial tip	27.1	20.5	0.759			
9	Annealed - before TJ	30.0	22.9	0.764			
9					> 1000±2.5	[1.2 - 25.4]	1.4
9	Annealed - after TJ	32.1	24.7	0.770			
10	Initial tip	24.0	17.9	0.747			
10	Annealed - before TJ	22.8	16.7	0.736			
10					16	[4.5 - 4.5]	2.5
10	Annealed - after TJ	23.0	17.0	0.739			
11	Initial	14.5	9.8	0.674			
11	Annealed - before TJ	31.2	24.0	0.767			
11					11.2±1.3	[2.2 - 10.6]	2.9
11	Annealed - after TJ	32.6	25.4	0.780			

Figure 8.4: Comparison of tip geometry using field emission (mesoscopic) and field emission at tunnel junction (TJ). (a) Mesoscopic field emission current vs. voltage for three tips. (b) Fowler-Nordheim (FN) plots for same tips as shown in (a). Field emission currents below 10 pA (0.5 nA for STM tip 10, initial and before TJ) were excluded from fitting. (c) Field emission at TJ on Au-on-mica(111) metal surface of same tips as shown in (a). Tips 4, 5 and 6, showed no macroscopic field emission when applying a voltage up to 500 V. Table 8.1: comparison of estimated radii using FN and image corrected FN performed at mesoscopic scale with radii obtained using Eq. 3.8 performed at TJ. An arbitrary height of 1.2 nm was added to each tip. Initial parameters used for *z(V)* ramping: 0.4 V, 100 pA for STM tip 9 - 11, respectively.

to occur at the TJ, our results indicate our tip characterization method at the mesoscopic scale is relatively insensitive to nanoscopic/atomic changes occurring at the apex. At the TJ, estimated radii show significant deviations both when comparing individual *z(V)* profiles for a respective tip and with expected radii obtained from mesoscopic field emission. Only STM tip 10 show comparable radii when averaging over multiple samples, while deviating significantly for individual measurements. The significant variation in estimated radii between individual profiles and the observation of an abnormally high radii occurring following some fittings (e.g. tip 9), suggests several limitations of Eq. 3.8. Often fitting variables to Eq. 3.8 result in asymptotic values when the denominator gets close to zero. Also, Eq. 3.8 assumes that field emission intersects at $z = 0$ for $V = 0$. As a result, knowledge of the absolute tip-sample height is required for accurate fitting of the tip radius. For more reliable automated characterization of tip apexes for at the TJ, we suggest applying a more suitable method relying on two criteria: the non-linearity of the tip-sample displacement, and the magnitude of the tip-sample displacement as a function of the bias voltage.

Chapter 9

Conclusions

Scanning probe microscopes offer the opportunity to investigate and manipulate matter at the atomic and molecular scale. While scanning tunneling microscopes can be utilized on conducting surfaces, atomic force microscope can, in principle, can be carried on any surface or material. The principle nature of the scanning probes is that they rely on the interactions between tip and surface of interest. When operated on the atomic scale, these interactions take place between the individual atom at the tip apex and the surface. Thus when utilizing SPM, it becomes critical to understand or control the specific nature of the tip apex.

Throughout this thesis, the effects of the tip structure in imaging and manipulating surfaces have been examined. As the overall theme of this thesis is focused on the role the tip plays on when interacting with the surface, we have performed our experiments on different types of surfaces (semiconductor and metal surfaces) and been applied to investigate different types of surface phenomena. We have found that the specific nature of the tip apex and the role it plays during an experiment, is essential to understand surface phenomena and tip-sample interactions. Specifically, we find that in order to investigate a specific surface phenomena, the tip apex needs needs to be carefully considered. Based on our result, we outline strategies for obtaining the "right" tip state for the specific purpose.

Chapter 5 the role of the tip is examined when imaging the surface using

STM. We find that observed surface geometry is a convolution of the probe and surface states (which we generally refer to as tip imaging states) and is therefore critically dependent on the electronic properties of both the probe and the surface. We propose using AFM/STM investigations combined with DFT simulations to examine which tip apex geometries give rise to these surface features.

We then moved on to examine the role of the probe state when performing atomic scale manipulations in the next chapter. For H:Si(100)-(2×1) surfaces the tip imaging states can mainly be classified into broad groups: row, dimer, atomic, and asymmetric based on the appearance of the atomic scale features. The efficiency/precision of hydrogen desorptions is examined using these broad groups. We find that the tip imaging state plays a crucial role for performing hydrogen desorption on H:Si(100) surfaces.

In chapter 7, the role of the probe apex was examined in detail for a particular system; ascertaining if the diffusion of surface adsorbates can be reliably estimated, provided that the probe is in the right state. We find that detecting and estimating the kinetics of surface adsorbates is critically dependent on the nature of the tip apex. Through systematic examination the residence time distributions of PTCDA molecules, our results suggest that an attractive interaction between tip and adsorbate occurs and indicate a possible applied field dependence on the interaction. To measure anisotropic diffusion, our atom-tracking apparatus was modified to perform high-frequency movement around a circular trajectory. By analyzing adsorbate interaction with the circular detection area of the probe, the diffusion tensor of the adsorbate can, in principle, be extrapolated. Currently we, and our collaborators at Osnabrük University, are in the process of deriving diffusion coefficients and diffusion tensors based on acquired experimental FIP and ROP acquisitions, in the hope of providing a better understanding of the diffusion properties of surface adsorbates.

Finally, in chapter 8, characterization of the tip apex structure is examined, for the purpose of allowing reliable characterization of the of the tip apex on-the-fly while performing experiments on the surface. Our results suggest that field emission measurements at the tunnel junction are sensitive to changes in the nanoscopic/mesoscopic tip apex structure, thus opening up the possibility of fully automating the process of characterization the tip apex structure.

9.1 Outlook

Our ultimate goal, is to perform fully autonomous SPM operation for imaging, manipulation and examination on surfaces without human intervention. A crucial element for achieving this is being able to identify the underlying surface features of interest and determining which which features are physically relevant to a particular application. We have found that the state of the probe plays a crucial role in not only the way the surface is "viewed" but is also crucial for performing atomic scale manipulations and for investigation surface phenomena. As a result, for autonomous SPM to become possible, certain image processing, analytical techniques and decision making programs would need to be implemented. The autonomous program would need to include protocols for modifying the state of the probe and subsequently identify various surface features or surface properties. The desirable state could be characterized either by identifying specific spectroscopic properties or by identifying or searching for specific imaging features. In all likelihood, in order to investigate a specific surface phenomena, a certain understanding of the surface properties would need to be inputted.

Currently, we are considering combining our image analysis and tip modification software with our automated hydrogen atom extraction routine for conducting autonomous SPM manipulations on hydrogen passivated silicon surfaces. By combining this protocol with various decision making tools, this system could provide a test bed for establishing the the reliability of performing autonomous SPM manipulations. The technique could then, in theory, be extended to other surfaces and for other purposes for a more general-use SPM autonomous applications.

An important aspect for controlling and modifying the probe structure autonomously involves being able characterize the probe structure/shape on-the-fly. At the tunnel junction, the probe apex radius of curvature can, in principle, be derived from their relative tip-sample displacements using field emission measurements. One of the main limitations of using field emission for tip characterization is due to fluctuations in the emission profiles. These fluctuations are caused by instabilities of the tip, and have been attributed to sudden atomic changes on the tip surface [199]. As a result, reliable characterization of the probe structure becomes exceedingly difficult. Our results show that, although field emission profiles can vary considerably between individual measurements, field emission profiles are less sensitive to atomic scale changes in the tip structure, when averaging over an ensemble of measurements. For further tip characterization using field emission, we propose using strategies for stabilizing the tip structure, e.g. by conditioning the tip at the tunnel junction, coating the tip [197] or using materials with more stable field emission properties.

Appendices

Appendix A

Passivation and imaging: additional tip states

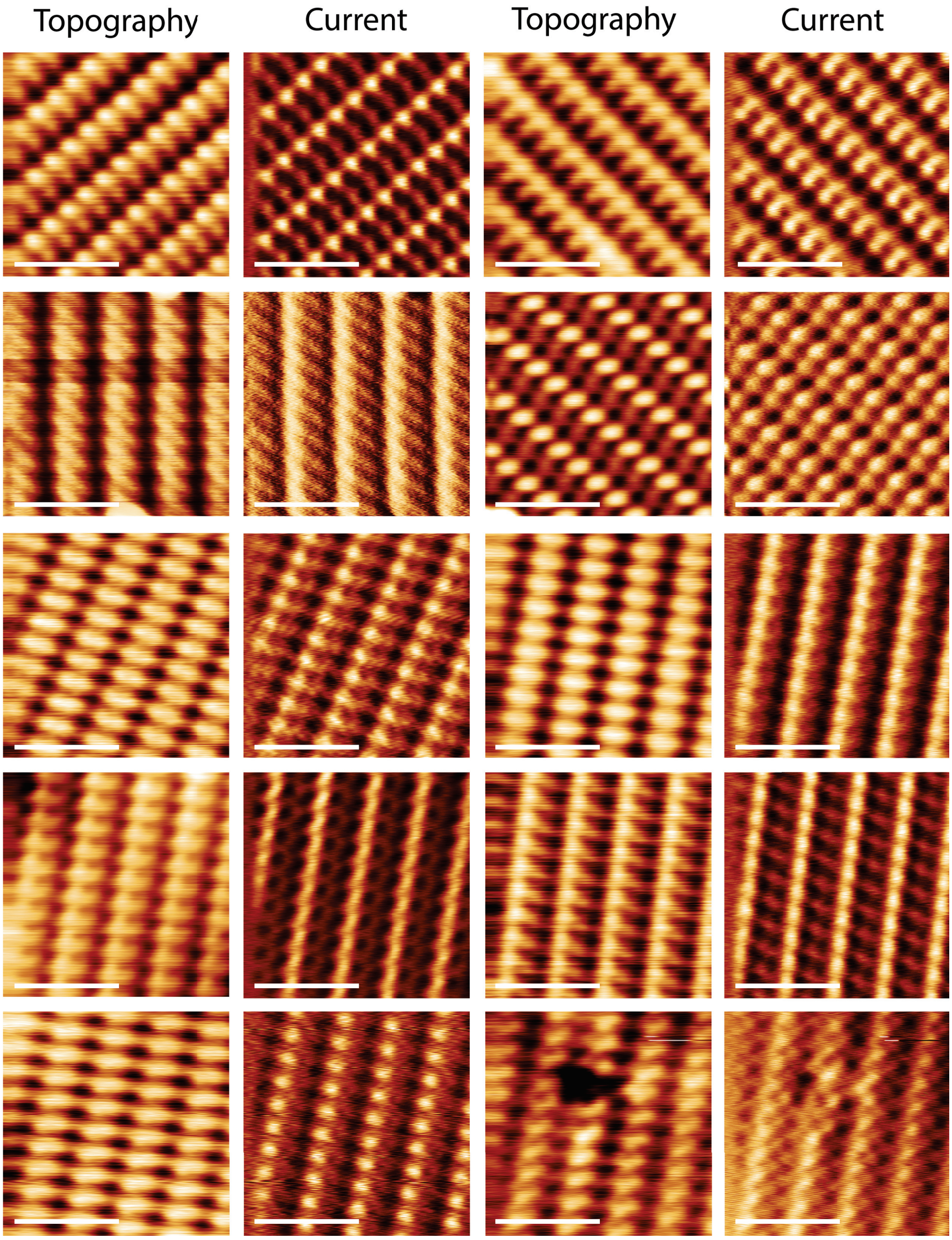

Figure A.1: Selection of STM images using same imaging conditions (1.6 V, 10 pA). By applying the same imaging conditions, the different surface contrasts should therefore represent different tip states.

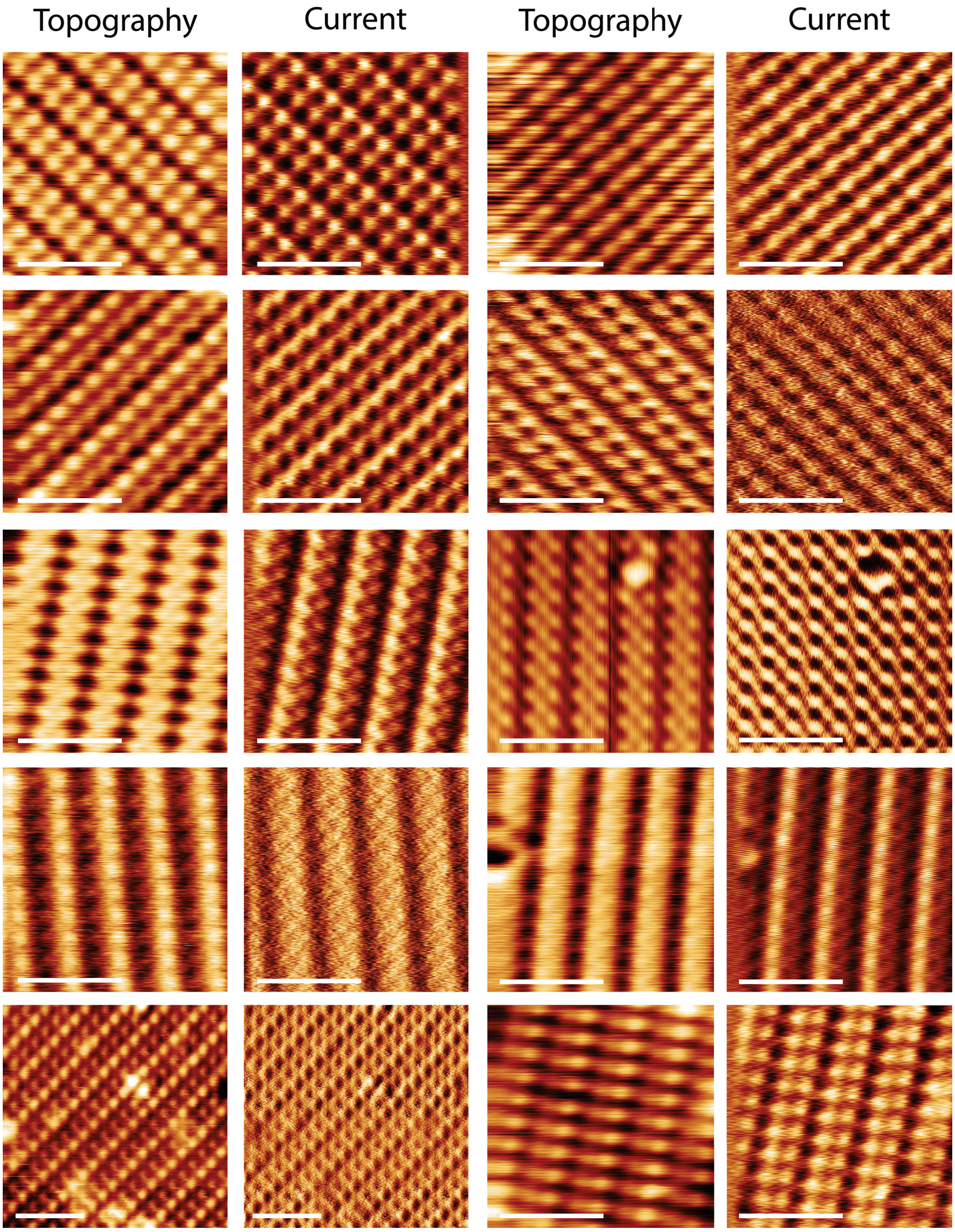

Figure A.2: Selection of STM images using same imaging conditions (1.6 V, 10 pA). By applying the same imaging conditions, the different surface contrasts should therefore represent different tip states.

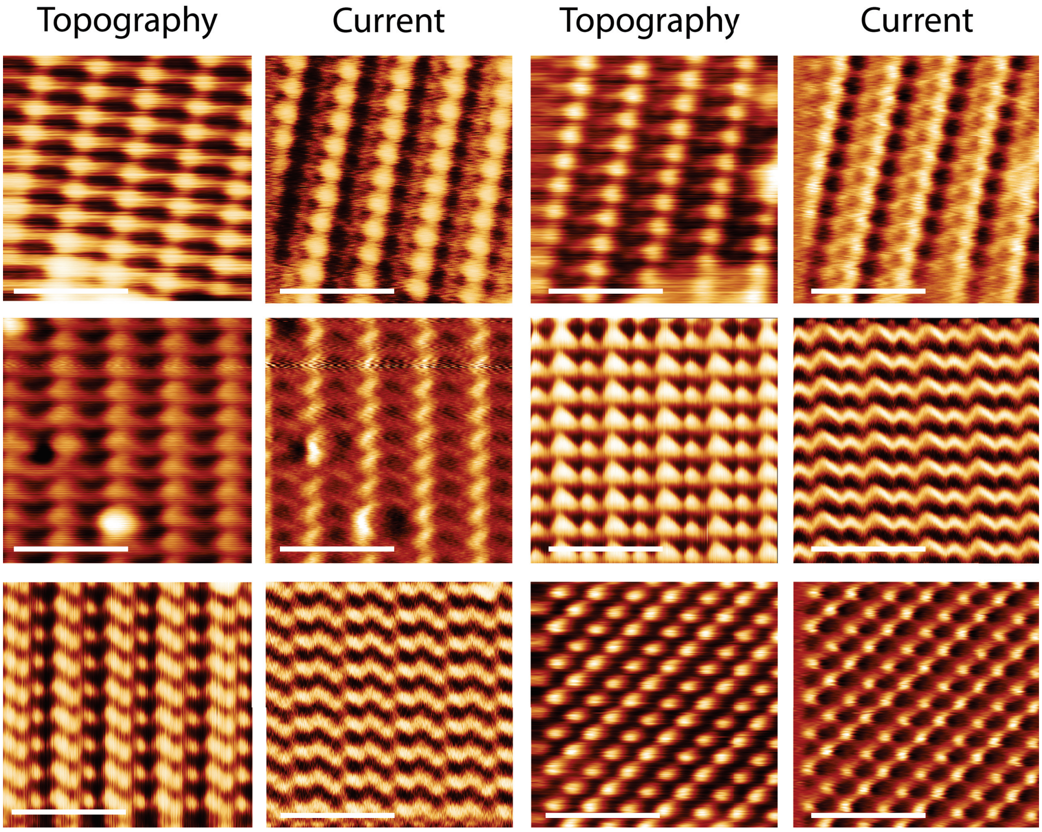

Figure A.3: Selection of STM images using same imaging conditions (1.6 V, 10 pA). By applying the same imaging conditions, the different surface contrasts should therefore represent different tip states.

Appendix B

Desorption efficiency: supplementary information

In this supplementary chapter we examine more closely possible additional influences and limitations to dangling bond generations. An important aspect in achieving as high as possible desorption yield with single-atom specificity is to understand the physical aspects of the desorption process and its limitations with respect to writing accuracy. We have therefore examined features such as: how often single atoms are generated as compared to multiple DB's (Appendix B.2), how often DB's are generated at desired coordinates (Appendix B.3), and examined their distribution on the surface (Appendix B.4).

B.1 Tip state changes during desorption

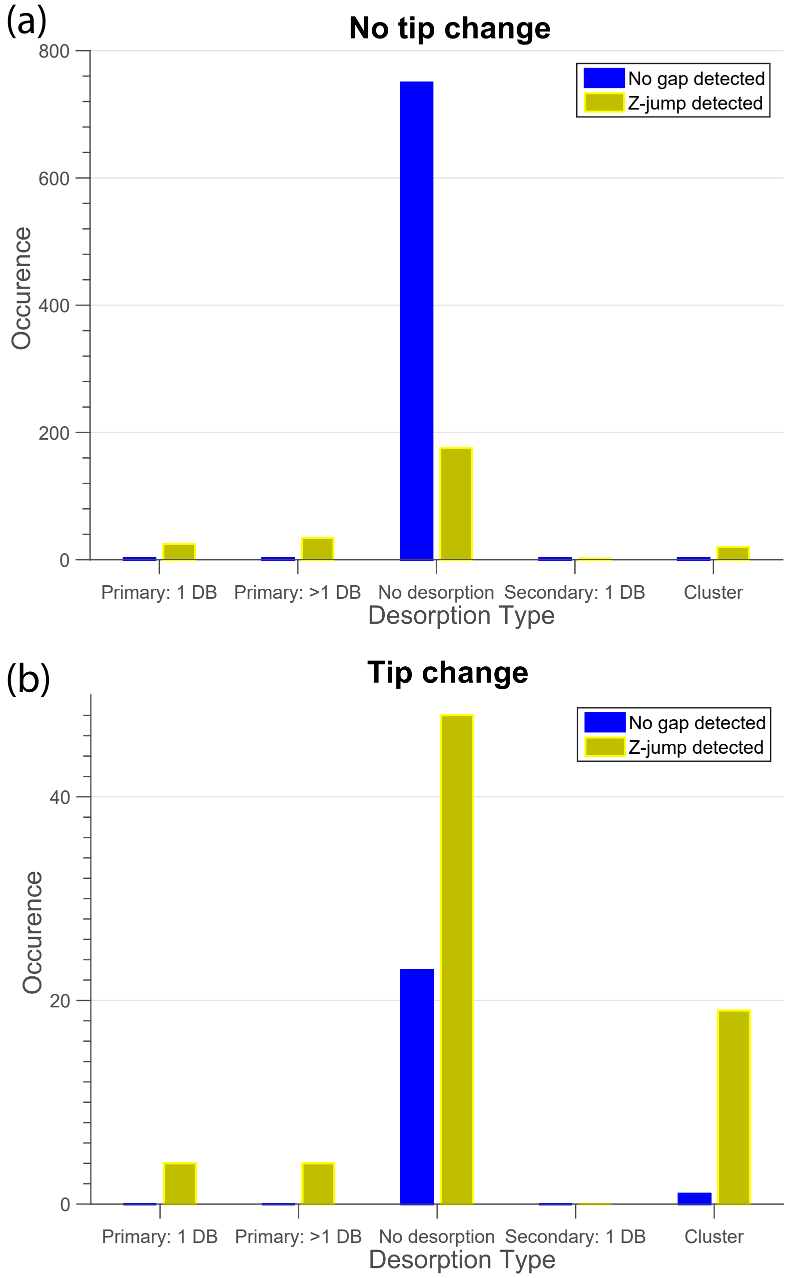

Figure B.1: Efficiency of desorption detection when (a) no tip change and (b) a tip change occurs.

B.2 Number DB's generated

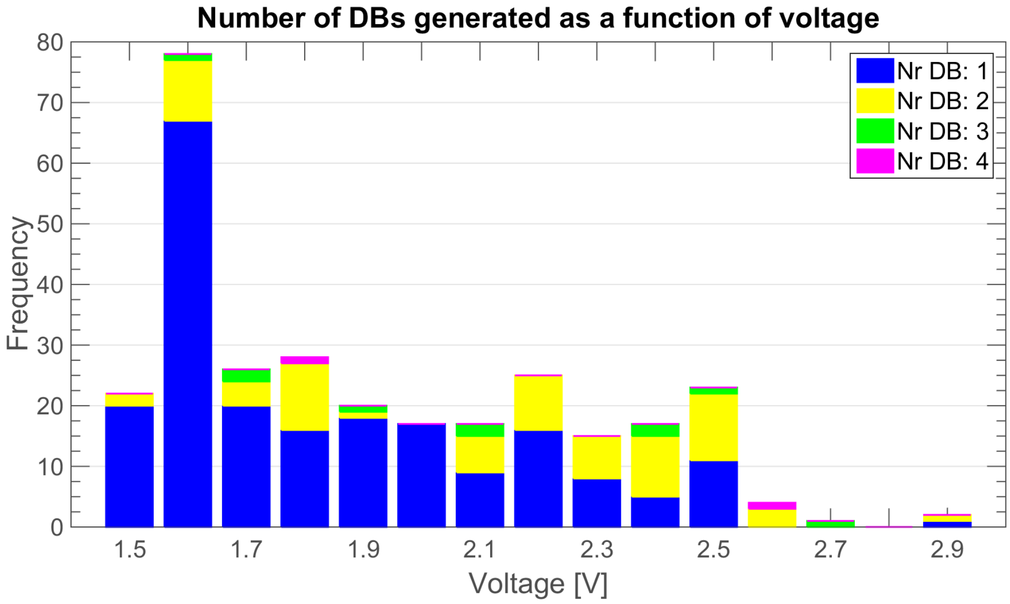

Figure B.2: Number of DB's generated as a function of voltage.

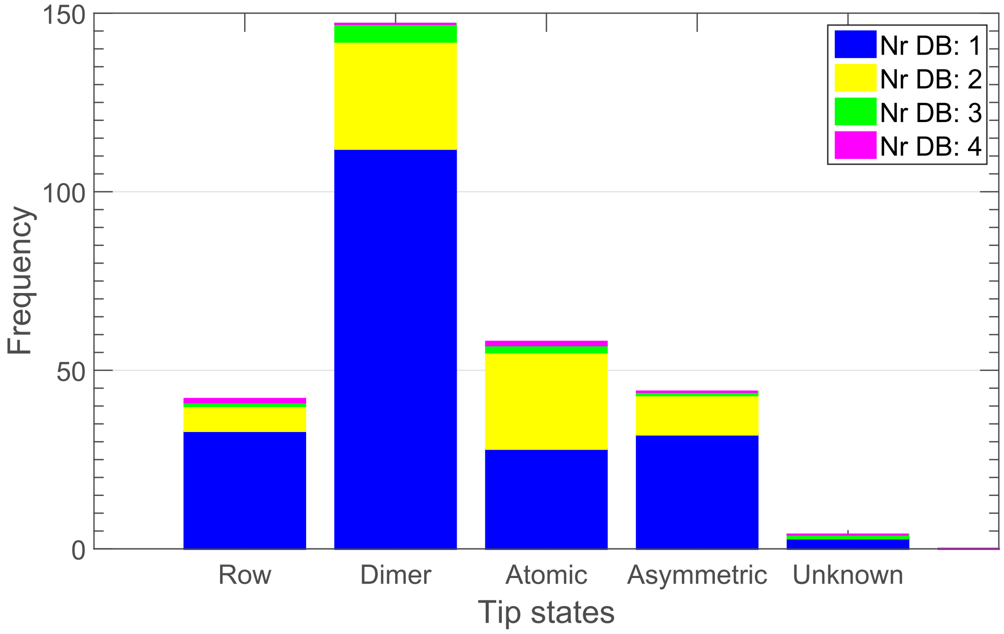

Figure B.3: Number of DBs generated for different tip states.

B.3 Primary vs. secondary desorptions

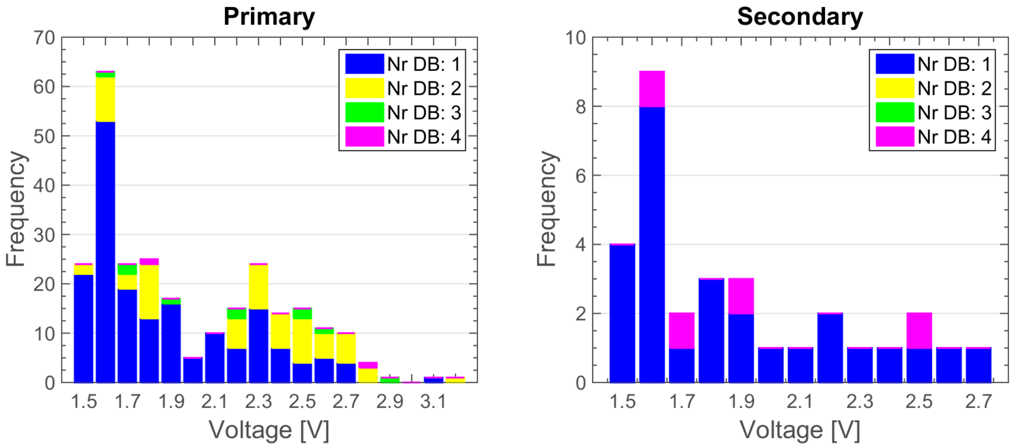

Figure B.4: comparison of primary vs secondary desorption site DB efficiency.

B.4 Intra/inter-dimer and inter-row generation

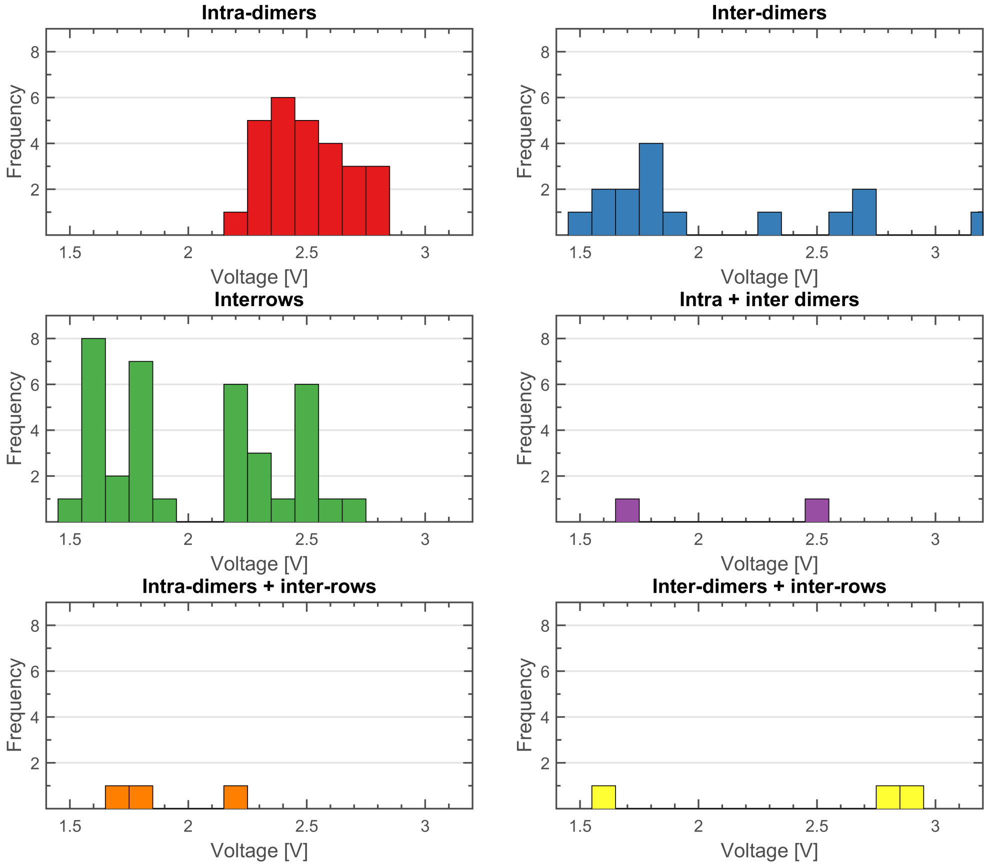

Figure B.5: Number of intra/inter-dimers and inter-rows generated as a function of voltage.

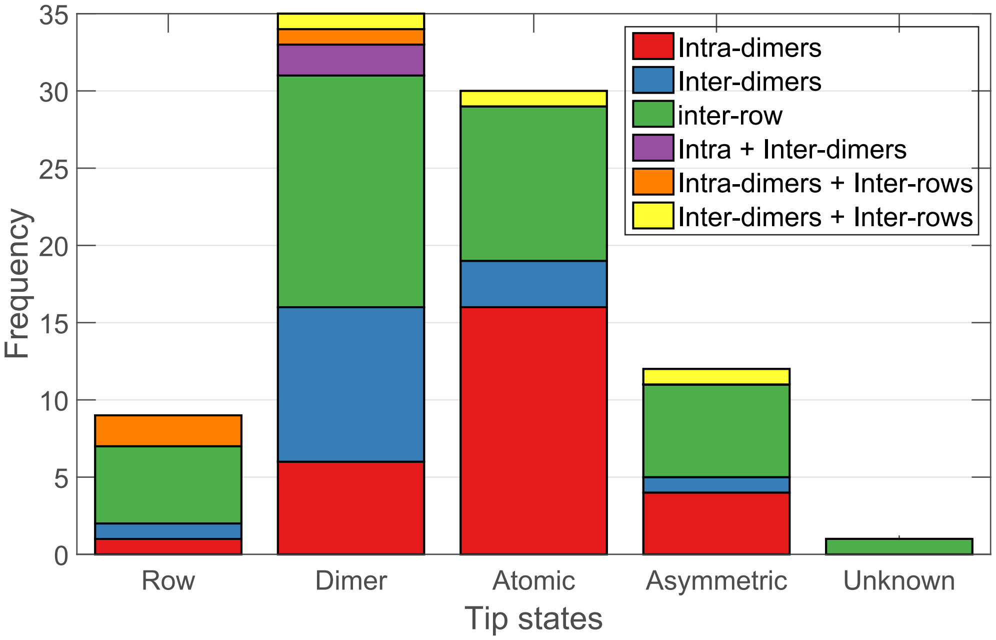

Figure B.6: Number of intra/inter dimers for different tip states.

Appendix C

Diffusion

C.1 Tip imaging states

In this section, FIP acquisitions for tip imaging states *A*, *B*, and *C* and over the clean (Ag) Ag(110) surface shown in Fig. 7.9 where the tip states (A.1, A.2 ...) are examined in more detail. The different tip state data are also acquired with different parameters.

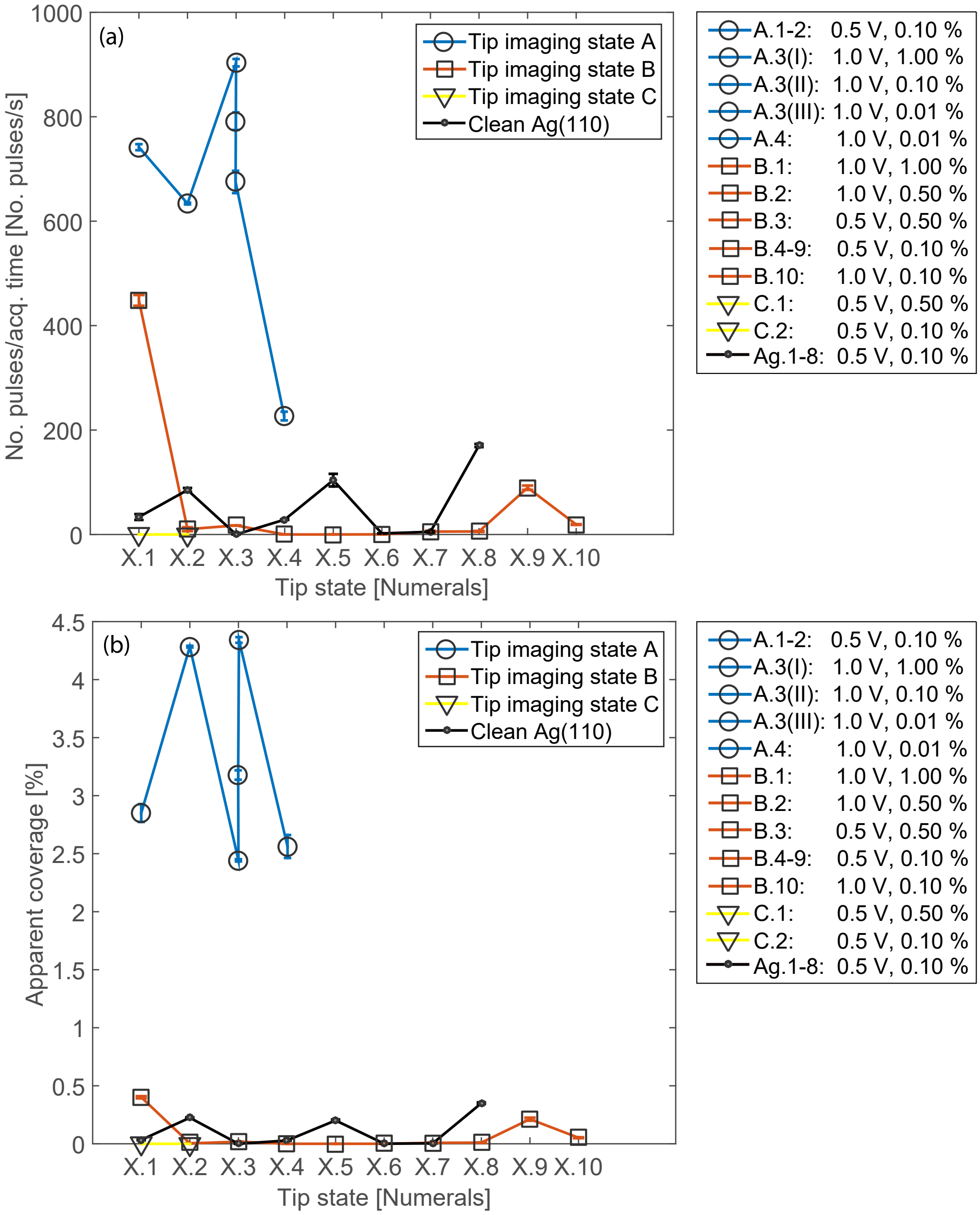

Figure C.1: Comparison of (a) number of pulses and (b) coverages for different tip states (X.1, X.2, ...) where $X = A, B, C$ and $X =$ Ag for the clean Ag(110) surface for each line shown in legend. Roman numerals represent parameter changes.

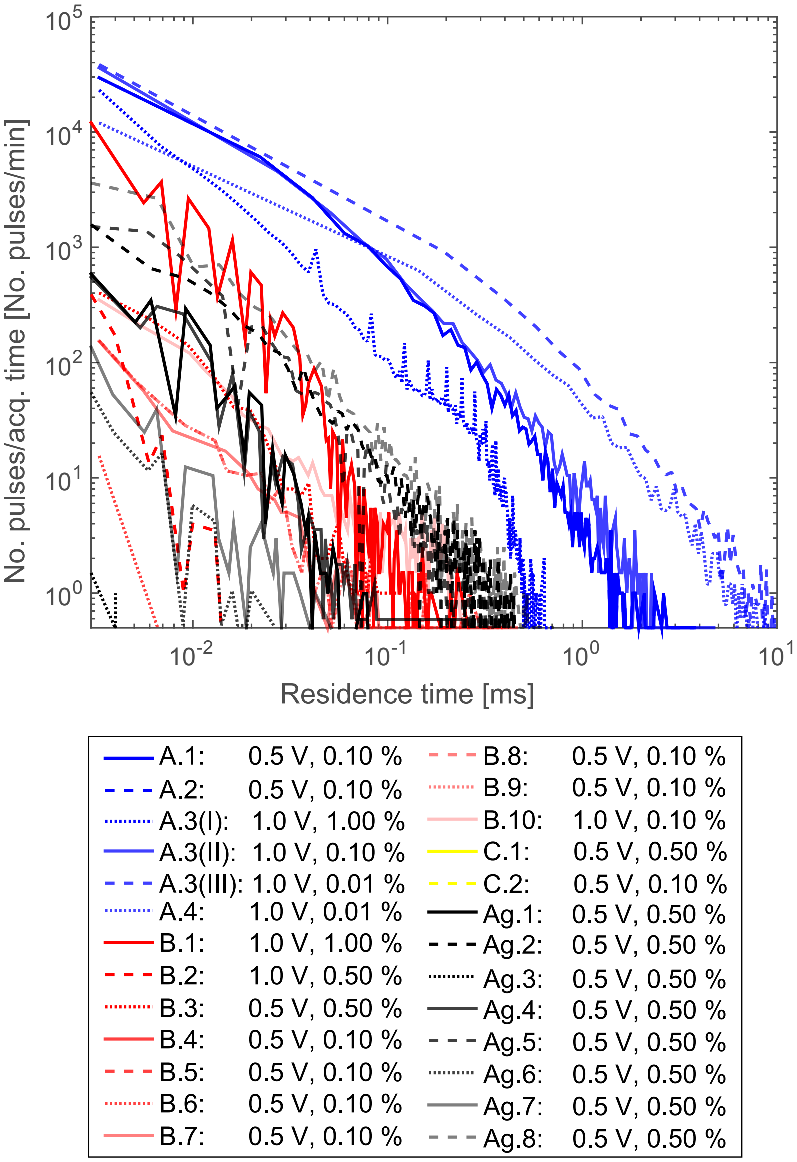

Figure C.2: RTDs for various tip states (A.1, A.2, ...) for tip imaging states *A*, *B*, and *C*, and for the clean Ag(110) surface. Roman numerals represent parameter changes.

C.2 Bias and current setpoint influence

In this section, the influence of changing the bias ((a)-(b) for every figure) and current setpoint ((c)-(d) for every figure) is examined for the bare Ag(110) surface (Fig. C.3), the mobile phase (Fig. C.4), and over the islands (Fig. C.4) of the PTCDA covered Ag(110) surface, respectively. It should be noted that these experiments were performed when we experienced mechanical instabilities of the Omicron VT system due to loose sample springs. As such, for FIP acquisitions at high current setpoints (1 nA), tip changes may be present as a result of mechanical instabilities.

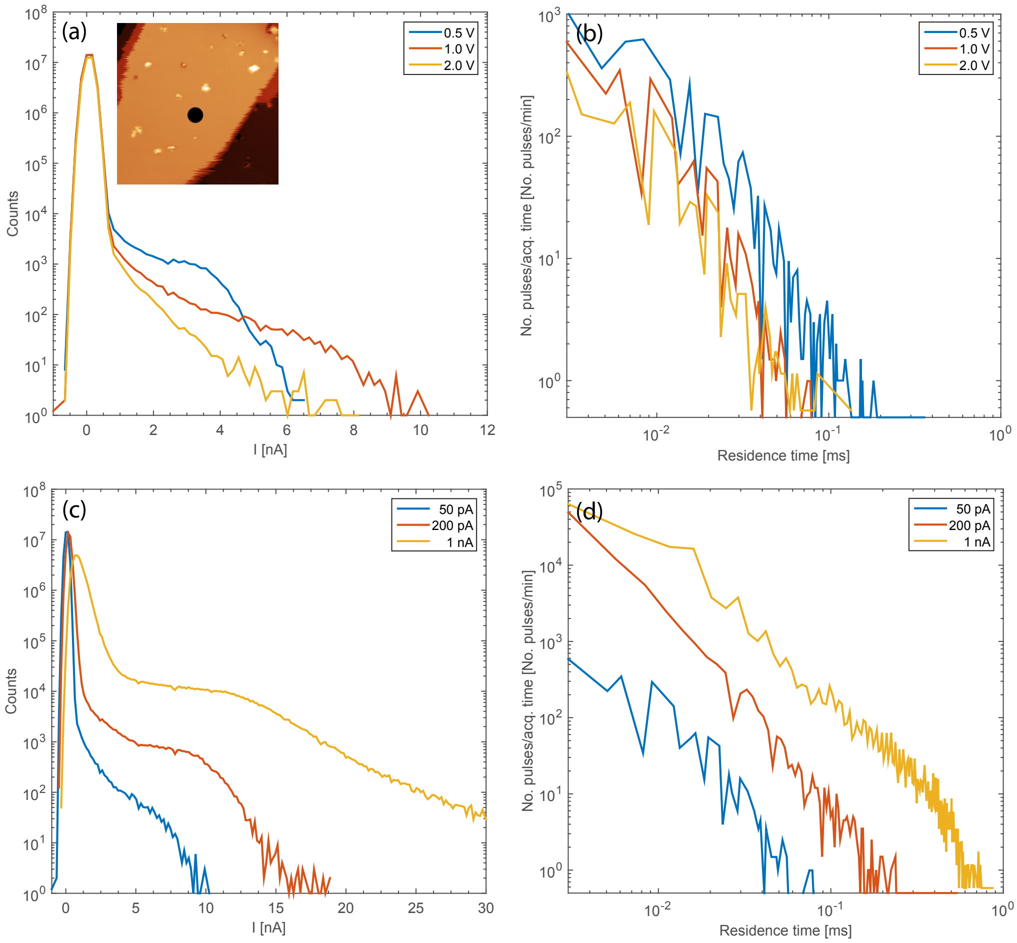

Figure C.3: Bias (a)-(b) and current (c)-(d) influence on RTD distributions. Histograms of FIP measurements performed on bare Ag(110) surface. (a) and (b) performed at 50 pA, (c) and (d) at 1 V. Loop gain = 0.5% for all measurements.

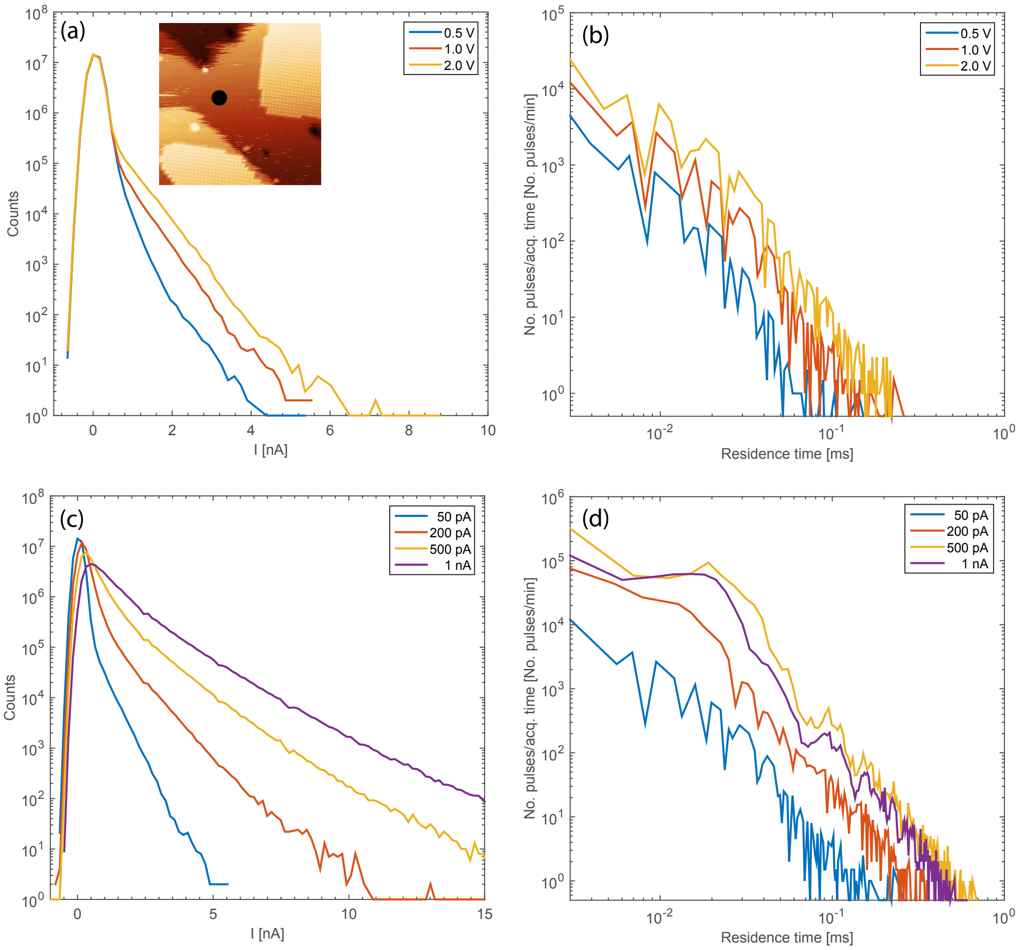

Figure C.4: Bias (a)-(b) and current (c)-(d) influence on RTD distributions. Histograms of FIP measurements performed on mobile part of PTCDA covered Ag(110). (a) and (b) performed at 50 pA, (c) and (d) at 1 V. Loop gain = 1.0% for all measurements.

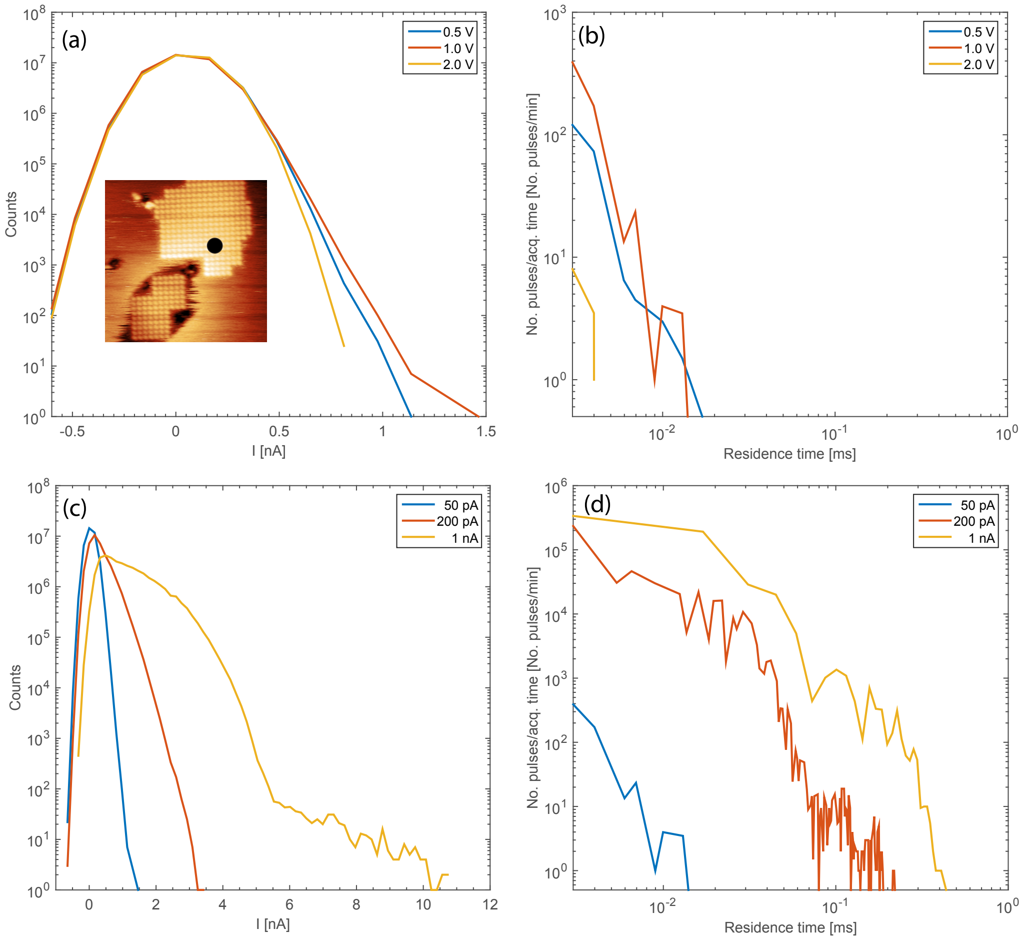

Figure C.5: Bias (a)-(b) and current (c)-(d) influence on RTD distributions. Histograms of FIP measurements performed on PTCDA island of Ag(110) surface. (a) and (b) performed at 50 pA, (c) and (d) at 1 V. Loop gain = 0.5% for all measurements.

C.3 On island

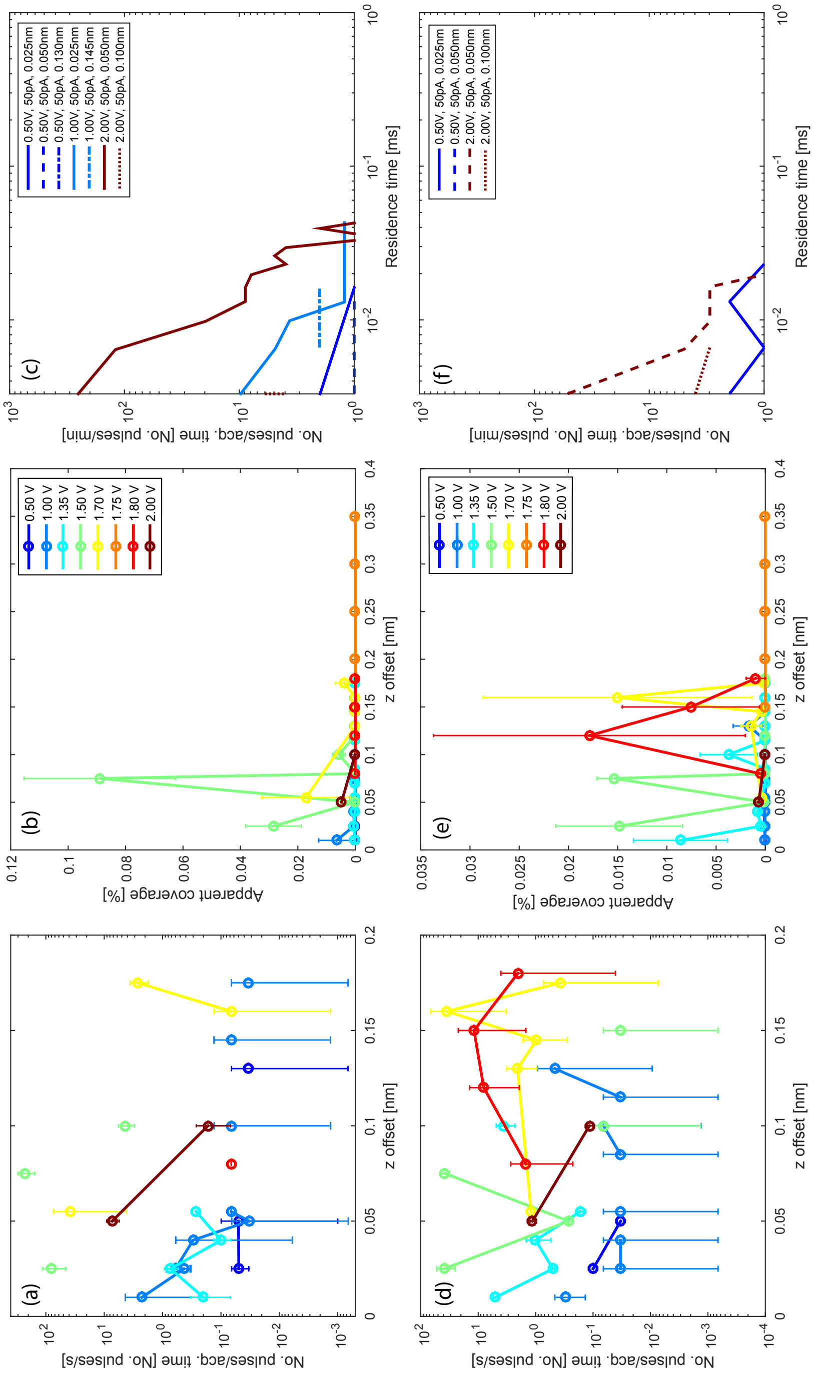

Figure C.6: Corresponding on-island FIP acquisitions using experimental on-off-on protocol for constant height measurements presented in Fig. 7.16 using same parameters.

Bibliography

[1] F. J. Giessibl. Advances in atomic force microscopy. *Rev. Mod. Phys.*, 75(3):949–983, 2003.

[2] G. Binnig, H. Rohrer, Ch. Gerber, and E. Weibel. 7 × 7 reconstruction on Si(111) resolved in real space. *Phys. Rev. Lett.*, 50(2):120, 1983.

[3] D. M. Eigler and E. K. Schweizer. Positioning single atoms with a scanning tunnelling microscope. *Nature*, 344(6266):524–526, 1990.

[4] M. F. Crommie, C. P. Lutz, and D. M. Eigler. Imaging standing waves in a two-dimensional electron gas. *Nature*, 363(6429):524–527, 1993.

[5] F. J. Giessibl. Atomic resolution of the silicon (111)-(7×7) surface by atomic force microscopy. *Science*, 267(5194):68–71, 1995.

[6] F. J. Giessibl, S. Hembacher, H. Bielefeldt, and J. Mannhart. Subatomic features on the silicon (111)-(7×7) surface observed by atomic force microscopy. *Science*, 289(5487):422–425, 2000.

[7] M. C. Hersam, N. P. Guisinger, and J. W. Lyding. Silicon-based molecular nanotechnology. *Nanotech.*, 7:70–76, 2000.

[8] A. J. Heinrich, C. P. Lutz, J. A. Gupta, and D. M. Eigler. Molecule cascades. *Science*, 298(5597):1381–1387, 2002.

[9] J. Repp, G. Meyer, S. M. Stojkovi, A. Gourdon, and C. Joachim. Molecules on Insulating Films: Scanning-Tunneling Microscopy Imaging of Individual Molecular Orbitals. *Phys. Rev. Lett.*, 294:026803, 2005.

[10] N. Oyabu, O. Custance, I. Yi, Y. Sugawara, and S. Morita. Mechanical vertical manipulation of selected single atoms by soft nanoindentation using near contact atomic force microscopy. *Phys. Rev. Lett.*, 90(17):176102, 2003.

[11] Y. Sugimoto, M. Abe, S. Hirayama, N. Oyabu, O. Custance, and Seizo Morita. Atom inlays performed at room temperature using atomic force microscopy. *Nat. Mater.*, 4(2):156–159, 2005.

[12] Y. Sugimoto, P. Pou, O. Custance, P. Jelinek, M. Abe, R. Perez, and Morita S. Complex patterning by vertical interchange atom manipulation using atomic force microscopy. *Science*, 322(5900):413–417, 2008.

[13] Y. Sugimoto, P. Pou, M. Abe, P. Jelinek, R. Perez, S. Morita, and O. Custance. Chemical identification of individual surface atoms by atomic force microscopy. *Nature*, 446(7131):64–67, 2007.

[14] F. Mohn L. Gross, N. Moll, P. Liljeroth, and G. Meyer. The chemical structure of a molecule resolved by atomic force microscopy. *Science*, 325(5944):1110–1114, 2009.

[15] J. Welker and F. J. Giessibl. Revealing the Angular Symmetry of Chemical Bonds by Atomic Force Microscopy. *Science*, 336(6080):444–449, 2012.

[16] K. K. Gomes, W. Mar, W. Ko, F. Guinea, and H. C. Manoharan. Designer Dirac fermions and topological phases in molecular graphene. *Nature*, 483(7389):306–310, 2012.

[17] S. Kawai, A. S. Foster, F. F. Canova, H. Onodera, S. I. Kitamura, and E. Meyer. Atom manipulation on an insulating surface at room temperature. *Nat. Comm.*, 5(4403), 2014.

[18] R. J. Celotta, S. B. Balakirsky, A. P. Fein, F. M. Hess, G. M. Rutter, and Joseph A. Stroscio. Invited Article: Autonomous Assembly of Atomically Perfect Nanostructures Using a Scanning Tunneling Microscope. *Rev. Sci. Instrum.*, 84(121301), 2014.

[19] S. Kawai, A. S. Foster, T. Björkman, S. Nowakowska, J. Björk, F. F. Canova, L. H. Gade, T. A. Jung, and E. Meyer. Van der Waals interactions and the limits of isolated atom models at interfaces. *Nat. Comm.*, 7(11559), 2016.

[20] D. Keller. Reconstruction of STM and AFM images distorted by finite-size tips. *Surf. Sci.*, 253(1-3):353–364, 1991.

[21] J. A. Stroscio and W. J. Kaiser. *Scanning Tunneling Microscopy.* Academic Press, 1st edition, 2001.

[22] C. Julian Chen. *Introduction to Scanning Tunneling Microscopy.* Oxford University Press, 2nd edition, 2008.

[23] G. Binning and H. Rohrer. Scanning tunneling microscopy. *Surf. Sci.*, 126:236–244, 1983.

[24] M. Pivetta, F. Silly, F. Patthey, J. P. Pelz, and W.-D. Schneider. Reading the ripples of confined surface-state electrons: Profiles of constant integrated local density of states. *Phys. Rev. B*, 67:193402, 2003.

[25] G. Meyer and N. M. Amer. Novel optical approch to atomic force microscopy. *Appl. Phys. Lett.*, 53:2400, 1988.

[26] P. Günther, U. C. Fischer, and K. Dransfield. Scanning near-field acoustic microscopy. *Appl. Phys. B*, 48:89, 1989.

[27] F. J. Giessibl. Forces and frequency shifts in atomic-resolution dynamic-force microscopy. *Phys. Rev. B.*, 56:16010, 1997.

[28] F. J. Giessibl. A direct method to calculate tip-sample forces from frequency shifts in frequency-modulation atomic force microscopy. *Appl. Phys. Lett.*, 78(1):123, 2001.

[29] F. J. Giessibl and H. Bielefeldt. Physical interpretation of frequency-modulation atomic force microscopy. *Phys. Rev. B.*, 61(15), 2000.

[30] M. Abramowitz and I. Stegum. *Handbook of Mathematical functions.* Dover, 9th edition, 1970.

[31] J. E. Sader and S. P. Jarvis. Accurate formulas for interaction force and energy in frequency modulation force spectroscopy. *Appl. Phys. Lett.*, 84(10):1801–1803, 2004.

[32] A. J. Melmed. The art and science and other aspects of making sharp tips. *J. Vac. Sci. Technol. B*, 9:601–608, 1991.

[33] A. J. Caama no, Y. Pogorelev, O. Custance, J. Mėndez, A. M. Barȯ, J. Y. Velluillen, J. M. Gȯmez-Rodriguez, and J. J. Sȧnez. Field emission interferometry with the scanning tunneling microscope. *Surf. Sci.*, 426:L420–L425, 1999.

[34] H. Rohrer. *Scanning Tunneling Microscopy and Spectroscopy for STM experiments: Theory, Techniques and Applications.* VCH, New York, 1993.

[35] I. Ekvall, E. Wahlström, D. Claesson, H. Olin, and E. Olsson. Preparation and characterization of electrochemically etched W tips for STM. *Meas. Sci. Tech.*, 10:11–18, 1999.

[36] A.-S-Lucier. Preparation and Characterization of Tungsten Tips Suitable for Molecular Electronics Studies. Master's thesis, Center for the Physics of Materials Department of Physics McGill University Montreal, Quebec Canada, 2004.

[37] J. P. Ibe, P. P. Bey Jr., S. L. Brandow, R. A. Brizzolara, N. A. Burnham, D. P. DiLella, K. P. Lee, C. R. K. Marrian, and R. J. Colton. On the electrochemical etching of tips for scanning tunneling microscopy. *Vac. Sci. Tech.*, 8(4):3570, 1990.

[38] S. W. H. Yih and C. T. Wang. *Tungsten: Sources, Metallurgy, Properties, and Applications.* Plenum Press, 2nd edition, 1979.

[39] Vu Thien Binh. In situ fabrication and regeneration of microtips for scanning tunneling microscopy. *Journal of Microscopy*, 152:355–361, 1988.

[40] O. Albrektsen, H. W. M. Salemink, K. A. Mørch, and A. R. Tholen. Reliable tip preparation for high-resolution scanning tunneling microscopy. *Vac. Sci. Tech.*, 12(6):3187–3190, 1994.

[41] M. J. Vasile, D. Grigg, J. E. Griffith, E. Fitzgerald, and P. E. Russell. Scanning probe tip geometry optimized for metrology by focused ion beam ion milling. *J. Vac. Sci. Technol. B*, 9:3569–3572, 1991.

[42] C. Schiller, A. A. Koomans, T. L. van Rooy, C. Schönenberger, and H. L. van Elswijk. Decapitation of tungsten field emitter tips during sputter sharpening. *Surf. Sci.*, 339:L925–L930, 1995.

[43] G. J. de Raad, P. M. Koenraad, and J. H. Wolter. Use of the Schiller decapitation process for the manufacture of high quality tungsten scanning tunneling microscopy tips. *Vac. Sci. Tech.*, 17(5):1946–1952, 1999.

[44] S. Morishita and F. Okuyama. Sharpening of monocrystalline molybdenum tips by means of inert-gas ion sputtering. *J. Vac. Sci. Technol. A*, 9:167–169, 1991.

[45] J. A. Kubby and B. M. Siegel. High-resolution structuring of emitter tips for the gaseous field-ionization source. *J. Vac. Sci. Technol. B*, 4:120–125, 1986.

[46] G. Carter, M. J. Nobes, and R. P. Webb. 2nd-order erosion slowness theory of the development of surface-topography by ion-induced sputtering. *J. Mater. Sci.*, 16:2091–2102, 1981.

[47] R. M. Bradley and J. M. E. Harper. Theory of ripple topography induced by ion-bombardment. *J. Vac. Sci. Technol. A*, 6:2390–2395, 1988.

[48] Shi-Dong Lang. *Quantum Tunneling and Field Electron Emission Theories.* World Scientific, 2014.

[49] R. Gomer. *Field Emission and Field Ionization.* Number 9 in Harvard Monographs in Applied Science, 1961.

[50] A. Fischer, M. S. Mousa, and R. G. Forbes. Influence of barrier form on fowler-nordheim plot analysis. *J. Vac. Sci. and Tech. B*, 31(3):032201, 2013.

[51] P. H. Cutler, J H. N. M. Miskovsky, T. E. Sullivan, and B. Weiss. Theory of electron emission in high fields from atomically sharp emitters: Validity of the fowler-nordheim equation. *Prog. Surf. Sci.*, 42:169, 1993.

[52] R. Uoung, J. Ward, and F. Scire. The Topografiner: An Instrument for Measuring Surface Microtopography. *Rev. Sci. Instr.*, 43(7):999–1011, 1972.

[53] H. N. Waltenburg and J. T. Yates Jr. Surface chemistry of Silicon. *Chem. Rev.*, 95:1589–, 1995.

[54] R. E. Schlier and H. E. Farnsworth. Structure and Adsorption Characteristics of Clean Surfaces of Germanium and Silicon. *J. Chem. Phys.*, 30:917, 1959.

[55] Adam Marc Sweetman. *Forces at the nanoscale: interactions in atomic force microscopy and dielectrophoresis.* PhD thesis, University of Nottingham, 2009.

[56] D. J. Chadi. Atomic and Electronic Structures of Reconstructed Si(100) Surfaces. *Phys. Rev. Lett.*, 43:43–47, 1979.

[57] R. J. Hamers, R. M. Tromp, and J. E. Demuth. Scanning tunneling microscopy of si(001). *Phys. Rev. B*, 34:5343, 1986.

[58] J. Dabrowski and M. Scheffler. Self-consistent study of the electronic and structural properties of the clean Si(001)(2×1) surface. *Appl. Surf. Sci.*, 56-58:15–19, 1992.

[59] N. Roberts and R. J. Needs. Total energy calculations of dimer reconstructions on the silicon (001) surface. *Surf . Sci.*, 236:112–121, 1990.

[60] J. E. Northrup. Electronic structure of Si(100)c(4×2) calculated within the GW approximation. *Phys. Rev. B*, 47:10032–10035, 1993.

[61] R. M. Tromp, R. J. Hamers, and J. E. Demuth. Si(001) Dimer Structure Observed with Scanning Tunneling Microscopy. *Phys. Rev. Lett.*, 55:1303, 1985.

[62] R. A. Wolkow. Direct observation of an increase in buckled dimers on Si(001) at low temperature. *Phys. Rev. Lett.*, 68:2636, 1992.

[63] C. -C. Fu, M. Weissmann, and A. Sal. Molecular dynamics study of dimer flipping on perfect and defective Si(001) surfaces. *Surf. Sci.*, 494:119, 2001.

[64] L. Kantorovich and C. Hobbs. Probing the Si(001) surface with a Si tip: An ab initio study. *Phys. Rev. B*, 73:245420, 2006.

[65] M. Suemitsu, H. Nakazawa, and N. Miyamoto. Temperature-programmed-desorption study of the process of atomic deuterium adsorption onto Si(100)2x1. *Appl. Surf. Sci.*, 82-83:449–453, 1994.

[66] F. S. Tautz and J. A. Schaefer. Ultimate resolution electron energy loss spectroscopy at H/Si(100) surfaces. *J. Appl. Phys.*, 84:6636, 1998.

[67] X. D. Wang, T. Hashizume H. Lu, H. W. Pickering, and T. Sakurai. Atomic hydrogen chemisorption on Si(100)(2 X 1) studied by FI-STM. *Appl. Surf. Sci.*, 67:266, 1993.

[68] H. Lu, X. D. Wang, C. L. Bai, T. Hashizume, and T. Sakurai. Interaction of atomic hydrogen with the Si(100)2x1 surface. *Appl. Phys. A*, 58:203, 1994.

[69] Z. H. Lu, K. Griffiths, P. R. Norton, and T. K. Sham. Adsorption of atomic hydrogen on Si(100) surface. *Phys. Rev. Lett.*, 68:1343, 1992.

[70] C. C. Cheng and Jr. J. T. Yates. H-induced surface restructuring on Si(100): Formation of higher hydrides. *Phys. Rev. B*, 43:4041–4095, 1991.

[71] Y.J. Chabal. High-resolution infrared spectroscopy of adsorbates on semiconductor surfaces: Hydrogen on Si(100) and Ge(100). *Surf. Sci.*, 168:594–608, 1986.

[72] K. Ueda and A. Takano. Hydrogen termination study of silicon dangling bonds by electron stimulated desorption spectroscopy (TOF-ESD). *Surf. Sci.*, 287/288:506–509, 1993.

[73] K. Ueda, S. Kodama, and A. Takano. Desorption study of a proton from H/Si(100) by electron stimulated desorption spectroscopy. *Surf. Sci.*, 283:195, 1993.

[74] J. J. Boland. Structure of the H-saturated Si(100) surface. *Phys. Rev. Lett.*, 65:3325–3328, 1990.

[75] J. J. Boland. Role of bond-strain in the chemistry of hydrogen on the Si(100) surface. *Surf. Sci.*, 261:17–28, 1992.

[76] Y. J. Chabal and K. Raghavachari. New Ordered Structure for the H-Saturated Si(100) Surface: The (3×1) Phase. *Phys. Rev. Lett.*, 54:10551058, 1985.

[77] D. T. Jiang, G. W. Anderson, K. Griffiths, T. K. Sham, and P. R. Norton. Adsorption of atomic hydrogen on Si(100)-2×1 at 400 K. *Phys. Rev. B*, 48:4952–4955, 1993.

[78] X. P. Qin and P. R. Norton. Scanning tunneling microscopy of the phase transition between H/Si(100)-(2×1) and H/Si(100)-(3×1). *Phys. Rev. B*, 53:11100–11107, 1996.

[79] H. Froitzheim, U. Köhler, and H. Lammering. Adsorption states and adsorption kinetics of atomic hydrogen on silicon crystal surfaces. *Surf. Sci.*, 149:537–557, 1985.

[80] T. Sakurai and H. D. Hagstrum. Interplay of the monohydride phase and a newly discovered dihydride phase in chemisorption of H on Si(100)2 × 1. *Phys. Rev. B*, 14:1593–1596, 1976.

[81] J. J. Boland. Scanning Tunneling Microscopy Study of the Adsorption and recombinative desorption of Hydrogen from the Si(100)-2×1 surface. *J. Vac. Sci. Tech. A*, 10:2458–2464, 1992.

[82] A. Bellec, D. Riedel, an G. Dujardin. Dihydride dimer structures on the Si(100):H surface studied by low-temperature scanning tunneling microscopy. *Phys. Rev. B*, 78:165302, 2008.

[83] E. J. Buehler and J. J. Boland. Identification and characterization of a novel silicon hydride species on the Si(100) surface. *Surf. Sci.*, 425:L363–L368, 1999.

[84] Peter Sharp. *Passivated Silicon and Diamond surfaces: Imaging, modification, and molecular adsorption.* PhD thesis, University of Nottingham, 2013.

[85] S. Schofield, N. Curson, M. Y. Simmons, F. Ruess, T. Hallam, L. Oberbeck, and R. Clark. Atomically Precise Placement of Single Dopants in Si. *Phys. Rev. Lett.*, 91:136104, 2003.

[86] T. Hallam, F. J. Ruess, N. J. Curson, K. E. J. Goh, L. Oberbeck, M. Y. Simmons, and R. G. Clark. Effective Removal of Hydrogen Resists Used To Pattern Devices in Silicon Using Scanning Tunneling Microscopy. *Appl. Phys. Lett.*, 86:143116, 2005.

[87] T. Hallam, T. C. Reusch, L. Oberbeck, N. J. Curson, M. Y. Simmons. Scanning Tunneling Microscope Based Fabrication of Nano- and Atomic Scale Dopant Devices in Silicon: The Crucial Step of Hydrogen Removal. *J. Appl. Phys.*, 101:34305, 2007.

[88] S. F. Bent. Organic Functionalization of Group IV Semiconductor Surface: Principles, Examples, Applications, and Prospects. *Surf. Sci.*, 500:879–903, 2002.

[89] X. J. Zhou and K. T. Leung. Competetion between Associative and Dissociative Adsorption of 1,2-Dihalogenated Benzenes on Si(100 2 ×1: Formation of Dihalocyclohexadiene, Halophenyl and Phenylene Adstructures. *Surf. Sci.*, 600:3285–3296, 2006.

[90] X. J. Zhou and K. T. Leung. Surface Chemistry of Monochlorinated and Dichlorinated Benzenes on Si(100)2 ×1: Comparison Study of Chlorine Content and isomeric Effects. *J. Phys. Chem. B*, 110:9601–9607, 2006.

[91] J. H. G. Owen, K. Miki, and R. D. Bowler. Self-Assembled Nanowires on Semiconductor Surfaces. *J. Mater. Sci.*, 41:4568–4603, 2006.

[92] R. D. Bowler. Atomic-Scale Nanowires: Physical and Electronic Structure. *J. Phys.: Condens. Matter*, 16:R721–R754, 2004.

[93] M. Fuechsle, J. A. Miwa, S. Mahapatra, H. Ryu, S. Lee, O. Warschkow, L. C. L. Hollenberg, G. Klimeck, and M. Y. Simmons. A single-atom transistor. *Nat. Nanotech.*, 2012.

[94] H. Labidi, L. Kantorovich, and D. Riedel. Atomic-Scale Control of Hydrogen Bonding on a bare Si(100)-2×1 Surface. *Phys. Rev. B*, 86:165441, 2012.

[95] X. Tong and R. A. Wolkow. Electron-induced H atom desorption patterns created with a scanning tunneling microscope: Implications for controlled atomic-scale patterning on HSI(100). *Surf. Sci.*, 600:L199–L203, 2006.

[96] F. Bianco, D. R. Bowler, J. H. G. Owen, S. A. Köster, M. Longobardi, and C. Renner. Scalable Patterning of One-Dimensional Dangling Bond Rows on Hydrogenated Si(100). *ACS Nano*, 7:4422–4428, 2013.

[97] J. J. Boland. Scanning Tunneling Microscopy of the Interaction of Hydrogen with Silicon Surfaces. *Adv. Phys.*, 42:129–171, 1993.

[98] D. R. Bowler, J. H. G. Owns C. M. Goringe, K. Miki, and G. A. D. Briggs. An Experimental-Theoretical Study of the Behavior of Hydrogen on the Si(001) Surface. *J. Phys. Condens. Matter*, 12:7655–7670, 2000.

[99] F. Bianco, J. H. G. Owen, S. A. Köster, D. Mazur, C. Renner, and D. R. Bowler. Endotaxial Si Nanolines in Si(01):H. *Phys. Rev. B*, 84:35328, 2011.

[100] R. J. Hamers, Ph. Avouris, and F. Bozso. Imaging chemical-bond formation with the scanning tunneling microscope: NH_3 dissociation on Si(001). *Phys. Rev. Lett.*, 59:2071–2074, 1987.

[101] J. J. Boland. Evidence of pairing and its role in the recombinative desorption of hydrogen from the Si(100)-2×1 surface. *Surf. Sci.*, 67:1539, 1991.

[102] J. A. Applebaum, G. A. Baraff, and D. R. Hamann. The Si (100) surface. III. Surface reconstruction. *Phys. Rev. B*, 14:588, 1976.

[103] L. Perdigão, D. Deresmes, B Grandidier, M. Dubois, C. Delerue, G. Allan B, and D. Stiévenard. Semiconducting Surface Reconstructions of p-Type Semiconducting Surface Reconstructions of p-Type Si(100) Substrates at 5 K. *Phys. Rev. Lett.*, 92:216101, 2004.

[104] M. Dubois, L. Perdigão, G. Allan B, Grandidier, D. Deresmes, and D. Stiévenard. Scanning tunneling microscopy and spectroscopy of reconstructed Si(100) surface. *Phys. Rev. B*, 71:165322, 2005.

[105] S. Ciraci, R. Butz, E. M. Oellig, and H. Wagner. Chemisorption of hydrogen on the Si(100) surface: Monohydride and dihydride phases. *Phys. Rev. B*, 30:711–720, 1984.

[106] M. A. Walsh and M. C. Hersam. Atomic-Scale templates Patterned by Ultrahigh Vacuum Scanning Tunneling Microscopy onsilicon. *Annu. Rev. Phys. Chem.*, 60:193–216, 2009.

[107] J. W. Lyding, G. C. Abeln, T. C. Shen, C. Wang, and J. R. Tucker. Nanometer-scale patterning and oxidation of silicon surfaces with an ultrahigh-vacuum scanning tunneling microscope. *J. Vac. Sci. Technol. B*, 12:3735–3740, 1994.

[108] C. G. Van de Walle and R. A. Street. Structure, energetics, and dissociation of the Si-H bonds at dangling bonds in silicon. *Phys Rev. B*, 49:14766, 1994.

[109] P. Avouris, R. E. Walkup, A. R. Rossi, H. C. Akpati, P. Nordlander, T. C. Shen, G. C. Abeln, and J. W. Lyding. Breaking individual chemical bonds via STM-induced excitations. *Surf. Sci.*, 363:368–377, 1996.

[110] T. C. Shen, C. Wang, G. C. Abeln, J. R. Tucker, J. W. Lyding, Ph. Avouris, and R. E. Walkup. Atomic-scale desorption through electronic and vibrational excitation mechanisms. *Science*, 268:1590–1592, 1995.

[111] P. Avouris, R. E. Walkup, A. R. Rossi, T. C. Shen, G. C. Abeln, J. R. Tucker, and J. W. Lyding. STM-induced H atom desorption from Si(100): isotope effects and site selectivity. *Chem. Phys. Lett.*, 257:148–154, 1996.

[112] L. Soukiassian, A. J. Mayne, M. Carbone, and G. Dujardin. Atomic-scale desorption of H atoms from the Si(100)-2×1:H surface: inelastic electron interactions. *Phys. Rev. B*, 68:035303, 2003.

[113] U. Höfer, L. Li, and T. F. Heinz. Multimode hydrogen depassivation lithography: A method for optimizing atomically precise write times. *J. Vac. Sci. Tech. B*, 31:06FC01–1–06FC01–6, 2013.

[114] R. G. Clark, R. Brenner, T. M. Buehler, V. Chan, N. J. Curson, A. S. Dzurak, E. Gauja, H. S. Goan, A. D. Greentree, T. Hallam, A. R. Hamilton, L. C. L. Hollenberg, D. N. Jamieson, J. C. McCallum, G. J. Milburn, J. L. O'Brien, C. I. Pakes L. Oberbeck, S. D. Prawer, D. J. Reilly, F. J. Ruess, S. R. Schofield, M. Y. Simmons, F. E. Stanley, R. P.

Starrett, C. Wellard, and C. Yang. Progress in silicon-based quantum computing. *Phil. Trans.*, 361:1451–1471, 2003.

[115] L. Soukiassian, A. J. Mayne, M. Carbone, and G. Dujardin. Atomic wire fabrication by STM induced hydrogen desorption. *Surf. Sci.*, 528:121–126, 2003.

[116] S. Chen, H. Xu, K. E. J. Goh, L. Liu, and J. N. Randall. Patterning of sub-1 nm dangling-bond lines with atomic precision alignment on HSi(100) surface at room temperature. *Nanotech.*, 23, 2012.

[117] M. C. Hersam, N. P. Guisinger, and J. W. Lyding. Isolating, imaging, and electrically characterizing individual organic molecules on the Si(100) surface with the scanning tunneling microscope. *J. Vac. Sci. Technol. A*, 18:1349–1353, 2000.

[118] `http://www.specs.de/cms/front_content.php?idart=245`.

[119] M. Ternes. *Scanning Tunneling Spectroscopy at the single atom scale.* PhD thesis, École Polytechnique Fédérale De Lausanne, 2006.

[120] M. A. Lantz, H. J. Hug, R. Hoffmann, P. J. A. van Schendel, P. Kapenberger, S. Martin, A. Baratoff, and H.-J. Guntherodt. Quantitative measurement of Short-Range chemical bonding forces. *Science*, 291(5513):2580–2583, 2001.

[121] M. L. Goldstein, S. A. Morris, and G. G. Yen. . *The European Physical Journal B*, 41:255, 2004.

[122] Philipp Alexander Rahe. *The Calcite 10$\bar{1}$4) Surface: A Versatile Substrate for Molecular Self-Assembly.* PhD thesis, Johannes Gutenberg-Universität Mainz, 2011.

[123] D. Pohl and W. R. Möller. Tracking Tunneling Microscopy. *Rev. of Sci. Inst.*, 59(6):840, 1988.

[124] B. S. Swartzentruber. Direct measurement of surface diffusion using atom tracking scanning tunneling microscopy. *Phys. Rev. Lett.*, 76(3):459–62, 1996.

[125] B. S. Swartzentruber, A. P. Smith, and Jónsson H. Experimental and Theoretical Study of the Rotation of Si Ad-dimers on the Si(100) Surface. *Phys. Rev. Lett.*, 77:2518, 1996.

[126] X. R. Qin, B. S. Swartzentruber, and M. G. Lagally. Diffusional Kinetics of SiGe Dimers on Si(100) Using Atom-Tracking Scanning Tunneling Microscopy. *Pys. Rev. Lett.*, 85:3660, 2000.

[127] M. Krueger, B. Borovsky, and E. Ganz. Diffusion of adsorbed Si dimers on Si(001). *Surf. Sci.*, 385(1):146, 1997.

[128] M. Abe, Y. Sugimoto, O. Custance, and S. Morita. Room-temperature reproducible spatial force spectroscopy using atom-tracking technique. *Phys. Rev. Lett.*, 87(17):173503, 2005.

[129] M. Abe, Y. Sugimoto, O. Custance, and S. Morita. Atom tracking for reproducible force spectroscopy at room temperature with non-contact atomic force microscopy. *Nanotech.*, 16(12):3029, 2005.

[130] M. Abe, Y. Sugimoto, T. Namikawa, K. Morita, N. Oyabu, and S. Morita. Drift-compensated data acquisition performed at room temperature with frequency modulation atomic force microscopy. *Appl. Phys. Lett.*, 90(20):2013103, 2007.

[131] `http://www.omicron.de/en/products/variable-temperature-spm/instrument-concept`.

[132] Samuel P. Jarvis. *The effect of tip structure in atomic manipulation - a combined DFT and AFM study.* PhD thesis, University of Nottingham, 2012.

[133] Z. Majzik, A. Bettac M. Setvin, A. Feltz, V. Chab, and P. JelÃnek. Simultaneous current, force and dissipation measurements on the Si(111)

7×7 surface with an optimized qPlus AFM/STM technique. *Beil. J. Nanoech.*, 3:249–259, 2012.

[134] A. J. Weymouth, T. Wutscher, J. Welker, T. Hofmann, and F. J. Giessibl. Phantom force induced by tunneling current: A characterization on si(111). *Phys. Rev. Lett.*, 106:226801, 1994.

[135] J. W. Lyding, T. C. Shen, J. S. Hubacek, J. R. Tucker, and G. C. Abeln. Nanoscale patterning and oxidation of h-passivated si (100)-2× 1 surfaces with an ultrahigh vacuum tunneling microscope. *Appl. Phys. Lett.*, 64(15):2010–2012, 1994.

[136] Morten Møller, Laurent Guirnet, Samuel J. Jarvis, Peter Sharp, Richard Woolley, and Philip Moriarty. Automated extraction of single atoms: tip state dependency. *Nanotech.*, 28(7):075302, 2017.

[137] J. N. Randall, J. W. Lyding, Schmucker, J. R. Von Ehr, J. Ballard, R. Saini, H. Xu, and Y. Ding. Atomic precision lithography on Si. *J. Vac. Sci. Tech. B*, 27:2764, 2009.

[138] `http://www.Zyvexlabs.com`.

[139] J. Stirling, R. A. J. Woolley, and P. Moriarty. Scanning probe image wizard: A toolbox for automated scanning probe microscopy data analysis. *Rev. Sci. Instrum.*, 84(113701), 2013.

[140] R. A. J. Woolley, J. Sterling, A. Radocea, N. Krasnogor, and P. Moriarty. Automated probe microscopy via evolutionary optimization at the atomic scale. *Appl. Phys. Lett.*, 98(253104):253104–1–3, 2011.

[141] Duncan Davis. Towards Autonomous Scanning Probe Microscopy, 2015. unpublished.

[142] Ben Woodward. Towards autonomous scanning probe microscop, 2015. unpublished.

[143] Julian Stirling. *Scanning Probe Microscopy from the Perspective of the Sensor.* PhD thesis, University of Nottingham, 2014.

[144] T. Huff, H. Labidi, M. Rashidi, M. Koleini nad R. Achal, M. Salomons, and R. A. Wolkow. Atomic white-out: Enabling atomic circuitry through mechanically induced bonding of single H atoms to a silicon surface. In *eprint arXiv:1706.05287 [cond-mat.mes-hall]*, 2017.

[145] Y. Suwa, S. Matsuura, M. Mujimori, S. Heike, T. Onogi, H. Kajiyama, T. Hitosugi, K. Kitazawa, T. Uda, and T. Hashizume. Dopant-pair structures segregated on a hydrogen-terminated si(100) surface. *Phys. Rev. Lett.*, 90(15):156101, 2003.

[146] A. Bellec, D. Riedel, and G. Dujardin. Dihydride dimer on the si(100):h surface studied by low-temperature scanning tunneling microscopy. *Phys. Rev. B*, 78:165302, 2008.

[147] K. Stokbro, C. Thirstrup, M. Sakurai, U. Quaade, B. Y. K. Hu, F. Perez-Murano, and F. Grey. Stm-induced hydrogen desorption via a hole resonance. *Phys. Rev. Lett.*, 80(12):2618–2621, 1998.

[148] T. C. Shen, C. Wang, and J. R. Tucker. Al nucleation on monohydride and bare si(001) surfaces: Atomic scale patterning. *Phys. Rev. Lett.*, 78(7):1271–1274, 1997.

[149] T. C. Shen and Ph. Avouris. Electron stimulated desorption induced by the scanning tunneling microscope. *Surf. Sci.*, 390:35–44, 1997.

[150] B. N. J. Persson and Ph. Avouris. The effects of the electric field in the stm on excitation localization. implications for local bond breaking. *Chem. Phys. Lett.*, 242:483–489, 1995.

[151] H. C. Akpati, P. Nordlander, L. Lou, and Ph. Avouris. The effects of an external electric field on the adatom-surface bond: H and al adsorbed on si(111). *Surf. Sci.*, 372:9–20, 1997.

[152] E. T. Foley, A. F. Kam, J. W. Lyding, and Ph. Avouris. Cryogenic uhv-stm study of hydrogen and deuterium desorption from si(100). *Phys. Rev. Lett.*, 80(6):1336–1339, 1998.

[153] T. Hitosugi, T. Hashizume, S. Heike, H. Kajiyama, Y. Wada, S. Watanabe, T. Hasegawa, and K. Kitazawa. Scanning tunneling microscopy/spectroscopy of dangling-bond wires fabricated on the si(100)-2×1-h surface. *Appl. Surf. Sci.*, 130–132:340–345, 1998.

[154] P. G. Piva, G. A. DiLabio, J. L. Pitters, J. Zikovsky, M. Rezeq, S. Dogel, W. A. Hofer, and R. A. Wolkow. Field regulation of single-molecule conductivity by a charged surface atom. *Nature*, 435:658–661, 2005.

[155] A. Bellec, D. Riedel, G. Dujardin, O. Boudrioua, L. Chaput, L. Stauffer, and P. Sonnet. Electronic properties of the n-doped hydrogenated silicon (100) surface and dehydrogenated structures at 5 K. *Phys. Rev. B.*, 80:245434, 2009.

[156] J. V. Barth. Transport of adsorbates at metal surfaces: from thermal migration to hot precursors. *Surf. Sci. Rep.*, 40(3-5):75–149, 2000.

[157] R. Brown. Brief Account of Microscopical Observations Made in the Months of June, July and August 1827, on the Particles Contained in the Pollen of Plants; and on the General Existence of Active Molecules in Organic and Inorganic Bodies. *Phil. Mag.*, 4:161, 1828.

[158] R. Brown. Additional remarks on active molecules. *Phil. Mag.*, 6:161, 1829.

[159] M. Tringides, M. Gupalo, Q. Li, and X. Wang. *Equilibrium versus non-equiilibrium surface diffusion measurements in Anomalous Diffusion From Basics to Applications.* Springer, Heidelberg, 1999.

[160] K. D. Wang, C. Zhang, M. M. T. Loy, and X. D. Xiao. Time-dependent tunneling spectroscopy for studying surface diffusion confined in nanostructures. *Phys. Rev. Lett.*, 94:036103, 2005.

[161] J. Ikonomov, P. Bach, R. Merkel, and M. Sokolowski. Surface diffusion constants of large organic molecules determined from their residence times under a scanning tunneling microscope tip. *Phys. Rev. B*, 81:161412(R), 2010.

[162] S. Hahne, J. Ikomov, M. Sokolowski, and P. Maass. Determining molecule diffusion coefficients on surfaces from a locally fixed probe: Analysis of signal fluctuations. *Phys. Rev. B*, 87:085409, 2013.

[163] S. Hahne, P. Rahe, and P. Maass. Determination of diffusion tensors from oscillating and circulating scanning probe tips. *EPL draft*, 2015.

[164] A. Paulheim, M. Muller, C. Marquadt, M. Sokolowski. Fluorescence spectroscopy of ptcda molecules on the kcl(100) surface in the limit of low coverages: Site selection and diffusion. *Phys. Chem. Chem. Phys.*, 15:4906, 2013.

[165] K. Glöckler, C. Seidel, A. Soukopp, M. Sokolowski, E. Umbach, M. Böhringer, R. Berndt, and W. -D. Schneider. Highly ordered structures and submonolayer scanning tunnelling microscopy contrast of PTCDA and DM-PBDCI monolayers on Ag(111) and Ag(110). *Surf. Sci.*, 405:1–20, 1998.

[166] Y. Zou, L. Kilian, A. Schöll, Th. Schmidt, R. Fink, and E. Umbach. Chemical bonding of PTCDA on Ag surfaces and the formation of interface states. *Surf. Sci.*, 600:1240–51, 2006.

[167] M. Böhringer, W. D. Schneider, K. Glöckler, E. Umbach, and R. Berndt. Adsorption site determination of PTCDA on Ag(110) by manipulation of adatoms. *Surf. Sci.*, 419(1):L95, 1998.

[168] V. Shklover, F.S. Tautz, R. Scholz, S. Sloboshanin, M. Sokolowski, J. A. Schaefer, and E. Umbach. Differences in vibronic and electronic excitations of PTCDA on Ag(111) and Ag(110). *Surf. Sci.*, 454:60, 2000.

[169] F. S. Tautz, S. Sloboshanin, V. Shklover, R. Scholz, M. Sokolowski, J. A. Schaefer, and E. Umbach. Substrate influence on the ordering of organic submonolayers: a comparative study of PTCDA on Ag(110) and Ag(111) using HREELS. *Appl. Surf. Sci.*, 166(1):363, 2000.

[170] V. G. Ruiz, W. Liu, and A. Tkatchenko. Density-functional theory with screened van der waals interactions applied to atomic and molecular adsorbates on close-packed and non-close-packed surfaces. *Phys. Rev. B.*, 93:035118, 2016.

[171] Susanne Hahne. *Determination of single molecule diffusion from signal fluctuation.* PhD thesis, Universität Osnabrück, 2014.

[172] V. Caciuc, H. Hölscher, D. Weiner, H. Fuchs, and A. Schirmeisen. Noncontact atomic force microscopy imaging mechanism on ag(110): Experiment and first-principles theory. *Phys. Rev. B.*, 77:045411, 2008.

[173] S. Rusponi, C. Boragno, and U. Valbusa. Ripple Structure on Ag(110) Surface Induced by Ion Sputtering. *Phys. Rev. Lett.*, 78(14):2795, 1997.

[174] J. Ikonomov, C. H. Schmitz, and M. Sokolowski. Diffusion-limited island decay of PTCDA on Ag(100): Determination of the intermolecular interaction. *Phys. Rev. B*, 81:195428, 2010.

[175] Hari Singh Nalwa. *Advances in Surface Science.* Experimental Methods in the Physical Sciences. Academic Press, 2001.

[176] J. H. Coombs and J. K. Gimzewski. Fine structure in field emission resonances at surfaces. *J. Micr.*, 152:841–851, 1988.

[177] M. Chelvayohan and C. H. B. Mee. Work function measurements on (110), (100) and (111) surfaces of silver. *J. Phys. C: Solid State Phys.*, 15:2305–2312, 1982.

[178] S. Ernst. Optimisation of the preparation process for tips used in scanning tunneling microscopy. Master's thesis, Max-Planck-Institut fur Chemische Physik fester Stoffe, Dresden, 2006.

[179] J. H. Coombs and J. K. Gimzewski. Image charge at the metal surface. *J. Micr.*, 31:7651–7661, 1985.

[180] G. Binnig and H. Rohrer. Scanning Tunneling Microscopy. *Surf. Sci.*, 126:237, 1983.

[181] P. Masss. private communication, 2016.

[182] P. Rahe, J. Schütte, W. Schniederberend, M. Reichling, M. Abe, Y. Sugimoto, and A. Kühnle. Flexible drift-compensation system for precise 3d force mapping in severe drift environments. *Rev. Sci. Instr.*, 82:063704, 2011.

[183] J. A. Stoscio and D. M. Eigler. Atomic and molecular manipulation with the scanning tunneling microscope. *Science*, 254:1319–1326, 1991.

[184] D. M. Eigler, C. P. Lutz, and W. E. Rudge. An atomic switch realized with the scanning tunnelling microscope. *Nat.*, 352:600–603, 1991.

[185] J. L. Whitman, J. A. Stroscio, R. A. Dragoset, and R. J. Celotta. An atomic switch realized with the scanning tunnelling microscope. *Sci.*, 251:1206, 1991.

[186] C. Girard, C. Joachim, C. Chavy, and P. Sautet. The electric field under a stm tip apex: implications for adsorbate manipulation. *Surf. Sci.*, 282:400–410, 1993.

[187] J. N. Israelachvili. *Intermolecular and Surface Forces.* Academic Press, 3rd edition, 2011.

[188] J. A. Stroscio and D. M. Eigler. Atomic and molecular manipulation with the scanning tunneling microscope. *Science*, 254(5036):1319–1326, 1991.

[189] Paul Constantin Rusu. *Charge transfer and dipole formation at metal-organic interface.* PhD thesis, University of Twente, 2007.

[190] F. Terenziani, A. Painelli, and Z. G. Soos. Static polarizability of molecular materials: Environmental and vibrational contributions. In George Maroulis, editor, *Computational aspects of electric polarizability calculations: Atoms, molecules and clusters*, pages 469–487. IOS Press, University of Patras, Greece, 2006.

[191] E.V. Tsiper and Z. G. Soos. Charge redistribution and polarization energy of organic molecular crystals. *Phys. Rev. B*, 64:195124, 2001.

[192] P. H. Moon and D. E. Spencer. *Field Theory for Engineers.* Van Nostrand, 1961.

[193] O. Bauer, G. Mercurio, M. Willenbockel, W. Reckien, C. H. Schmitz, B. Fiedler, S. Soubatch, T. Bredow, F. S. Tautz, and M. Sokolowsk. Role of functional groups in surface bonding of planar π-conjugated molecules. *Phys. Rev. B*, 86:235431, 2012.

[194] T. Sonnleitner, I. Swart, N. Pavlicek, A. Pöllmann, and J. Repp. Molecular symmetry governs surface diffusion. *Phys. Rev. Lett.*, 186103, 2011.

[195] E. Ganz, S. K. Theiss, I.-S. Hwang, and J. Golovchenko. Direct measurement of diffusion by hot tunneling microscopy - activation energy, anisotropy, and long jumps. *Phys. Rev. Lett.*, 68:1567, 1992.

[196] H. Risken. *The Fokker-Planck Equation.* Springer, 2nd edition, 1989.

[197] S. W. Schmucker, N. Kumar, J. R. Abelson, S. R. Daly, G. S. Girolami, M. R. Bischof, D. L. Jaeger, R. F. Reidy, B. P. Gorman, J. Alexander, J. B. Ballard, J. N. Randall, and J. W. Lyding. Field-directed sputter sharpening for tailored probe materials and atomic-scale lithorgraphy. *Nature Communications*, 3(935):1–8, 2012.

[198] D. P. Adams, T. M. Mayer, and B. S. Swartzentruber. Nanometer-scale lithography on Si(001) using adsorbed H as an atomic layer resist. *J. Va. Sci. Tech. B*, 14:1642, 1996.

[199] Alexander le Fèbre. *Field emission sensing for non-contact probe recording.* PhD thesis, Universiteit Twente, 2008.